

ASSESSMENT OF DEWATERING / DEPRESSURIZATION REQUIREMENTS  
FOR THE CELTIKCI COAL BASIN, ANKARA - TURKEY

A THESIS SUBMITTED TO  
THE GRADUATE SCHOOL OF NATURAL AND APPLIED SCIENCES  
OF  
MIDDLE EAST TECHNICAL UNIVERSITY

BY

AYŞE PEKSEZER SAYIT

IN PARTIAL FULFILLMENT OF THE REQUIREMENTS  
FOR  
THE DEGREE OF DOCTOR OF PHILOSOPHY  
IN  
GEOLOGICAL ENGINEERING

NOVEMBER 2019



Approval of the thesis:

**ASSESSMENT OF DEWATERING / DEPRESSURIZATION  
REQUIREMENTS FOR THE CELTIKCI COAL BASIN, ANKARA -  
TURKEY**

submitted by **AYŞE PEKSEZER SAYIT** in partial fulfillment of the requirements for the degree of **Doctor of Philosophy in Geological Engineering Department, Middle East Technical University** by,

Prof. Dr. Halil Kalıpçılar  
Dean, Graduate School of **Natural and Applied Sciences**

\_\_\_\_\_

Prof. Dr. Erdin Bozkurt  
Head of Department, **Geological Engineering**

\_\_\_\_\_

Prof. Dr. Hasan Yazıcıgil  
Supervisor, **Geological Engineering, METU**

\_\_\_\_\_

**Examining Committee Members:**

Prof. Dr. Mehmet Ekmekçi  
Hydrogeological Engineering Dept., Hacettepe University

\_\_\_\_\_

Prof. Dr. Hasan Yazıcıgil  
Geological Engineering, METU

\_\_\_\_\_

Prof. Dr. M. Zeki Çamur  
Geological Engineering Dept., METU

\_\_\_\_\_

Assist. Prof. Dr. Levent Tezcan  
Hydrogeological Engineering Dept., Hacettepe University

\_\_\_\_\_

Assoc. Prof. Dr. Özlem Yağbasan  
Geography Teaching Dept., Gazi University

\_\_\_\_\_

Date: 15.11.2019

**I hereby declare that all information in this document has been obtained and presented in accordance with academic rules and ethical conduct. I also declare that, as required by these rules and conduct, I have fully cited and referenced all material and results that are not original to this work.**

Name, Surname: Ayşe Peksezer Sayıt

Signature:

## **ABSTRACT**

### **ASSESSMENT OF DEWATERING / DEPRESSURIZATION REQUIREMENTS FOR THE CELTIKCI COAL BASIN, ANKARA - TURKEY**

Peksezer Sayıt, Ayşe  
Doctor of Philosophy, Geological Engineering  
Supervisor: Prof. Dr. Hasan Yazıcıgil

November 2019, 180 pages

The dewatering requirements and their anticipated impacts on groundwater resources were evaluated for both open pit and a representative longwall panel using a 3D numerical groundwater flow model developed by FEFLOW software. Eleven years of mining in the open pit was simulated by hydraulic head boundary conditions, whereas the modulation functions were used to de-/activate boundary conditions according to mine advance. The simulation results indicate that average groundwater inflow rate to the open pit is 79 L/s excluding the effects of direct rainfall and surface water flow from the benches. The impact of 11 years of mining in the area is evaluated in terms of (i) timewise change of baseflow component of Kirmir stream, and (ii) areal distribution of cone of depression. The longwall mine simulations, on the other hand, were conducted for a representative panel, where modulation functions are used to simulate the mine advance and time varying material properties are utilized in the simulation of changes in hydraulic parameters. Six different simulations were conducted where the complexity in the system that will result from longwall mining was increased progressively. The average groundwater inflow to the panel ranges from 261 L/s to 444 L/s based on the simulation results. The impacts of longwall mining are assessed in terms of (i) simulated water table profile at the end of mining, (ii) areal

distribution of the cone of depression and (iii) timewise change of simulated hydraulic head values at the monitoring wells in the vicinity of the panel.

Keywords: Open Pit, Longwall Mining, FEFLOW, Numerical Modeling, Impact Assessment

## ÖZ

### ÇELTİKÇİ KÖMÜR HAVZASI İÇİN SUSUZLAŞTIRMA / BASINÇSIZLANDIRMA GEREKSİNİMLERİNİN DEĞERLENDİRİLMESİ, ANKARA - TÜRKİYE

Peksezer Sayıt, Ayşe  
Doktora, Jeoloji Mühendisliği  
Tez Danışmanı: Prof. Dr. Hasan Yazıcıgil

Kasım 2019, 180 sayfa

Açık ocak ve temsili bir uzunayak paneli için susuzlaştırma gereksinimlerinin belirlenmesi ve yeraltısuyu sistemine etkilerinin değerlendirilmesi amacıyla FEFlow yazılımı kullanılarak 3 boyutlu sayısal yeraltısuyu akım modeli geliştirilmiştir. Açık ocakta onbir yıl sürmesi beklenen madencilik faaliyetleri hidrolik yük sınır koşulu kullanılarak simüle edilirken, modülasyon fonksiyonları madenciliğin ilerleyişine bağlı olarak sınır koşullarının aktif olup olmamasını sağlamıştır. Simülasyon sonuçlarına göre, açık ocağa gelecek ortalama yeraltısuyu miktarı, doğrudan yağış ve ocak yamaçlarından gelecek yüzeysuyu akışı hariç, 79 L/s'dir. Onbir yıllık madenciliğin etkileri (i) Kırmir çayı baz akım bileşeninin zamana karşı değişimi ve (ii) düşüm konisinin alansal dağılımı kullanılarak değerlendirilmiştir. Diğer taraftan, uzunayak madencilik simülasyonları ise temsili bir panel için yapılmış, madenciliğin ilerleyişi modülasyon fonksiyonları, zamana bağlı değişen materyal özellikleri ise hidrolik parametrelerin değişimini simüle etmek amacıyla kullanılmıştır. Uzunayak madenciliği sonucu, sistemdeki karmaşıklığın arttığı altı adet simülasyon yapılmıştır. Simülasyon sonuçları, panele gelecek ortalama yeraltısuyu akış değerlerinin 261 L/s ile 444 L/s arasında değiştiğini göstermektedir. Uzunayak madenciliği sonucu yapılan susuzlaştırma çalışmalarının etkileri ise (i) madencilik sonucunda oluşan su tablası

profili, (ii) dūřüm konisinin alansal dađılımı ile (iii) panel evresinde yer alan gzlem kuyularında simüle edilen hidrolik yk deđerlerinin zamana karřı deđiřimi aılarından deđerlendirilmiřtir.

Anahtar Kelimeler: Aık Ocak, Uzunayak Madenciliđi, FEFlow, Sayısal Modelleme, Etki Deđerlendirmesi

To my beloved family, Kaan and Alp...

## ACKNOWLEDGEMENTS

I would like to thank my supervisor Prof. Dr. Hasan Yazıcıgil for his support, guidance, criticism, encouragement and trust not only for this study but also for each project I was involved. He always give me the chance to work in different projects with different difficulty levels. With his guidance and valuable perspective on the concepts, I had the opportunity to overcome the problems every time. His unique approach in teaching contributes a lot to my academic progress.

I would also like to thank Prof. Dr. M. Zeki Çamur and Assoc. Prof. Dr. Koray K. Yılmaz for their valuable contributions in the projects, which formed the basis of my thesis. I am also grateful to Assist. Prof. Dr. Levent Tezcan for his tolerance and gentillesse in addition to his theoretical support and perspective on the modeling part.

Thanks are extended to Asia Minor Mining for funding the projects entitled “Hydrogeological Characterization and Investigation of the Çeltikçi Coal Basin”, “Water Supply Evaluation of Çeltikçi Coal Mine and Thermal Plant”, and “Groundwater Flow Model Development, Dewatering System Design and Impact Assessment of Çeltikçi Coal Basin”, which formed the basis for this thesis.

Special thanks are for my colleagues and dear roommates Hatice Kılıç Germeç and Çidem Argunhan Atalay, who not only share the room but also the joy and grief associated with the academic life. With their support, kindness, understanding and friendship, even tough times become lovely memories.

My deepest gratitude are for my dear parents, my sister, my grandmother and also other family members for their endless love, care, support and encouragement throughout my life.

My final words are for Kaan Sayıt, who is the love of my life, a great academician, great husband and the greatest father that I know. Without his love, support and encouragement, this thesis would not be possible.

## TABLE OF CONTENTS

ABSTRACT .....	v
ÖZ .....	vii
ACKNOWLEDGEMENTS .....	x
TABLE OF CONTENTS .....	xi
LIST OF TABLES .....	xv
LIST OF FIGURES .....	xvi
CHAPTERS	
1. INTRODUCTION .....	1
1.1. Purpose and Scope.....	2
1.2. Location of the Study Area.....	3
1.3. Previous Studies .....	3
2. LITERATURE SURVEY .....	5
2.1. Open Pit Mining .....	5
2.2. Underground Mining .....	6
3. DESCRIPTION OF THE STUDY AREA .....	9
3.1. Topography .....	9
3.2. Climate and Meteorology .....	9
3.2.1. Precipitation .....	12
3.2.2. Temperature .....	17
3.2.3. Relative Humidity .....	19

3.2.4. Evaporation .....	19
3.3. Geology.....	20
3.3.1. Regional Geology.....	20
3.3.2. Local Geology .....	21
3.3.2.1. Stratigraphy.....	21
3.3.2.2. Structural Geology.....	27
4. HYDROGEOLOGY .....	29
4.1. Water Resources .....	29
4.1.1. Surface Water Resources.....	29
4.1.2. Spring and Fountains.....	36
4.1.3. Wells.....	40
4.2. Hydrogeology of the Study Area .....	42
4.2.1. Hydraulic Parameters .....	46
4.2.2. Groundwater Levels .....	49
4.2.2.1. Spatial variations in groundwater levels.....	49
4.2.2.2. Temporal variations in groundwater levels .....	51
5. CONCEPTUAL MODEL .....	55
5.1. Conceptual Model of the Study Area.....	55
5.2. Conceptual Hydrologic Budget.....	56
5.3. Conceptual Groundwater Budget.....	59
5.3.1. Upper Aquifer.....	59
5.3.2. Lower Aquifer .....	62
6. GROUNDWATER FLOW MODEL .....	65
6.1. Computer Code .....	65

6.2. Model Geometry and Layering .....	66
6.2.1. Layer Design.....	66
6.2.2. Mesh Design .....	67
6.3. Boundary Conditions.....	68
6.4. Model Parameters .....	70
6.4.1. Recharge .....	71
6.4.2. Hydraulic Conductivity.....	71
6.4.3. Storage Parameters .....	74
6.5. Calibration .....	75
6.5.1. Groundwater Levels.....	75
6.5.2. Baseflow .....	77
6.5.3. Calibrated Groundwater Budget .....	78
6.6. Sensitivity Analysis .....	80
7. OPEN PIT DEWATERING .....	85
7.1. Open Pit Dewatering Requirements .....	85
7.2. Groundwater Levels After Open Pit Dewatering .....	89
7.3. Impacts of Open Pit Dewatering on Groundwater Resources.....	90
8. UNDERGROUND MINE DEWATERING.....	93
8.1. Impacts of the Longwall Mining on the Groundwater System .....	94
8.1.1. Changes in Hydraulic Conductivity.....	100
8.1.2. Change in Storage Capacity.....	101
8.2. Dewatering Requirements of Longwall Panel.....	102
8.2.1. Steady State Dewatering .....	104
8.2.2. Transient Dewatering.....	106

8.2.2.1. Simulation No. 1 .....	107
8.2.2.2. Simulation No. 2 .....	109
8.2.2.3. Simulation No. 3 .....	111
8.2.2.4. Simulation No. 4 .....	113
8.2.2.5. Simulation No. 5 .....	115
8.2.2.6. Simulation No. 6 .....	116
8.3. Impacts of Longwall Panel Dewatering on Groundwater Resources .....	122
8.3.1. Simulation No. 2 .....	123
8.3.2. Simulation No. 4 .....	127
8.3.3. Simulation No. 6 .....	130
9. DISCUSSION .....	135
9.1. Open Pit Simulations .....	135
9.2. Longwall Simulations .....	136
10. CONCLUSIONS AND RECOMMENDATIONS .....	141
REFERENCES .....	147
A. Surface Water Flow Rates .....	157
B. Spring / Fountain Discharge Measurements .....	161
C. Groundwater Level Measurements .....	167
CURRICULUM VITAE .....	179

## LIST OF TABLES

### TABLES

Table 3.1. Information about meteorological stations .....	12
Table 3.2. Estimation of long-term monthly precipitation value for the Çeltikçi meteorological station .....	17
Table 4.1. Information about the dams located in and around the study area.....	31
Table 4.2. Information about the stream gauging stations in the vicinity of the study area .....	31
Table 4.3. Information about the surface water monitoring points.....	35
Table 4.4. Information about the springs / fountains .....	38
Table 4.5. Well details for the wells drilled by the Bank of Provinces, pumping and monitoring wells .....	43
Table 4.6. Summary of the calculated hydraulic conductivity and storativity parameters of formations.....	48
Table 4.7. Summary of the calculated hydraulic conductivity and storativity parameters of composite wells .....	49
Table 5.1. Monthly conceptual water budget results .....	60
Table 5.2. Annual water budget results.....	61
Table 5.3. Conceptual groundwater budget .....	63
Table 6.1. Hydraulic conductivity values assigned to the model.....	73
Table 6.2. Calibrated groundwater budget.....	78
Table 6.3. Comparison of the conceptual and calibrated model budgets.....	79
Table 8.1. Assigned hydraulic conductivity values at the goaf and collapsed zone for Simulation No. 6 .....	119
Table 10.1. Summary of calculated groundwater inflow rates for longwall simulations .....	143

## LIST OF FIGURES

### FIGURES

Figure 1.1 Location map of the study area .....	4
Figure 3.1. Topographic contour distribution and location of hills within the study area .....	10
Figure 3.2. Digital elevation model of the study area.....	10
Figure 3.3. Location of the meteorological stations in the vicinity of study area .....	11
Figure 3.4. Annual precipitation and cumulative deviation from mean annual precipitation graph for the Kızılcama station .....	13
Figure 3.5. Mean monthly precipitation data for the Kızılcama and Çeltikçi stations (1987 – 1993) .....	13
Figure 3.6. Monthly total precipitation values measured in the Kızılcama station for the 2012 – 2015 period.....	14
Figure 3.7. Scatter diagrams for monthly total precipitation data of the Kızılcama and Çeltikçi meteorological stations (1986 – 1994) .....	16
Figure 3.8. Mean monthly, monthly average minimum and monthly average maximum temperature graphs .....	18
Figure 3.9. Mean monthly relative humidity graph .....	19
Figure 3.10. Mean monthly evaporation graph .....	20
Figure 3.11. Regional geological map (a) and generalized columnar section (b) (modified from Rojay, 2013).....	21
Figure 3.12. Geological map of the study area (modified from AMM, 2015 & MTA maps).....	22
Figure 3.13. Geological cross sections .....	23
Figure 3.14. Generalized columnar section (AMM, 2015) .....	24
Figure 4.1. Location of the stream gauging stations, dams, and watersheds of the Kirmir stream and Kurtboğazi creek .....	30

Figure 4.2. Monthly average flow rates measured at the Kızılcahamam – Mandra stream gauging station for 1960 – 2013 period.....	32
Figure 4.3. Monthly average flow rates measured at the Kızılcahamam – Mandra stream gauging station for the periods of 1960 – 1991 and 1992 – 2013 .....	33
Figure 4.4. Location of the surface water monitoring points.....	34
Figure 4.5 Location of the springs .....	37
Figure 4.6. Location of the springs on the geological map.....	37
Figure 4.7. Location of the wells drilled within the study area (close-up view of the monitoring and pumping wells on geology is also shown).....	41
Figure 4.8. Groundwater level map of the area on geological map .....	50
Figure 4.9. Groundwater levels measured in the nested wells.....	52
Figure 5.1. Area showing the conceptual groundwater budget calculation is conducted .....	61
Figure 6.1. Model domain and dimensions.....	66
Figure 6.2. Finite element mesh design and layering (a: 3D view of the model domain, b: finite element mesh of the slice 1, c: A-A' cross section showing the model layers) .....	68
Figure 6.3. Delaunay criteria (a) violates, (b) obeys the criteria.....	69
Figure 6.4. Boundary conditions applied to the model .....	70
Figure 6.5. Aerial distribution of recharge in the model domain.....	72
Figure 6.6. Hydraulic conductivity distribution within the model (above: slice 1 and below: cross sections (AA' and BB')) .....	74
Figure 6.7. Observed vs calculated groundwater levels.....	76
Figure 6.8. Calculated groundwater levels and comparison of the observed and calculated groundwater levels .....	77
Figure 6.9. Sensitivity analysis of hydraulic conductivities of lithologies .....	82
Figure 6.10. Sensitivity analysis of recharge from precipitation .....	82
Figure 6.11. Sensitivity analysis of hydraulic conductivities of faults .....	83
Figure 7.1. Yearly progress of open pit.....	87
Figure 7.2. Simulated groundwater inflow rate to the open pit .....	87

Figure 7.3. Calculated maximum, minimum and average groundwater inflow rates throughout the mine life.....	88
Figure 7.4. Time wise change of the groundwater inflow rate to the pit for different hydraulic conductivity values assigned to the Kirmir 2 and Karataş faults .....	89
Figure 7.5. Simulated groundwater levels and pit bottom elevations at the observation wells after open pit dewatering.....	90
Figure 7.6. Change of baseflow component of the Kirmir stream during the operational period of open pit.....	91
Figure 7.7. Simulated drawdown contours at the end of open pit dewatering .....	92
Figure 8.1. Lower seam layout .....	95
Figure 8.2. Upper seam layout.....	95
Figure 8.3. (a) Plan view of a typical longwall mine layout and (b) schematic view of the fracture system developed as a result of longwall mining.....	96
Figure 8.4. Schematic view of the hydrological response zone .....	97
Figure 8.5. Cross-section view along the short dimension of a panel showing parameters that affect the height of groundwater inflow zone (H).....	98
Figure 8.6. Expected post-mining hydraulic head profile above the longwall panels (modified from Tammeta 2013) .....	99
Figure 8.7. Conceptual model proposed by Tammeta (2015) .....	101
Figure 8.8. Hydrogeological conceptual model developed by Tammeta (2015) ....	102
Figure 8.9. Location of the selected panel .....	103
Figure 8.10. Location of the selected panel on geological map .....	104
Figure 8.11. Hydraulic head profile along the section passing through the center of the panel: (a) continuous hydraulic head field with zero pressure contours (white lines), and (b) hydraulic head contours .....	105
Figure 8.12. Schematic representation of longwall mine progress, selected panel is divided into 12 subregions.....	108
Figure 8.13. Simulated groundwater inflow rate into the panel with respect to time for Simulation No. 1.....	108

Figure 8.14. Schematic representation of longwall mine progress, selected panel is divided into 36 subregions .....	109
Figure 8.15. Simulated groundwater inflow rate into the panel with respect to time for Simulation No. 2 .....	110
Figure 8.16. Comparison of the calculated groundwater inflow rates of Simulation No. 1 and Simulation No. 2 .....	110
Figure 8.17. Hydraulic conductivity change of the goaf with respect to time and mine progress in Simulation No. 3.....	112
Figure 8.18. Simulated groundwater inflow rate into the panel with respect to time for Simulation No. 3 .....	112
Figure 8.19. Comparison of the calculated groundwater inflow rates of Simulation No. 2 and Simulation No. 3 .....	113
Figure 8.20. Comparison of the hydraulic conductivity change with respect to time simulated at (a) Simulation No. 3, and (b) Simulation No. 4.....	114
Figure 8.21. Simulated groundwater inflow rate into the panel with respect to time for Simulation No. 4 .....	115
Figure 8.22. Comparison of the calculated groundwater inflow rates of Simulation No. 3 and Simulation No. 4 .....	115
Figure 8.23. (a) Schematic representation of the assigned hydraulic conductivity field in the goaf and collapsed zone, and (b) Hydraulic conductivity change of the goaf and collapsed zone with respect to time and mine progress in Simulation No. 5 .....	117
Figure 8.24. Simulated groundwater inflow rate into the panel with respect to time for Simulation No. 5 .....	118
Figure 8.25. Hydraulic conductivity change of the goaf and collapsed zone with respect to time and mine progress in Simulation No. 6 .....	120
Figure 8.26. Simulated groundwater inflow rate into the panel with respect to time for Simulation No. 6 .....	121
Figure 8.27. Comparison of the calculated groundwater inflow rates of Simulation No. 5 and Simulation No. 6 .....	121

Figure 8.28. Location of the monitoring wells used in the impact assessment of longwall mining .....	123
Figure 8.29. Water table profile as a result of Simulation No. 2.....	124
Figure 8.30. Simulated drawdown contours at day 3960 for Simulation No. 2 .....	125
Figure 8.31. Simulated time vs hydraulic head change at the monitoring points as a result of Simulation No. 2.....	126
Figure 8.32. Simulated cone of depression of Simulation No. 2 at the upper aquifer .....	126
Figure 8.33. Water table profile as a result of Simulation No. 4.....	127
Figure 8.34. Simulated drawdown contours at day 3960 for Simulation No. 4 .....	128
Figure 8.35. Simulated time vs hydraulic head change at the monitoring points as a result of Simulation No. 4.....	129
Figure 8.36. Simulated cone of depression of Simulation No. 4 at the upper aquifer .....	130
Figure 8.37. Water table profile as a result of Simulation No. 6.....	131
Figure 8.38. Simulated drawdown contours at day 3960 for Simulation No. 6 .....	131
Figure 8.39. Simulated time vs hydraulic head change at the monitoring points as a result of Simulation No. 6.....	132
Figure 8.40. Simulated cone of depression of Simulation No. 6 at the upper aquifer .....	133

## **CHAPTER 1**

### **INTRODUCTION**

Water in mining excavations can cause many problems in terms of operational, economic and safety point of view; including flooding, delaying of operation, slope instability, increase in drilling costs, etc. (Aryafar et al., 2009; Connelly and Gibson, 1985; Fernandez-Rubio and Lorca, 1993). In order to satisfy dry and safe working conditions, dewatering requirements should be determined and accomplished prior to mining. Depressurization, on the other hand, is necessary to lower the pressure in the deep aquifer to avoid floor heave and instability and to maintain safe operating conditions as mine develops in size and depth.

In the prediction of the groundwater inflow rate to open cast mines, many approaches ranging from simple analytical methods to complex numerical models have been widely used. The selection of the modeling approach is based on the scale of the problem, availability of data, hydrogeological conditions, etc. On the other hand, studies that estimate the groundwater inflow rate to underground panels are very limited due to the complex nature of the longwall mining. The longwall mining brings along strata collapse phenomena, which results in intense fracturing and change of geotechnical and hydraulic properties of the overlying strata. Hence, conversion of the confined systems to unconfined, change in groundwater recharge and discharge mechanisms, loss of surface water, etc. are widely observed.

The studies also indicate that dewatering applies significant stress on the regional groundwater flow system, and hence can negatively affect groundwater resources. Drying of the water supply wells and springs as a result of lowering of water table, decrease in the baseflow rates, subsidence, changing in water quality and formation of sinkholes can be given as some examples of the impacts of dewatering (Ardejani et

al., 2003; Brunetti et al., 2013; Booth 2006; Younger et al., 2002; Thomas, 2013, Ekmekci and Yazicigil 2016).

Although assessment of dewatering requirements of open pit with the help of numerical models were studied for different mines in Turkey (Unsal and Yazicigil 2016; Peksezer-Sayit et al. 2015), the prediction of the amount of groundwater inflow to underground mines with the help of numerical models is a new topic. This study intends to determine the amount of groundwater inrush with respect to time for both the open pit and underground panels throughout the mine life, and evaluate the anticipated impacts of dewatering/depressurization on the groundwater resources.

### **1.1. Purpose and Scope**

The main purposes of this study are:

- to quantify dewatering/depressurization requirements by predicting the groundwater inflow rates of open pit and longwall panels according to mine advance,
- to assess the impacts of both open pit and longwall dewatering on groundwater resources.

In order to achieve the purposes given above, the available topographical, meteorological, geological, hydrological, and hydrogeological data related to the site were compiled and reviewed, and hydrogeological characterization of the site was completed. Following the characterization, a conceptual model was developed, and a numerical three-dimensional groundwater flow model was constructed and calibrated in order to use it as a tool to simulate the operational and the post-closure groundwater system. Finally, dewatering simulations and their impacts on the groundwater resources were evaluated using the calibrated model under transient conditions.

## **1.2. Location of the Study Area**

The study area is located approximately 50 km northwest of the Ankara, Turkey. It is bounded by the amlidere dam reservoir in the north and Kurtboęazi dam reservoir in the east, covering an area of 602.5 km<sup>2</sup>. The study area lies between 32°22'36''-32°40'42'' E (UTM 446900 – 475000) longitudes and 40°12'51'' - 40°27'35'' N (UTM 4452300 – 4478900) latitudes. The largest settlement in the study area is eltiki district, located at the junction of Kirmir and Pazar streams. The other settlements in the area are Bezcikuzören, Kocalar, Doęanözü, Ařaęıadaköy, Demirciören, Kızılca, Alibey, Binkoz, avuřlar, Mahkemeaęcın, Deęirmenönü, Doymuřören, Baęlıca and Gümele villages (Figure 1.1).

## **1.3. Previous Studies**

The recent geological studies about the eltiki Coal basin were conducted by Asia Minor Mining within the scope of 43-101 Technical Report (2012), Rojay (2013) and AMM (2015). The 1/25000 and 1/100000 scaled geological maps of the area were published by the General Directorate of Mineral Research and Exploration (MTA).

The hydrological and hydrogeological studies related to the eltiki coal basin are recent and comprehensive. Yazıcıgil et al. (2014) conducted the hydrological and hydrogeological characterization of the area. Following the characterization, a study covering groundwater flow model development, dewatering well design and its impacts on groundwater resources was also conducted by Yazıcıgil et al (2015a). In addition, water supply evaluation of the coal mine and thermal power plant was also assessed by Yazıcıgil et al. (2015b). The groundwater and surface water interaction in Kirmir Stream is investigated using thermal remote sensing and in-stream measurements (Varlı and Yılmaz 2018). Apart from them, in 2007, the Bank of Provinces drilled three water supply wells in the alluvium of the Pazar stream. Also, in 2008, the planning report of Doęanözü Dam was prepared by Akar-Su Engineering and Consultancy Co. Ltd. for the 5<sup>th</sup> Regional Directorate of State Hydraulic Works (DSİ).



## CHAPTER 2

### LITERATURE SURVEY

#### 2.1. Open Pit Mining

Dewatering applications in open pit mines are required to obtain dry and safe working conditions. The problems that may arise due to inadequate dewatering can be listed as flooding, slope stability problems, equipment corrosion, etc (Aryafar et al. 2009; Connelly and Gibson 1985; Fernandez-Rubio and Lorca 1993; Morton and Mekerck 1993; Williamson and Vogwill 2001).

Both analytical and numerical models have been widely used to estimate the rate of groundwater inflow to the mine excavations based on the scope of the study. Analytical methods are preferred when a preliminary rate is required, mainly at the prefeasibility phase, since these methods involve simplifying assumptions, which brings uncertainty about the validity of the assumptions (Fontaine et al. 2003; Marinelli and Niccoli 2000; Singh and Atkins 1985). On the other hand, numerical models can simulate more complex systems (Ardejani et al. 2003; Aryafar et al. 2009; Bochenska et al. 2000; Brouyere et al. 2009; Rapantova et al. 2007; Zaidel et al. 2010, Peksezer-Sayit et al. 2015). The selection of the modeling approach depends on site conditions, available data, scale of the model and type of mining, etc. (Adams and Younger 2001). In the design of dewatering systems, optimization techniques are also used (Jiang et al. 2013, Tokgoz et al. 2002).

Dewatering can apply significant stresses to groundwater system, and hence impact assessment is an important issue in dewatering studies. The main impacts of dewatering on groundwater resources include loss of community water supply as water table declines, drying of springs, decrease in the baseflow rates, subsidence, changing in water quality, formation of sinkholes, etc. (Booth 2006, Ardejani et al.

2003, Brunetti et al. 2013, Younger et al., 2002; Thomas, 2013, Ekmekci and Yazicigil 2016).

As the dewatering ceases at the open pit mines, the water table starts to rise at the excavated area, unless the pit will backfilled. Groundwater inflow to the pit along with direct precipitation and surface runoff will result in formation of pit lake (Castendyk and Eary 2009, Gammons 2009). The shape and orientation of the pit as well as climatic conditions affect the interaction of the pit and surrounding groundwater regime (Huber et al. 2008, Miller et al. 1996). There are many studies where numerical models are used in simulation of open pit dewatering and pit lake formation (Jones 2002, Dowling et al. 2004, Müller and Eulitz 2010, Unsal and Yazıcıgil 2016).

## **2.2. Underground Mining**

Underground coal mining is mainly achieved by room and pillar or longwall mining methods. Although room and pillar method is widely used in traditional coal mining, with the improved coal extraction rates, reduced costs and safe working conditions longwall mining is gaining popularity in coal mining industry. In the Çeltikçi coal basin, in addition to open pit mining, underground mining will be conducted by longwall method. Therefore, in this chapter, literature including longwall mining and its impacts is presented.

The strata collapse phenomena resulted from longwall mining applies significant pressure to the overlying layers, which modifies geomechanical behavior of the system. The numerical models that simulate stresses associated with longwall mining are widely used in the literature (Vakili et al. 2010, Pongpanya et al. 2017, Wang and Park 2003). The most commonly used codes include FLAC 3D and Map3D, which can simulate both the small strain and large strain behavior of the system. The propagation of the fractured zone due to longwall mining can also be determined with FLAC 3D models (Wu et al. 2015).

The longwall mining impacts the groundwater system due to groundwater inflow to the mine and change in hydraulic properties of the overlying strata as a result of

deformation. The strata deformation associated from mining and anticipated impacts on the groundwater system was studied conceptually by Booth in 1986. Kendorski (1993) developed a well accepted subsurface model which conceptually represents the hydrological responses of the overlying subsided strata to the longwall mining.

The determination of the height of the fractured zone developed as a result of longwall mining plays an important role since major changes in the system occurs at that zone. Many empirical equations are developed to relate the height of the fracture zone (Sing and Kendorski 1981, Kesseru 1982, Garritty 1983, Singh 1986, Kendosrky 2006, Tammeta 2013).

The information about the impacts of longwall mining on water resources is mainly obtained from monitoring data, where pre-mining and post-mining groundwater levels, surface water flows or spring discharge rates are intensely observed. The loss of surface water flow or swamps, decline in groundwater levels due to dilation of fractures, change in water quality can be given as some examples of impacts of longwall mining on water resources (Kadnuck 1995, Booth et al. 1998, Booth et al. 2000, Bell and Genske 2001, Booth 2007, Kibria et al. 2012, Fan and Zhang 2015). The change in the recharge and discharge zones due to longwall mining induced change in permeability of the overlying strata and also change in groundwater-surface water interaction are also reported by many (Booth et al. 1998, Jankowski and Spies 2007, Jankowski and Madden 2009).

The change in hydraulic conductivity field due to longwall mining is quantified by pumping and packer tests (Booth and Spande 1992). Also, evaluation of core-log analysis, face advance rates and downhole monitoring data leads to determine the relationship between fracturing and changes in hydraulic conductivity values due to longwall mining (Karacan and Goodman 2009).

The most recent comprehensive conceptual models that evaluates the impact of longwall mining in terms of groundwater were developed by Tammeta (2013, 2015, and 2016).

The attempts to link the strata deformation with groundwater flow models were started in 1995 (Matetic et al. 1995), where a 2D finite element model was developed to couple overlying strata deformation with groundwater flow. A nonlinear finite element model was developed by Elsworth and Liu (1995) to relate the hydraulic conductivity changes with the strain field in order to evaluate the impact of longwall mining on groundwater resources, when premining hydraulic conductivity field, fracture spacing, mining geometry and material properties including Elastic modulus and Poisson ratio data is available in advance. Guo et al. (2009) used a 3D numerical model, namely COSFLOW to simulate mechanical stress changes and deformation of layered strata, which is coupled with two –phase dual porosity model to assess the water and gas flow. In 2015, Li et al. developed a finite element groundwater model namely GGU-SS-FLOW3D to predict pre- and post-mining water tables in the panels under steady state conditions. The simulation optimization models, on the other hand, are used to determine optimal dewatering rates that is required to prevent groundwater inrush to underground coal seams (Meng et al. 2018).

## CHAPTER 3

### DESCRIPTION OF THE STUDY AREA

#### 3.1. Topography

The study area is located on a steep and undulating topography, where the elevations range from 760 – 780 m along the Kirmir stream to 1820 m at the Ardıçlıkıran hill, located along the watershed divide, at the northern part of the area. Another main ridge within the study area is located at the southeastern part of the Binkoz village, where elevations reach 1690 m at the Hıdırdede hill (Figure 3.1). The mean elevation of the whole study area is calculated as 1140 m.

The altitude of the open pit changes between 830 m and 1000 m, at the northwestern corner and southern border, respectively. Similarly, above the longwall panels, the topographic elevations approximately range from 800 m to 1100 m along NW-SE direction.

The digital elevation model (DEM) of the study area was produced from 1/25000 scaled topographical maps, where 10 m interval contours were used. For the area enclosing the mine site, refined DEM obtained from detailed topographical mapping studies conducted by Asia Minor Mining was used. The resulting DEM of the study area is represented by Figure 3.2.

#### 3.2. Climate and Meteorology

The study area is mainly under the influence of continental climate with higher humidity, due to its closeness to the Black Sea region. Based on the Thornthwaite Climate Classification conducted by the Turkish State Meteorological Service, the study area is located in a semi dry – low humid (2<sup>nd</sup> degree mesothermal) climate class. The area is characterized by hot and dry summers and snowy winters, where most of the precipitation is observed in winter and spring.

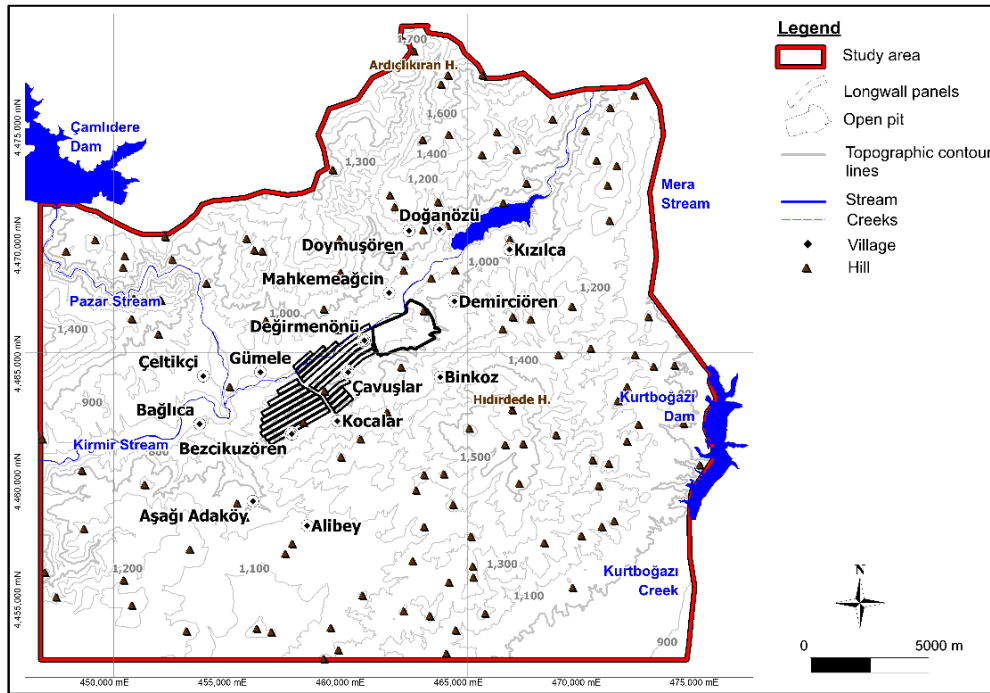


Figure 3.1. Topographic contour distribution and location of hills within the study area

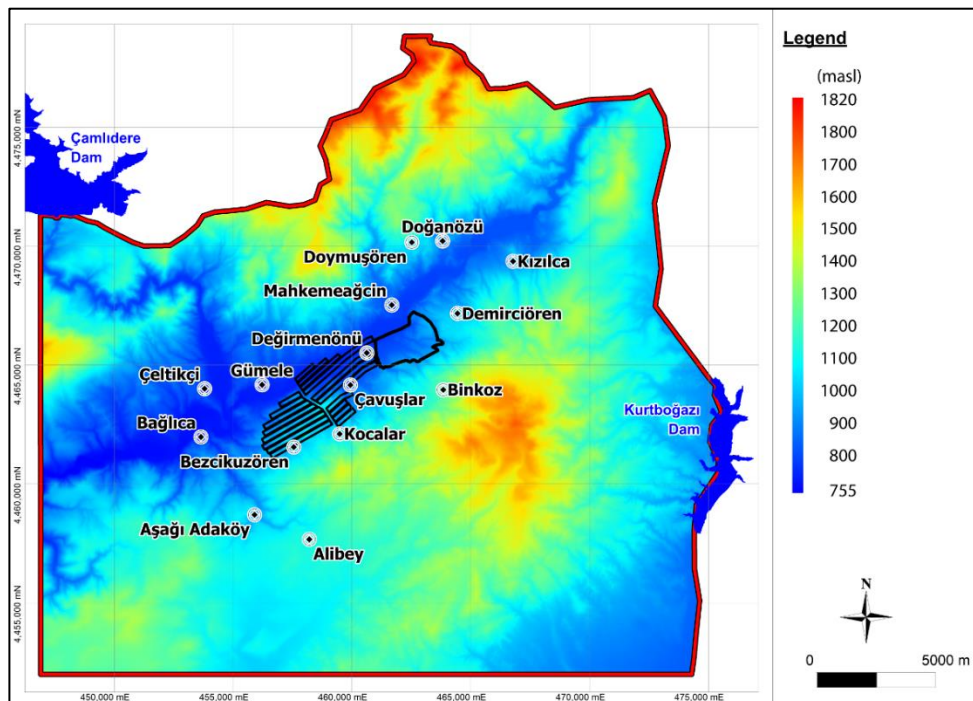


Figure 3.2. Digital elevation model of the study area

In order to determine the meteorological characteristics of the study area, meteorological stations located in the close vicinity of the area were investigated (Figure 3.3). Among them, the Kızılcahamam meteorological station (station no: 17664) has the longest record and the Çeltikçi meteorological station (station no: 2375) is the closest station to the planned mine site. Therefore in this study, these two meteorological stations were used. Although a site-specific meteorological station (i.e. the Binkoz station) was established in May 23, 2013 at the western part of Binkoz village, regular measurements could not be collected due to the malfunction of some sensors. The information about meteorological stations can be seen in Table 3.1.

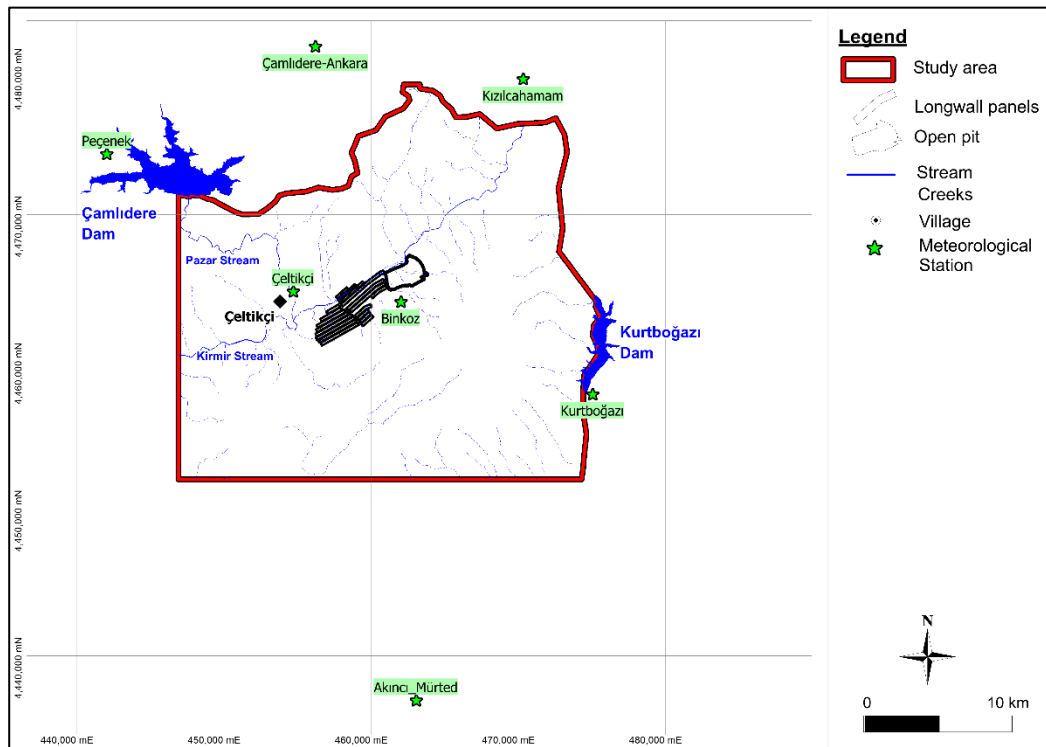


Figure 3.3. Location of the meteorological stations in the vicinity of study area

Table 3.1. *Information about meteorological stations*

Station No	Station Name	Operator	Coordinate (UTM)		Elevation (m)	Operational Period
			Northing	Easting		
-	Binkoz	IKA Mining Inc.	461704	4464083	1083	2013
2375	Çeltikçi	MGM	454700	4464888	775	1986 - 1994
12042	Kurtboğazı	DSI	475046	4457900	981	1965 - 2004
17664	Kızılcahamam	MGM	469831	4480307	1033	1929 - to date
2042	Çamlidere-Ankara	MGM / DSI	456207	4481529	1175	1963 - 1999
2200	Peçenek	MGM	442021	4474233	1042	1988 - 1999
17127	Akıncı-Mürted	MGM	463059	4437093	831	1964 - 2013

### 3.2.1. Precipitation

Kızılcahamam meteorological station was used to determine the long-term precipitation trend of the study area. For the 1957 – 2018 period, annual total precipitation and cumulative deviation from mean annual precipitation graphs were prepared and represented in Figure 3.4. Within the operational period, 1977 is the driest and 2009 is the wettest year, where annual precipitation values are 340 mm and 876 mm, respectively. The mean annual precipitation value is calculated as 578.2 mm. On the other hand, cumulative deviation from mean annual precipitation graph indicates that 1962 – 1972, 1995 – 2001, 2009 – 2012, 2014, and 2016 correspond to wet periods, whereas dry periods are observed between 1957 – 1961, 1973 – 1994, 2002 – 2008, 2013 and 2015.

The average monthly precipitation data measured in Kızılcahamam and Çeltikçi stations are given in Figure 3.5 for the overlapping operational period (i.e. 1987 – 1993). Although the Kızılcahamam station has distinctly more precipitation compared to the Çeltikçi station, both stations show similar precipitation trends. Most of the precipitation (about 60%) is observed in winter and spring, whereas minimum

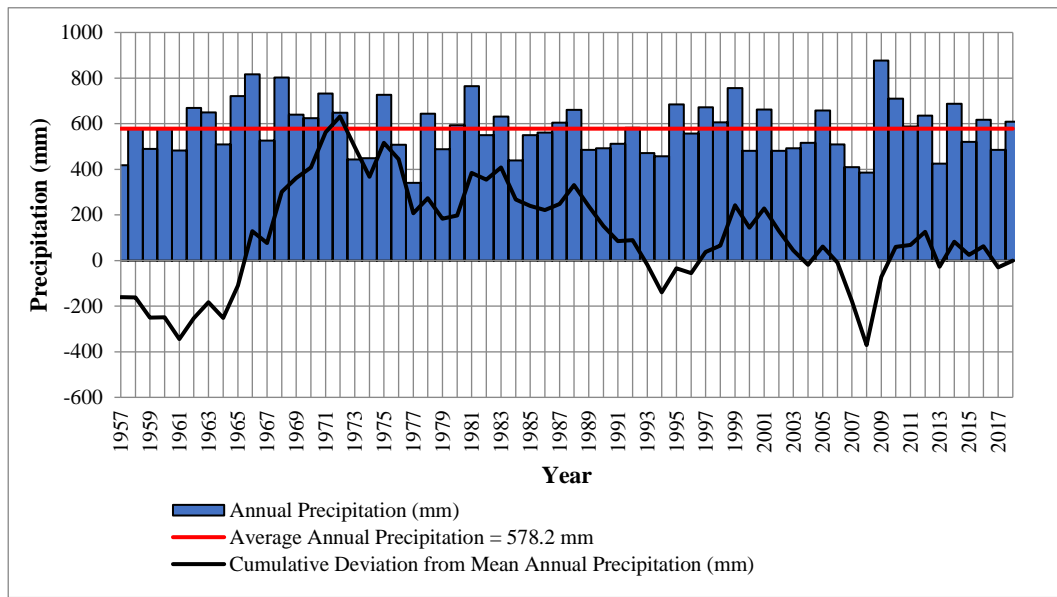


Figure 3.4. Annual precipitation and cumulative deviation from mean annual precipitation graph for the Kızılcahamam station

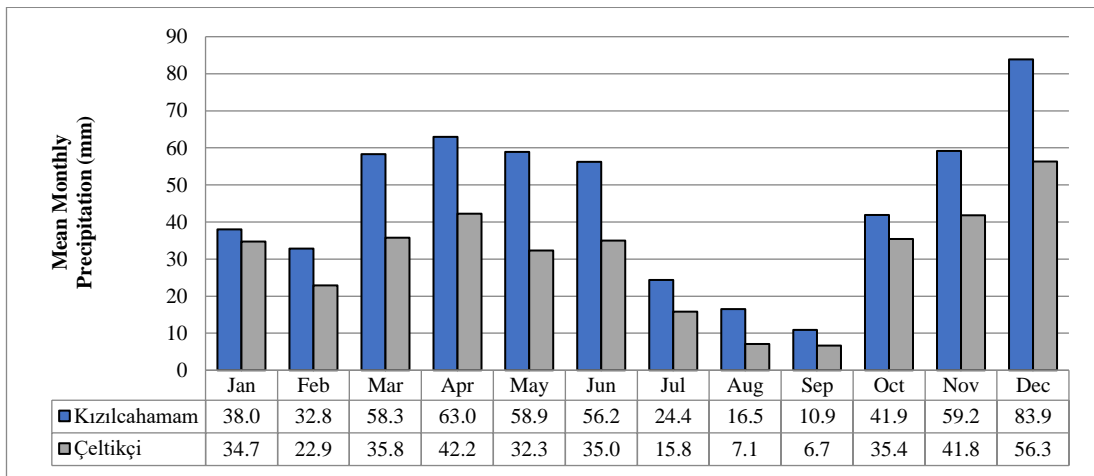


Figure 3.5. Mean monthly precipitation data for the Kızılcahamam and Çeltikçi stations (1987 – 1993)

precipitation (about 15 %) is measured in summer. In both stations, based on the mean monthly precipitation data for 1987 – 1993 years, December is the wettest month, whereas August and September are the driest months. Considering the similarity

between the short-term average monthly precipitation trends of Kızılcahamam and Çeltikçi stations, this similarity is expected to continue in the long term.

The precipitation regime in the study area was also investigated in detail for 2012 – 2015 period, where instantaneous discharge measurements at surface water monitoring points, springs / fountains and groundwater level measurements from wells are actively monitored. The total precipitation values measured in the Kızılcahamam station are 635.6 mm, 425.4 mm, 687.5 mm and 520 mm for 2012, 2013, 2014 and 2015, respectively. The mean monthly precipitation data for 2012 – 2015 period are also shown in Figure 3.6. According to the graph, in winter significant decrease in precipitation is observed in 2013 relative to 2012. Similarly, in 2014, precipitation values in winter are also lower than 2013 for January and February. Although the lowest precipitation values are expected in summer months, in 2012 and 2013, the driest season is autumn.

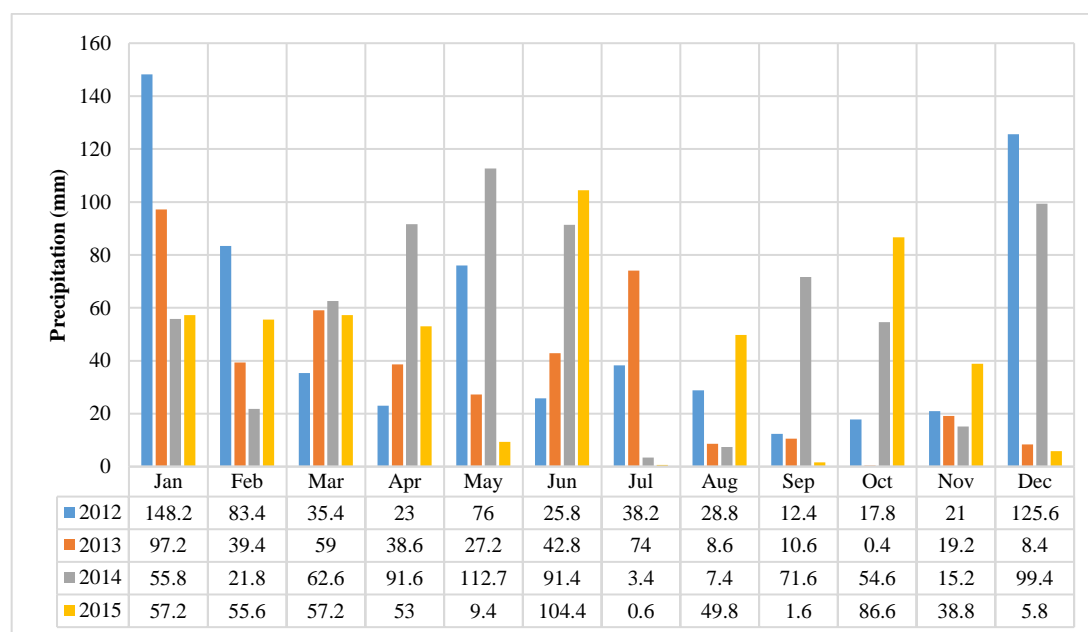


Figure 3.6. Monthly total precipitation values measured in the Kızılcahamam station for the 2012 – 2015 period

The site-specific precipitation data plays a critical role in hydrogeological studies. In the study area, the Çeltikçi and Binkoz meteorological stations are the closest stations to the planned mine site, but due to short-term record periods, they could not be used to determine the long-term precipitation trend in the area. Therefore, having long-term data, the Kızılcahamam meteorological station data are quite important. When the short term average monthly precipitation trends of Kızılcahamam and Çeltikçi stations were examined (Figure 3.5), similar trends were observed, and this similarity is expected to continue in the long term. Hence, in order to obtain site-specific long-term data, the precipitation values measured at the Kızılcahamam station were compared with the Çeltikçi station by using the monthly % bias values for the 1986 – 1994 period.

In the bias correction method, the aim is to obtain a statistical relationship between observed and modeled parameters within the selected historical period. Then, by using this relationship, the measured long-term precipitation data in Kızılcahamam station were corrected, and long-term site-specific precipitation data were obtained.

The scatter plots of monthly precipitation values measured at Kızılcahamam and Çeltikçi meteorological stations are given in Figure 3.7. Since the precipitation values measured in Kızılcahamam station are continuously higher than those of the Çeltikçi station (below 1:1 line (red line) and %bias<0), the precipitation values for the Çeltikçi station were obtained by decreasing the precipitation values of Kızılcahamam station by using calculated %Bias values. The estimated long-term precipitation data for Çeltikçi station are given in Table 3.2. The long-term average annual precipitation value for the study area was determined as 392.4 mm.

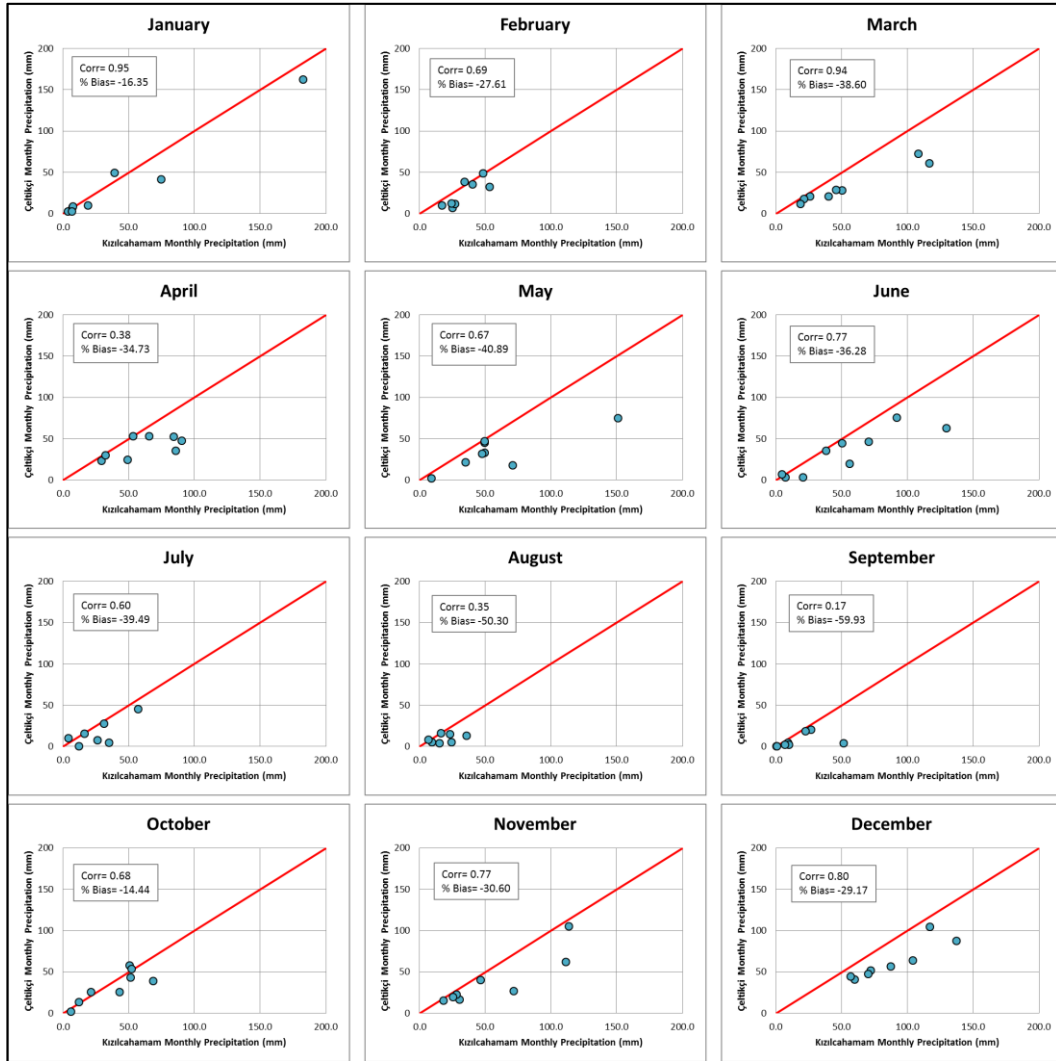


Figure 3.7. Scatter diagrams for monthly total precipitation data of the Kızılcahamam and Çeltikçi meteorological stations (1986 – 1994)

Table 3.2. Estimation of long-term monthly precipitation value for the Çeltikçi meteorological station

	Jan	Feb	Mar	Apr	May	Jun	Jul	Aug	Sep	Oct	Nov	Dec
Kızılcahamam (1957 - 2018)	71.6	55.6	56.3	58.0	62.9	45.7	23.6	21.4	23.2	36.7	44.2	80.8
Kızılcahamam - Çeltikçi (%bias)	-16.4	-27.6	-38.6	-34.7	-40.9	-36.3	-39.5	-50.3	-59.9	-14.4	-30.6	-29.2
Çeltikçi estimated (1957 - 2018)	59.9	40.3	34.6	37.9	37.2	29.1	14.3	10.6	9.3	31.4	30.7	57.2

### 3.2.2. Temperature

The mean, minimum and maximum monthly temperature values measured in Kızılcahamam and Çeltikçi stations are given in Figure 3.8. In the plots, all available temperature data were used, i.e. 1987 – 1993 period for the Çeltikçi and 1959 – 2018 period for the Kızılcahamam stations. The long-term (1959 – 2018) and short-term (1987 – 1993) temperature values measured in the Kızılcahamam station are also shown in the graphs separately. As can be seen from the figures, in the Kızılcahamam station, long-term and short-term monthly temperatures are compatible with each other.

According to Figure 3.8, the mean monthly temperature values show seasonality. July and August are the hottest months (mean temperature values are higher than 20°C) whereas the mean monthly temperatures are below zero in winter. For the overlapping operational period, for each month, the mean monthly temperature values measured in the Çeltikçi station are higher than those of the Kızılcahamam station. The minimum monthly temperature values indicate that for the Çeltikçi and Kızılcahamam stations, apart from May, June, July, August and September, the minimum temperatures are below 0°C, hence within this period, snow cover can be seen. The minimum temperature values measured in the Çeltikçi station are higher than those of the Kızılcahamam station for the 1987 – 1993 period. Similar to the minimum

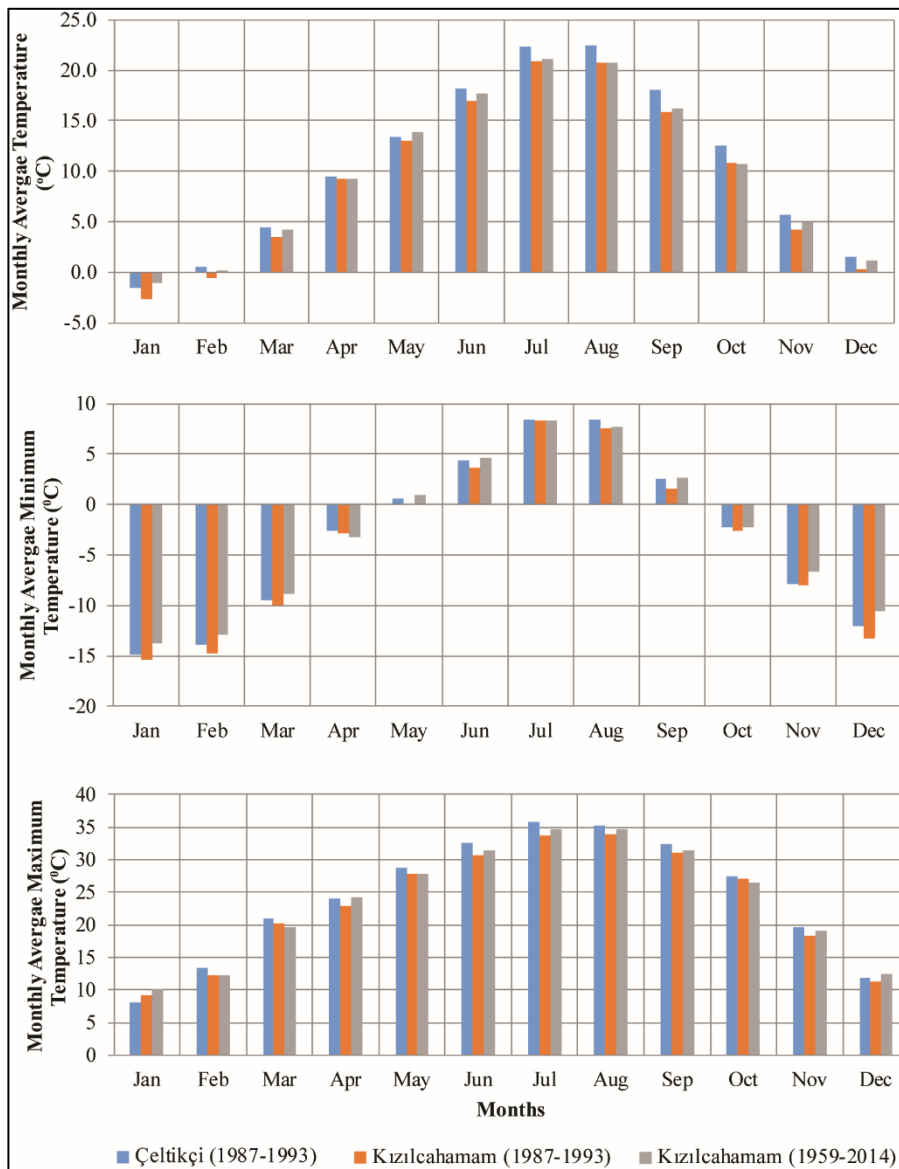


Figure 3.8. Mean monthly, monthly average minimum and monthly average maximum temperature graphs

temperature data, the measured maximum temperature values are higher in the Çeltikçi station compared to the Kızılcahamam station. July and August are the hottest months where the maximum monthly temperatures are above 34°C, whereas January is the coldest month.

### 3.2.3. Relative Humidity

The relative humidity values measured in the Kızılcahamam and Çeltikçi stations are given in Figure 3.9. The short-term and long-term relative humidity values measured in Kızılcahamam station show similar trends. As can be seen from Figure 3.9, relative humidity values measured at the Çeltikçi station are lower than those of the Kızılcahamam station for every month. The difference between relative humidity values approaches 10% in summer. The highest relative humidity value is observed in December (75%), whereas the minimum value is measured in August (46%).

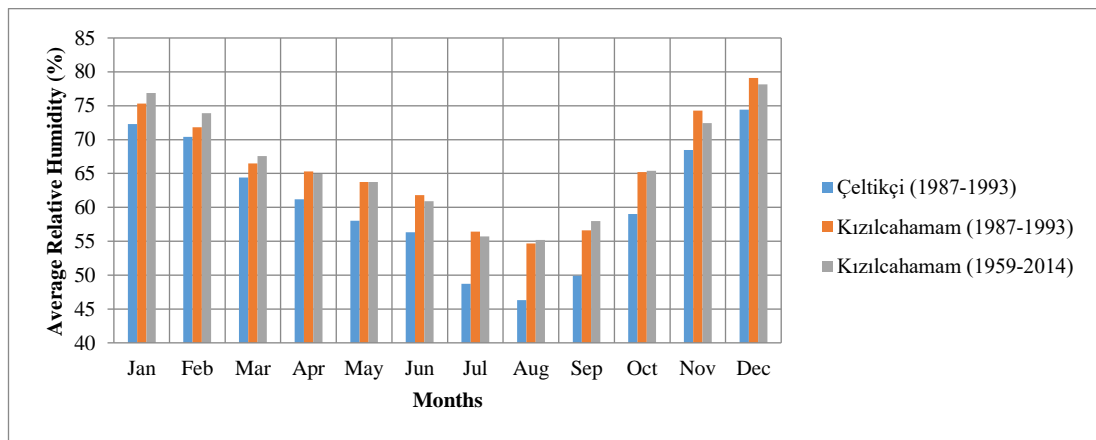


Figure 3.9. Mean monthly relative humidity graph

### 3.2.4. Evaporation

The evaporation data are only available for the Kızılcahamam station, for the May – September period (Figure 3.10). According to the graph, the mean monthly maximum

evaporation value is measured in August as 211 mm, whereas the minimum evaporation is observed in September as 79.5 mm.

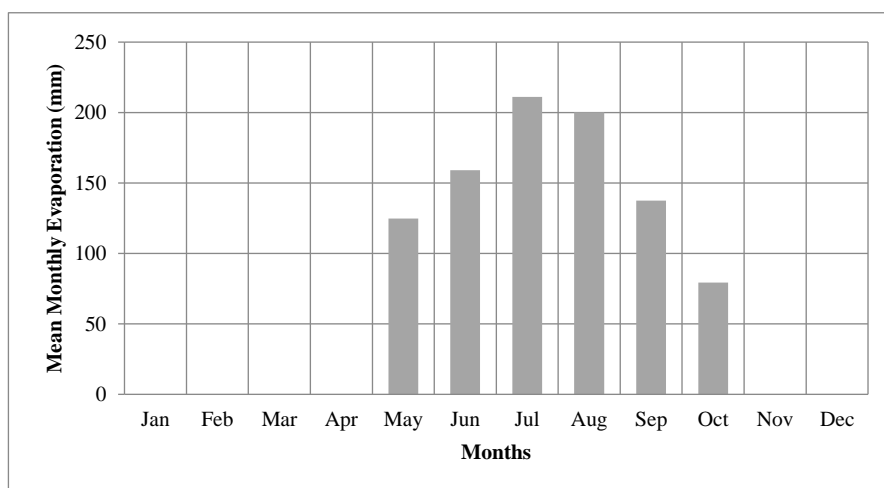


Figure 3.10. Mean monthly evaporation graph

### 3.3. Geology

#### 3.3.1. Regional Geology

In terms of regional geology, the study area is located at the southern part of the “Galatian Volcanic Province, (GVP)”, which is bounded by North Anatolian Fault Zone in the north and Cretaceous accretionary prism in the south (Öngür, 1976). The rock units observed in the area are mainly composed of pre-Miocene aged rocks, which are unconformably overlain by Miocene clastics and volcanics. These Miocene sequences are unconformably overlain by the interfingering of several eruptive phase lavas and volcanoclastics of the GVP. The organic layers and coal beds were formed within the Miocene and Pliocene sequences. Quaternary deposits unconformably overlain all the units. The regional geological map and corresponding columnar section are provided in Figure 3.11.

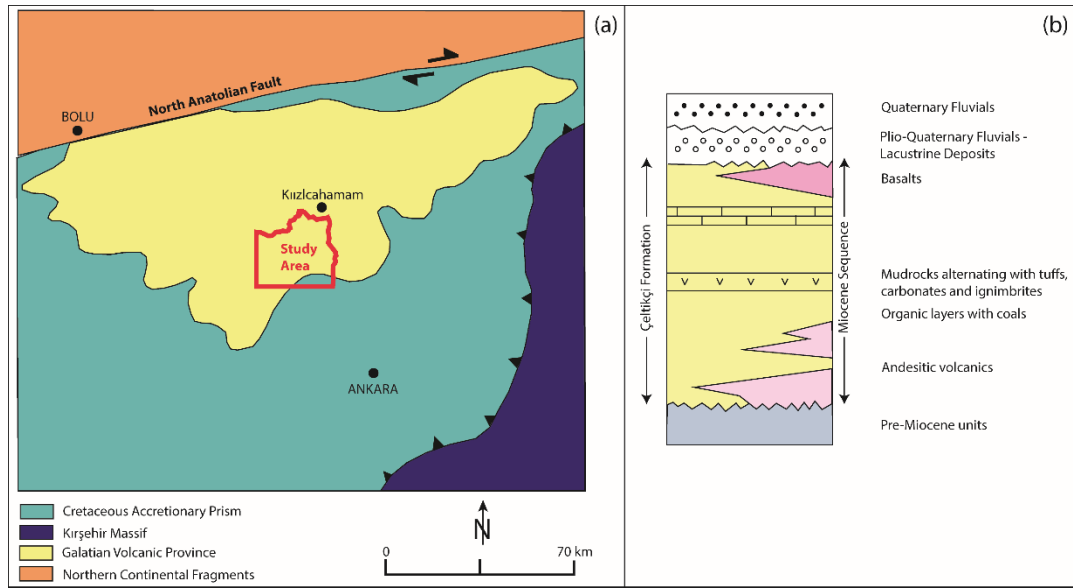


Figure 3.11. Regional geological map (a) and generalized columnar section (b) (modified from Rojay, 2013)

### 3.3.2. Local Geology

The detailed geology of the study area, especially in and around the mine units were studied by AMM (2015) and Rojay (2013), where 1/25000 scaled geological maps were prepared and revised at 1/10000 scale. The geological data for the other parts of the study area were obtained from 1/100000 scaled geological maps prepared by MTA.

#### 3.3.2.1. Stratigraphy

The geological map of the study area is given in Figure 3.12, whereas the cross sections on the planned mine site are shown in Figure 3.13. The generalized columnar section is provided in Figure 3.14.

The rock units cropping out in the study area include, from oldest to youngest, volcanic basement rocks, the Çeltikçi formation, Plio-Quaternary units and Quaternary alluvium. The Miocene units, which display conformable relationship

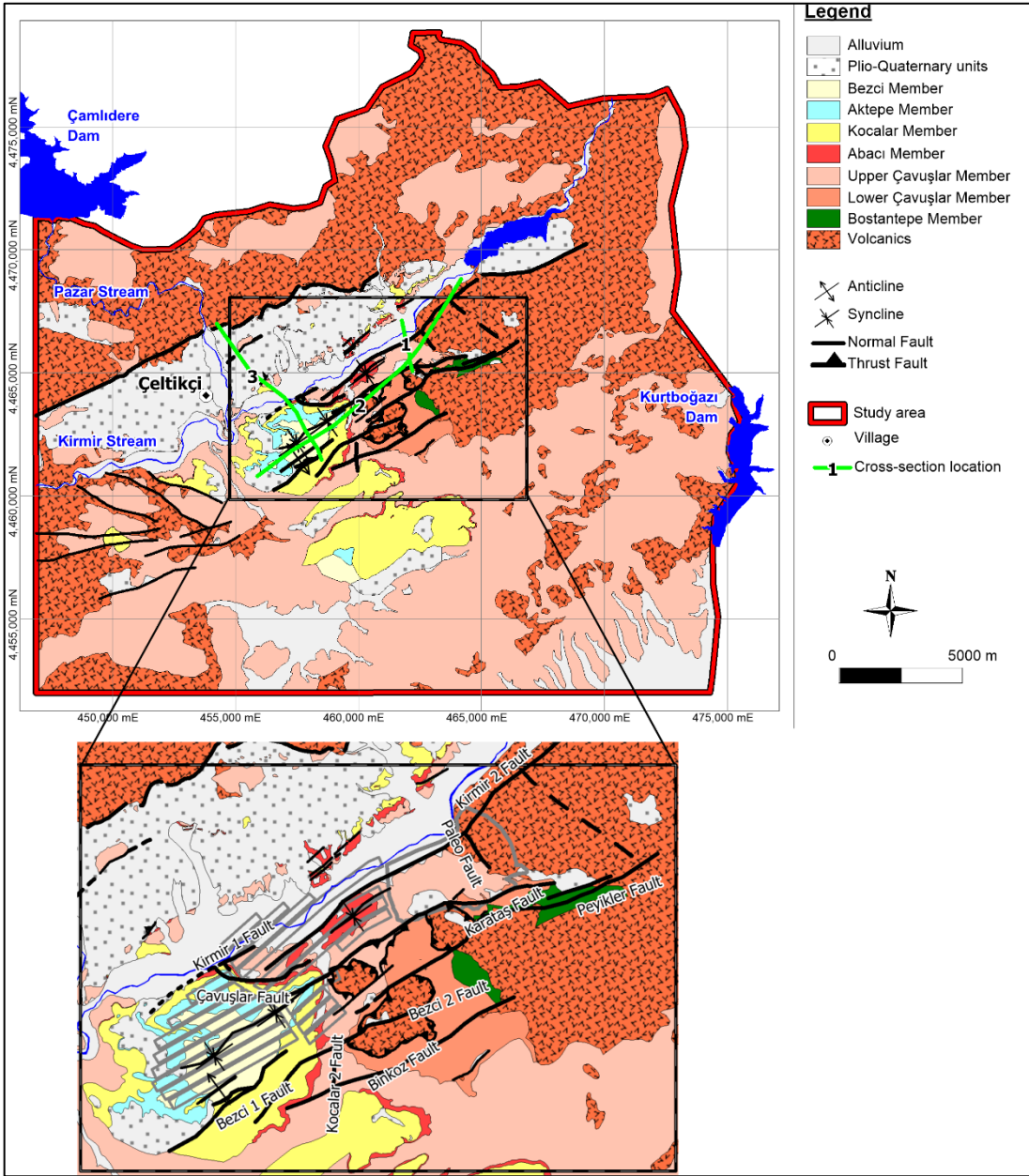


Figure 3.12. Geological map of the study area (modified from AMM, 2015 & MTA maps)

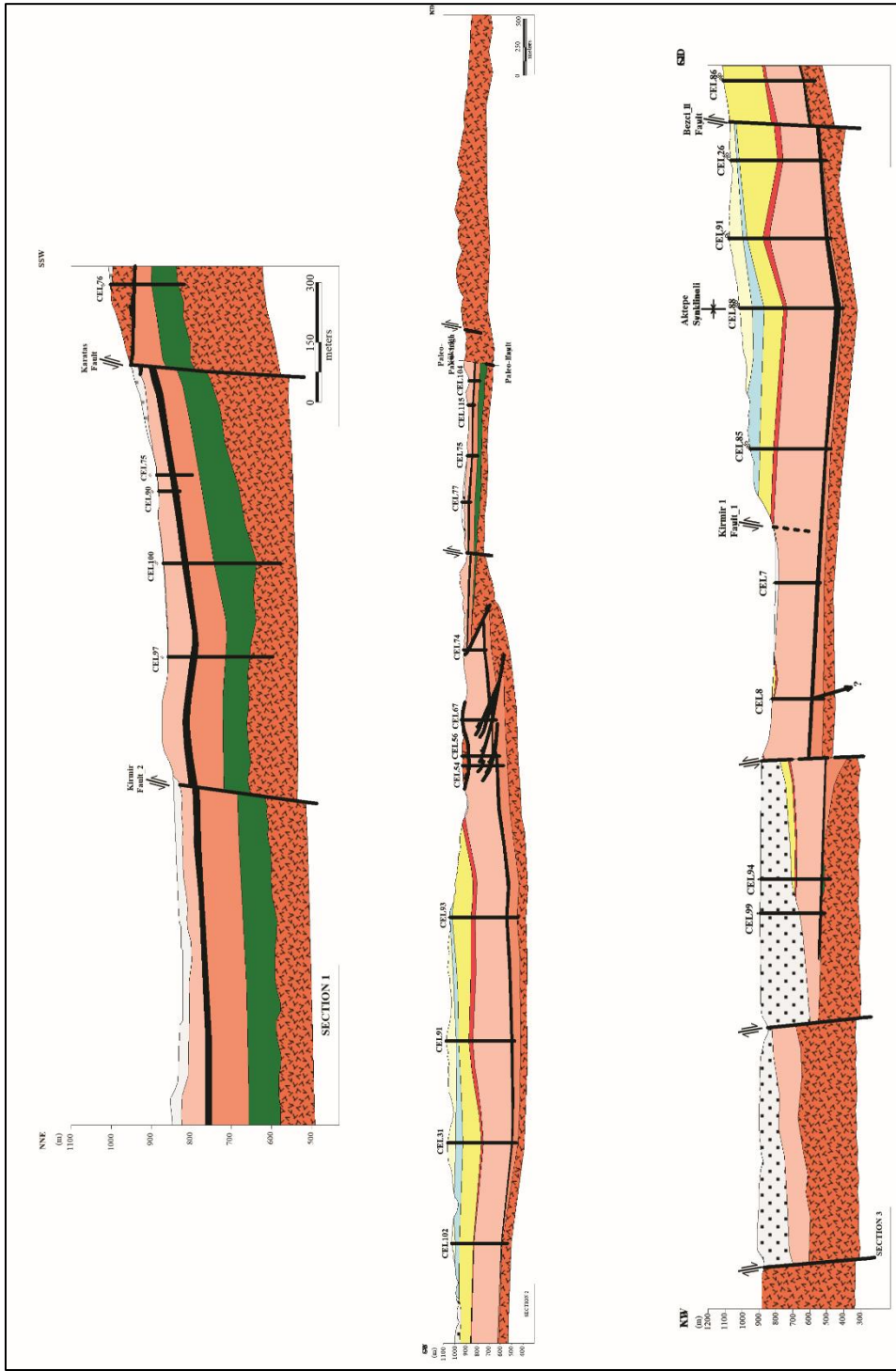


Figure 3.13. Geological cross sections

Age	Unit		Thickness (m)	Lithology	Description
	Formation	Member			
Quat.	Alluvium				Fluvial deposits.
Plio-Quaternary	Talus to fan deposits		>200		Fault-controlled continental deposits in the form of talus to alluvial fan.
		Bezci	>60		Reddish to brown, thick bedded, continental clastics.
	Aktepe	~70		Cream to brown, moderately silicified limestone.	
	Kocalar		170		Cream to light green, massive to faintly laminated claystone, mudstone and siltstone alternation.
		Abacı	40		Cream to light gray ignimbrite.
		Upper Çavuşlar		275	
					Coal (lignite) member
	Lower Çavuşlar		110		Dark brown, thin bedded, moderately to highly silicified claystone including immature coal seams and alternation of oolitic layers-varves.
	Bostantepe		70		Light gray to green sandstone and conglomerates with fragments derived from volcanic rocks.
Miocene	ÇELTIKÇI	Volcanic Basement	>400		Dark colored, massive, andesitic-basaltic lava flows and pyroclastics.

Figure 3.14. Generalized columnar section (AMM, 2015)

with each other, were grouped under the name of “Çeltikçi” formation. The Çeltikçi formation is composed of the Bostantepe, Lower Çavuşlar, Upper Çavuşlar, Abacı, Kocalar, Aktepe and Bezci members. The coal seams were found at the lower parts of the Upper Çavuşlar unit (Figure 3.14).

The volcanic basement rocks form the oldest rock unit in the study area and mainly outcrop at the northern, eastern and western part of the area (Figure 3.12). They are composed of lava flows, tuffs, and andesitic-basaltic pyroclastics (Figure 3.14). The total thickness of the unit is about 400 m. The Çeltikçi formation unconformably overlies these rocks.

The Bostantepe member forms the lowest part of the Çeltikçi formation. It overlies the basement volcanics and underlies the Lower Çavuşlar member. The thickness of the unit is about 100 m at the eastern part of the area and gradually decreases towards the western part, and finally diminishes at the western part of the Çavuşlar village (Figure 3.12). The Bostantepe member is usually represented by fine to medium-grained clastic sedimentary rocks, where the dominant lithology is sandstone deposited in a fluvial environment (Figure 3.14).

The Lower Çavuşlar member is mainly observed around the Çavuşlar, Kocalar and Binkoz villages (Figure 3.12). It overlies the Bostantepe member at the eastern part, whereas at the western part, it unconformably overlies the volcanics. The Upper Çavuşlar member conformably overlies the unit. The Lower Çavuşlar member is composed of alternating oolitic limestone and varve, which are intercalated with thin-bedded immature coal seams and tuff layers, moderately to highly silicified chert layers, from top to bottom (Figure 3.14). The silicified levels occur as lenses and layers in the formation.

The frequently observed unit in the study area is the Upper Çavuşlar member (Figure 3.12). This unit conformably overlies the Lower Çavuşlar member and conformably underlies the Abacı member. It is composed of cream to white and light green mudrocks alternated with sandstones, tuffs and coal-bearing levels (Figure 3.14). The thickness of the unit is about 250 m.

The Abacı member is stratigraphically located in the middle of Miocene lacustrine sequence and composed of a single ignimbrite layer. This unit conformably overlies the Upper Çavuşlar member and underlies the Kocalar member (Figure 3.13). The thickness of the Abacı member is about 40 m. Lithologically the member is composed of two parts: (i) silicified, impervious massive tuff layer of maximum 5 m thickness located at the lower part; and (ii) highly porous, light-colored pumice-bearing tuff layer forming the upper part. In some areas, the Abacı member is hydrothermally altered along the preexisting joints and crosscut by basaltic dykes.

The Kocalar member is composed of beige-cream colored mudrocks with sandstone beds and tuff layers. The upper part is gradually dominated by beige-light gray to white-colored, thick-bedded, highly porous limestones-dolomitic mudrocks with silica nodules-lenses that grade into the Aktepe formation at the top. The unit conformably overlies the Abacı member and underlies the Aktepe member (Figures 3.12 and 3.14).

The Aktepe member is observed around the Gümele, Çavuşlar and Bezcikuzören villages (Figure 3.12), and composed of beige-cream colored carbonates at the bottom and grades upwards into mudrocks with silica nodules and lenses. The unit conformably overlies the Kocalar member and underlies the Bezci member (Figure 3.14).

The Bezci member is the youngest unit of the Çeltikçi formation and mainly observed around the Bezcikuzören, Çavuşlar and Gümele villages (Figure 3.12). The member conformably overlies the Aktepe member and is unconformably overlain by the Plio-Quaternary units. The Bezci member is composed of red to pink, bedded clastic rocks, where sandstone and conglomerate are the common lithologies. Several thin limestone layers also exist in the sequence. Total thickness of the member is about 60 m (Figure 3.14).

Plio-Quaternary units are commonly observed in the area and are associated with the faults mapped in the region (Figure 3.12). They are talus-to-fan type deposits derived from the upthrown block and deposited over the downthrown blocks of the fault. They form a gentle topography with a slope of a few degrees. The unit is mainly composed of sandstones-siltstones-conglomerates with some limnic-organic horizons (Figure 3.13).

Recent alluvial fans, terrace deposits, alluvium and talus form the Quaternary units. This unit is mainly observed along the Kirmir and Pazar streams (Figure 3.12).

### **3.3.2.2. Structural Geology**

A detailed structural analysis was conducted in the vicinity of the mine units. The study area is divided by thrust and normal faults. Thrust faults and related structures are seen at the western part of Kocalar village (Figure 3.12). On the other hand, most of the normal faults are observed at the southern part of Kirmir stream. The general strike direction of the normal faults is NE-SW, and the dip is towards NW (Kirmir 1, Kirmir 2, Karataş, Peyikler, Bezci 1, Bezci 2, Peyikler, and Binkoz faults). On the other hand, Kocalar 2 fault trends in N-S and Çavuşlar faults extends in E-W direction.

The folds observed in the area are located at the southern part of the Kirmir stream, having NE-SW trend and elongated parallel to the thrust faults (Figure 3.12). Concerning the bedding analysis, a total of 1027 measurements were conducted, which reveal two dominant directions, namely;  $14^{\circ}/322^{\circ}$  and  $13^{\circ}/170^{\circ}$ . This analysis indicates a symmetric non-plunging folding in the area.



## CHAPTER 4

### HYDROGEOLOGY

The detailed hydrogeological characterization of the study area was conducted by Yazıcıgil et al. (2014). The monitoring program and groundwater level measurements were continued till 2015 (Yazıcıgil et al. 2015a, and 2015b). The data presented herein were compiled from these studies and summarized below.

#### 4.1. Water Resources

##### 4.1.1. Surface Water Resources

In the regional scale, the study area is mainly located in two watersheds, namely the Kirmir stream and Kurtboğazı creek watersheds (Figure 4.1). The main surface water in the study area is the Kirmir stream, which originates from the Işık and Çiçekliyayla mountains and flows in northeast – southwest direction. The Pazar stream flows in north – south direction and joins the Kirmir stream near the Çeltikçi village. It forms the second important surface water. The total catchment area for the Kirmir and Pazar streams is about 2000 km<sup>2</sup>.

The dams located in and around the study area (namely the Doğanözü, Eğrekkaya, Çamlıdere and Akyar dams) control the flows of Kirmir and Pazar streams. The streams draining the eastern part of the study area are mainly located in the Kurtboğazı creek watershed, having an area of 300 km<sup>2</sup>, and discharges to the Kurtboğazı dam. The Çamlıdere dam, which is located at the upstream part of Pazar stream, is the biggest water reservoir in the area with a lake volume of 1226 hm<sup>3</sup>. These dams are mainly used for irrigation and water supply purposes. The detailed information about the dams is provided in Table 4.1.

The discharge rates monitored at the stream gauging stations were investigated in order to determine the surface water potential of the watersheds around the study area. There are four stream gauging stations established in the Kirmir stream and its tributaries by DSI and Electrical Power Resources Survey and Development Administration (EIEI). The locations of the stream flow gauging stations in and around the study area and detailed information about them are given in Figure 4.1 and Table 4.2, respectively. Among the stream gauging stations, the Kızılcahamam – Mandra station (12-017), which is located at the upstream part of the Kirmir stream, has the longest record (approximately 50 years).

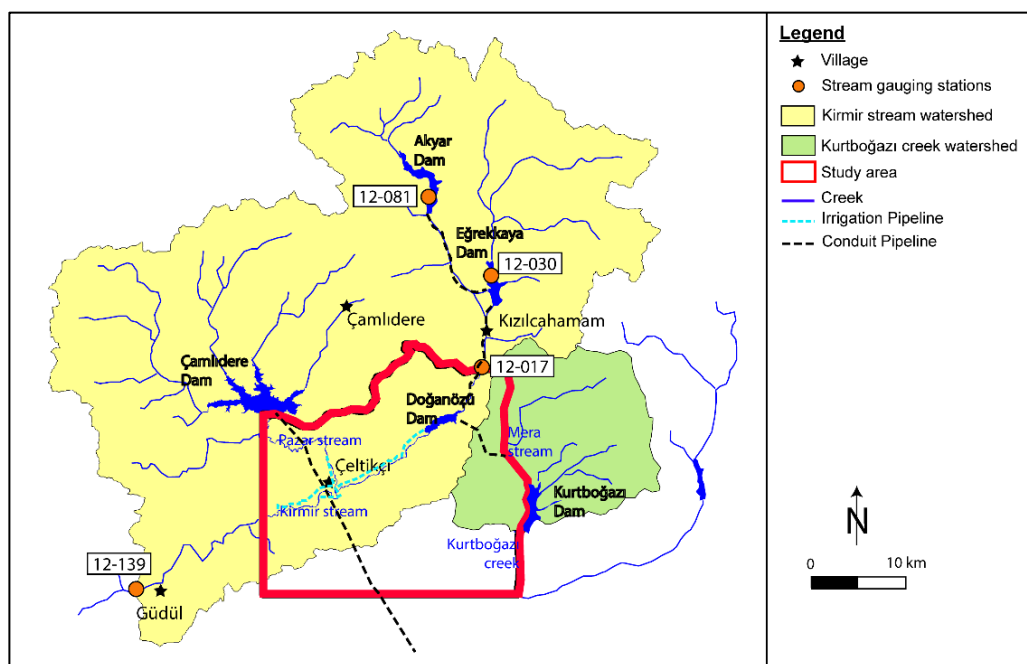


Figure 4.1. Location of the stream gauging stations, dams, and watersheds of the Kirmir stream and Kurtboğazi creek

Table 4.1. Information about the dams located in and around the study area

Name	Location	Stream Name	Completion Year	Purpose*	Lake Volume (hm <sup>3</sup> )	Irrigation Area (ha)	Water Supply (hm <sup>3</sup> /yr)
Doğanözü Dam	Doğanözü	Kirmir	2013	IR, WS	32.7	2777	25
Çamlidere Dam	Çamlidere	Bayındır	1985	WS	1226	-	142
Akyar Dam	Kızılcahamam	Bulak	2001	WS	56	-	45
Eğrekkaya Dam	Kızılcahamam	Sey	1992	WS	113	-	79
Kurtboğazi Dam	Kazan	Kurtboğazi	1967	IR, WS	96.9	2800	60

\*IR: irrigation, WS: water supply

Table 4.2. Information about the stream gauging stations in the vicinity of the study area

Station No.	Station Name	Operator	Coordinates		Elevation (m)	Watershed Area (km <sup>2</sup> )	Operational Period
			Latitude	Longitude			
12-017	Mandra	DSI/EIEI	40.4350	32.6500	903	907.5	1959 - 1963 / 1965 - 1999 / 2001 - 2013
12-139	Güdül	DSI	40.2140	32.2430	780	2239	1976 - 1999
12-030	Saray	DSI	40.5239	32.6606	957	384.2	1960 - 1965 / 1972 - 1980 / 1982 - 1989
12-081	Derinece	DSI	40.6000	32.5833	1080	274	1966 - 1969 / 1980 - 1991

The flow rates measured at the Kızılcıhamam – Mandra station show seasonal variations (Figure 4.2). The maximum discharge rates are measured in spring due to the snow melting, whereas the minimum values are recorded in summer. The significant decrease in measured flow rates with time resulted from the construction of the Eğrekkaya dam in 1992 and the Akyar dam in 2001. The maximum monthly flow rates measured within 1960 – 2013 period are recorded as 14.5 m<sup>3</sup>/s and 15.2 m<sup>3</sup>/s for March and April, respectively.

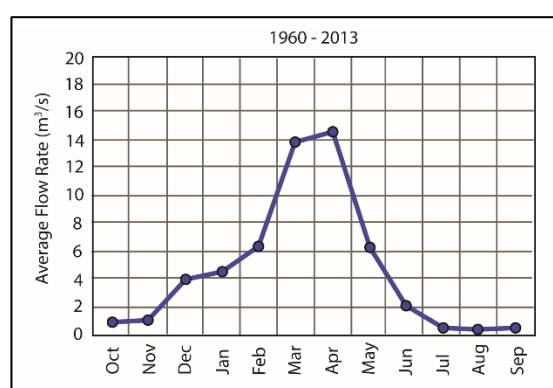


Figure 4.2. Monthly average flow rates measured at the Kızılcıhamam – Mandra stream gauging station for 1960 – 2013 period

The monthly average flow rates recorded after the construction of Eğrekkaya and Akyar dams are shown in Figure 4.3. In summer, the flow rates decrease rapidly and become very low. Before the construction of any dam, i.e. when the flow is uncontrolled, the average monthly flow rates show the same trend with higher maximum flow rates (i.e. 18.9 m<sup>3</sup>/s and 18.5 m<sup>3</sup>/s for March and April, respectively). When the flow is controlled by the Eğrekkaya and Akyar dams, the measured flow rates decrease significantly (i.e. 9.3 m<sup>3</sup>/s in April).

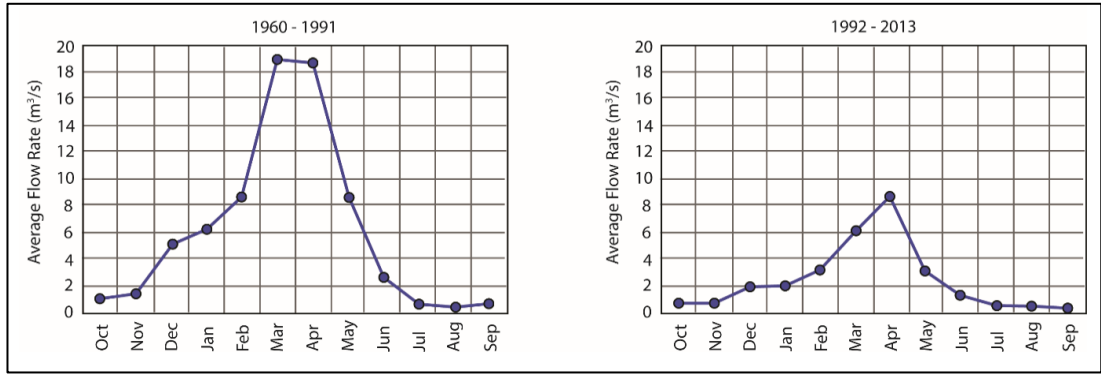


Figure 4.3. Monthly average flow rates measured at the Kızılcahamam – Mandra stream gauging station for the periods of 1960 – 1991 and 1992 – 2013

The drainage pattern at the mine site and its vicinity are presented in Figure 4.4. Thirty flow monitoring stations (SW-1 – SW-27) were established on the ephemeral creeks draining the mine site and its vicinity between March 2012 and July 2015. The locations of these monitoring points and drainage areas are also shown in Figure 4.4. Among the in-site flow monitoring points, SW-1 and SW-16 are located along the Kirmir stream, representing upstream and downstream parts, respectively. Similarly, SW-11 and SW-12 monitoring points are located at the upstream and downstream part of the Pazar stream. SW-1B point is aimed to monitor the discharge rates at the upstream part of the Doğanözü dam. In order to determine the flow rates before and after the Kirmir stream joins the Pazar stream, the monitoring points SW-25, SW-26 and SW-27 were selected. Remaining monitoring points are aimed to determine the discharge rates in the creeks draining to the Kirmir stream.

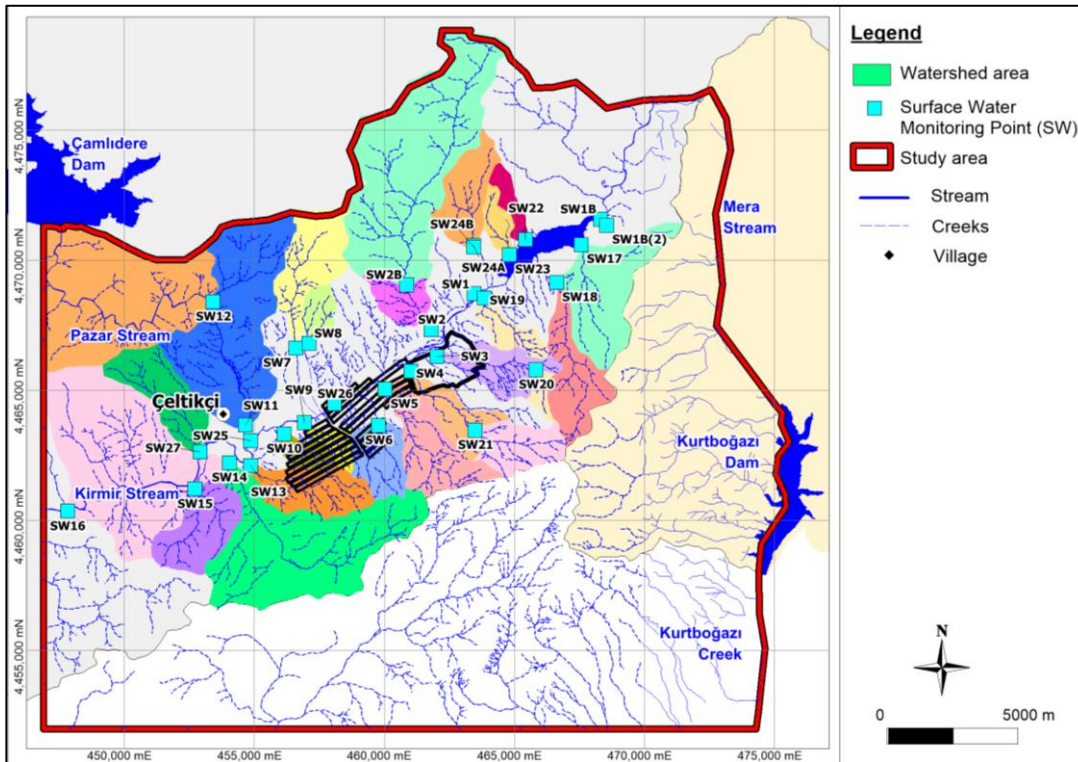


Figure 4.4. Location of the surface water monitoring points

The instantaneous flow rates were measured on a monthly basis at all monitoring points. The coordinate, monitored period and measured minimum, maximum and average flow rates of the flow monitoring stations are summarized in Table 4.3. The hydrographs representing instantaneous discharge measurements at the monitoring points together with the precipitation data are given in Appendix A. Because the monitored flow rates at the surface water monitoring locations are generally low (below  $0.1 \text{ m}^3/\text{s}$ ), the logarithmic scale was used in the hydrographs for discharge rates. On the other hand, precipitation data is represented by arithmetic scale. According to these graphs, maximum flow rates are generally observed between January and May, as a result of excess rainfall and snow melt. In summer months, seasonal decrease in flow rates is seen. Among the monitoring stations, SW-7, SW-8, SW-10, SW-13, SW-17, SW-19, SW-22, SW-23 and SW-24B are generally dry throughout the monitoring period. The highest flow rates are measured at the monitoring points located on the

Table 4.3. Information about the surface water monitoring points

Monitoring Point	Coordinates (UTM)		Monitored Period	Discharge Rate (m <sup>3</sup> /s)		
	X	Y		Min	Max	Ave
SW-1	463455	4468722	March 2012 - July 2015	dry	5.4400	0.3189
SW-1B	468306	4471580	October 2014 - July 2015	0.1874	1.2983	0.6333
SW-2	461775	4467331	March 2012 - July 2015	dry	1.0469	0.0862
SW-2B	460847	4469061	October 2014 - July 2015	0.0101	0.3976	0.1463
SW-3	462014	4466327	April 2012 - July 2015	dry	0.0336	0.0027
SW-4	461019	4465709	March 2012 - July 2015	dry	0.1867	0.0204
SW-5	460027	4465044	March 2012 - July 2015	dry	0.1210	0.0097
SW-6	459749	4463693	March 2012 - July 2015	dry	0.0044	0.0003
SW-7	457110	4466815	March 2012 - July 2015	dry	0.0080	0.0002
SW-8	456589	4466727	March 2012 - July 2015	dry	0.0270	0.0010
SW-9	456928	4463763	March 2012 - July 2015	dry	0.0435	0.0072
SW-10	456143	4463343	March 2012 - July 2015	dry	0.0120	0.0005
SW-11	454656	44463595	March 2012 - July 2015	0.0695	1.3204	0.4084
SW-12	453263	4468483	March 2012 - July 2015	0.0685	1.1700	0.3786
SW-13	454861	4462095	March 2012 - July 2015	dry	0.0647	0.0018
SW-14	454043	4462231	March 2012 - July 2015	dry	0.2653	0.0229
SW-15	452711	4461213	March 2012 - July 2015	dry	0.0581	0.0086
SW-16	447865	4460487	March 2012 - July 2015	0.3840	8.0200	1.6659
SW-17	467554	4470611	April 2013 - July 2015	dry	0.0061	0.0002
SW-18	446677	4469058	April 2013 - July 2015	dry	0.3981	0.0270
SW-19	463837	4468532	April 2013 - July 2015	dry		
SW-20	465818	4465787	April 2013 - July 2015	0.0022	0.0236	0.0101
SW-21	463511	4463454	April 2013 - July 2015	dry	0.0638	0.0145
SW-22	465427	4470802	October 2014 - July 2015	dry		
SW-23	464805	4470210	October 2014 - July 2015	dry		
SW-24A	463436	4470557	October 2014 - July 2015	dry	0.0202	0.0084
SW-24B	463424	4470502	October 2014 - July 2015	dry		
SW-25	454853	4463068	January 2015 - July 2015	0.3647	1.9922	0.9121
SW-26	458084	4464491	January 2015 - July 2015	0.3149	1.3890	0.7786
SW-27	452921	4462639	February 2015 - July 2015	0.8074	3.2803	2.0156

Kirmir stream (i.e. SW-1 & SW-16) and Pazar stream (SW-11 & SW-12) in April 2012. The measured flow rates are 5.44 m<sup>3</sup>/s and 8.02 m<sup>3</sup>/s on April 2012, at SW-1 and SW-16, respectively. At monitoring points SW-2, SW-4, SW-5, SW-11, SW-12, SW-16 and SW-21 a significant decrease in discharge rates are observed between January – May in 2014 when compared to the same period in 2013. The decrease in flow rates indicates the presence of a dry period in 2013, which can also be seen in Figure 3.6.

#### **4.1.2. Spring and Fountains**

Within the study area, in the vicinity of the mine units, 70 springs were identified during the field studies conducted between 2012 - 2015 and the discharge rates and field parameters were monitored (Figures 4.5 and 4.6). The springs in the study area were mainly used for water supply purposes. The spring locations are also shown on the geological map to assess the effects of lithology and structural changes (Figure 4.7). The information regarding the coordinates, elevation, measured minimum, maximum and average discharge rates are given in Table 4.4.

The discharge rates of the springs were measured periodically to monitor the seasonal variations. The monitored discharge rates with respect to time are given in Appendix B. In the graphs, precipitation data and monitored period of all springs are also included. Except for F28, the discharge rates of springs are low, where the average discharge rates are between 0.002 and 1.82 L/s. At F28, which is located at the eastern part of the Pazar stream, the average discharge rate is measured as 7.52 L/s. The measured elevated discharge rates of F28 are related to the fault zone passing through northern part. Among the springs, F60, F62 and F78 are completely dry throughout the monitoring period. At F46 only one measurement can be taken and except for April 2012, F39 is also dry. Similarly, at F77 only two measurements could be conducted in September and October 2014, with a discharge rate of 0.009 L/s. Typically, the discharge rates of the springs increase in the winter period and peaks in the spring time, which is followed by a dry or low flow during the summer period.

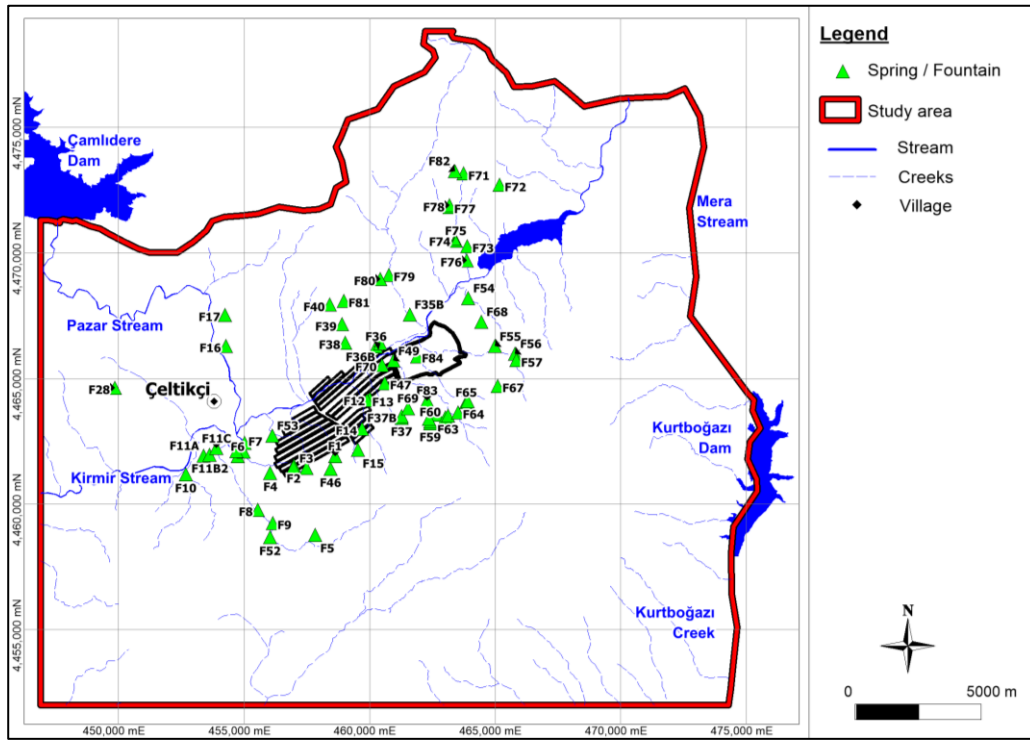


Figure 4.5 Location of the springs

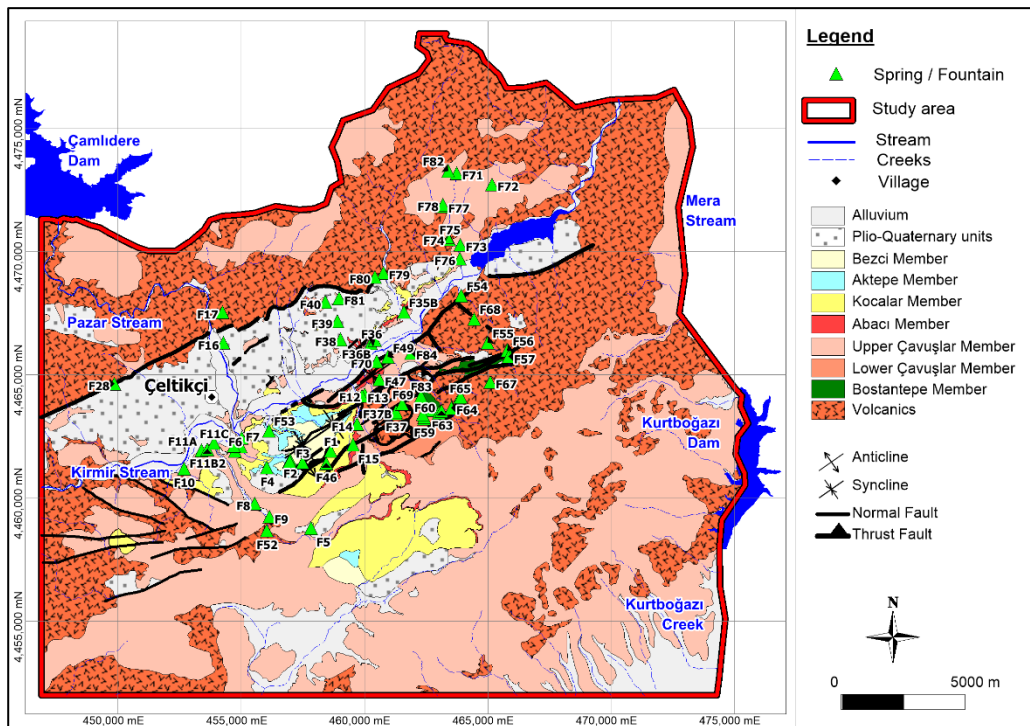


Figure 4.6. Location of the springs on the geological map

Table 4.4. *Information about the springs / fountains*

Monitoring Point	Coordinates (UTM)		Elevation (m)	Discharge Rate (L/s)		
	Easting	Northing		Min	Max	Ave
F1	458621	4461908	1090	0.02	0.09	0.04
F2	456969	4461556	1006	0.08	0.25	0.15
F3	457483	4461431	1024	0.01	1.45	0.19
F4	456040	4461236	948	0.1	0.34	0.23
F5	457832	4458783	1090	dry	1.68	0.19
F6	454784	4461905	823	0.008	0.06	0.02
F7	454978	4462099	797	dry	0.05	0.02
F8	455540	4459778	924	0.05	0.27	0.16
F9	456141	4459238	985	0.01	0.09	0.06
F10	452684	4461189	783	dry	0.18	0.06
F11A	453382	4461931	798	0.02	0.1	0.04
F11C	453888	4462232	812	0.03	0.18	0.12
F12	460012	4464187	895	0.05	0.41	0.19
F13	459903	4464144	893	dry	2.25	0.25
F14	459699	4462994	964	dry	0.84	0.22
F15	459524	4462160	1056	dry	0.49	0.16
F16	454280	4466292	831	dry	1.52	0.12
F17	454243	4467531	895	dry	1.46	0.41
F28	449845	4464638	998	2.33	16.87	7.52
F35B	461594	4467547	869	0.01	0.62	0.30
F36	460263	4466277	840	0.01	0.05	0.03
F36B	460415	4466400	836	0.03	0.06	0.04
F37	461268	4463440	1035	dry	0.08	0.02
F37B	461268	4463500	1027	dry	0.27	0.02
F38	459025	4466427	940	dry	0.36	0.08
F39	458890	4467160	1040	dry	0.02	0.002
F40	458411	4467940	1166	dry	0.49	0.05
F45	455017	4462435	798	0.02	0.19	0.08
F46	457530	4461592	1039			0.08
F47	460609	4464813	880	dry	0.35	0.05
F49	460943	4465714	841	dry	0.36	0.12
F51	454691	4462106	792	dry	0.32	0.17
F52	456035	4458678	980	0.01	1.95	0.87
F53	456117	4462735	874	dry	0.29	0.09
F54	463925	4468208	900	dry	0.67	0.17

Table 4.5 Cont.ed

Monitoring Point	Coordinates (UTM)		Elevation (m)	Discharge Rate (L/s)		
	Easting	Northing		Min	Max	Ave
F55	464981	4466294	1102	0.01	2	0.61
F56	465792	4465988	1161	0.01	0.23	0.06
F57	465841	4465728	1200	0.04	0.31	0.13
F58	462679	4463557	1137	0.05	0.96	0.29
F59	462413	4463223	1153	0.1	0.41	0.21
F60	462420	4463283	1146	dry		
F61	462356	4463400	1136	0.18	0.43	0.30
F62	463008	4463445	1157	dry		
F63	463127	4463516	1164	0.05	0.07	0.05
F64	463516	4463658	1190	0.02	0.1	0.04
F65	463851	4464064	1239	0.11	1.89	0.47
F66	463901	4464106	1244	0.02	0.62	0.13
F67	465092	4464703	1394	dry	0.53	0.08
F68	464449	4467268	1040	0.03	0.51	0.32
F69	461531	4463814	1031	dry	0.17	0.07
F70	460484	4465545	838	0.13	0.45	0.26
F71	463738	4473162	1310	0.01	0.66	0.20
F72	465176	4472708	1200	dry	0.01	0.003
F73	463887	4470269	940	0.05	0.28	0.14
F74	463414	4470527	957	dry	0.4	0.18
F75	463432	4470495	956	dry	0.5	0.12
F75B	463433	4470498	954	0.14	0.5	0.32
F76	463867	4469705	891	0.07	0.28	0.13
F77	463176	4471825	1124	0.01	0.01	0.01
F78	463178	4471903	1100	dry		
F79	460766	4469129	930	0.06	0.45	0.11
F80	460423	4468965	1032	0.02	0.04	0.03
F81	458965	4468088	1170	dry	0.02	0.01
F82	463394	4473262	1334	0.002	0.44	0.13
F83	462283	4464129	1084	0.55	3.99	1.82
F84	461885	4465884	863	0.07	1.2	0.51

### 4.1.3. Wells

The wells drilled within the study area can be divided into four categories; namely (i) wells drilled by the Bank of Provinces, (ii) water supply wells, (iii) monitoring wells and (iv) pumping wells. The location of the wells is shown in Figure 4.7.

In 2007, three wells were drilled by the Bank of Provinces in the alluvium around the Pazar stream, namely L-1, L-2, and L-3. Although these wells were aimed to supply water for the Çeltikçi village, they have not been in operation yet.

In order to supply water for the Bağören, Gümele and Binkoz villages, three wells were drilled. These wells were aimed to provide water for the village depots. Among these wells, the Binkoz water supply wells have not been in operation yet. Also, at the south eastern part of the study area, 174 wells were drilled for water supply purposes, where 164 of them are private wells and the remaining 10 wells are used by Anadolu-Efes Brewery Company.

For the mining activities, a total of 156 exploration wells have been drilled in the vicinity of the planned mine site. Among these 156 wells, 65 of them were converted to the monitoring wells in order to determine the hydrogeological conditions and hydraulic parameters, and also to monitor the groundwater level and quality. For the selection of monitoring wells from existing exploration wells, several factors, including the target geologic units, structural features, topographical conditions, and the location of the mine units were taken into account. Also in 2015, two monitoring wells were drilled in the northern and southern part of the open pit area, namely PW-8A and PW-9A. Starting from 2012, following the completion of the wells, groundwater elevation or pressure and discharge rates (if free flow exists) have been measured at the monitoring wells on bimonthly basis. In addition, slug tests were conducted at the large diameter monitoring wells to determine the hydraulic properties. In order to determine the vertical hydraulic gradients, nested monitoring wells, which were screened at different depths, were drilled.

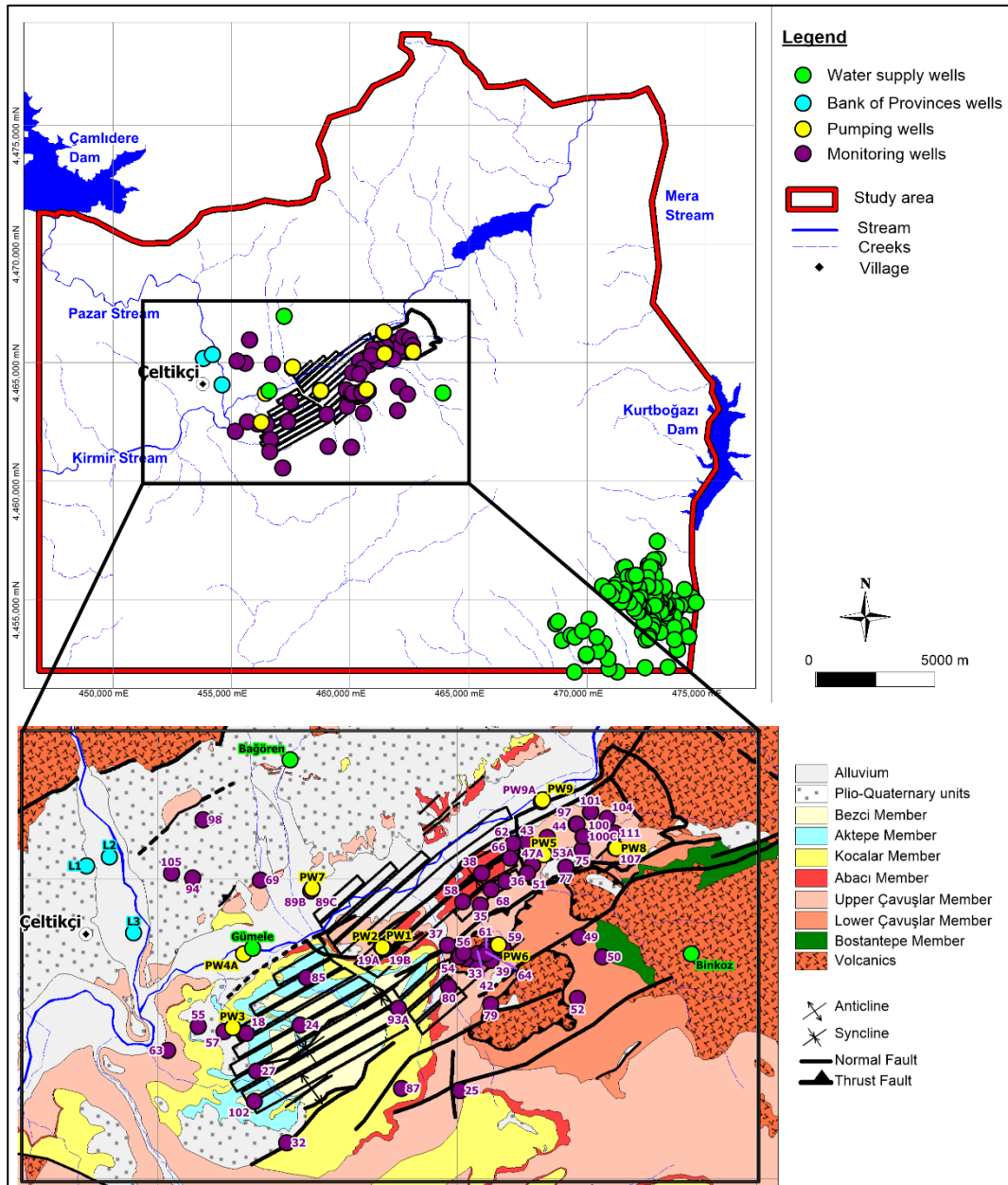


Figure 4.7. Location of the wells drilled within the study area (close-up view of the monitoring and pumping wells on geology is also shown)

Within the study area, nine large diameter pumping wells were drilled. The groundwater elevation or pressure, and discharge rates (if free flow exists) have been measured on a bimonthly basis. Also, aquifer tests were conducted to determine the hydraulic properties. The aquifer tests consist of pumping, recovery and free flow tests.

The location of Bank of Provinces wells, pumping wells and monitoring wells on geology is also given in Figure 4.7. The well details including coordinates, well depth and screened interval are provided in Table 4.5.

## **4.2. Hydrogeology of the Study Area**

The hydrogeology of the study area was determined based on the information gathered from the field studies, monitoring and pumping wells, and springs and fountains. Since the monitoring points (wells, springs and fountains) are clustered around the planned mine site, the detailed hydrogeological investigation is mainly focused on that area. In the area, the Kocalar 2 fault is a key structure, where the area reflects two different characteristics on the eastern and western part of it.

The Miocene aged volcanic rocks, outcropping mainly at the northern and northeastern part of the study area, form the basement. The discontinuities that resulted from the fractured nature of this unit transmits water. The volcanics form a confined aquifer at the western part of Kocalar 2 fault, where measured groundwater temperatures reach 40 °C (at PW-1 and PW-4A). At some locations along the Kirmir stream valley, free flow conditions are also observed. On the other hand, at the eastern part of the Kocalar 2 fault, the volcanics form an unconfined aquifer.

The volcanics are overlain by the Bostantepe member (composed of fine to medium-grained clastic sedimentary rocks, where the dominant lithology is sandstone deposited in a fluvial environment) at the southeastern part of the open pit area. For the remaining parts, the Lower Çavuşlar member (composed of alternating oolitic limestone and varve with intercalation of thin-bedded immature coal seams and tuff

Table 4.5. Well details for the wells drilled by the Bank of Provinces, pumping and monitoring wells

Well No.	Well Type*	Coordinate (UTM)		Elevation (m)	Well Depth (m)	Screen Interval (m)		Screened Formation**
		Easting	Northing			From	To	
L-1	WS	453806	4465254	821	42	14	35	A
L-2	WS	454189	4465407	810	32	10	18	A
L-3	WS	454593	4464137	800	27	10	18	A
PW1	PW	458729	4463904	865.8	284.0	240.0	272.0	V
PW2	PW	458748	4463892	867.9	180.0	168.0	76.0	UÇM
PW3	PW	456244	4462552	906.4	140.0	36.0	128.0	AKM
PW4A	PW	456425	4463782	799.0	440.0	393.8	432.3	V
PW5	PW	461441	4465444	867.7	145.0	113.8	133.3	C
PW6	PW	460683	4463933	929.3	172.0	144.0	160.0	C
PW7	PW	457574	4464880	828.5	96.0	12.0	88.0	UÇM
PW8	PW	462649	4465547	906.36	72.0	32.0	68.0	C/LÇM
PW9	PW	461422	4466356	830.44	60.0	4.0	56.0	A & UÇM
PW8A	MW	462627	4465558	901.50	12.0	6.0	10.0	UÇM
PW9A	MW	461394	4466331	829.63	32.0	4.0	28.0	A & UÇM
CEL18	MW	456478	4462460	937.6	475.0	446.0	464.0	V
CEL19A	MW	458776	4463867	870.8	235.0	214.0	228.0	LÇM
CEL19B	MW	458779	4463869	870.9	216.0	192.5	212.5	C/LÇM
CEL19D	MW	458773	4463871	870.6	206.5	152.0	182.0	UÇM
CEL24	MW	457373	4462596	971.6	490.0	460.0	484.0	LÇM
CEL25	MW	460043	4461503	1177.3	263.7	225.0	250.0	V
CEL27	MW	456647	4461827	1004.3	505.4	481.0	499.0	V
CEL32	MW	457149	4460632	1092.5	441.0	411.0	429.0	V
CEL33	MW	460294	4463646	954.6	387.0	363.0	381.0	LÇM
CEL35	MW	460380	4464598	869.4	303.7	277.0	300.0	LÇM
CEL36	MW	460806	4464994	877.5	302.0	270.0	299.0	LÇM
CEL37	MW	459836	4463927	892.5	385.0	361.0	379.0	LÇM
CEL38	MW	460401	4465133	859.0	330.3	306.0	324.0	LÇM
CEL39	MW	460560	4463679	969.2	223.2	199.0	217.0	LÇM
CEL42	MW	460339	4463793	951.5	314.3	301.0	319.0	LÇM
CEL43	MW	461157	4465652	851.1	240.0	220.0	237.1	LÇM
CEL44	MW	461500	4465731	857.5	202.0	180.5	197.6	LÇM

Table 4.5. Cont.ed

Well No.	Well Type*	Coordinate (UTM)		Elevation (m)	Well Depth (m)	Screen Interval (m)		Screened Formation**
		Easting	Northing			From	To	
CEL46	MW	460135	4463703	942.2	352.3	328.0	346.0	LÇM
CEL47	MW	461253	4465279	874.0	392.5	175.7	187.1	LÇM
CEL47A	MW	461250	4465277	874.0	157.0	143.6	152.1	C
CEL49	MW	462033	4464066	1091.6	140.0	120.0	137.1	V
CEL50	MW	462417	4463736	1114.9	151.0	131.0	148.1	V
CEL51	MW	461170	4465131	887.7	215.5	191.6	205.9	LÇM
CEL52	MW	462001	4463046	1155.1	197.6	180.4	194.7	V
CEL53	MW	461502	4465467	868.8	224.7	200.7	218.7	BM
CEL53A	MW	461501	4465463	868.8	130.1	106.8	124.8	C
CEL54	MW	460039	4463733	932.9	350.2	336.0	354.0	LÇM
CEL55	MW	455672	4462576	864.7	350.6	326.6	344.6	V
CEL56	MW	460097	4463796	935.5	325.0	300.0	318.0	C/LÇM
CEL57	MW	456107	4462490	924.0	423.1	391.0	409.0	V
CEL58	MW	460087	4464655	857.7	310.3	286.0	304.0	LÇM
CEL59	MW	460762	4463878	919.2	206.0	169.0	199.0	LÇM
CEL59A	MW	460761	4463881	919.1	130.0	106.0	124.0	C
CEL59B	MW	460763	4463880	919.1	110.5	86.5	104.5	UÇM
CEL61	MW	460488	4463856	958.8	255.0	237.8	252.1	LÇM
CEL62	MW	460931	4465632	844.1	260.3	236.0	254.0	LÇM
CEL63	MW	455159	4462171	811.4	270.0	246.0	264.0	V
CEL64	MW	460475	4463784	958.5	265.0	245.0	262.1	LÇM
CEL66	MW	460880	4465383	862.6	241.8	218.0	236.0	C
CEL68	MW	460559	4464855	873.2	275.0	251.0	269.0	C/LÇM
CEL69	MW	456711	4465016	849.7	361.0	337.0	355.0	LÇM
CEL75	MW	457574	4464880	889.7	88.6	64.6	82.6	LÇM
CEL77	MW	461804	4465232	935.3	71.5	47.5	65.5	UÇM/C
CEL79	MW	460558	4462946	1058.4	149.3	125.3	143.3	V
CEL80	MW	459857	4463231	949.1	392.0	266	284	LÇM
CEL85	MW	457481	4463388	951.3	475.0	439	457	C/LÇM
CEL87	MW	459065	4461535	1185.5	430.0	412	424	V
CEL89B	MW	457553	4464840	826.4	350.0	320	332	C
CEL89C	MW	457549	4464838	826.5	32.0	17.7	29.14	UÇM
CEL93A	MW	459015	4462875	1044.8	160.4	103.2	154.68	KM
CEL94	MW	455580	4465054	889.5	409.0	379	397	V
CEL97	MW	461980	4465956	860.5	260.0	230	248	V
CEL97A	MW	461992	4465953	861.9	77.2	59.2	71.2	C

Table 4.5. Cont.ed

Well No.	Well Type*	Coordinate (UTM)		Elevation (m)	Well Depth (m)	Screen Interval (m)		Screened Formation**
		Easting	Northing			From	To	
CEL98	MW	455752	4466021	925.9	330.0	312	324	V
CEL100	MW	462099	4465741	874.5	90.0	78.56	87.14	LÇM
CEL100C	MW	462105	4465742	874.8	65.0	50.7	59.28	C
CEL101	MW	462222	4466152	862.0	80.1	38.1	80.1	C/LÇM
CEL101A	MW	462220	4466154	862.1	200.3	182.3	194.3	V
CEL102	MW	456607	4461323	1027.4	74.0	48.26	71.14	AM
CEL104	MW	462497	4466044	876.8	92.0	74	86	LÇM
CEL105	MW	455223	4465129	870.2	352.1	340.1	346.1	V
CEL107	MW	462633	4465557	904.1	56.5	33.62	53.64	C/LÇM
CEL107A	MW	462635	4465555	904.2	75.0	66.42	72.14	LÇM
CEL107B	MW	462638	4465553	903.9	129.0	106.12	126.14	BM
CEL111	MW	462629	4465798	927.8	170.0	152	164	BM

\*WS: water supply well, PW: pumping well, MW: monitoring well

\*\* A: Alluvium, UÇM: Upper Çavuşlar Member, AM: Aktepe Member, BM: Bostantepe Member, C: coal, LÇM: Lower Çavuşlar Member, KM: Kocalar Member, V: Volcanics

layers, moderately to highly silicified chert layers) overlies the volcanics. The Upper Çavuşlar member (composed of cream to white and light green mudrocks with sandstones, tuffs and coal-bearing levels) overlies these both units. The volcanics, together with the Bostantepe, Lower and Upper Çavuşlar members acting together, form the lower aquifer in the study area. The lower aquifer has confined character at the western part of the Kocalar 2 fault and forms an unconfined aquifer at the eastern part. The sudden changes in topography also result in free flow conditions in the lower aquifer. The presence of silicified, impervious massive tuff layer at the bottom of Abacı ignimbrite forms an impervious boundary above the Upper Çavuşlar member and result in development of confined conditions at the western part of the Kocalar 2 fault.

The second important aquifer in the study area includes the Kocalar member (composed of beige-cream colored mudrocks with sandstone beds and tuff layers), Aktepe member (composed of beige-cream colored carbonates at the bottom and

grades upward into mudrocks with silica nodules and lenses) and Bezci member (composed of red to pink, bedded clastic rocks, where sandstone and conglomerate are common lithologies). These units form the upper aquifer in the study area, which is an unconfined aquifer developed in a synclinal basin. Hence, at the western part of Kocalar 2 fault, there is an upper unconfined aquifer underlain by a confined lower aquifer.

The Quaternary aged alluvial deposits observed along the Pazar and Kirmir streams form an unconfined aquifer. However, the limited areal extent and thickness of the alluvium reduce the yield of Alluvium aquifer.

#### **4.2.1. Hydraulic Parameters**

Hydraulic conductivity and storativity are the main hydraulic parameters that govern the groundwater flow. These parameters are generally obtained from pumping tests. Hence, pumping tests and recovery tests were conducted after the completion of well development in each pumping well if sufficient pumping yield could be obtained. Otherwise, slug test was conducted to assess the hydraulic conductivity. The slug tests were also performed in the monitoring wells having sufficient diameter.

In order to test the hydraulic properties of various rock units in the study area, each well was screened within the target formation and differentiated from the other units into which it penetrates. Since none of the monitoring and pumping wells were screened in alluvium only, the hydraulic properties of this unit was determined by evaluating pumping test data of the wells drilled by the Bank of Provinces.

Constant discharge pumping tests, followed by recovery tests, were conducted on the groundwater pumping wells PW-1, PW-3, PW-5, PW-6, PW-7, PW-8 and PW-9. At PW-4A free flow test and at PW-2 slug test was applied. The slug tests were also conducted at ten monitoring wells (CEL25, CEL36, CEL43, CEL44, CEL49, CEL50, CEL51, CEL52, CEL61, PW-8A, CEL-93A and CEL89C). These wells were pumped with a high discharge rate, which was followed by a rapid decrease in water level, and then the rising heads were recorded. The hydraulic properties, indicating minimum,

maximum and average values based on each formation, are summarized in Table 4.6. Table 4.7 shows the composite hydraulic conductivity and storage values obtained from wells screened at more than one geologic unit.

In the study area, the maximum hydraulic conductivity values are observed in the alluvium, coal, and the Lower Çavuşlar member. The hydraulic conductivity of alluvium ranges between  $4.27 \times 10^{-6}$  m/s and  $5.59 \times 10^{-5}$  m/s, with a geometric mean of  $1.36 \times 10^{-5}$  m/s. Among the wells, which were screened in the coal (PW-5, PW-6, CEL-47A, CEL-53A and CEL-59A), the minimum ( $1.26 \times 10^{-7}$  m/s) and maximum ( $2.26 \times 10^{-6}$  m/s) hydraulic conductivity values are calculated in PW-6 and CEL-53A, respectively. The geometric mean of hydraulic conductivity is determined as  $6.78 \times 10^{-7}$  m/s for the coal. The hydraulic conductivity of the Lower Çavuşlar member is determined from 10 wells drilled in that formation (CEL-19A, CEL-36, CEL-43, CEL-44, CEL-47, CEL-51, CEL-59, CEL-61, CEL-64 and CEL-107A), where hydraulic conductivities range from  $5.52 \times 10^{-9}$  m/s to  $7.59 \times 10^{-5}$  m/s, with a geometric mean of  $1.17 \times 10^{-6}$  m/s. In the study area, the volcanics, Upper Çavuşlar member and Aktepe and Kocalar members have lower hydraulic conductivity values. According to PW-3 and CEL-93A test data, which were screened in the Aktepe and Kocalar members, the hydraulic conductivities range from  $2.66 \times 10^{-8}$  m/s to  $1.42 \times 10^{-6}$  m/s, with a geometric mean of  $2.11 \times 10^{-7}$  m/s. Among the wells screened in the Upper Çavuşlar member (PW-2, PW-7, CEL-59B, and PW-8A), the minimum ( $1.31 \times 10^{-8}$  m/s) and maximum ( $1.55 \times 10^{-6}$  m/s) hydraulic conductivity values are calculated in PW-2 and CEL-59B, respectively. The geometric mean of hydraulic conductivity is determined as  $1.17 \times 10^{-7}$  m/s for the Upper Çavuşlar member. The volcanics were tested in six wells (PW-1, PW-4A, CEL-25, CEL-49, CEL-50 and CEL-52). The minimum hydraulic conductivity is calculated as  $4.89 \times 10^{-9}$  m/s (CEL-25), whereas the maximum value is computed as  $2.86 \times 10^{-5}$  m/s (PW-1). The geometric mean is determined as  $2.08 \times 10^{-7}$  m/s. The hydraulic properties of Bostantepe member could not be tested due to insufficient number of wells drilled in that unit.

Table 4.6. Summary of the calculated hydraulic conductivity and storativity parameters of formations

<b>Hydraulic Conductivity, K (m/s)</b>					
<b>Formation</b>	<b>Minimum</b>	<b>Maximum</b>	<b>Average</b>		<b>Tested Wells</b>
			<b>Arithmetic</b>	<b>Geometric</b>	
<b>Alluvium</b>	4.27x10 <sup>-6</sup>	5.59 x10 <sup>-5</sup>	1.80 x10 <sup>-5</sup>	1.36 x10 <sup>-5</sup>	L1-L2-L3
<b>Aktepe and Kocalar Members</b>	2.66 x10 <sup>-8</sup>	1.42 x10 <sup>-6</sup>	5.24x10 <sup>-7</sup>	2.11 x10 <sup>-7</sup>	PW3-CEL93A
<b>Upper Çavuşlar Member</b>	1.31x10 <sup>-8</sup>	1.55 x10 <sup>-6</sup>	2.55 x10 <sup>-7</sup>	1.17 x10 <sup>-7</sup>	PW2-PW7-CEL59B-PW8A-CEL89C
<b>Coal</b>	1.26 x10 <sup>-7</sup>	2.26 x10 <sup>-6</sup>	8.72 x10 <sup>-7</sup>	6.78 x10 <sup>-7</sup>	PW5-PW6-CEL47A-CEL53A-CEL59A
<b>Lower Çavuşlar Member</b>	5.52 x10 <sup>-9</sup>	7.59 x10 <sup>-5</sup>	9.43 x10 <sup>-6</sup>	1.17 x10 <sup>-6</sup>	CEL19A-CEL36-CEL43-CEL44-CEL47-CEL51-CEL59-CEL61-CEL64-CEL107A
<b>Volcanics</b>	4.89 x10 <sup>-9</sup>	2.86 x10 <sup>-5</sup>	5.18 x10 <sup>-6</sup>	2.08 x10 <sup>-7</sup>	PW1-PW4A-CEL25-CEL49-CEL50-CEL52
<b>Storativity, S</b>					
<b>Formation</b>	<b>Minimum</b>	<b>Maximum</b>	<b>Average</b>		<b>Tested Wells</b>
			<b>Arithmetic</b>	<b>Geometric</b>	
<b>Upper Çavuşlar Member</b>	3.15 x10 <sup>-4</sup>				CEL59B
<b>Coal</b>	2.16 x10 <sup>-5</sup>	1.54 x10 <sup>-4</sup>	5.67 x10 <sup>-5</sup>	4.41 x10 <sup>-5</sup>	CEL47A-CEL53A-CEL59A
<b>Lower Çavuşlar Member</b>	2.24 x10 <sup>-5</sup>	8.92 x10 <sup>-2</sup>	2.11 x10 <sup>-2</sup>	4.89 x10 <sup>-3</sup>	CEL19A-CEL47-CEL59-CEL107A

Table 4.7. Summary of the calculated hydraulic conductivity and storativity parameters of composite wells

Hydraulic Conductivity, K (m/s)					
Formation	Minimum	Maximum	Average		Tested Wells
			Arithmetic	Geometric	
Alluvium and Upper Çavuşlar Member	$6.16 \times 10^{-8}$	$9.21 \times 10^{-5}$	$6.14 \times 10^{-5}$	$1.61 \times 10^{-5}$	PW9-PW9A
Coal and Lower Çavuşlar Member	$3.09 \times 10^{-7}$	$1.22 \times 10^{-6}$	$8.17 \times 10^{-7}$	$7.45 \times 10^{-7}$	PW8-CEL107
Storativity, S					
Formation	Minimum	Maximum	Average		Tested Wells
			Arithmetic	Geometric	
Alluvium and Upper Çavuşlar Member	$1.72 \times 10^{-2}$	$9.43 \times 10^{-1}$	$2.30 \times 10^{-1}$	$6.12 \times 10^{-2}$	PW9A
Coal and Lower Çavuşlar Member	$1.37 \times 10^{-4}$	$1.16 \times 10^{-2}$	$3.77 \times 10^{-3}$	$1.58 \times 10^{-3}$	PW8-CEL107

The storativity values in the study area are generally low and can be determined for the coal, Upper and Lower Çavuşlar members. The geometric mean of storativity values is maximum for the Lower Çavuşlar member ( $4.89 \times 10^{-3}$ ) and minimum for the coal ( $4.41 \times 10^{-5}$ ).

#### 4.2.2. Groundwater Levels

##### 4.2.2.1. Spatial variations in groundwater levels

A groundwater elevation map was prepared for the lower aquifer, which includes the coal layer. Due to a lack of monitoring wells drilled in the upper aquifer and alluvium aquifer, a groundwater elevation map could not be prepared. The groundwater level data measured at the available monitoring and pumping wells as well as spring elevations were used in the preparation of groundwater elevation map (Figure 4.8). Since the groundwater level monitoring period covers both wet and dry periods, in the

preparation of the groundwater level map, average values were used. The distribution of the groundwater level monitoring points (i.e. monitoring wells and springs) constrains the areal distribution of the groundwater elevation map. Therefore, the spatial distribution of the groundwater levels of the lower aquifer can be given for a restricted area enclosing the mine units.

In the vicinity of the planned mine site, the groundwater flow in the lower aquifer is generally towards the Kirmir stream. The groundwater elevations vary from 1150 m at the southeastern part of the area to 800 – 850 m along the Kirmir stream. The faults located in the southern part of the Kirmir stream control the groundwater flow in those locations. At the northern part of the Kirmir stream, the groundwater flow is towards the Pazar and Kirmir streams.

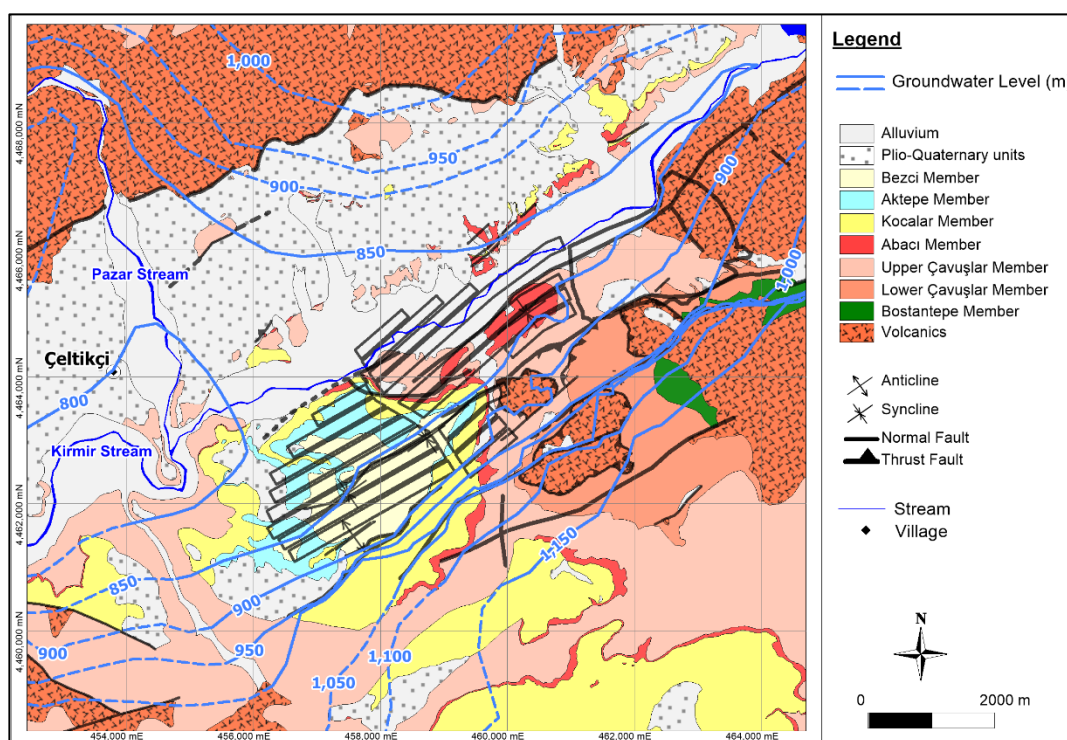


Figure 4.8. Groundwater level map of the area on geological map

#### **4.2.2.2. Temporal variations in groundwater levels**

The biweekly monitoring of groundwater levels has started immediately after the completion of each well. The groundwater levels measured in the monitoring and pumping wells, between June 2012 and August 2015, indicate that seasonal variations in groundwater levels are limited. The fluctuations in the groundwater levels generally result from well development or pumping tests conducted in the vicinity of wells. The measured groundwater level at each monitoring well with respect to time is provided in the Appendix C. In the graphs, precipitation data are also included.

The monitoring of groundwater levels reveal that artesian behavior is also observed at wells PW-4A, PW-5, CEL35, CEL-47A, CEL-53A, CEL-59A, CEL-59B, CEL-97, CEL-100, CEL-100C, CEL-104, CEL-107, CEL-107A, and CEL-107B.

The vertical hydraulic relation among the coal, Upper and Lower Çavuşlar members were evaluated with the help of nested wells. In this regard, the measured groundwater levels of the PW-1/ PW-2, CEL-47/47A, CEL-19/19A/19B, CEL-59/59A/59B, CEL-89B/89C, CEL-97/97A, CEL-100/100C, CEL-101/101A and CEL107/107A/107B are plotted in Figure 4.9.

In the western part of the Kocalar 2 fault, the groundwater levels measured at well screened in the volcanics (PW-1) is 18 m higher than the well screened in the Upper Çavuşlar member (PW-2). Similarly, the water level measured in the Lower Çavuşlar member (CEL-19A) and coal (CEL-19B) are close to each other, and about 10 m higher than that of the Upper Çavuşlar member (CEL-19D). Thus, it can be concluded that, in the western part of the Kocalar 2 fault, there exists an upward hydraulic gradient from the volcanics and Lower Çavuşlar member towards the Upper Çavuşlar member.

In the eastern part of the Kocalar 2 fault, CEL-47 and CEL-47A wells were screened above and within the coal layer, respectively. In this area, the measured groundwater levels within the coal are higher than those above the coal. Likewise, among the wells

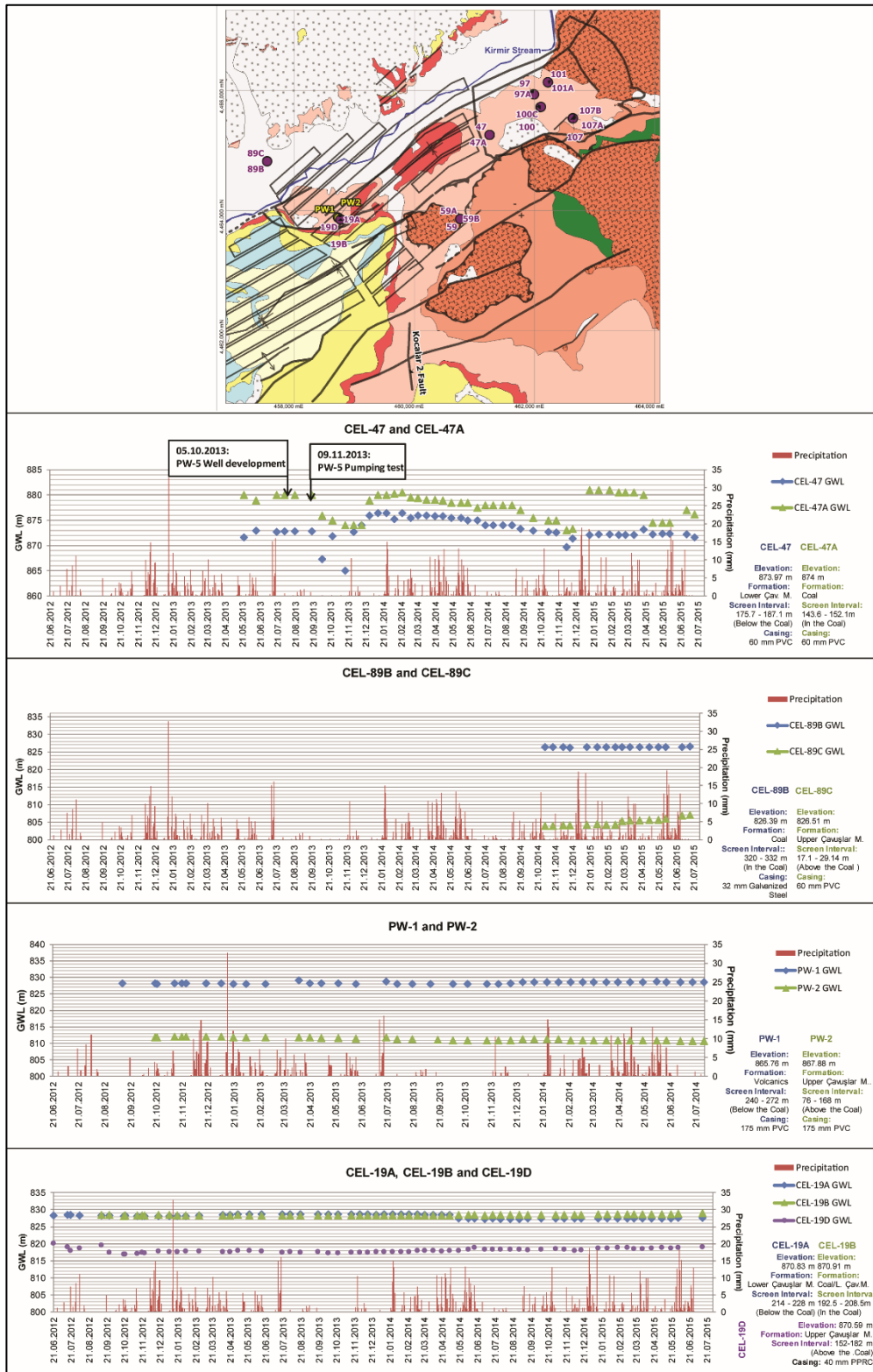


Figure 4.9. Groundwater levels measured in the nested wells

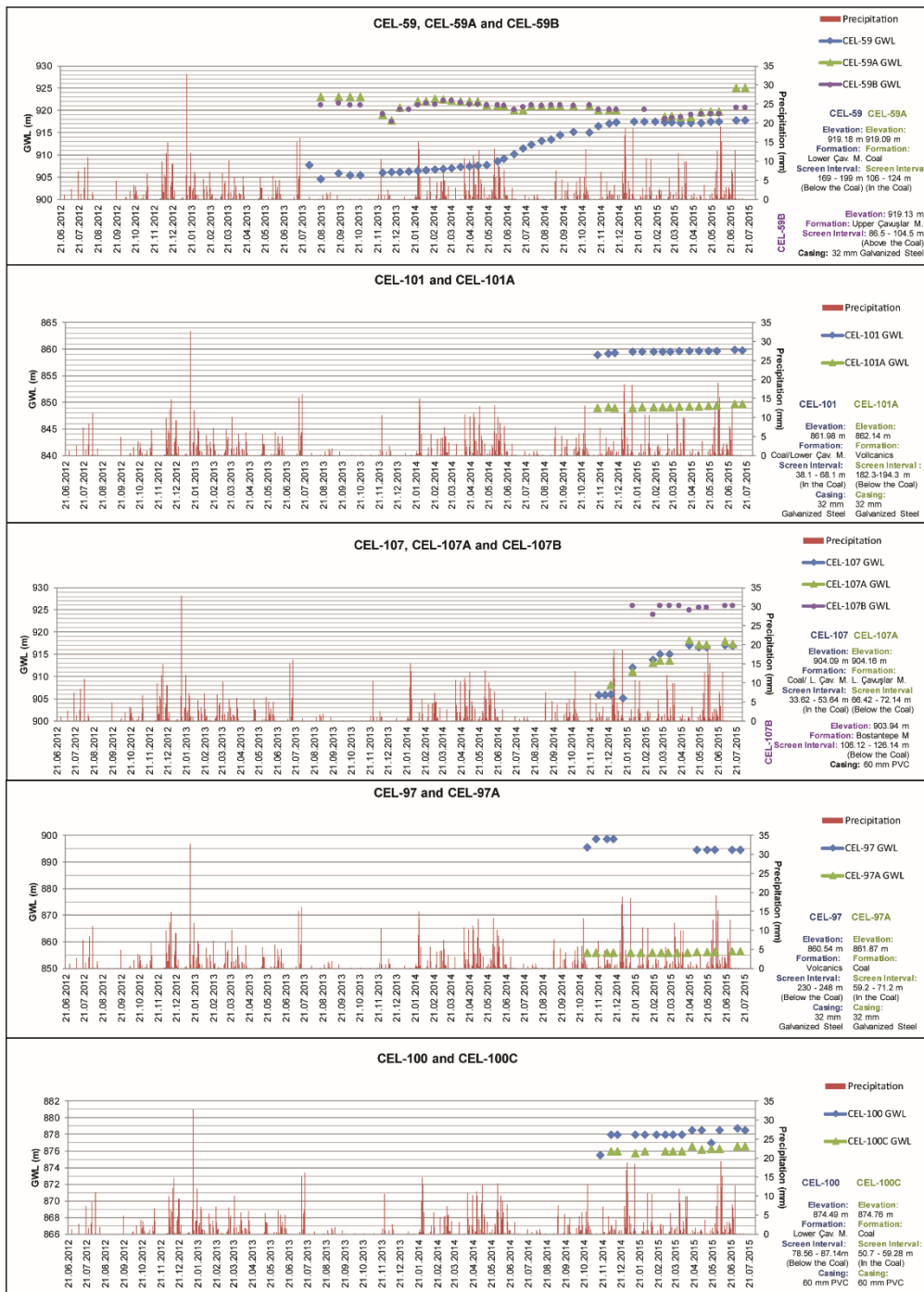


Figure 4.9. cont.ed

CEL-59, CEL-59A and CEL-59B, measured groundwater levels are close for the wells screened above and within the coal, and lower than the wells screened below the coal.

At the northern part of Kirmir stream, groundwater levels measured CEL-89B (screened within the coal) are about 20 m higher than that of CEL-89C (screened above the coal).

Around the planned open pit area, hydrographs of CEL97 / CEL-97A and CEL-100 / CEL-100C indicate that groundwater levels are higher in below coal layers than within coal layers. On the other hand, a reverse relation is observed at wells CEL-101 and CEL-101A. Also, among the wells CEL-107 (screened within the coal), CEL-107A (screened in the Lower Çavuşlar member) and CEL-107B (screened in the Bostantepe member), the measured groundwater levels are close to each other in CEL-107 and CEL-107A and higher in CEL-107B. It can be concluded that in the planned open pit area, a vertical hydraulic gradient exists from below the coal layers to above the coal layers.

## CHAPTER 5

### CONCEPTUAL MODEL

A conceptual model can be explained as the gathering of the all known information of a site (Anderson et al., 2015). In order to simplify a complex system and organize the field data to analyze the system more easily, conceptual model development is a crucial step. The conceptual model mainly involves (i) description of thickness, continuity, lithology of the aquifers and confining layers, and their relations with the structural features, (ii) preparation of groundwater budget and (iii) defining the flow system. In other words, conceptual model reflects the hydrogeological characterization of the area and forms the basis for numerical modeling.

The conceptual model of the area is focused on the area covering the mine units where all the available information about the site (monitoring and pumping wells, springs, surface water monitoring points, aquifer test data, etc.) is concentrated. Therefore, the conceptual hydrologic budget and hydrogeological budget of the study area are also restricted in that area.

#### **5.1. Conceptual Model of the Study Area**

In the study area, there are three main aquifers, namely the Upper aquifer, Lower aquifer and Alluvium aquifer. The Upper aquifer consists of the Kocalar member (composed of alternation of claystone, mudstone and siltstone), Aktepe member (composed of moderately silicified limestone) and Bezci member (composed of continental clastics). The spatial distribution of the Upper aquifer is limited. It is observed at the western part of the Kocalar 2 fault and differentiated from the Lower aquifer by the Abacı Ignimbrite. The Lower aquifer includes the Upper Çavuşlar member (composed of cream to white and light green mudrocks with sandstones, tuffs and coal-bearing levels), Lower Çavuşlar member (composed of alternating oolitic

limestone and varve with intercalation of thin-bedded immature coal seams and tuff layers, moderately to highly silicified chert layers), Bostantepe member (composed of fine- to medium-grained clastic sedimentary rocks, where the dominant lithology is sandstone) and Volcanics (composed of lava flows and pyroclastics). The Lower aquifer has the broadest extension within the study area. It has confined character at the western part of the Kocalar 2 fault and forms an unconfined aquifer elsewhere. Quaternary alluvial deposits, which are observed along the Pazar and Kirmir streams, form the Alluvium aquifer, which has unconfined character. It has limited areal extent and thickness.

The recharge and discharge mechanisms for the Alluvium aquifer cannot be determined due to the limited areal extent and thickness of the alluvium in the area and also lack of monitoring wells drilled in the alluvium.

The Upper aquifer is recharged from direct precipitation and discharged by the springs located at the perimeter of the Upper aquifer. The groundwater flow from the Upper to Lower aquifer is another component of the discharge mechanism in the Upper aquifer.

The Lower aquifer is widely observed in the study area. It has confined character in the western part of the Kocalar 2 fault and unconfined character elsewhere. The main recharge mechanism for the Lower aquifer is the recharge from direct precipitation. The aquifer is recharged from the mountainous areas. Also the recharge from the Upper aquifer is another recharge component. The groundwater discharges to the Kirmir and Pazar streams. The springs located in the area also discharge the groundwater. The groundwater level map could only be prepared for the Lower aquifer, due to insufficient monitoring wells drilled in the Upper aquifer and Alluvium aquifer (Figure 4.8).

## **5.2. Conceptual Hydrologic Budget**

When precipitation occurs in an area, it is transformed into runoff, infiltration or evapotranspiration components. In water budget calculations, the ratio of these

components to precipitation is calculated. The hydrologic water budget of the area is computed for each month by using corrected long-term average meteorological data. The “Thornthwaite method” and the “Curve Number method” are used to calculate potential evapotranspiration and surface runoff, respectively. The remaining portion of precipitation is assumed to be equal to infiltration into groundwater.

In the Thornthwaite method (1948), the monthly total precipitation, the mean monthly temperature and latitude values of the study area are required. The long-term monthly total precipitation values for the study area were determined by correlating the measured data of the Kızılcahamam meteorological station to the Çeltikçi meteorological station. The mean monthly temperature values were obtained from the Kızılcahamam meteorological station. The uncorrected monthly potential evaporation (UPET; mm/month) is calculated by Thornthwaite methods as:

$$UPET_m = 16 \times \left(\frac{10t_m}{I}\right)^a \quad (Eq. 5.1)$$

$$a = (675 \times 10^{-9})I^3 - (771 \times 10^{-7})I^2 + (179 \times 10^{-4})I + 0.492 \quad (Eq. 5.2)$$

$$I = \sum_{i=1}^{12} \left(\frac{t_i}{5}\right)^{1.514} \quad (Eq. 5.3)$$

where  $m$ : month index,  
 $t$ : mean monthly temperature ( $^{\circ}\text{C}$ ),  
 $I$ : annual heat index (equals to the sum of monthly heat indices( $i$ )),  
 $a$ : coefficient that depend on heat index

In the Curve Number (CN) method, which was developed by U.S. Soil Conservation Service (SCS, 1964), the surface runoff values are calculated on the basis of: (a) direct runoff (or excess rainfall),  $P_e$ , is less than or equal to total precipitation ( $P$ ); (b) soil moisture retention occurring after runoff begins ( $F_a$ ) is less than or equal to the potential soil moisture retention ( $S$ ). Until precipitation reaches a certain value ( $I_a$ , initial abstraction) runoff is not observed; thus, potential runoff is equal to  $P - I_a$ . In the CN method, the ratio of two real and two potential values mentioned above, are

equal, and by applying the continuity principle, direct runoff (or excess rainfall,  $P_e$ ) can be computed as:

$$P_e = \frac{(P-I_a)^2}{P-I_a+S} \quad (\text{Eq. 5.4})$$

For small watersheds, it is generally assumed that  $I_a=0.2 \times S$ , hence the generalized form of the CN method is obtained as:

$$P_e = \frac{(P-0.2S)^2}{P+0.8S} \quad (\text{Eq. 5.5})$$

The Curve number is derived from curves drawn based on the relationship between  $P$  and  $P_e$  from data corresponding to many basins. CN is related to potential soil moisture retention by  $CN=1000/(S+10)$  or  $S(\text{in})=1000/(CN-10)$ . Thus, runoff curve numbers (CNs) indicate the runoff potential from a hydrologic soil-cover complex during periods when the soil is not frozen. A higher CN indicates a higher runoff potential.

Runoff curve numbers (CNs) depend on land use, landcover, and hydrologic soil groups. Hydrologic soil groups are divided into four types, namely Group A, B, C and D. From Group A to D, the runoff potential increases whereas infiltration rates decrease.

In order to calculate CN for the study area, the Landuse/landcover data were obtained from the National Soil Database (UTVT). The soils in the study area are classified as hydrologic soil group type B, having moderate runoff and infiltration potential. Also, the gradient and soil depth information in UTVT database was used. For each subwatershed, the areal distribution of landuse/landcover and hydrologic soil groups were computed, and a weighted curve number value for each subwatershed was calculated. The calculated curve number values range between 71 and 77; with a weighted average value of 74 (Yazıcıgil et al. 2015).

The components of long-term hydrologic water budget were determined conceptually for each month using the calculated CN for the study area, long-term mean monthly

precipitation and potential evapotranspiration data obtained from the Thornthwaite method (Table 5.1). The monthly potential evapotranspiration values were obtained by corrected the UPET value by using the coefficient “r”, which is based on the latitude of the area (40°). The surface runoff was calculated by using monthly precipitation values and curve number (CN=74). The difference between monthly precipitation and runoff is equal to infiltration. The soil moisture capacity was assumed to be 100 mm, and for each month, change in soil moisture was computed. Based on these calculations, actual evapotranspiration, surface runoff and groundwater recharge values were determined.

According to the water budget calculations, the average annual groundwater recharge from direct precipitation is calculated as 55 mm, which comprises 14 % of the annual precipitation (Table 5.2).

### **5.3. Conceptual Groundwater Budget**

The conceptual groundwater budget of the study area was developed for the area bounded by Kirmir stream in the north and Binkoz village in the south, covering an area of 52 km<sup>2</sup> (Figure 5.1). The existence of pumping and monitoring wells, springs and surface water discharge measurement locations in that area, make groundwater budget calculations available.

#### **5.3.1. Upper Aquifer**

The surface area of the Upper aquifer in that particular region is about 14 km<sup>2</sup>. Since groundwater recharge from precipitation is calculated as 55 mm/yr, the groundwater recharge in the Upper aquifer is computed as  $8.09 \times 10^5$  m<sup>3</sup>/yr.

The discharge components are composed of discharge from springs and discharge to the Lower aquifer. The discharge amount of the Upper aquifer to the underlying Lower aquifer was determined by Darcy's equation. The ratio of horizontal to vertical hydraulic conductivity was taken as 500 and the value of the hydraulic gradient was calculated by dividing the hydraulic head difference measured between PW-3

Table 5.1. Monthly conceptual water budget results

Parameter	Jan	Feb	Mar	Apr	May	Jun	Jul	Aug	Sep	Oct	Nov	Dec	TOTAL	Ratio to Precipitation
Mean Monthly Temperature (°C)	-1.0	0.1	4.1	9.3	13.9	17.8	21.1	20.8	16.2	10.8	5.0	1.1		
i	0.0	0.0	0.7	2.6	4.7	6.8	8.8	8.7	5.9	3.2	1.0	0.1	42.6	
a	1.2	1.2	1.2	1.2	1.2	1.2	1.2	1.2	1.2	1.2	1.2	1.2	14.0	
UPET	0.0	0.2	15.3	39.8	63.6	84.9	103.5	101.8	76.0	47.4	19.3	3.3	555.1	
PET	0.0	0.2	15.8	44.2	78.9	106.1	131.4	120.1	79.1	45.5	16.0	2.7	639.9	
r	0.8	0.8	1.0	1.1	1.2	1.3	1.3	1.2	1.0	1.0	0.8	0.8		
Precipitation (mm)	59.9	40.3	34.6	37.9	37.2	29.1	14.3	10.6	9.3	31.4	30.7	57.2	392.4	
Surface Runoff coefficient	1.0	1.0	1.0	1.0	1.0	1.0	0.0	0.0	0.0	1.0	1.0	1.0		
Surface Runoff (mm)	13.5	4.5	2.6	3.7	3.4	1.3	0.0	0.0	0.0	1.8	1.6	12.0		
Infiltration (I)	46.4	35.8	31.9	34.2	33.7	27.8	14.3	10.6	9.3	29.6	29.1	45.2		
I-PET	46.4	35.6	16.2	-10.0	-45.1	-78.2	-117.1	-109.5	-69.8	-15.8	13.0	42.5		
TOTAL (P-PET)	0.0	0.0	0.0	-10.0	-55.1	-133.3	-250.5	-360.0	-429.8	-445.6	0.0	0.0		
Soil Moisture	100.0	100.0	100.0	90.5	57.6	26.4	8.2	2.7	1.4	1.2	14.2	56.7		
Change in Soil Moisture	43.3	0.0	0.0	-9.5	-32.9	-31.3	-18.2	-5.4	-1.4	-0.2	13.0	42.5		
AET	0.0	0.2	15.8	43.7	66.6	59.1	32.5	16.1	10.7	29.8	16.0	2.7	293.1	75%
Excess Precipitation	16.6	40.1	18.8	3.7	3.4	1.3	0.0	0.0	0.0	1.8	1.6	12.0	99.3	
Surface Runoff	13.5	4.5	2.6	3.7	3.4	1.3	0.0	0.0	0.0	1.8	1.6	12.0	44.4	11%
Groundwater Recharge	3.1	35.6	16.2	0.0	0.0	0.0	0.0	0.0	0.0	0.0	0.0	0.0	54.9	14%
													TOTAL	100%
													392.4	

Table 5.2. Annual water budget results

Hydrologic Component	Amount (mm/year)	Ratio to Precipitation (%)
Precipitation	392.4	100
Evapotranspiration	293.1	75
Surface Runoff	44.4	11
Groundwater Recharge	54.9	14

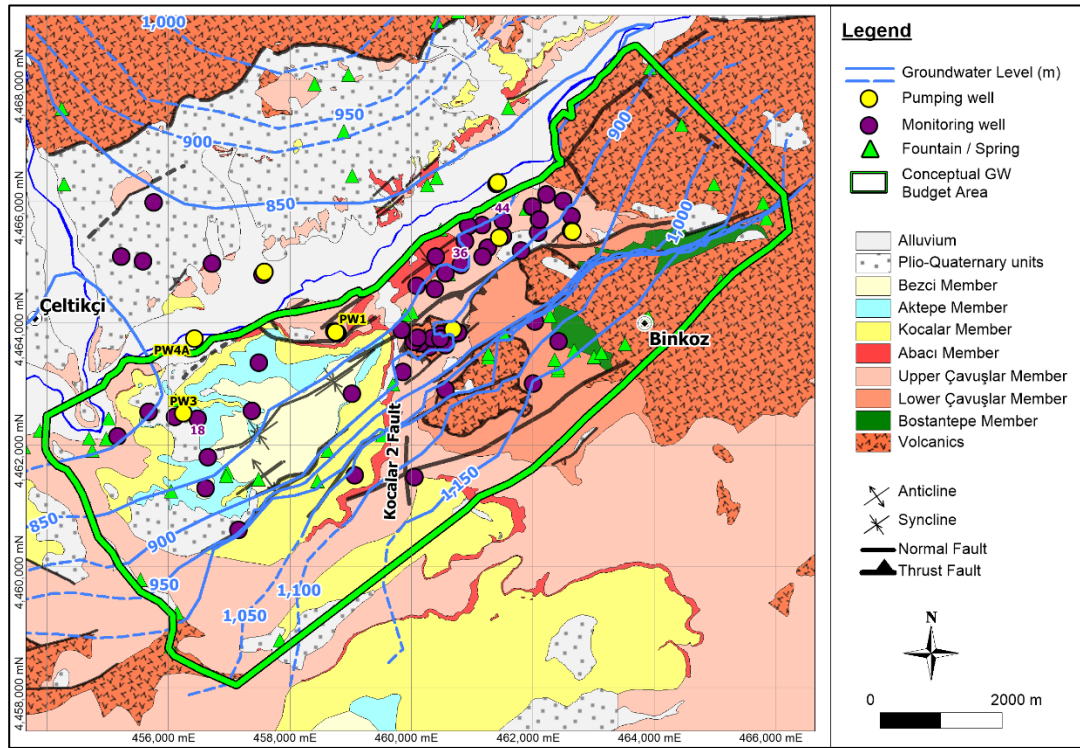


Figure 5.1. Area showing the conceptual groundwater budget calculation is conducted

(screened in the Upper aquifer) and CEL18 (screened in the Lower aquifer) to thickness of the silicified tuff separating the two aquifers. The discharge amount is computed as  $7.53 \times 10^5 \text{ m}^3/\text{yr}$ . The average total discharge rate of the nine springs (F1,

F2, F3, F4, F5, F6, F7, F45, F51 and F53) is calculated as 1.13 L/s. Apart from the monitored springs, nine springs were also determined from the topographic map, and the average discharge rate was assumed as 0.07 L/s. Thus, total groundwater discharge from springs is calculated as 1.76 L/s.

### **5.3.2. Lower Aquifer**

The groundwater recharge components in the Lower aquifer are groundwater recharge from precipitation, lateral inflow and recharge from the Upper aquifer. The surface area of the unconfined portion of the Lower aquifer is about 38 km<sup>2</sup>. Therefore, the groundwater recharge from precipitation is calculated as 2.11x10<sup>6</sup> m<sup>3</sup>/yr. The lateral inflow to the Lower aquifer occurs from the southern part of the area, from the volcanics and Lower Çavuşlar member and Upper Çavuşlar member at the eastern and western part of the Kocalar 2 fault, respectively. The hydraulic gradient and recharge area were calculated from the groundwater level map and cross-sections. The total lateral inflow to the Lower aquifer is calculated as 3.48x10<sup>6</sup> m<sup>3</sup>/yr. With the addition of recharge from the Upper aquifer, total recharge in the Lower aquifer is calculated as 6.34x10<sup>6</sup> m<sup>3</sup>/yr.

Groundwater discharge mechanisms for the Lower aquifer are the discharge from springs and lateral outflow. There are 28 monitored springs located within the area, where average flow rates are measured as 6.02 L/s. Therefore, the groundwater discharge from the springs is calculated as 1.9x10<sup>5</sup> m<sup>3</sup>/yr. The lateral outflow from the Lower aquifer to the Kirmir stream was calculated for the eastern and western part of the Kocalar 2 fault. For this purpose, hydraulic conductivity values measured at CEL-44, CEL-36, PW-1 and PW-4A were used. The hydraulic gradient and the discharge area were determined by using the groundwater level map and cross-sections. The outflow from this area is calculated as 1.89x10<sup>6</sup> m<sup>3</sup>/yr. Total discharge from the Lower aquifer is computed as 6.55x10<sup>6</sup> m<sup>3</sup>/yr.

The conceptual groundwater budget components were summarized in Table 5.3.

Table 5.3. Conceptual groundwater budget

<b>Upper Aquifer</b>			
<b>Recharge (m<sup>3</sup>/yr)</b>		<b>Discharge (m<sup>3</sup>/yr)</b>	
Precipitation	8.09x10 <sup>5</sup>	Springs	5.55x10 <sup>4</sup>
		Discharge to Lower Aquifer	7.53x10 <sup>5</sup>
<b>TOTAL</b>	<b>8.09x10<sup>5</sup></b>	<b>TOTAL</b>	<b>8.09x10<sup>5</sup></b>
<b>Lower Aquifer</b>			
<b>Recharge (m<sup>3</sup>/yr)</b>		<b>Discharge (m<sup>3</sup>/yr)</b>	
Precipitation	2.11x10 <sup>6</sup>	Springs	1.90x10 <sup>5</sup>
Recharge from Upper Aquifer	7.53x10 <sup>5</sup>	Lateral Outflow	6.36x10 <sup>6</sup>
Lateral Inflow	3.48x10 <sup>6</sup>		
<b>TOTAL</b>	<b>6.35x10<sup>6</sup></b>	<b>TOTAL</b>	<b>6.55x10<sup>6</sup></b>



## CHAPTER 6

### GROUNDWATER FLOW MODEL

A 3D numerical groundwater flow model is an essential tool to understand groundwater flow regime at the site, obtain hydraulic interactions between different aquifers/lithologies and to check the validity of the conceptual model as well as conceptual groundwater budget. With the help of numerical models, the anticipated impacts of any change (artificial or natural) in the system can be predicted, and hence required actions can be taken in advance.

#### 6.1. Computer Code

3D groundwater flow model of the study area is set up via FEFLOW 7.0 software. FEFLOW is developed by DHI-WASY (2015) and an acronym of “Finite Element subsurface FLOW simulation system”. It solves the governing equations of flow, mass and heat transport in porous and fractured media using finite element method for both saturated and unsaturated conditions.

The reasons for selecting FEFLOW in this study can be summarized as:

- FEFLOW can simulate a variety of in-situ hydrogeological factors in 3D,
- FEFLOW can simulate a number of geological elements (i.e. hydrogeological and heterogeneous and anisotropic units) as well as structural elements,
- Different hydrologic agents, such as rivers, streams, drains, springs, wells, etc. can be simulated by FEFLOW,
- FEFLOW is widely used throughout the world, and hydrological simulations used in FEFLOW have been tested through modeling work carried out across the world,
- Flexible finite element meshing enables simulation of complex boundaries

## 6.2. Model Geometry and Layering

The model domain covers an area of 602.5 km<sup>2</sup>. It is bounded by the Çamlıdere Dam Reservoir and the watershed divide in the north, Kurtboğazı Dam Reservoir and streams/creeks located at the upstream (Mera stream) and downstream part of this dam (Kurtboğazı creek) in the east. The south and west boundaries are located approximately 10 km away from the planned longwall panels and open pit, providing enough distance to avoid any boundary effect. The extent of the model domain in N-S and E-W directions are 26.8 and 28.7 km, respectively (Figure 6.1).

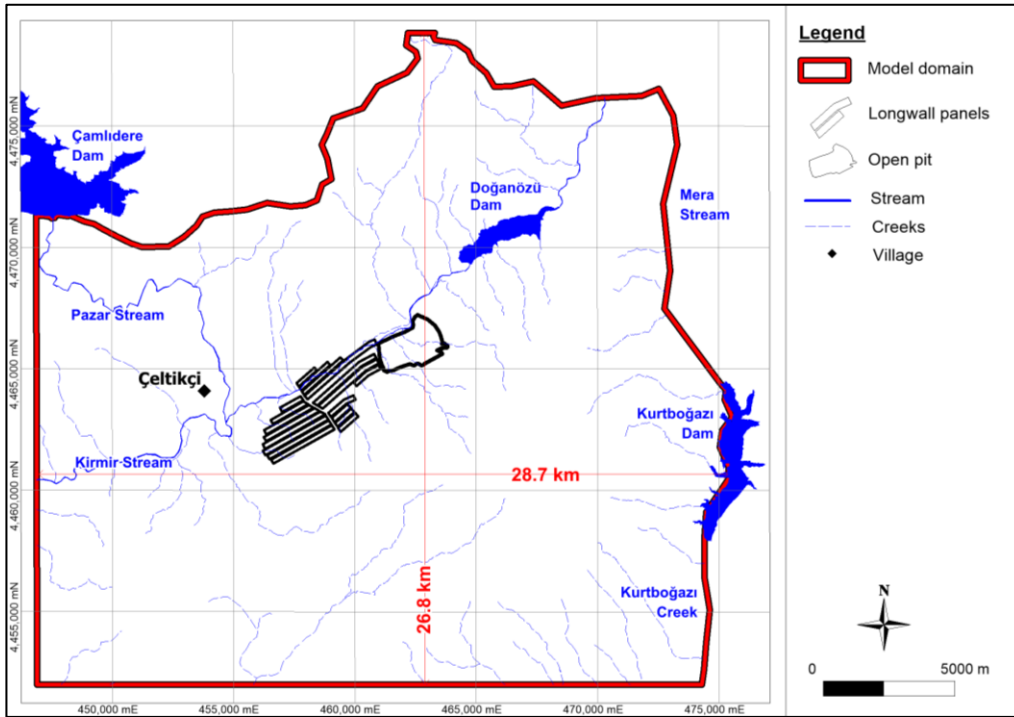


Figure 6.1. Model domain and dimensions

### 6.2.1. Layer Design

The model domain consists of 16 layers and 17 slices (Figure 6.2). The topographic surface is represented by slice 1, where the elevation ranges between 1820 and 755 m.

On the other hand, slice 17 has a uniform elevation of 0 m. For the domain of interest including the longwall panels and open pit layout, the well logs are used to define the top and bottom elevations of the layers. The alluvium is represented by layer 1, whereas layers 2-4 show the upper aquifer, where the thickness of upper aquifer is divided into three layers to increase the vertical resolution. The Abacı ignimbrite, which separates the upper and lower aquifers, is simulated by layer 5. The Upper Çavuşlar member, thickness of which reaches about 200 m in the domain of interest, is divided into five layers in vertical directions and represented by layers 6-10. The coal seams (upper and lower seam) are represented by layer 11 and layer 13, where the average layer thicknesses are determined as 4 m for the upper seam and 2 m for the lower seam based on well log data. Layer 12 is designed to simulate the interburden. The Lower Çavuşlar member is shown by layers 14 and 15, whereas the volcanics comprise the bottom layer. The thicknesses of lithological units were interpolated to obtain domain-wise distribution of layers. The pinch out of the units were simulated by using a minimum layer thickness of 10 m.

In the model, the layer types are determined as phreatic for the first slice and fixed for slice 17. In between the layer type is defined as dependent. In the phreatic layer option, the model stratigraphy remains solid when the water table drops below the first layer; hence it can be used when water table cut slices.

### **6.2.2. Mesh Design**

The finite element mesh contains 2,965,242 nodes and 5,570,944 elements. Each layer is composed of 348,148 elements, and each slice has 174,426 nodes. The total thickness is 1820 m (Figure 6.2). The element sizes range from 10-30 m in the vicinity of the planned mine area, and reach 500 m at the periphery of the model domain.

The meshing is done by triangulation, which can handle complex geometries and considers the polygons, points, and lines during the mesh generation process. Hence, the exact location of faults, creeks, streams, wells, springs, mine facilities, etc. can be simulated.

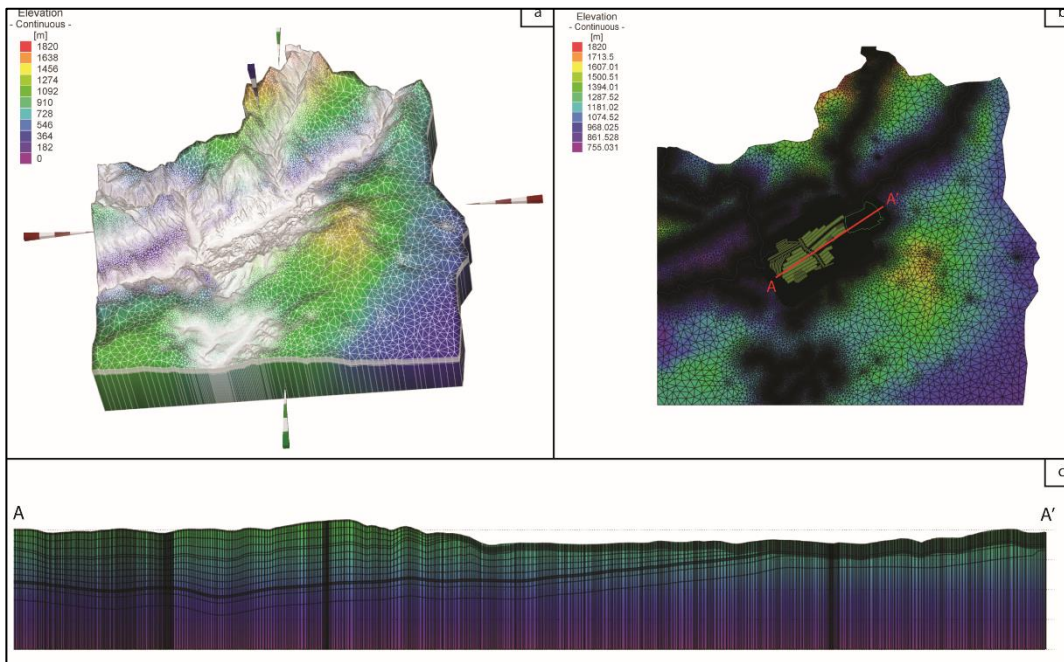


Figure 6.2. Finite element mesh design and layering (a: 3D view of the model domain, b: finite element mesh of the slice 1, c: A-A' cross section showing the model layers)

The mesh quality also plays an important role in finite element models. In the model domain mesh quality is checked by (i) Delaunay criteria, and (ii) maximum interior angle of triangles. Delaunay criteria violations occur when the circumcircle of the triangle belonging to an element includes a node of another element (Figure 6.3). In the model domain all the elements obey the Delaunay criteria. The maximum interior angles of all triangles are also constrained to  $120^\circ$  to obtain stable results.

### 6.3. Boundary Conditions

Definition of boundary conditions is one of the essential steps in groundwater modeling since they limit the model domain and provide a solution to the governing equations. In general, there are three types of boundary conditions, namely Dirichlet, Neuman, and Cauchy. In FEFLOW, the default boundary condition is no flow boundary.

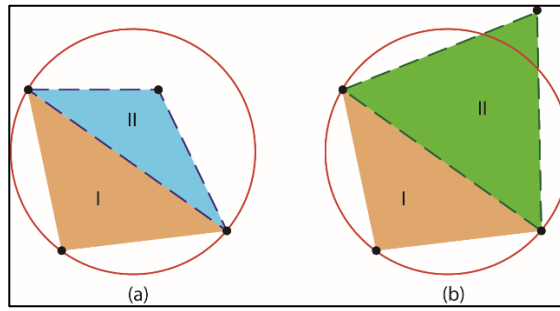


Figure 6.3. Delaunay criteria (a) violates, (b) obeys the criteria

Once the boundary conditions are applied in FEFLOW, they can also be constrained to simulate real case situations.

The boundary conditions applied to the model domain are shown in Figure 6.4. Within the model domain, the surface water reservoirs of Çamlıdere and Kurtboğazi dams are simulated by hydraulic head boundary conditions, where the hydraulic head equals to 1000 m and 964 m, respectively. The Doğanözü dam located within the model domain is also described by hydraulic head boundary condition with a value of 870 m. Throughout the model domain, the intermittent streams and springs are represented by hydraulic head boundary condition with the maximum flow rate constraint of  $0 \text{ m}^3/\text{d}$  in order to prevent any inflow to the groundwater system. Two main streams within the model domain, i.e. Kirmir and Pazar streams are simulated by fluid transfer boundary condition, where a pre-defined reference head is applied with a conductance parameter. Due to the lack of detailed hydrological data, stream stage elevations are estimated to be 2 m below the topographic elevation, and the conductance parameter is calculated by dividing the hydraulic conductivity of the clogging layer (assumed to be  $1 \times 10^{-6} \text{ m/s}$ ) by thickness of that layer (assumed to be 0.5 m). The Mera stream, which forms the eastern boundary, is also represented by the fluid transfer boundary condition. For the rest of the study area, no flow boundary condition is used.

The groundwater withdrawal resulting from drinking/irrigation water needs within the model domain is represented by multi-layer well boundary condition. The

hydrogeological studies reveal that 176 wells are used within the model domain. Among these, 2 of them are used as water supply wells for villages (Bağören and Gümele villages). 164 wells are private wells and used for irrigation purposes. Anadolu-Efes Brewery Company uses the remaining 10 wells. The assigned pumping rates for these wells are 2 L/s from Gümele village, 1 L/s from Bağören village well, 0.05 L/s from private wells and 44.30 L/s from Anadolu-Efes wells.

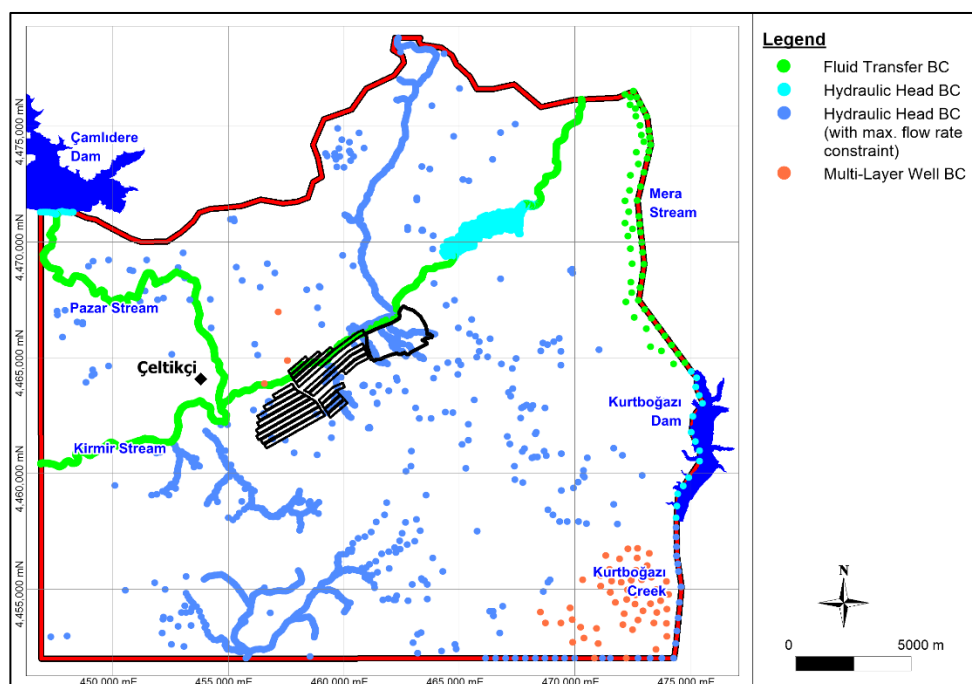


Figure 6.4. Boundary conditions applied to the model

## 6.4. Model Parameters

Model parameters, including recharge, hydraulic conductivity, and storage properties, were used to describe the properties of the porous media. The data obtained from hydrogeological characterization and field tests were modified during the calibration processes in order to achieve a good correlation between observed and simulated groundwater levels.

#### **6.4.1. Recharge**

The net infiltration to the model area is simulated by in/outflow on top/bottom material property in FEFLOW. The mean annual precipitation values for the study area were determined by correcting precipitation values measured at the Kızılcıhamam station according to calculated %Bias values. According to this calculation, the mean annual precipitation for the study area is determined as 392.4 mm. The water budget calculations, where Thornthwaite method was used to calculate potential evapotranspiration, and SCS curve number was used for surface runoff determinations, reveal that average annual groundwater recharge from direct precipitation in the study area is 55 mm, which comprises 14 % of the annual precipitation.

Since the study area is located in a steep and undulating topography, the distribution of groundwater recharge also varies within the study area. The precipitation depends on topography, and as the elevation increases, more precipitation is observed. Also, at higher altitudes, the precipitation may occur as snow, which results in more recharge at these areas. In this regard, assigned groundwater recharge values were distributed considering the median elevation of the model area. For the elevations below the median elevation a lower recharge rate (39 mm/yr), and for the elevations above the median elevation a higher recharge rate (97.5 mm/yr) was assigned. Hence, at the end of the calibration, the average recharge from precipitation for the model domain is calculated as 84.5 mm/yr (Figure 6.5).

#### **6.4.2. Hydraulic Conductivity**

The hydraulic conductivities of the geological units that outcrop within the study area were determined from the pumping and slug tests performed at various monitoring and pumping wells. The calculated hydraulic conductivity values obtained from these wells were exported to FEFLOW with very little alteration (Table 6.1). Nine different conductivity zones were determined based on the lithological characteristics and aquifer test results. On the other hand, the hydraulic properties of the fault zones were

determined during the model calibration due to the lack of data about the characteristics of the faults (Figure 6.6). Within the model domain, the ratio of vertical to horizontal hydraulic conductivity was set to 0.1 for all units, except the fault zones, where the flow was assumed to be isotropic.

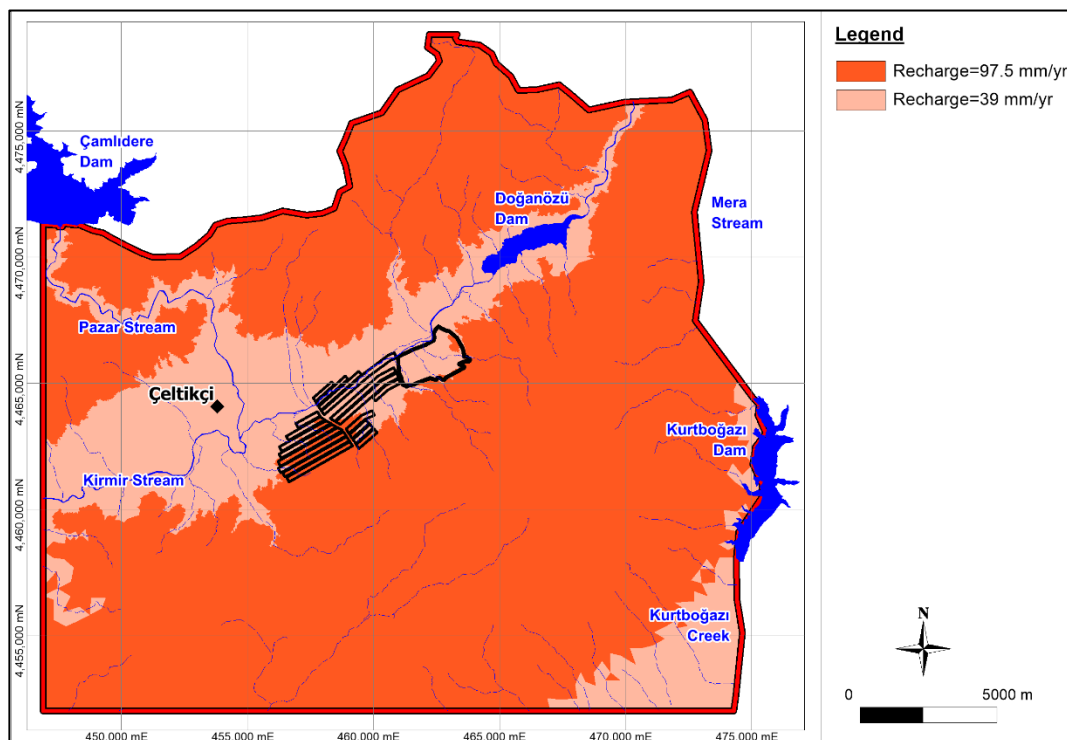


Figure 6.5. Aerial distribution of recharge in the model domain

Table 6.1. Hydraulic conductivity values assigned to the model

Hydraulic Conductivity of units, K (m/s)					
Formation	Minimum	Maximum	Average		Assigned Value
			Arithmetic	Geometric	
Alluvium	4.27x10 <sup>-6</sup>	5.59 x10 <sup>-5</sup>	1.80 x10 <sup>-5</sup>	1.36 x10 <sup>-5</sup>	1.00 x10 <sup>-5</sup>
Upper Aquifer	2.66 x10 <sup>-8</sup>	1.42 x10 <sup>-6</sup>	5.24 x10 <sup>-7</sup>	2.11 x10 <sup>-7</sup>	1.00 x10 <sup>-6</sup>
Upper Çavuşlar Member	1.31 x10 <sup>-8</sup>	1.55 x10 <sup>-6</sup>	2.55 x10 <sup>-7</sup>	1.17 x10 <sup>-7</sup>	2.00 x10 <sup>-7</sup>
Coal	1.26 x10 <sup>-7</sup>	2.26 x10 <sup>-6</sup>	8.72 x10 <sup>-7</sup>	6.78 x10 <sup>-7</sup>	7.00 x10 <sup>-7</sup>
Lower Çavuşlar Member	5.52 x10 <sup>-9</sup>	7.59 x10 <sup>-5</sup>	9.43 x10 <sup>-6</sup>	1.17 x10 <sup>-6</sup>	1.00 x10 <sup>-6</sup>
Volcanics	4.89 x10 <sup>-9</sup>	2.86 x10 <sup>-5</sup>	5.18 x10 <sup>-6</sup>	2.08 x10 <sup>-7</sup>	7.00 x10 <sup>-8</sup>
<b>Abacı Member</b>					1.00 x10 <sup>-9</sup>
<b>Bostantepe Member</b>					5.00 x10 <sup>-7</sup>
<b>Remaining Model Domain</b>					1.00 x10 <sup>-6</sup>
Hydraulic Conductivity of faults, K (m/s)					
Name		Assigned Value	Name		Assigned Value
<b>Kirmir 1 Fault</b>		5.00 x10 <sup>-5</sup>	<b>Bezci 1 Fault</b>		2.00 x10 <sup>-8</sup>
<b>Kirmir 2 Fault</b>		1.00 x10 <sup>-6</sup>	<b>Bezci 2 Fault</b>		7.00 x10 <sup>-9</sup>
<b>Çavuşlar Fault</b>		5.00 x10 <sup>-5</sup>	<b>Binkoz Fault</b>		7.00 x10 <sup>-9</sup>
<b>Paleo Fault</b>		1.00 x10 <sup>-6</sup>	<b>Kocalar 2 Fault</b>		1.00 x10 <sup>-4</sup>
<b>Karataş Fault</b>		2.00 x10 <sup>-6</sup>	<b>Peyikler Fault</b>		7.00 x10 <sup>-9</sup>

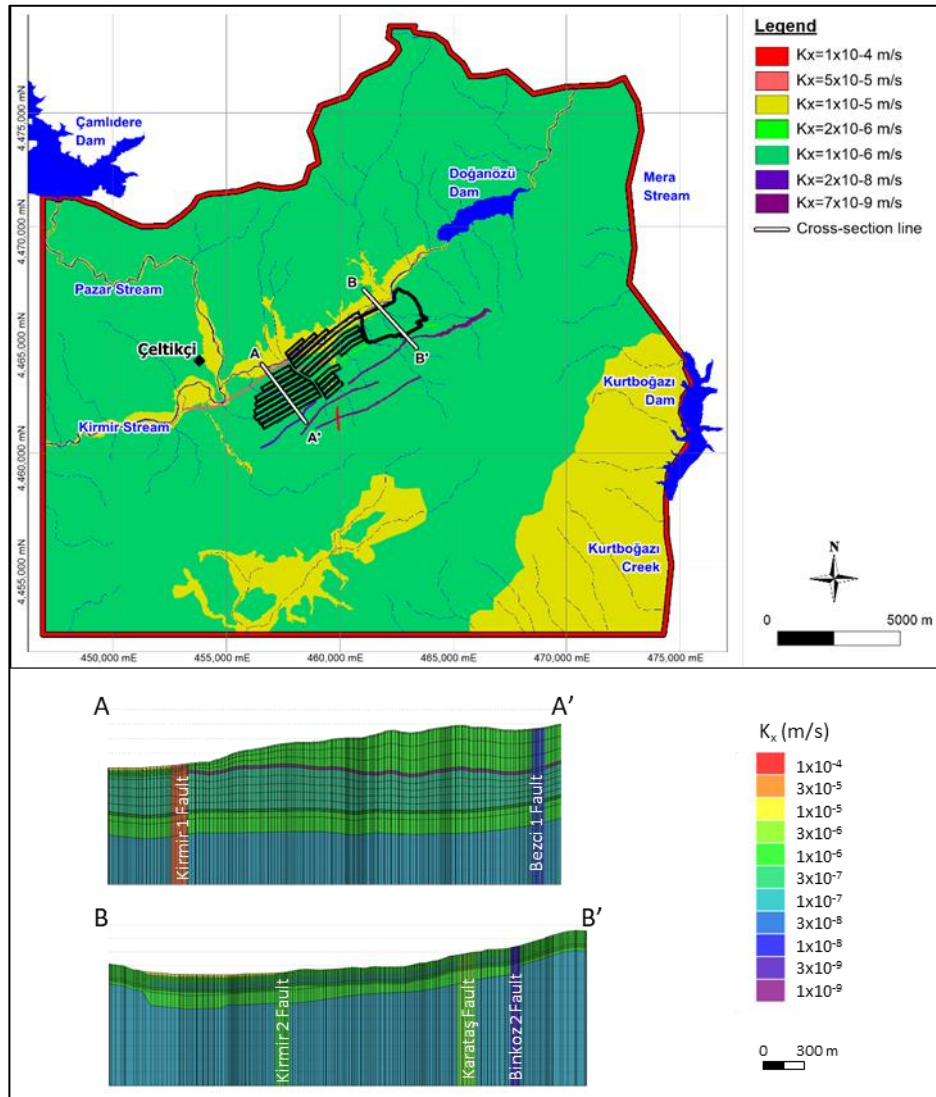


Figure 6.6. Hydraulic conductivity distribution within the model (above: slice 1 and below: cross sections (AA' and BB'))

### 6.4.3. Storage Parameters

The specific yield and specific storage values in the model domain were determined regarding the lithology of the units and aquifer test results. The specific yield for the alluvium is assumed to be 0.2. The pumping test conducted in PW-8, which is screened in Upper and Lower Çavuşlar members and coal, is simulated under transient conditions to estimate the specific yield value for the model domain. The simulation

results give best representation of pumping test with the values of 0.008. The specific storage parameter is also obtained from pumping test simulation of PW-8 and determined as  $3 \times 10^{-5} \text{ m}^{-1}$ .

## 6.5. Calibration

Calibration, by definition, is the process of obtaining a set of boundary conditions and hydraulic parameters so that an acceptable match is provided between the observed and calculated groundwater levels. Hence, during the calibration process assigned parameters are modified within the geological, hydrological, and hydrogeological limits by trial and error method. In addition to groundwater levels, the base flow to the Kirmir and Pazar streams and conceptual and calculated groundwater budgets are also compared.

### 6.5.1. Groundwater Levels

The average groundwater levels measured at 72 observation wells during 2012 – 2015 period were used in the steady state calibration. The goodness of the match between observed and calculated groundwater levels was acquired by minimizing the root mean square error (RMSE) and normalized RMSE (NRMSE) at the observation wells.

$$RMSE = \sqrt{\frac{1}{n} \sum_{i=1}^n (h_o - h_h)_i^2} \quad (\text{Eq. 6.1})$$

$$NRMSE (\%) = \frac{RMSE}{(h_o)_{max} - (h_o)_{min}} \quad (\text{Eq. 6.2})$$

where, n: total number of observation points

$h_o$ : observed groundwater level

$h_h$ : calculated groundwater level

$(h_o)_{max}$ : maximum value for observed groundwater level

$(h_o)_{min}$ : minimum value for observed groundwater level

The model was calibrated with an RMSE of 16.09 m and NRMSE of 4.56 %, indicating that the model was capable of simulating actual field conditions (Figure

6.7). The areal distributions of the calculated groundwater levels are shown in Figure 6.8. It is noted that the groundwater levels developed for the study area correspond to the lower aquifer, where most of the observation wells are screened. Thus, the calculated groundwater level map was given for the layers comprising the lower aquifer. The observed and calculated groundwater levels were also superimposed to check the consistency of the field measurements and model results in Figure 6.8.

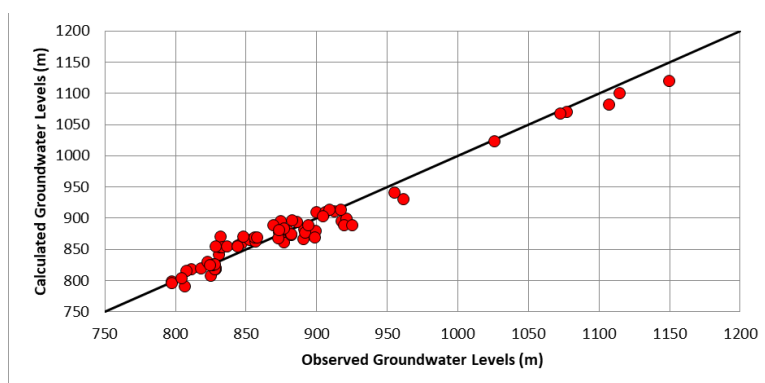


Figure 6.7. Observed vs calculated groundwater levels

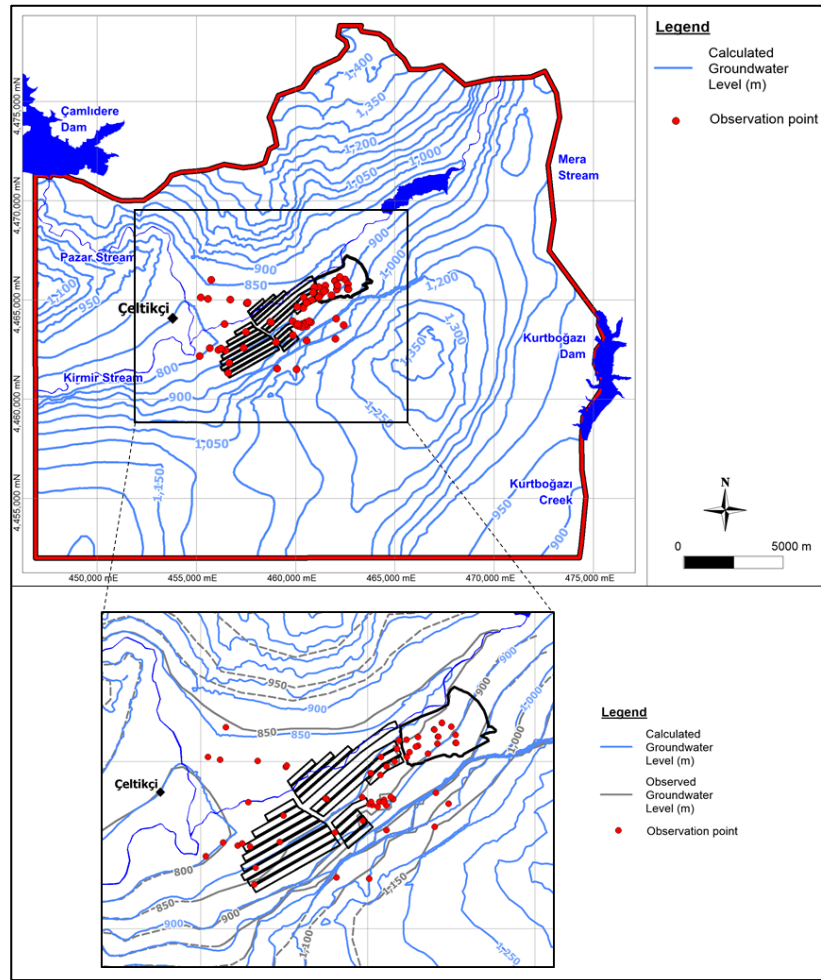


Figure 6.8. Calculated groundwater levels and comparison of the observed and calculated groundwater levels

### 6.5.2. Baseflow

In order to check the validity of the assigned fluid transfer boundary condition parameters (i.e. assigned hydraulic head and conductance), the observed and calculated baseflow rates of the Kirmir and Pazar streams were compared. For this purpose, the average instantaneous flow rates observed in October along the Pazar stream (SW-11 and SW-12) and Kirmir stream (SW-1 and SW-16) were used. The baseflow rate observed in October during 2012 – 2015 periods is determined as  $0.03 \text{ m}^3/\text{s}$  between SW-11 and SW-12 locations. The net groundwater discharge rate between these two observation points is calculated as  $0.033 \text{ m}^3/\text{d}$ , which is compatible

with the observed data. Similarly, the baseflow rate observed between SW-1 and SW-16 locations is 0.5 m<sup>3</sup>/s, whereas the calculated rate is 0.41 m<sup>3</sup>/s.

### 6.5.3. Calibrated Groundwater Budget

In addition to the groundwater levels, the calculated model budget was also controlled. The steady state calibration results were used to determine the recharge and discharge components of the model domain (Table 6.2). According to the results, the recharge components include (i) recharge from precipitation (71.5 %), (ii) surface waters (i.e. Kirmir, Pazar and Mera streams) (17.5 %), and (iii) dams (11 %). On the other hand, the discharge components can be summarized as (i) surface waters (i.e. Kirmir, Pazar and Mera streams) (59.1 %), (ii) creeks (26.3 %), (iii) springs (0.8 %), (iv) wells (2.6 %), and (v) dams (11.1 %).

In the conceptual model, a groundwater budget was also developed for both upper and lower aquifers over an area of 52 km<sup>2</sup>. The calibrated groundwater budget was also compared with the conceptual budget, for both Upper and Lower aquifers (Table 6.3). Although there are minor differences between the budgets, overall evaluation of the budget components reveals that the calibrated and conceptual budgets are consistent with each other. The differences within the budget components are explained below:

Table 6.2. *Calibrated groundwater budget*

Boundary Conditions	Budget Component	RECHARGE (hm <sup>3</sup> /yr)	DISCHARGE (hm <sup>3</sup> /yr)
Distributed Sink/Source	Recharge from precipitation	50.88	-
Cauchy BC	Kirmir and Pazar streams	6.83	34.04
	Mera stream	5.6	7.75
Dirichlet BC	Dams	7.86	7.85
	Springs	-	0.60
	Creeks		18.6
Well BC	Wells	-	1.82
<b>TOTAL</b>		<b>71</b>	<b>71</b>

Table 6.3. Comparison of the conceptual and calibrated model budgets

	Upper Aquifer			
	Conceptual Budget		Calibrated Budget	
	Recharge (hm <sup>3</sup> /yr)	Discharge (hm <sup>3</sup> /yr)	Recharge (hm <sup>3</sup> /yr)	Discharge (hm <sup>3</sup> /yr)
Recharge from precipitation	0.81	-	1.05	-
Springs	-	0.06	-	0.01
Discharge to Lower Aquifer	-	0.75	-	0.96
	Lower Aquifer			
	Conceptual Budget		Calibrated Budget	
	Recharge (hm <sup>3</sup> /yr)	Discharge (hm <sup>3</sup> /yr)	Recharge (hm <sup>3</sup> /yr)	Discharge (hm <sup>3</sup> /yr)
Recharge from precipitation	2.11	-	3.00	-
Recharge from Upper Aquifer	0.75	-	0.96	0.16
Springs	-	0.19		
Lateral flow	3.48	6.36	2.28	3.06
Kirmir-Pazar streams	not considered		0.04	1.72
Creeks	not considered		-	1.73

- In the calibrated model, the recharge from precipitation component is calculated higher than the conceptual model. Since in the calibrated model, the recharge from precipitation is divided into two zones to reflect the topographical differences in the area and a higher value is assigned compared to the conceptual model, the calculated amount of recharge from precipitation is more than the conceptual model.
- The discharge from springs in the conceptual budget is also lower than the calculated model budget for the Upper aquifer. Since for majority of the springs, the calculated hydraulic head values are lower than the topographic elevation, a lower discharge rate is obtained in the calculated groundwater budget. The calculated groundwater discharge rate from Upper aquifer to Lower aquifer is higher than the conceptual budget, which can be resulted from

the simulation of the faults and be ascribed to different hydraulic conductivity values.

- Some of the calculated budget components of the Lower aquifer, namely recharge/discharge from/to Kirmir stream and groundwater discharge from creeks are only included in the calibrated model budget. Thus, the lateral inflow/outflow component of the conceptual budget is more than the calibrated model budget. The simulation of the faults and assignment of different hydraulic conductivity values causes minor differences between the conceptual and calibrated model budgets.

## **6.6. Sensitivity Analysis**

Sensitivity analysis, as the name implies, explains which parameter(s) has an impact on the model results, which in turn is very helpful in reduction of model errors and future data collection processes. In order to test the sensitivity of the model parameters, a series of simulations were done, and the RMSE and NRMSE values are compared. The measured parameters includes (i) hydraulic conductivity values assigned to the lithologies (Figure 6.9), (ii) recharge from precipitation (Figure 6.10), and (iii) hydraulic conductivity values assigned to the faults (Figure 6.11).

The results indicate that the model is not sensitive to the change in hydraulic conductivity values of the alluvium and Abacı ignimbrite. Although the model is not sensitive to the decrease of hydraulic conductivity in the coal, Upper and Lower Çavuşlar members, it shows high sensitivity to the increase of this parameter. For the Bostantepe member, volcanics and model domain, the model is insensitive to the change of hydraulic conductivity values.

The sensitivity of recharge from precipitation was determined by assigning 55 mm/yr (as in conceptual model), 67 mm/yr, 84.4 mm/yr, and 100 mm/yr. The results indicate that the model is sensitive to the low recharge rates, but show insensitivity to the increase in recharge values.

For the fault zones, the model is insensitive to the change in hydraulic conductivity of Kirmir-1, Bezci-1, paleo and Kocalar-2 faults, whereas the model shows sensitivity to the change in hydraulic conductivity of the Peyikler and Bezci-2 faults. For the Kirmir-2, Karataş and Binkoz faults, the model is sensitive to decrease of hydraulic conductivity. On the other hand, the increase in hydraulic conductivity of the Çavuşlar fault make the model sensitive. Although the lowest RMSE and NRMSE values are obtained when the hydraulic conductivity of Karataş fault is decreased by 10 times, the calibrated conductivity value is kept unchanged to avoid any significant impact on dewatering simulations.

The overall evaluation of sensitivity analysis reveal that the parameters used in the calibrated model give the lowest error values.

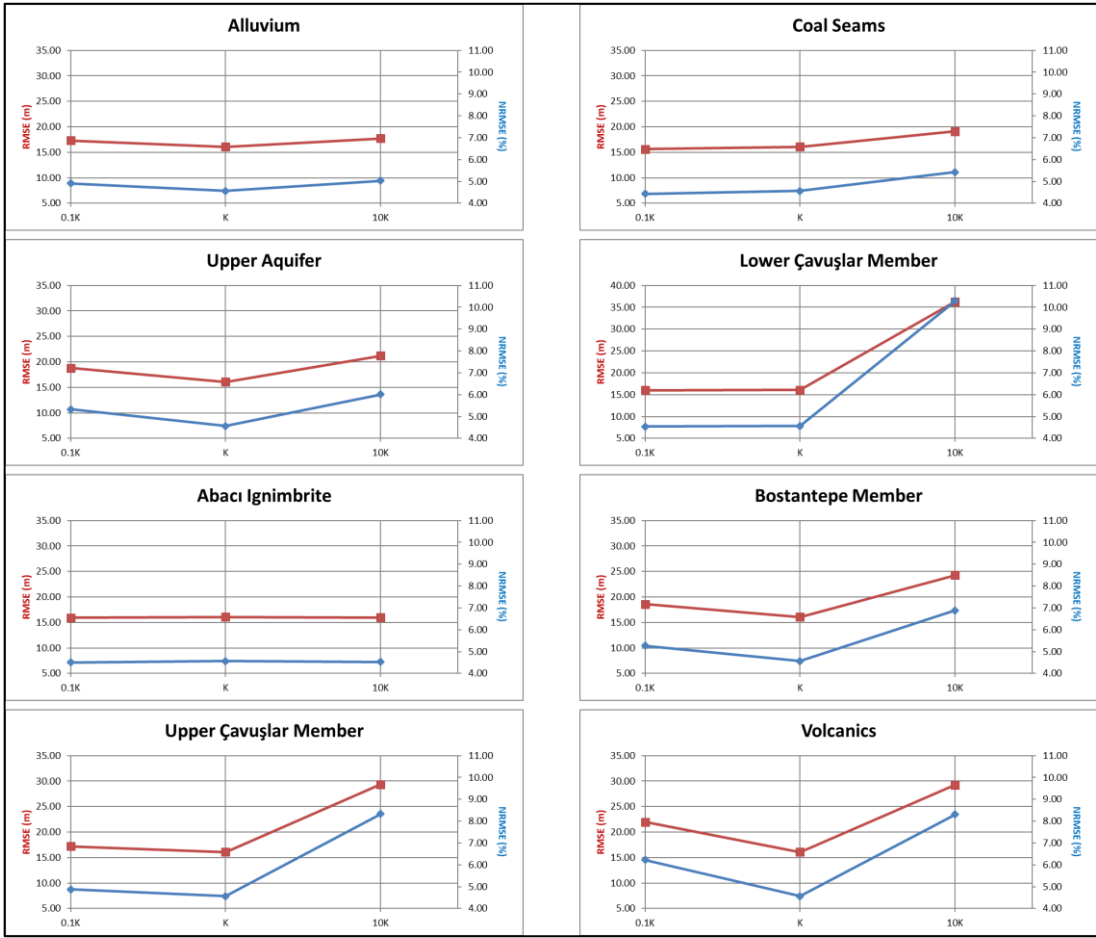


Figure 6.9. Sensitivity analysis of hydraulic conductivities of lithologies

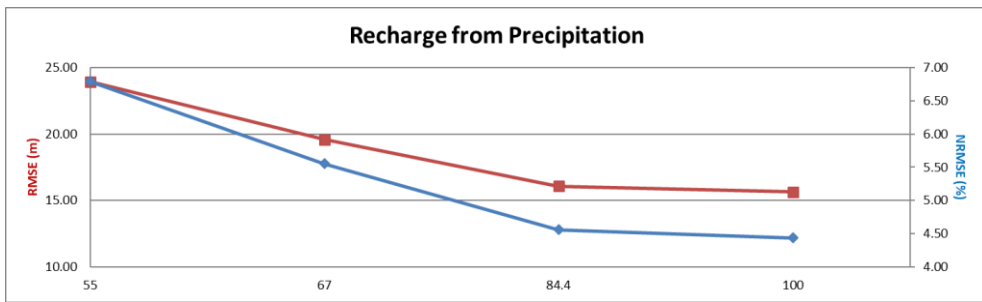


Figure 6.10. Sensitivity analysis of recharge from precipitation

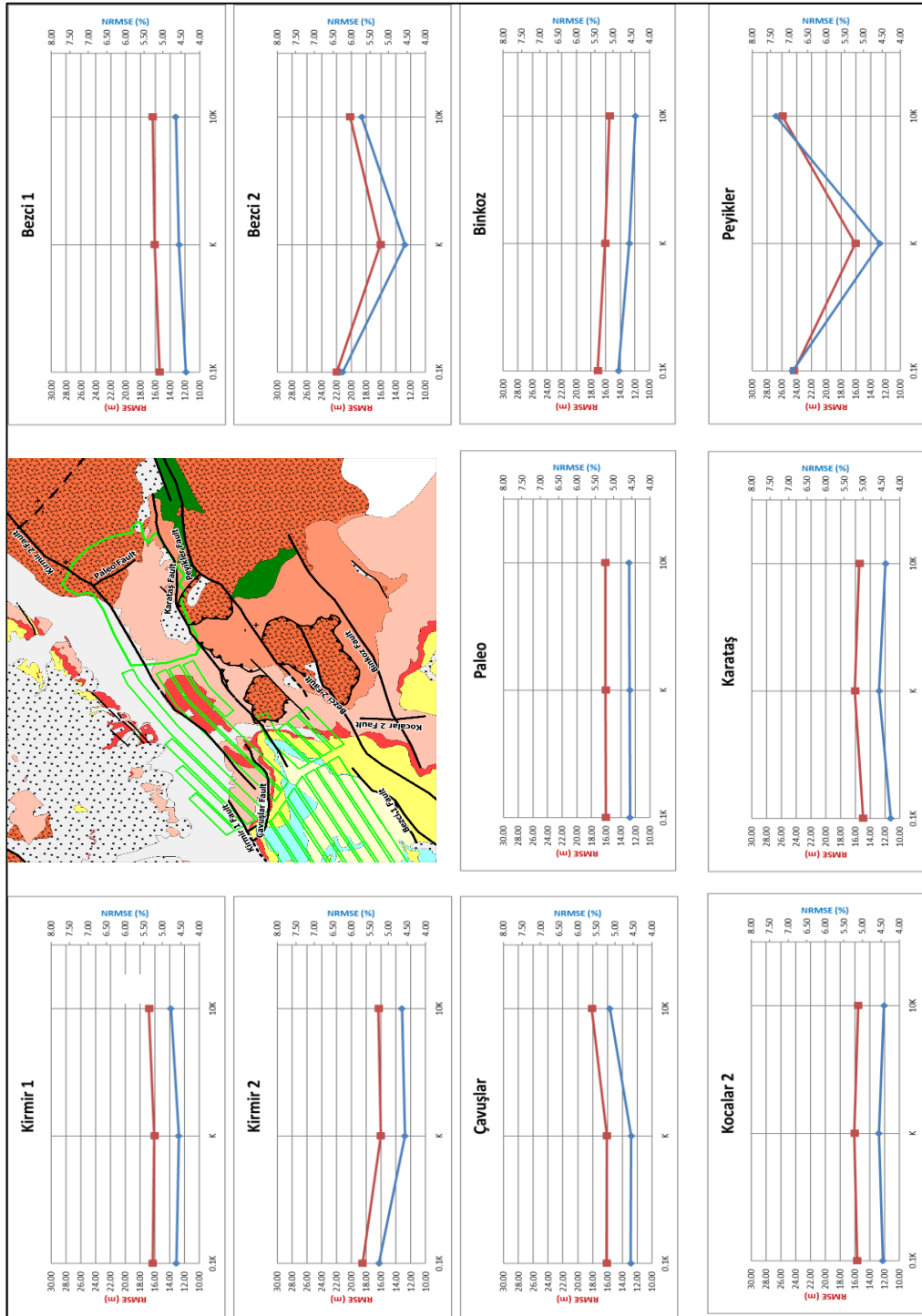


Figure 6.11. Sensitivity analysis of hydraulic conductivities of faults



## CHAPTER 7

### OPEN PIT DEWATERING

The pre-feasibility studies (Palaris 2015) reveal that 11 years of mining is to be planned from the open pit in the Çeltikçi coal basin, where approximately 37 million tons of coal can be extracted. During the open pit mining, satisfying dry working conditions is essential to avoid any economic, operational and safety problems. Therefore, during the operational period, to maintain dry and safe working conditions, dewatering requirements should be determined in advance.

The observed groundwater levels indicate that within the open pit groundwater levels lie between 830 m in the northwest and 960 m in the southeast, whereas the depth to the water table values approaches 100 m at the northwestern part. The hydrogeological studies show that, within the pit, there are artesian wells, which are screened at the coal seams. According to the mine plan, the yearly pit progress indicates that maximum excavation depth ranges from 70 m to 104 m throughout the operational period. Hence, throughout the mining, pit bottom is generally located below the water table, which makes dewatering inevitable.

In dewatering simulations, the calibrated groundwater flow model is taken as a base model, and the groundwater inflow rate to the pit void is predicted according to mine advance. The impacts of open pit dewatering on the groundwater system is also determined.

#### **7.1. Open Pit Dewatering Requirements**

The calibrated groundwater flow model under steady state conditions is transferred into the transient model in order to simulate open pit dewatering requirements. The storage parameters were obtained from the simulation of pumping test conducted at PW-8 well during calibration stage. The average annual recharge value is also

converted into monthly recharge series, based on the monthly water budget calculations (Table 5.1). Eleven years of mining is simulated by 132 periods, each corresponds to 30 days, with a total simulation time of 3960 days.

The amount of groundwater inflow rate into the open pit is simulated by drains, i.e. hydraulic head boundary conditions with maximum flow rate constraint. Since the mine plan is available for yearly basis, the hydraulic head value for the drains is assigned to be equal to the pit bottom elevation for the corresponding year. The boundary condition is constrained with maximum flow rate of  $0 \text{ m}^3/\text{d}$  in order to prevent any inflow to the groundwater system.

The yearly mine progress is shown in Figure 7.1. In the figure, only excavation areas corresponding to each year are shown. According to the pre-feasibility studies, previously excavated areas will be backfilled except for year 11. For each year, the drains become active at the nodes located within the excavation area. Hence, the amount of groundwater inflow rate to the pit coming from these nodes is determined. The simulation results indicate that average groundwater inflow to pit is 79 L/s. In the simulations, the effects of direct rainfall and surface water flow from the benches are not considered.

The time wise change of groundwater inflow rate obtained from the model results is provided in Figure 7.2. According to the graph, the groundwater inflow rate to the pit is started at day 60 and reaches the maximum value (285 L/s) at day 3660. The increasing trend in the flux corresponds to progress in the pit excavation, whereas decreasing trends indicate a decline in the dewatering demand. The peak dewatering requirements are observed at the beginning of each year where desired pit bottom for that particular year is achieved. Then groundwater inflow rates show decreasing trend until the start of mining in the next year. The dewatering requirements increase continuously as the mine progresses in advance except for year 6. Dewatering conducted at year 5 cause the lower dewatering requirement at year 6.

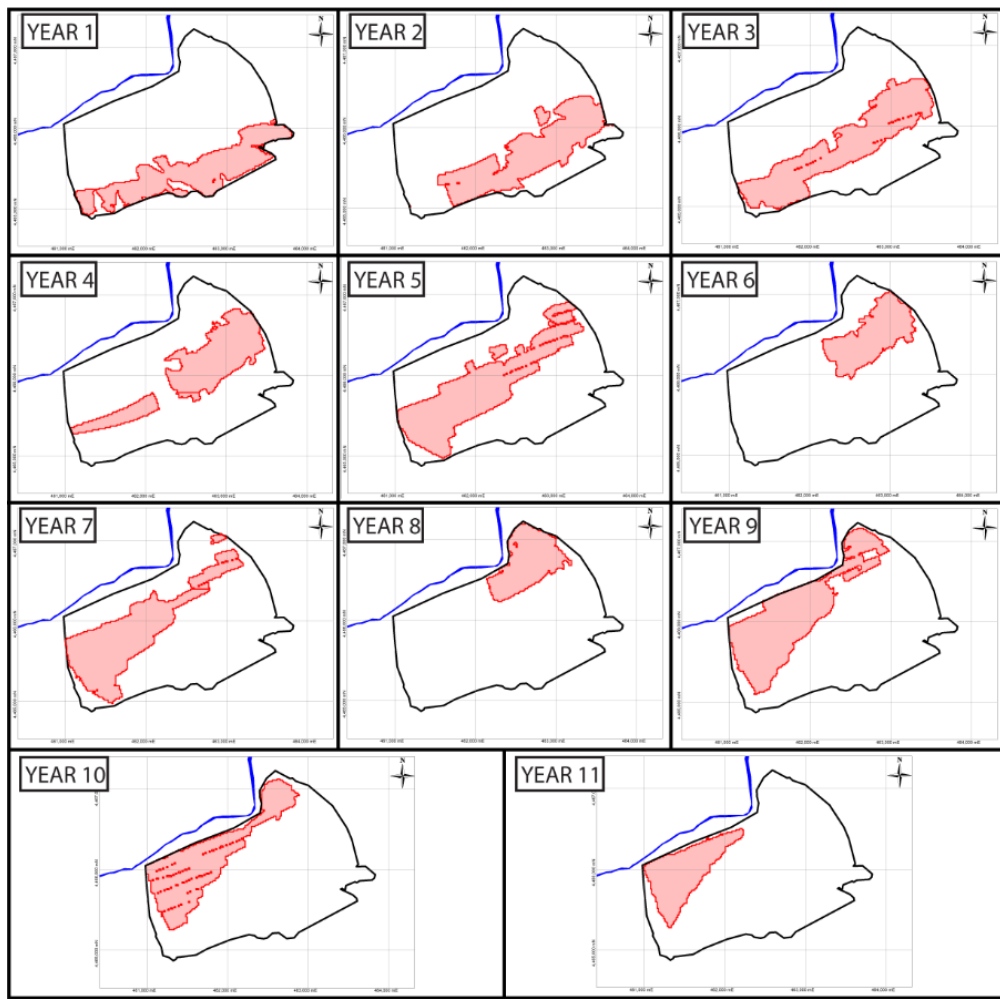


Figure 7.1. Yearly progress of open pit

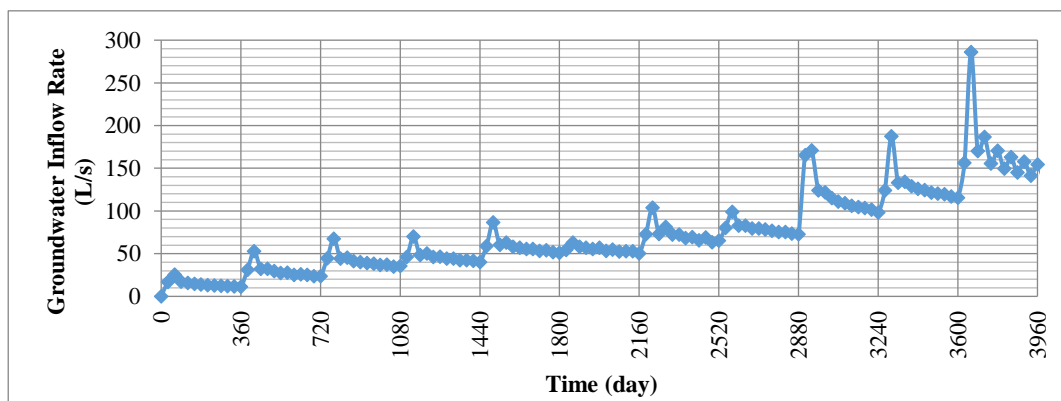


Figure 7.2. Simulated groundwater inflow rate to the open pit

The simulated average, maximum and minimum groundwater inflow rates are also given in Figure 7.3. The average groundwater inflow rate to the pit ranges from 13 L/s to 170 L/s, whereas at the end of each year, dewatering requirements range from 11 L/s to 154 L/s.

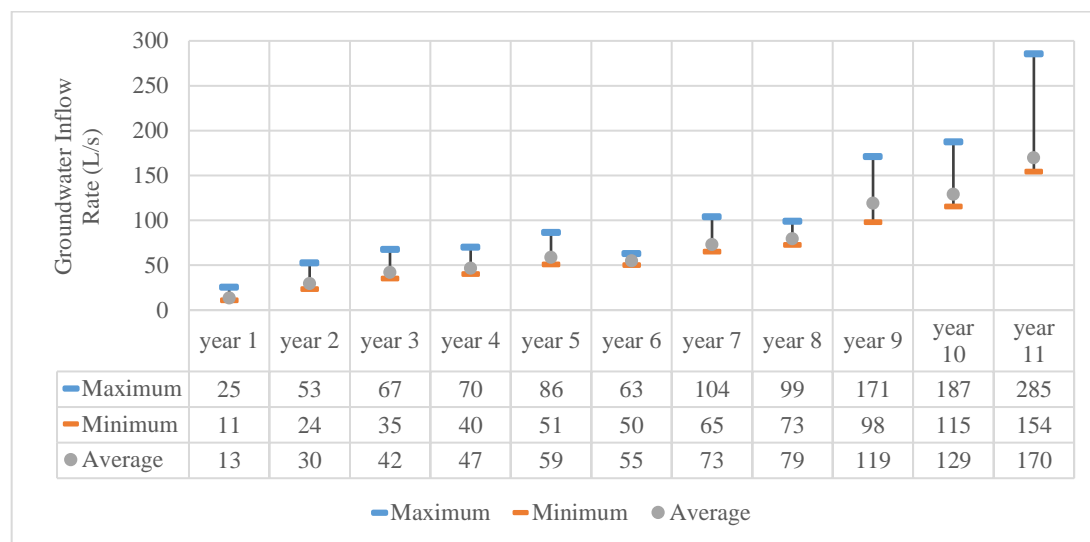


Figure 7.3. Calculated maximum, minimum and average groundwater inflow rates throughout the mine life

The prediction of groundwater inflow rate to the open pit is closely related to the hydraulic conductivity values assigned to the Kirmir 2 and Karataş faults, located at the northern and southern part of the open pit, respectively (Figure 3.12). The calibrated hydraulic conductivity values of the Kirmir 2 and Karataş faults are  $1 \times 10^{-6}$  m/s and  $2 \times 10^{-6}$  m/s, respectively. In order to observe the impacts of the hydraulic conductivity of the faults, simulations are repeated where the assigned hydraulic conductivity values are increased and decreased 10 times compared to the base model (Figure 7.4). The simulation results indicate that the average groundwater inflow rates ranges between 69 L/s and 114 L/s, when the assigned hydraulic conductivity values are decreased and increased 10 times, respectively. On the other hand, the maximum

inflow rate of 285 L/s is modified to 185 L/s and 690 L/s, when the hydraulic conductivity of the faults are decreased and increased 10 times, respectively.

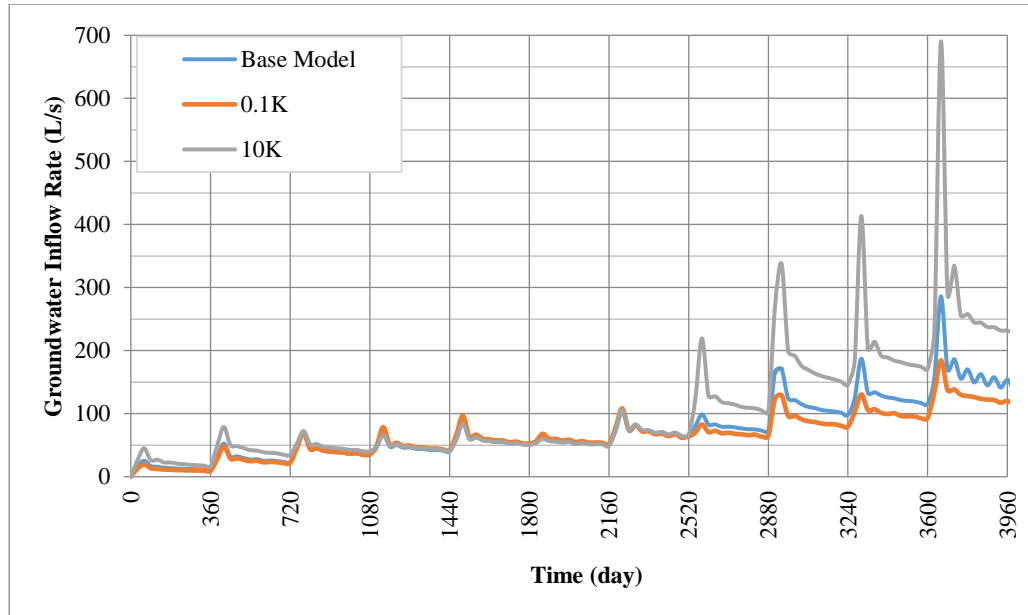


Figure 7.4. Time wise change of the groundwater inflow rate to the pit for different hydraulic conductivity values assigned to the Kirmir 2 and Karataş faults

## 7.2. Groundwater Levels After Open Pit Dewatering

The wells drilled in the open pit area and screened in the coal are used to check whether groundwater levels in the pit will be lowered to the desired levels. For that purpose, simulated groundwater levels at PW-5, PW-8, CEL-53A, CEL-77, CEL-97A, CEL-100C, CEL-101, and CEL-107 wells are compared to the pit bottom elevations at those points (Figure 7.5). As can be seen from Figure 7.5, the desired groundwater levels are obtained for dry working conditions at the open pit.

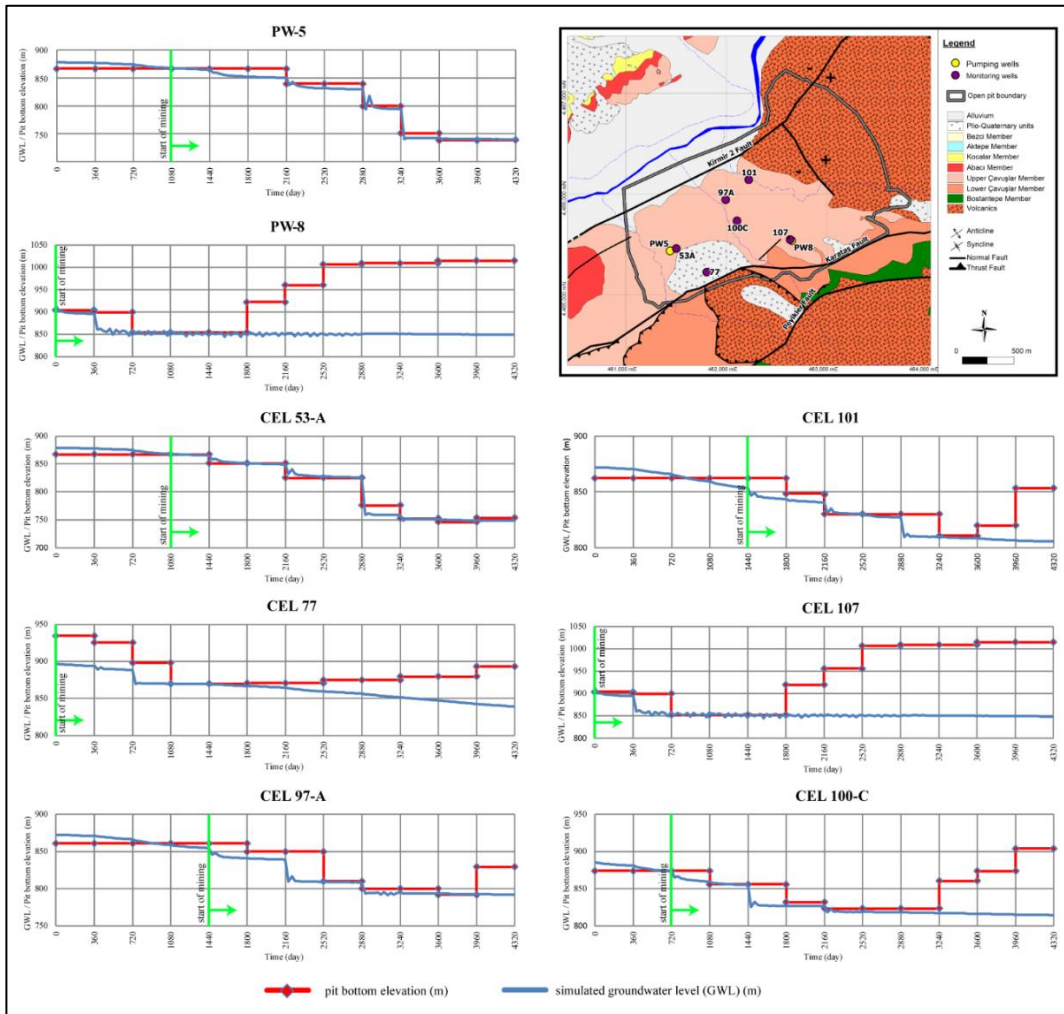


Figure 7.5. Simulated groundwater levels and pit bottom elevations at the observation wells after open pit dewatering

### 7.3. Impacts of Open Pit Dewatering on Groundwater Resources

The simulation results indicate that during 11 years of mining, an average of 79 L/s groundwater is required to be pumped out from the open pit in order to satisfy dry working conditions. The impacts of dewatering on groundwater resources are investigated in terms of (i) time wise change of baseflow component of Kirmir stream, and (ii) areal distribution of cone of depression as a result of dewatering.

The baseflow component of the Kirmir stream is determined as 0.41 m<sup>3</sup>/s in the calibrated model for the area between SW-1 and SW-16 monitoring points. Since the distance between Kirmir stream and northern boundary of open pit ranges between 50 m and 350 m, the dewatering activities in the open pit will impact the baseflow rate. In order to quantify that rate, yearly baseflow component is calculated for the area between SW-1 and SW-16 points (Figure 7.6). The simulation results indicate that, during 11 years of mining, the baseflow rate will decrease from 0.41 m<sup>3</sup>/s to 0.37 m<sup>3</sup>/s during the operational period of open pit. The simulated baseflow rates decrease significantly as the mining activities approaches to the Kirmir stream, mainly after 8<sup>th</sup> year of mining (Figure 7.1).

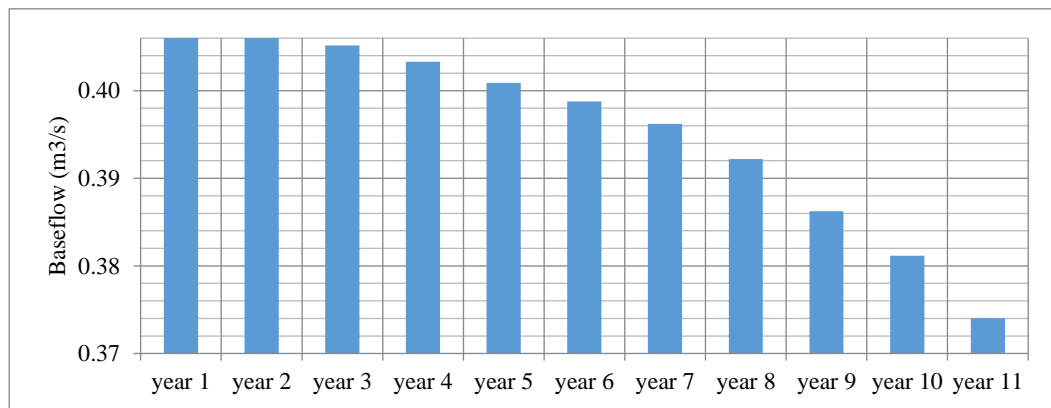


Figure 7.6. Change of baseflow component of the Kirmir stream during the operational period of open pit

The areal distribution of cone of depression at the end of the 11th year is given in Figure 7.7. The maximum drawdown is simulated as 161 m at the northwestern corner of the pit, which is excavated in the last year. Then drawdown values decrease to 50 m at a distance of 1 km. The fault zones in area mainly influence the areal extent of cone of depression. As a result of dewatering activities, considering the model errors, it is expected that springs and fountains located within 5 m drawdown contour will dry up. In that context, the springs that supply water to the Değirmenönü, Çavuşlar

and Peyikler villages as well as 29 monitored springs and fountains are expected to dry. The total average groundwater discharge rate from these springs is determined as 7 L/s, excluding the discharge rates of village water supply springs.

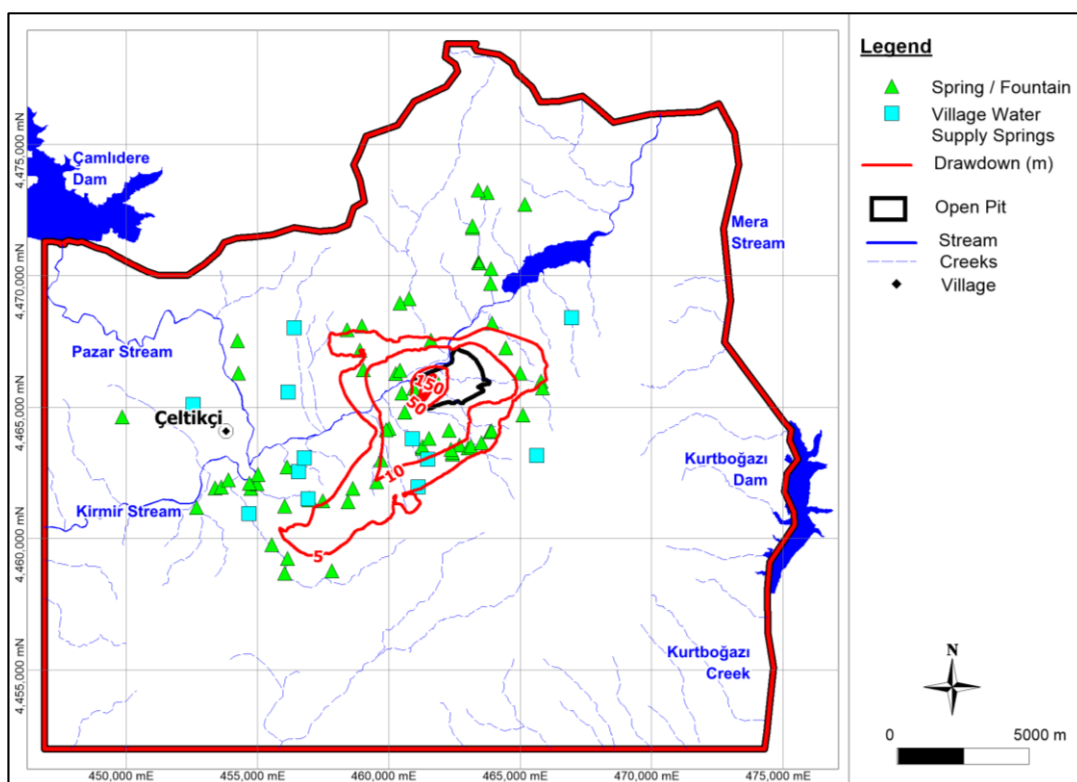


Figure 7.7. Simulated drawdown contours at the end of open pit dewatering

## CHAPTER 8

### UNDERGROUND MINE DEWATERING

In the Çeltikçi coal basin, in addition to open pit mining, underground mining will also be employed to extract about 67 million tones of coal. Based on the pre-feasibility studies (Palaris 2015), two main mining systems will be used in the area, namely the longwall mining method, and room and pillar method.

Longwall mining method gains attention in coal fields due to the improved safety, effective large-scale extraction, promoted productivity and reduced cost. The method involves development of large rectangular blocks (also known as longwall or panel), which are typically 150 m to 400 m wide and several kilometers long. The headings limit the panels and provide access to the workers and equipment. The coal is extracted by a shearer, which is placed at one end of a panel. The shearer moves back and forth along the short dimension of the panel and cuts the coal. The cut coal drops onto a conveyor and transported out of the mine via a series of conveyor belts. As the coal is cut, the roof strata are held in position by hydraulically powered roof supports, which provides a safe working environment for the workers and equipment. As the face advances, the roof supports and mining equipment move forward, and the immediate roof above the vacated area is allowed to collapse.

In the room and pillar method, coal deposits are mined in a network of rooms where pillars are left to support the mine roof. The pillars may contain up to 40 % of the total coal and can be extracted during secondary extraction. The room and pillars are generally arranged in a regular pattern.

The longwall mining is planned to extract the coal in the upper seam, whereas the lower seam will be mined via room and pillar method. The selection of different mining methods is made according to the characteristics and constraints of each seam.

In the area, the average thicknesses of the upper and lower seam are determined from the well logs as 4 m and 2.4 m, respectively. The seams are separated from each other by a thin interburden. The proposed mine plan for the upper and lower seams are given in Figure 8.1 and Figure 8.2, respectively.

Two mine plans were developed in the area based on the selection of the mined seams, namely both seam case and upper seam only case. Since the mine layout for the lower seam is based on very limited geotechnical data, feasibility of the mining of lower seam remains questionable (Palaris, 2015). In this study, upper seam only case, where longwall mining will be issued is considered.

The upper seam only mine plans involve 19 longwalls, which are generally 200 m wide. The panels are oriented in northeast – southwest direction. The design of the panels is constrained by the faults (namely Kirmir 1, Kirmir 2, Bezci 1, Karataş and Peyikler faults), highway and residential areas. Due to these constraints, the length of the panels varies, ranging between 1 km and 3.6 km. The depth of cover to the roof of the seams ranges from 120 m to 580 m, at the southeast (intersection of surface access drift) and center of the mining area, respectively. The groundwater levels of the lower aquifer at the longwall panels range between 800 m and 950 m, where depth to water table varies between 50 m to 150 m.

### **8.1. Impacts of the Longwall Mining on the Groundwater System**

As described briefly above, longwall mining results in the immediate collapse of the overlying strata as the shearer and hydraulic supports move forward. The collapsed strata are known as “gob” or “goaf” and along a panel, the dimensions of the gob are nearly equals to the mined panel dimensions. The collapsing strata result in subsidence, which can reach to the ground surface. During subsidence, the strata undergo compressive and tensile stresses; hence several changes including intense fracturing, opening of joints and bedding plane separations are observed.

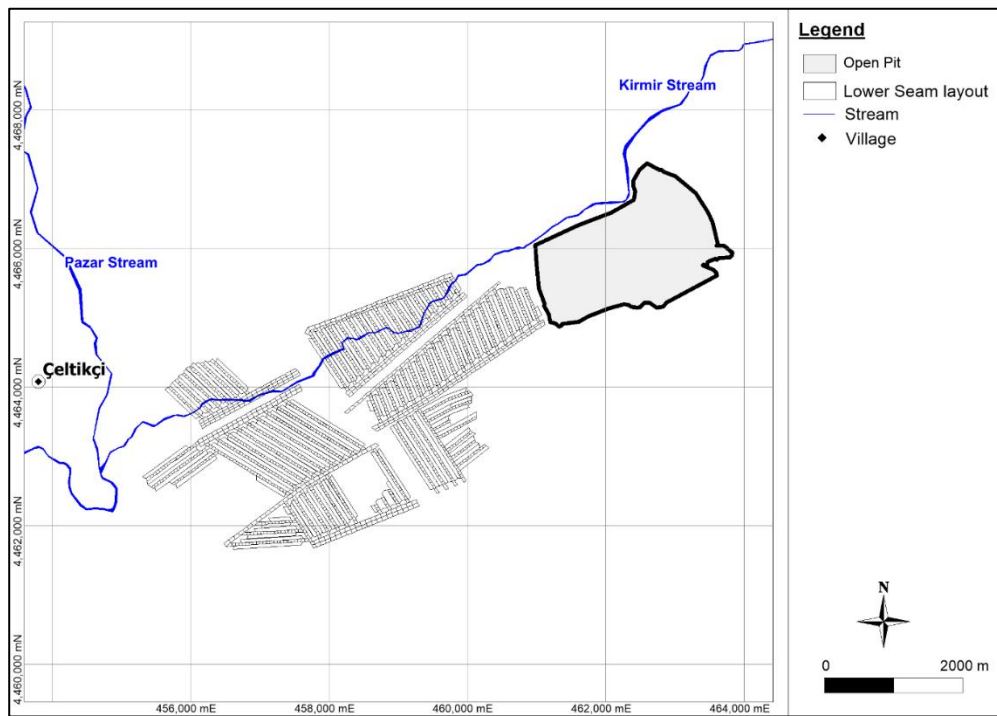


Figure 8.1. Lower seam layout

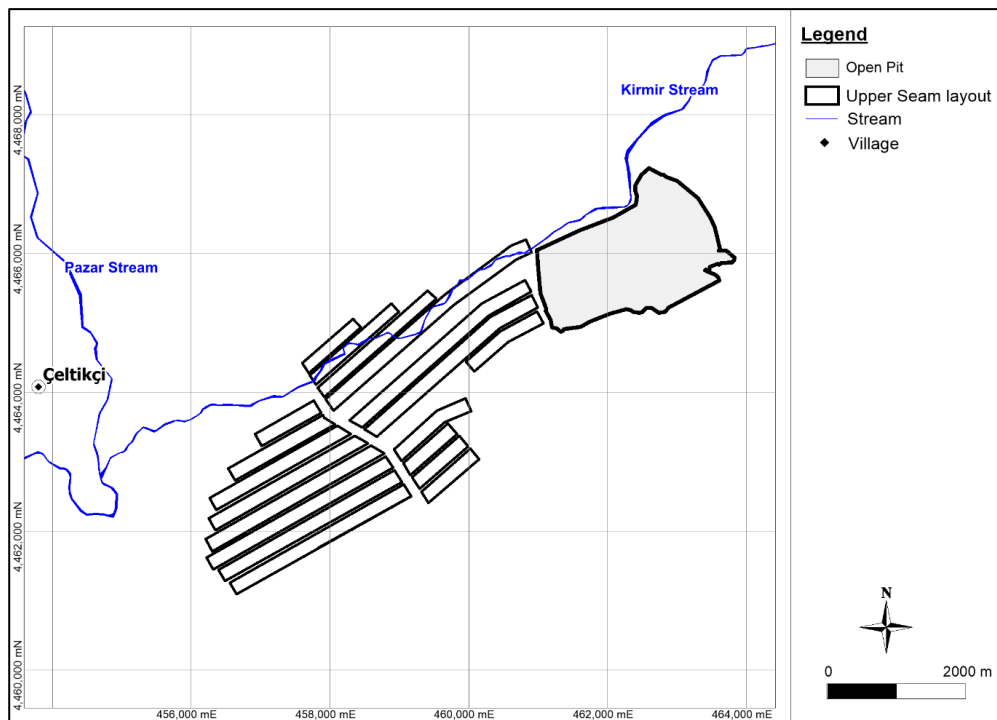


Figure 8.2. Upper seam layout

The plan view of a typical longwall mine layout and also schematic representation of fracture system development as a result of longwall mining are provided in Figure 8.3(a) and Figure 8.3(b), respectively.

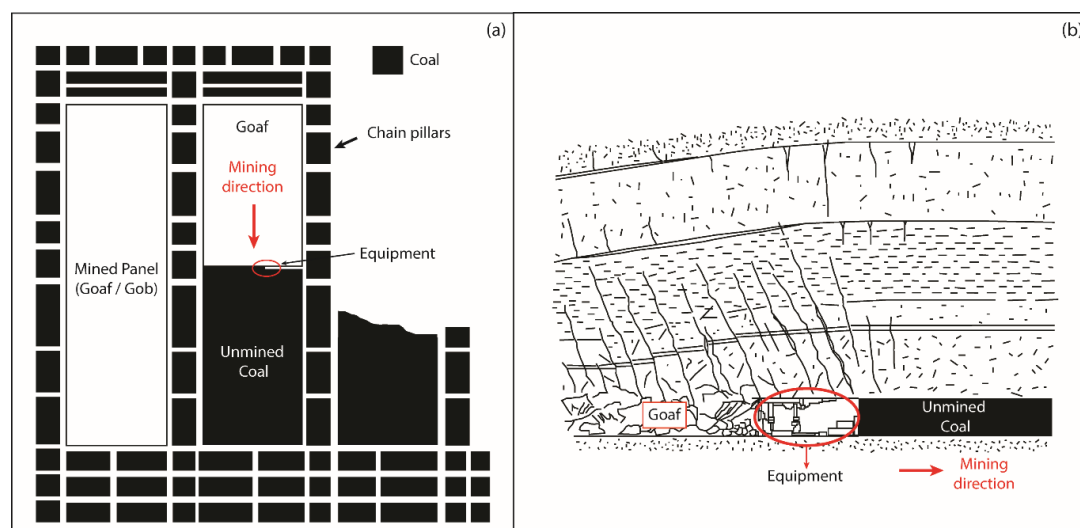


Figure 8.3. (a) Plan view of a typical longwall mine layout and (b) schematic view of the fracture system developed as a result of longwall mining

The intense fracturing of the overlying strata alters the stability and impacts hydraulic properties of the lithologies. The prominent impacts of longwall mining on groundwater resources can be listed as changes in hydraulic gradients, hydraulic conductivity and storage parameters and also water quality (Kadnuck 1995, Booth 1986, Booth et al. 1998, Tammeta 2015). Although these changes are expected as a result of longwall mining, neither areal distribution of the impacted zones nor the intensity / quantification of the impacts are known prior to mining.

A subsurface model was developed by Kendosrky (1993) which conceptually represents the hydrogeological responses of the overlying subsided strata to the longwall mining. According to this model, the overlying strata are divided into five zones, namely caved zone, fractured zone, dilated zone, constraint strata and surface

fracture zone. The caved zone, located at the bottom, is defined as the zone of complete disruption, which extends about 3 to 6 times of the mined coal seam. The fractured zone is located above the caved zone and includes vertically transmissive fractures. The thickness of fractured zone ranges between 24 and 30 times mined thickness. The fractured zone is followed by the dilated zone, where an increase in storativity with very little change in transmissivity is observed. The constrained zone can be present in the system if the mine is located deeper than the total thicknesses of the caved, fractured and dilated zones plus 50 ft. In the constraint zone mining is believed to have no impact on the transmissivity and storativity. The upper zone is composed of the surface fracture zone, which is bounded by ground surface and generally has a thickness of 50 ft. In this zone, vertically transmissive surface cracks can be observed. The schematic representation of each zone is given in Figure 8.4.

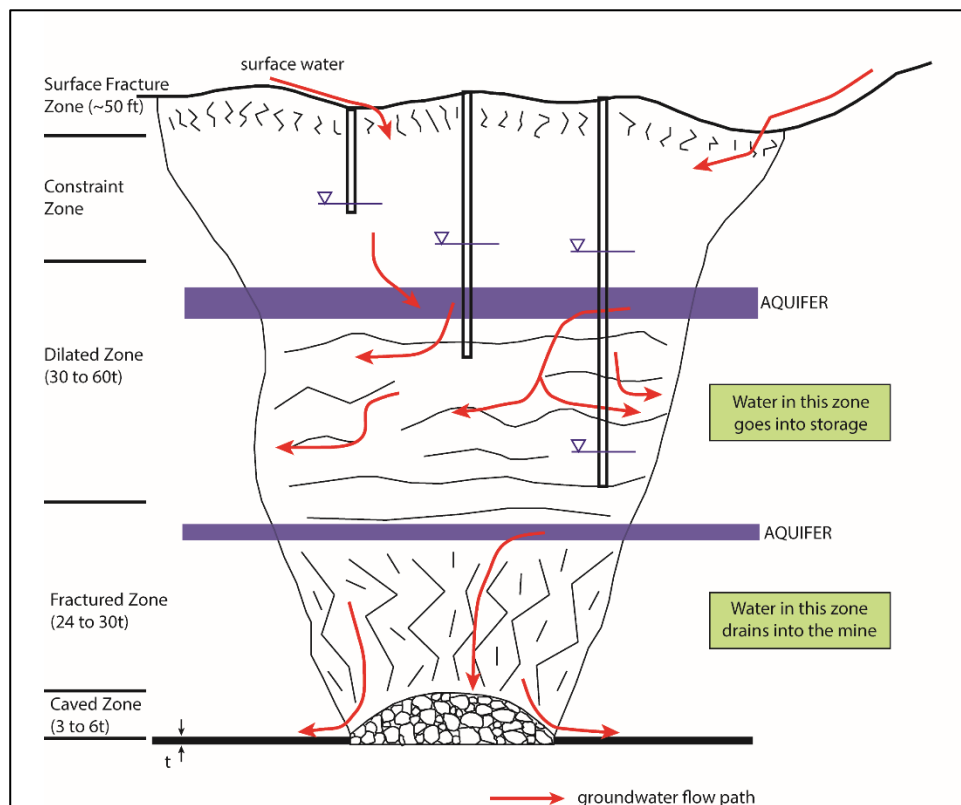


Figure 8.4. Schematic view of the hydrological response zone

According to the 1993 Model, water in the caved zone and fractured zone drains directly into the mine, dimensions of which depend only on the mined thickness. The determination of exact dimensions of the zone where groundwater inflow to the mine occurs plays a significant role in the assessment of the longwall impacts on groundwater resources. This zone is defined by Tammeta (2013) as “complete groundwater drainage zone”, where zero or negative pressure heads are observed in a short time following the caving. Starting from 1970s, several empirical equations were also developed to determine dimensions of the groundwater inflow zone (Garritty 1983, Singh 1986, Kendosrky 2006). These studies indicate that the dimensions of the groundwater inflow zone are related to the mine geometry, but mined thickness plays significant role. However, Tammeta (2013) shows that in addition to mine geometry (i.e. mined thickness and void width), the thickness of the overburden also impacts the height of the groundwater inflow zone above the longwall panels (Figure 8.5).

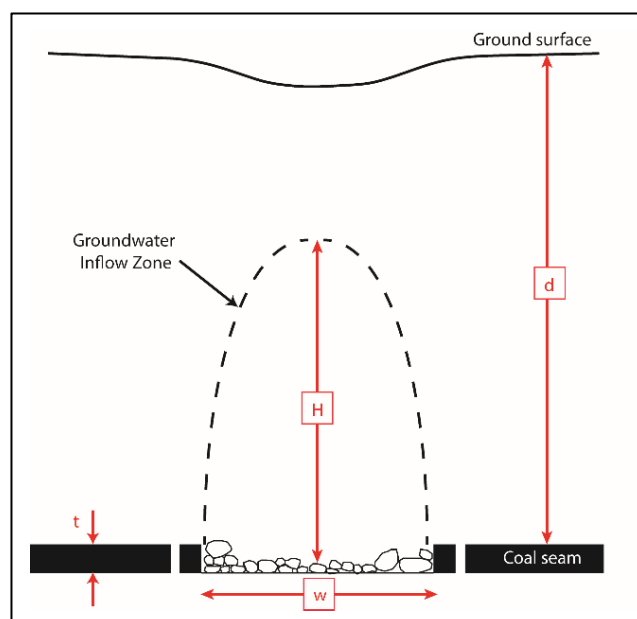


Figure 8.5. Cross-section view along the short dimension of a panel showing parameters that affect the height of groundwater inflow zone (H)

In Tammeta (2013), Tammeta used statistical analysis with more than 100 hydraulic head measurements and also ground movement datasets along longwall panels at various locations worldwide. The empirical formulae developed by Tammeta is given below (Eq. 8.1).

$$H = 1438 \ln(4.315 \times 10^{-5}u + 0.9818) + 26 \quad (\text{Eq. 8.1})$$

where H: height of groundwater inflow zone (m),

u: independent variable which can be calculated as  $u = w \times t^{1.4} \times d^{0.2}$  (w, d, and t in meters).

As a result of longwall mining, two main zones were formed, namely the collapsed zone and disturbed zone (Tammeta, 2013). The collapsed zone is characterized by parabolic shape, where maximum height can be interpreted by “H”. Due to the intense fracturing, in this zone, groundwater drains completely into the mined void, and negative or zero pressure head values are observed. Above the collapsed zone, a disturbed zone is formed. In the disturbed zone positive pressure head values are recorded. The expected shape of hydraulic head profile along the mined seam as a result of longwall mining is provided in Figure 8.6.

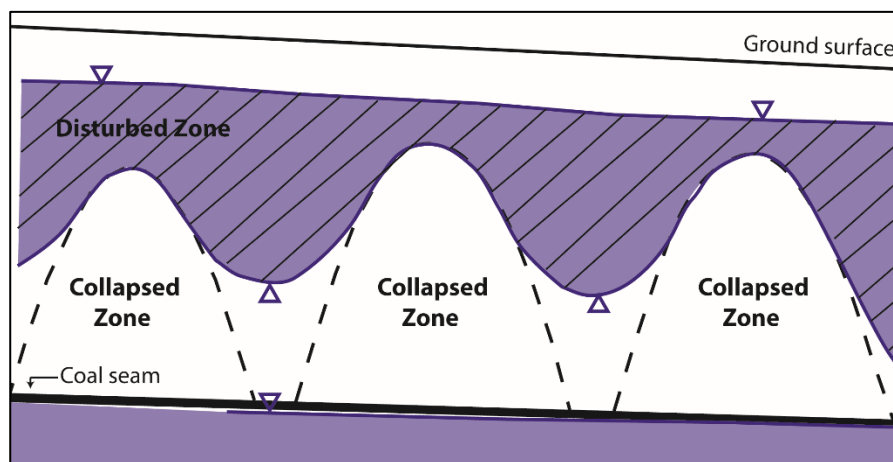


Figure 8.6. Expected post-mining hydraulic head profile above the longwall panels (modified from Tammeta 2013)

### **8.1.1. Changes in Hydraulic Conductivity**

The longwall mining along the panels result in the formation of the groundwater inflow zone. Due to the intense fracturing at this zone, groundwater directly moves into the panel as a result of major increase in hydraulic conductivity. In order to quantify the amount of groundwater inflow rate to the panels in advance and assess the impacts on groundwater system, the change of hydraulic conductivity in pre- and post-mining should be known.

The change of hydraulic conductivity during the longwall mining was studied by many researchers and empirical formulas were also developed to calculate post-mining permeability by using fracture analysis (Hutcheson et al. 2000, Whittles et al. 2006, Esterhuize and Karacan 2005). The complexity of quantification of hydraulic conductivity change as a result of the longwall mining arises from the facts that (i) the pre-mining hydraulic conductivities are related to the depth and (ii) post-mining hydraulic conductivities are related to the mine geometry and mining depth.

Tammeta (2015) presents a conceptual model related to the hydraulic conductivity changes as a result of longwall mining. In his study, he used 799 measurements of pre-mining and post-mining hydraulic conductivity values from 18 locations all over the world and obtained post-mining to pre-mining hydraulic conductivity ratios (defined as “R”). The majority of the hydraulic conductivity values within the data set were determined from packer tests, and also slug and pumping test data were used. According to the conceptual model, in the disturbed zone (above the groundwater inflow zone) the average R value is less than or equal to 10, whereas in the collapse zone, the R value is expected to be 40 or more. The ratio of post to pre-mining hydraulic conductivity is assumed to be infinite at the goaf (Figure 8.7). Due to the significant increase in the conductivity values in the collapsed zone, a dramatic increase in the vertical component of pre-mining hydraulic conductivity is expected in this zone.

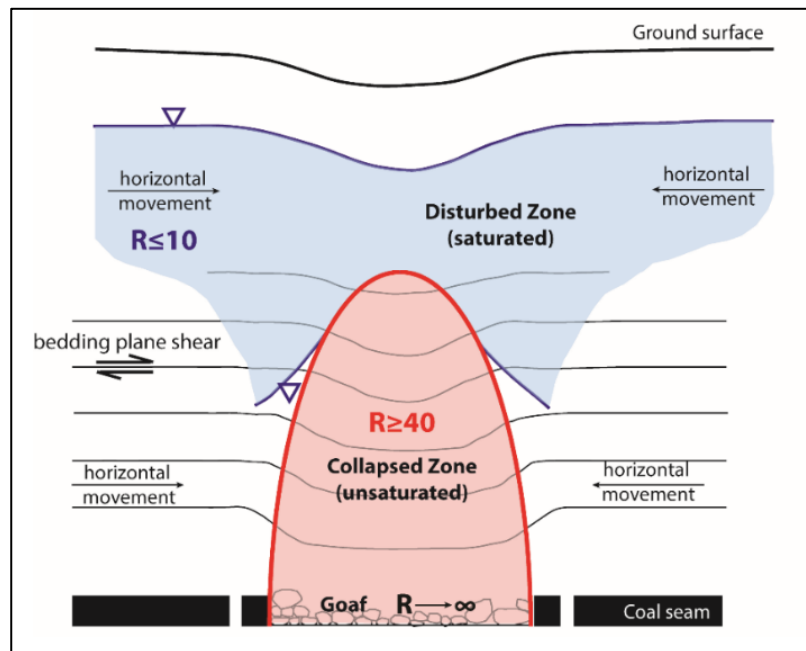


Figure 8.7. Conceptual model proposed by Tammeta (2015)

### 8.1.2. Change in Storage Capacity

As the overlying strata above the mined longwall panels undergo significant stresses, the storage capacity above the panels is also impacted. The estimations of changes in storage play an important role in determination of water level rebound times and water quality impacts associated with mining (Booth 1986, Hawkins and Dunn 2007). The post-mining storage values were generally determined from pumping tests conducted at the abounded mine pools. Therefore they mainly include average values and spatial distribution of change in storage is not mentioned (Younger and Adams 1999, Hawkins and Dunn 2007). The change in storage capacity as a result of longwall mining is conceptualized by Tammeta (2016) based on evaluation of data sets including goaf geometry, strata dilation, and pumping/drawdown analysis from mine pools (Figure 8.8). According to the conceptual model, the maximum increase in storage is expected at goaf as 0.07, where major deformation takes place. In the collapsed zone, the increase in storage capacity will be about 0.007. A minor increase in storage capacity is expected in the disturbed and surface zones, as 0.0004 and

0.0005, respectively. Along the pillars, where compression is dominant, the expected decrease in storage capacity is around 0.001.

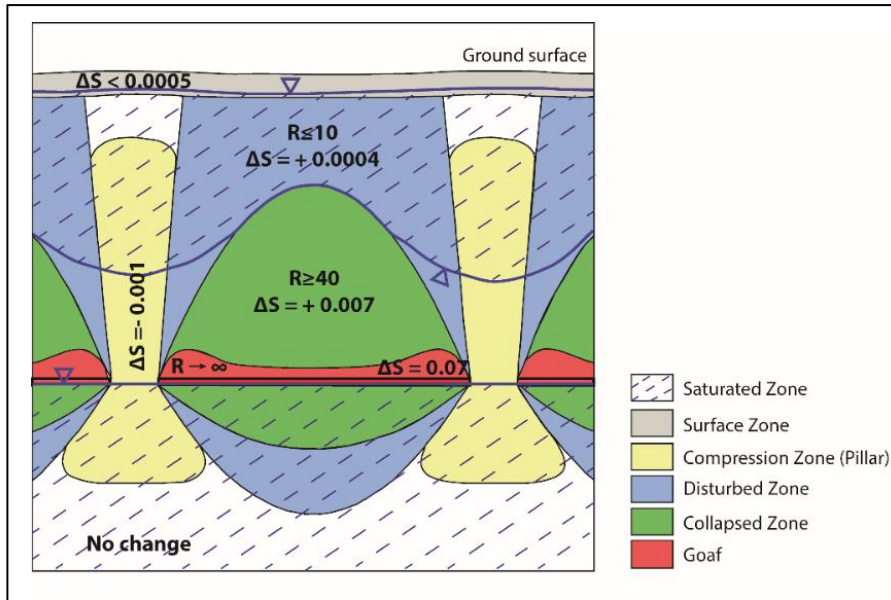


Figure 8.8. Hydrogeological conceptual model developed by Tammeta (2015)

## 8.2. Dewatering Requirements of Longwall Panel

The mining plan in the study area includes the extraction of the upper seam via longwall mining. The upper seam is composed of 19 longwalls, and oriented in northwest-southeast direction. The average thickness of the upper seam is determined as 4 m based on well log data and depth of overburden ranges between 120 m to 580 m. Due to the complex nature of longwall mining described above, along one representative panel, dewatering requirements and anticipated impacts associated with longwall mining were simulated (Figure 8.9).

The representative panel is located in the middle part of the longwall mining area, where one year of mining will be planned. The panel is 2 km in length and 200 m in width, where the thickness of upper seam is 4 m. Above the panel, the average

overburden thickness is calculated as 504 m. In the selection procedure, the location of the panel with respect to the Kirmir stream and faults is considered. The panel is situated about 1.5 km away from the Kirmir stream and about 1 km away from the Kirmir 1 and Bezci 1 faults. Also, presence of each hydrological response zones, i.e depth required to form collapsed and disturbed zones, is taken into account. The location of the selected panel on geological map is given in Figure 8.10.

The calibrated numerical groundwater flow model is taken as a base model in the dewatering simulations of the longwall panel. In the simulations various scenarios were simulated and their results were compared. The impacts of dewatering on the groundwater system were determined.

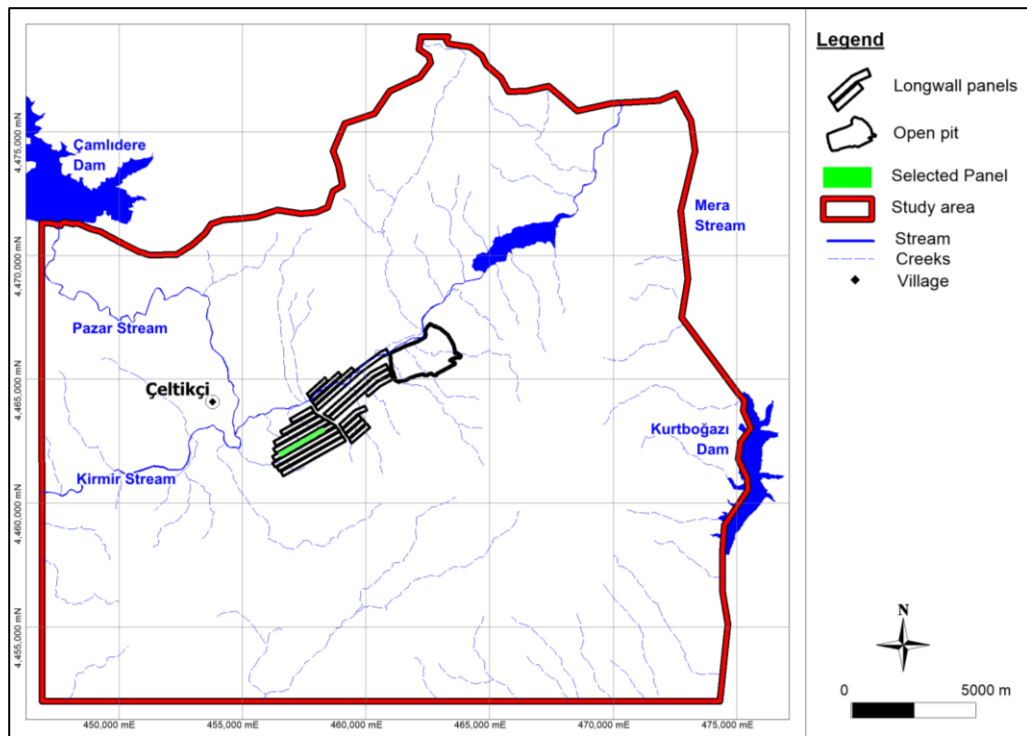


Figure 8.9. Location of the selected panel

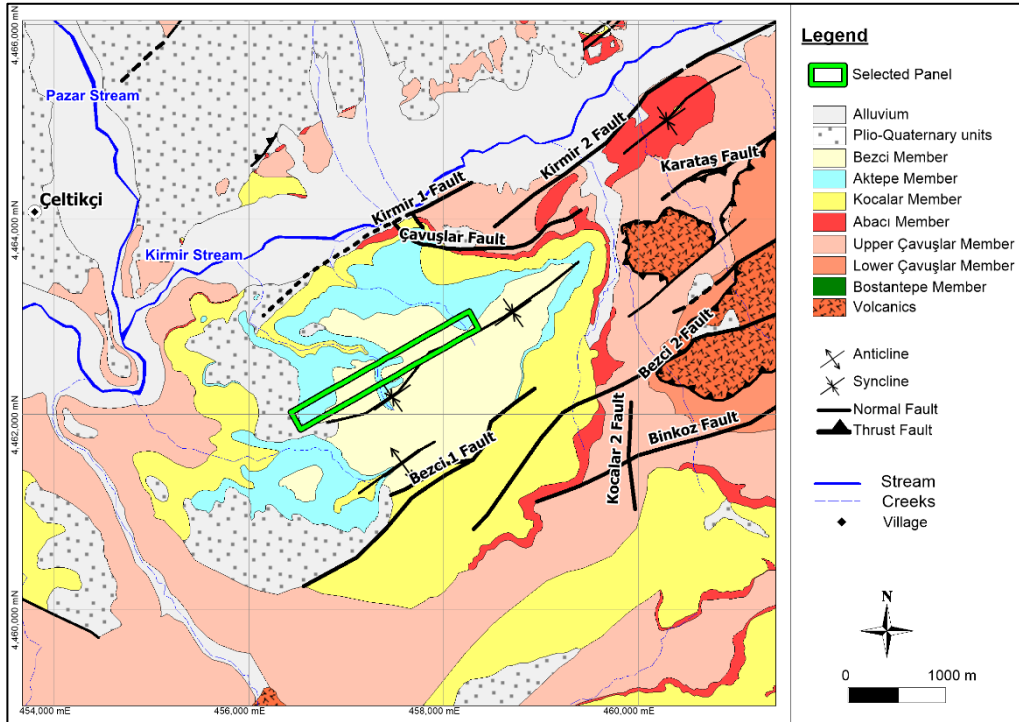


Figure 8.10. Location of the selected panel on geological map

### 8.2.1. Steady State Dewatering

The steady state evaluation of groundwater inflow rate provides an easy and preliminary approach despite the transient behavior of the mining. The steady state dewatering simulations were conducted by assigning the hydraulic head boundary condition with maximum flow rate constraint. The boundary condition is applied to the bottom of the upper seam (i.e. slice 12), where bottom elevation of upper seam was taken as hydraulic head values. The groundwater inflow rate into the panel is calculated as 230 L/s. The hydraulic head profile as a result of steady state dewatering is given in Figure 8.11. As a result of dewatering, an unsaturated zone is created around the selected panel. On the other hand, the water table profile corresponding to the upper aquifer system is preserved.

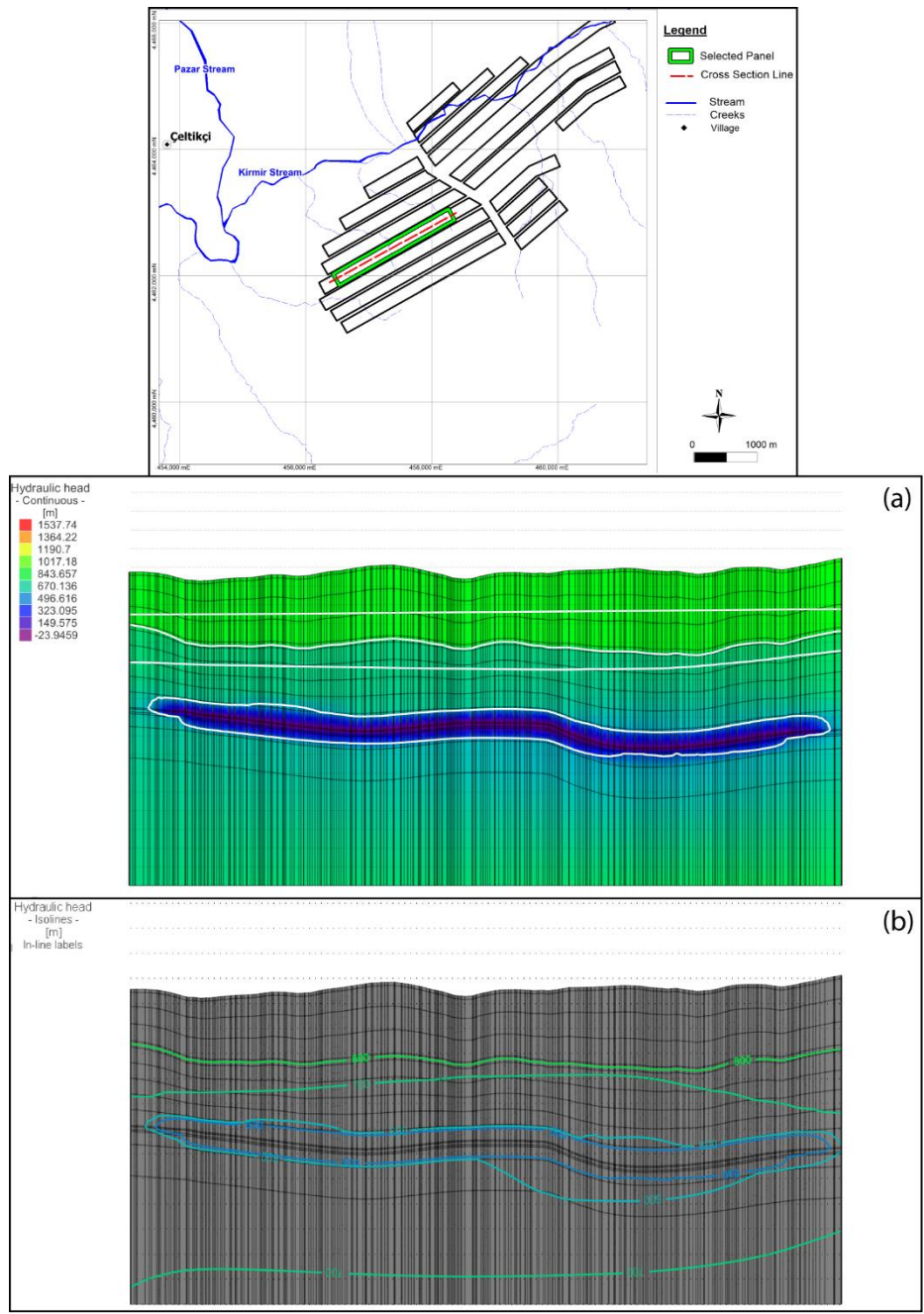


Figure 8.11. Hydraulic head profile along the section passing through the center of the panel: (a) continuous hydraulic head field with zero pressure contours (white lines), and (b) hydraulic head contours

### 8.2.2. Transient Dewatering

The calibrated steady state groundwater flow model is transferred into the transient model for dewatering simulations of the longwall panel. In order to convert the steady state model into the transient one, the storage parameters were obtained from the simulation of pumping test conducted at PW-8 well during calibration stage, and average annual recharge value is converted into monthly recharge series, based on the monthly water budget calculations (Table 5.1).

The conceptual models discussed in Section 8.1 reveal that determination of the limit of the collapsed zone is an important step in longwall simulations, where abrupt changes in hydraulic properties take place. The height of the collapsed zone of the selected panel is determined based on the empirical formula developed by Tammeta (Eq. 8.1). The thicknesses of the upper seam and overburden are determined as 4 m and 504 m, respectively. The width of the panel is 200 m. Hence, the height of the collapsed zone is calculated as 280 m, which corresponds to the Upper Çavuşlar member (simulated by Layers 6 – 10 in the model).

The mining in the selected panel is completed in one year, which is taken as 360 days in the simulations. In order to quantify the dewatering requirements, at the bottom of the upper seam, hydraulic head boundary condition with maximum flow rate constraint is assigned. Modulation functions (i.e. function of time dependent change of boundary conditions) are used to simulate the mine advance and time varying material properties are utilized in the simulation of changes in hydraulic parameters.

The total simulation time is determined as 20 years, where the first 10 years the model is run under transient conditions without additional stresses. As the mining in the panel started, significant changes in the system occur, and the impact of the longwall mining continues afterwards. Running the model 10 years without any stress is helpful to reduce the numerical errors arise from abrupt changes in the system in a short time. The last 10 years of the simulation is aimed to observe operational and post-mining response of the system.

The time step lengths are determined automatically by the software to allow the simulation of the dynamic changes in the system without ruling out any changes. In the simulations the maximum time step size is determined as 30 days whereas the minimum time step size reduced to orders of  $10^{-8}$  days.

For the determination of the dewatering requirements along the selected panel, various simulations were conducted, where the complexity of the system is increased further. The details of each simulation and results are described below.

#### **8.2.2.1. Simulation No. 1**

In the first simulation, the selected panel is divided into 12 regions; each corresponds to the monthly progress of longwall mining (Figure 8.12). The groundwater inflow rate to the panel is simulated by the hydraulic head boundary condition with maximum flow rate constraint. In this simulation, the change of hydraulic conductivity due to longwall mining is not considered. The mining in the panel occurs between day 3600 and 3960; hence modulation functions are activated in this period. In the simulations it is assumed that the regions are mined completely during the corresponding 30 day period. As a result, for each month, the maximum groundwater inflow rates are observed at the beginning, whereas the calculated inflow rates reduce to lower values at the end.

The groundwater inflow rate into the mined area with respect to time is given in Figure 8.13. The results indicate that the average groundwater inflow rate is 375 L/s between days 3600 and 3960, where the maximum rate is observed at day 3720 (i.e. 5<sup>th</sup> month) as 755 L/s. The peak discharge rates are observed at the beginning of the monthly simulated subregion, whereas the lower rates are generally calculated at the end. The longwall mining along the seam is handled in a relatively horizontal manner except for the region corresponding to mining in 5<sup>th</sup> month. Hence, it is believed that the change of the slope of the coal seam results in the simulation of the significantly high inflow rate. At the end of the simulation, groundwater inflow rate reduced to 227 L/s, which is very close to the results of the steady state dewatering simulation.

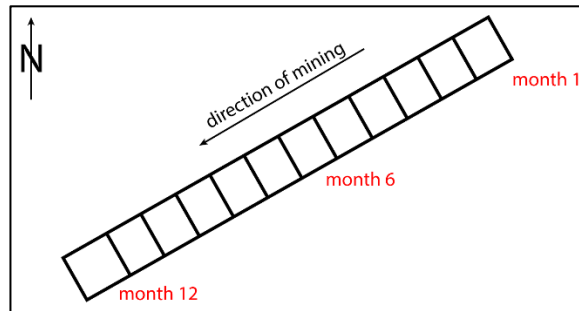


Figure 8.12. Schematic representation of longwall mine progress, selected panel is divided into 12 subregions

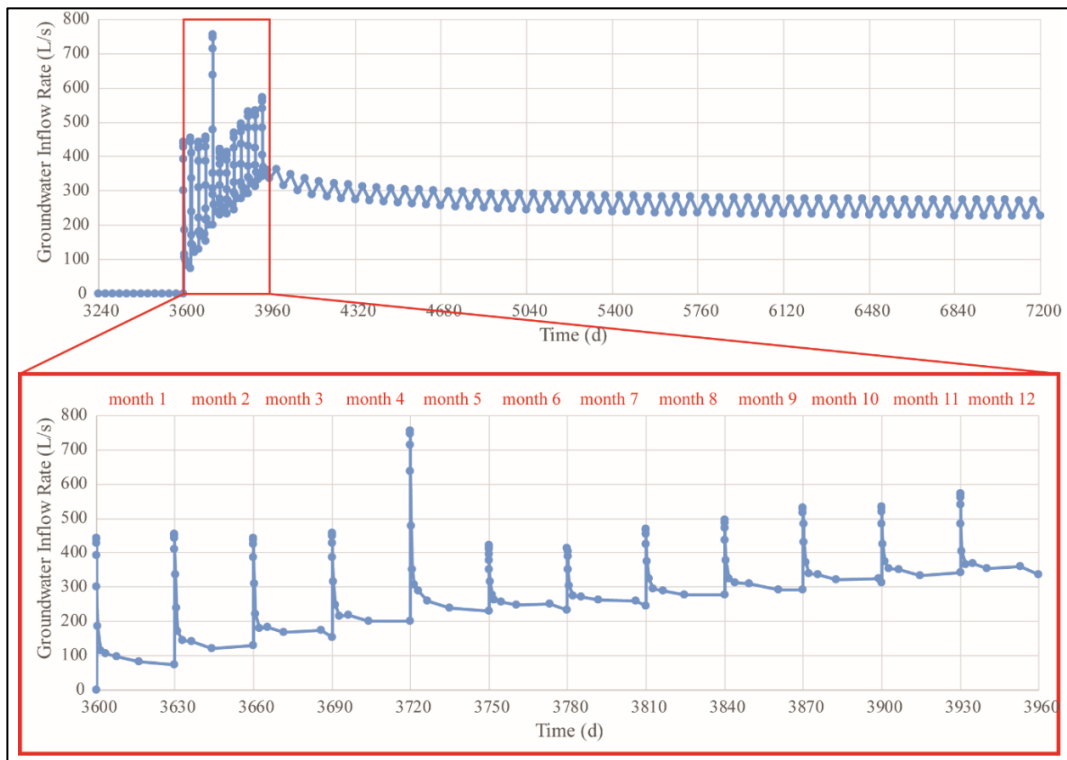


Figure 8.13. Simulated groundwater inflow rate into the panel with respect to time for Simulation No.

1

### 8.2.2.2. Simulation No. 2

In the second simulation, the selected panel is divided into 36 regions instead of 12, in order to obtain more realistic mine progress (Figure 8.14). In that way, mining in each region corresponds to 10-day interval, and it is assumed that the subregions are completely mined in that interval. Likewise Simulation No. 1, in this simulation, the groundwater inflow rate to the panel is simulated by hydraulic head boundary condition with maximum flow rate constraint, and the change of hydraulic conductivity due to longwall mining is not considered. The modulation functions are used to activate the boundary conditions as the mine progresses.

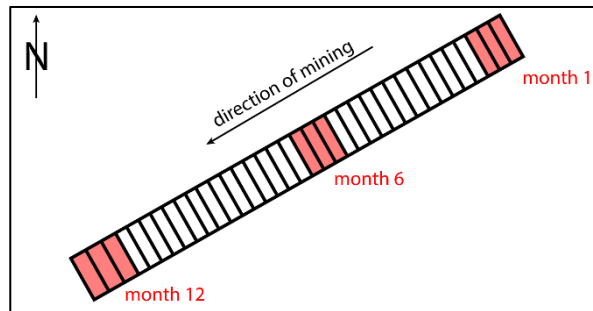


Figure 8.14. Schematic representation of longwall mine progress, selected panel is divided into 36 subregions

The groundwater inflow rate into the mined area with respect to time is given in Figure 8.15, and the comparison of Simulation No. 1 and No. 2 are provided in Figure 8.16. The results indicate that the average groundwater inflow rate is 261 L/s during the active mining of the panel. The significant increase in the groundwater inflow rate is observed at days 3720 and 3730, which corresponds to the 5<sup>th</sup> month in Simulation No. 1. The maximum groundwater inflow rate is observed at day 3940 (i.e. 12<sup>th</sup> month) as 406 L/s. When compared to Simulation No. 1, Simulation No. 2 calculates continuously lower inflow rates. The simulation of the mine progress with finer steps

results in the 70 % decline in the calculated average groundwater inflow rates, and on monthly basis, the rates are decreased about 30 - 60 %.

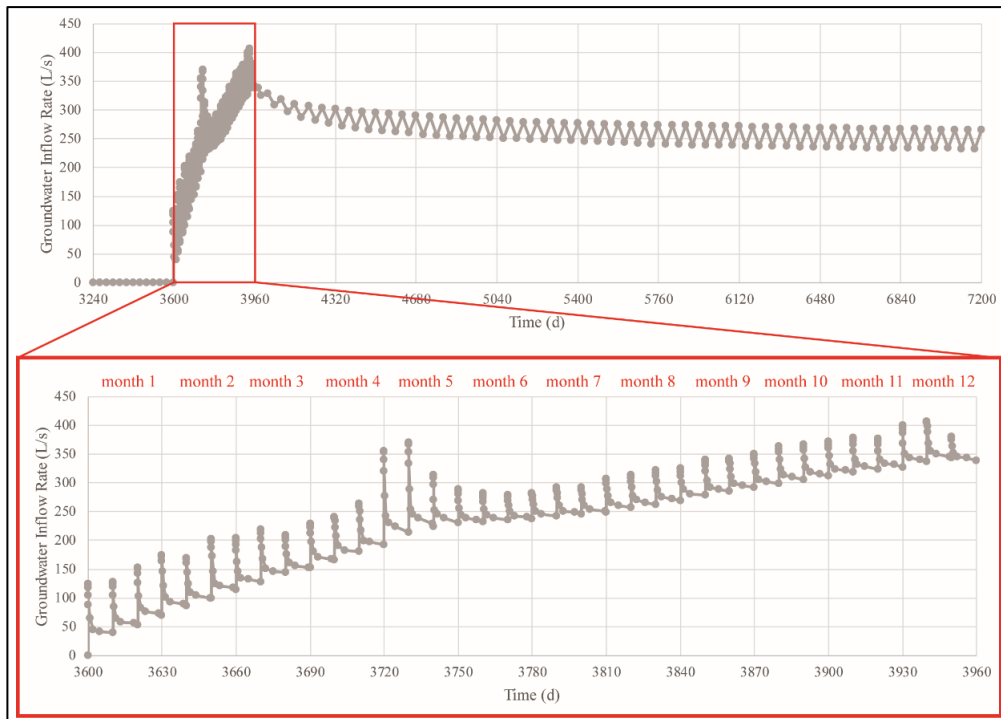


Figure 8.15. Simulated groundwater inflow rate into the panel with respect to time for Simulation No. 2

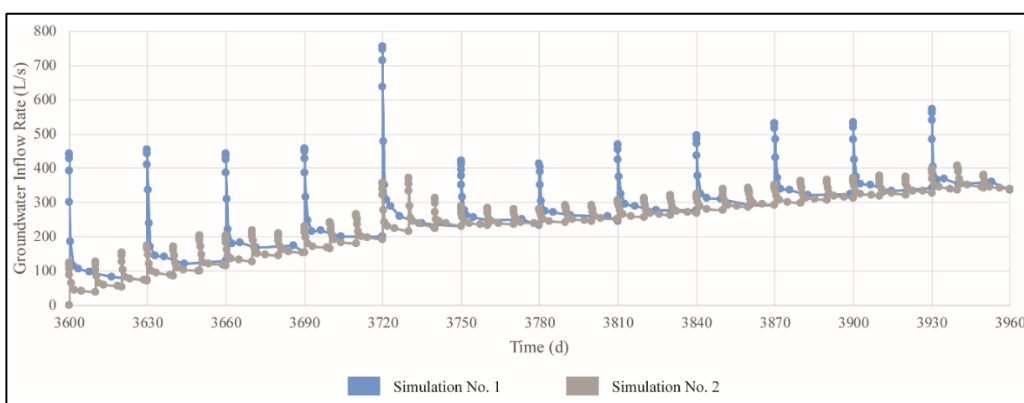


Figure 8.16. Comparison of the calculated groundwater inflow rates of Simulation No. 1 and Simulation No. 2

### 8.2.2.3. Simulation No. 3

The same panel division applied in Simulation No. 2 (i.e. 36 regions) is also used in Simulation No. 3. As described in section 8.1, the main deformation as a result of longwall mining occurs in the goaf, which is defined by the upper seam (i.e. Layer 11) in the numerical model. In the conceptual model developed by Tammeta (2015), a tremendous increase in the post-mining hydraulic conductivity of the goaf is described by the reach of post- to pre-mining hydraulic conductivity ratio to infinity. In this simulation, the hydraulic conductivity of the goaf is increased by 100 times for  $K_x$  and  $K_y$ . Since significant increase in the vertical component of the hydraulic conductivity is expected due to longwall mining, the original  $K_z$  value of the goaf is increased by 1000 times. Hence, the post-mining hydraulic conductivity of the goaf is assigned as  $7 \times 10^{-5}$  m/s for  $K_x$ ,  $K_y$  and  $K_z$ .

The hydraulic conductivity change with respect to time is handled in such a way that, as the mining starts in one region, the change in hydraulic conductivity is applied immediately and remains that way till the end of the simulation (Figure 8.17). In this simulation, the groundwater inflow rate to the panel is simulated by the hydraulic head boundary condition with maximum flow rate constraint, where modulations functions are also used to activate the boundary conditions.

Figure 8.18 represents the groundwater inflow rate into the panel with respect to time. The average groundwater inflow rate is calculated as 321 L/s, where the maximum rate is calculated as 819 L/s at day 3930 (i.e. 12<sup>th</sup> month). At the beginning of mining at each region results in sudden increase in the inflow rates, and the rates gradually decrease until the activation of the next region. The calculated lowest groundwater inflow rates at each region range between 35 L/s and 352 L/s.

The dramatic increase of the hydraulic conductivity at the goaf clearly seen at the groundwater flow rates when compared to Simulation No. 2 (Figure 8.19). The simulated rates increased by 1.5 to 3.5 times when hydraulic conductivity change at the goaf due to longwall mining is considered in Simulation No. 3.

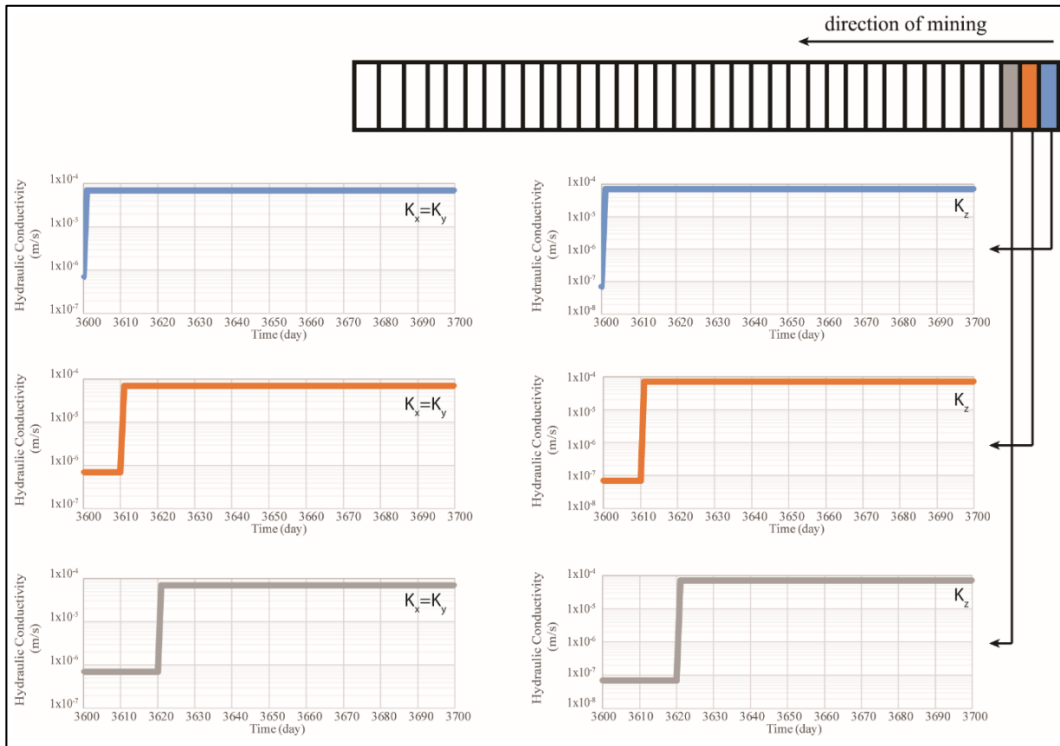


Figure 8.17. Hydraulic conductivity change of the goaf with respect to time and mine progress in Simulation No. 3

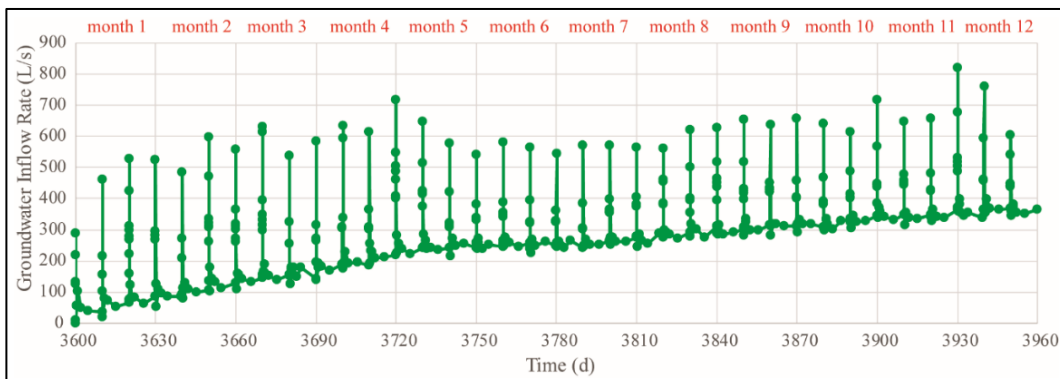


Figure 8.18. Simulated groundwater inflow rate into the panel with respect to time for Simulation No. 3

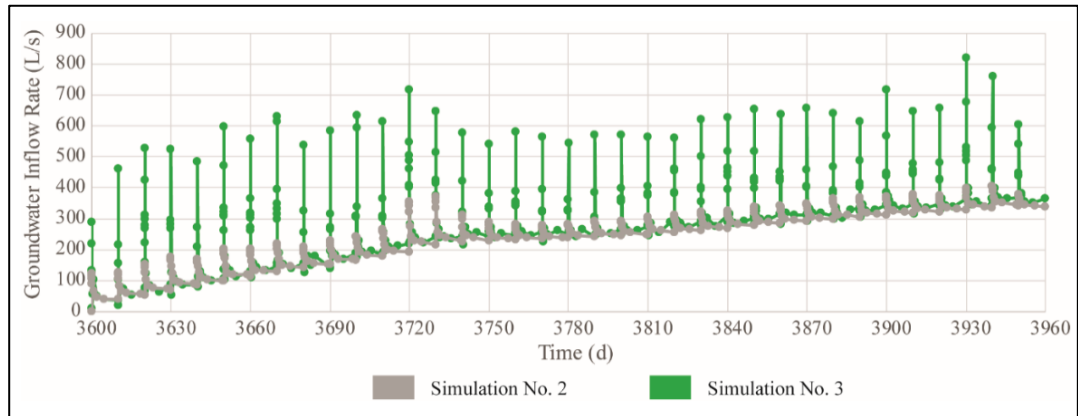


Figure 8.19. Comparison of the calculated groundwater inflow rates of Simulation No. 2 and Simulation No. 3

#### 8.2.2.4. Simulation No. 4

As Simulation No. 3 reveals the impact of hydraulic conductivity change at the goaf on groundwater inflow rate, this change is further investigated in Simulation No. 4. In this simulation, instead of sudden increase of hydraulic conductivity, gradual increase is applied in the material property functions, at the goaf only (Figure 8.20). Hence, instead of an abrupt increase of hydraulic conductivity of the goaf at day 1, the hydraulic conductivity value is increased day by day, where the maximum value is reached at the end of each 10-day interval. It should be noted that the 10-day interval corresponds to mining duration in each region in Figure 8.14. The same logic is applied in the assignment of hydraulic conductivity change with respect to time and mine progress as Simulation No. 3. The calibrated hydraulic conductivity values at the goaf area (i.e. Layer 11) are  $7 \times 10^{-7}$  m/s for  $K_x$  and  $K_y$ , whereas  $K_z$  value is 10 times lower than the  $K_x$  values. As a result of longwall mining, the post-mining hydraulic conductivity of the goaf is assigned as  $7 \times 10^{-5}$  m/s for  $K_x$ ,  $K_y$  and  $K_z$ . The groundwater inflow rate to the panel is simulated by the hydraulic head boundary condition with maximum flow rate constraint, where modulations functions are also used to activate the boundary conditions.

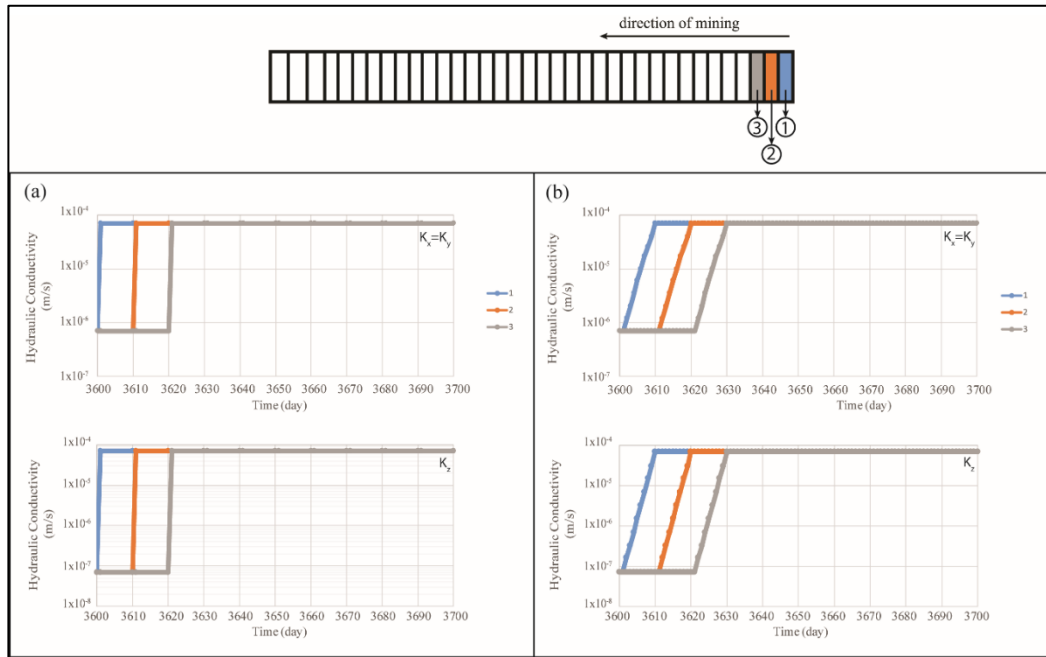


Figure 8.20. Comparison of the hydraulic conductivity change with respect to time simulated at (a) Simulation No. 3, and (b) Simulation No. 4

The simulated groundwater inflow rate into the mine is represented in Figure 8.21. As can be seen from the graph, the maximum inflow rate is calculated at day 3720 (i.e. 5th month) as 525 L/s, whereas the average groundwater inflow rate is determined as 266 L/s. The sudden increase in the rates is observed at the start of the simulation of each region, where calculated rates increase from 124 L/s (at day 3600) to 389 L/s (at day 3950). On the other hand, the rates calculated at the end of simulation of each region ranges from 32 L/s (at day 3610) to 356 L/s (at day 3960). In order to determine the impact of gradually increasing hydraulic conductivity values at the goaf compared to sudden increase, the simulation results of Simulation No. 3 and Simulation No.4 are plotted together in Figure 8.22. The decrease in the simulated groundwater inflow rates is evident when the hydraulic conductivity values are assigned in a gradually increasing manner. The average decline in the rates is determined as 50 %.

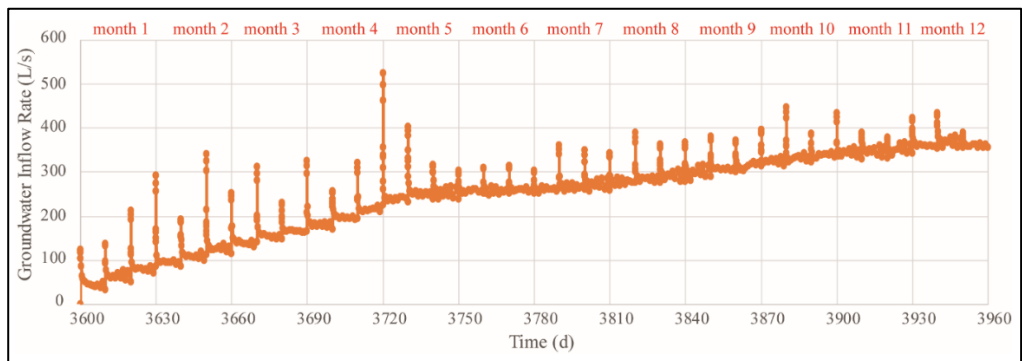


Figure 8.21. Simulated groundwater inflow rate into the panel with respect to time for Simulation No. 4

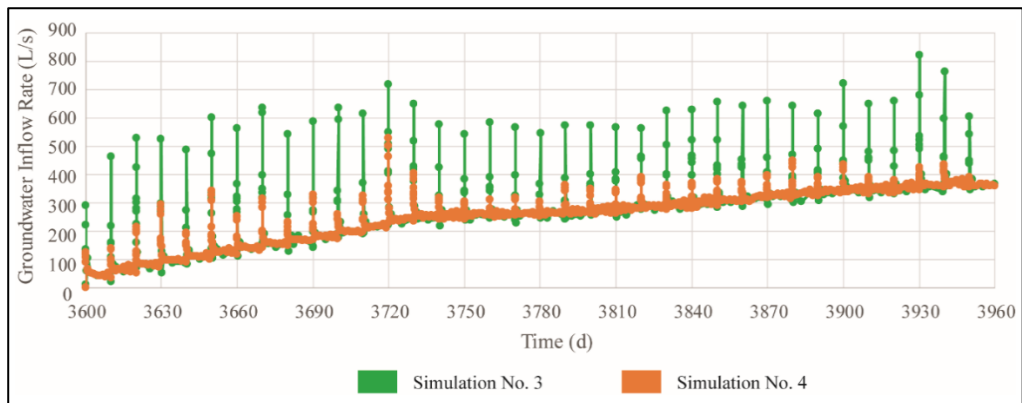


Figure 8.22. Comparison of the calculated groundwater inflow rates of Simulation No. 3 and Simulation No. 4

### 8.2.2.5. Simulation No. 5

The change of hydraulic conductivity as a result of longwall mining occurs not only at the goaf but also in the collapsed zone (Figure 8.7). The height of the collapsed zone (H) that is expected to form above the selected panel is calculated as 280 m, which includes layers 6 to 10 in the numerical model. The conceptual model developed by Tammeta (2015) reveals that the post-mining hydraulic conductivity values increased more than 40 times compared to the pre-mining values. Therefore, in Simulation No.

5, in addition to the hydraulic conductivity change in the goaf, the change in hydraulic conductivity in the collapsed zone is simulated.

Since the nature of the fractured system that will be developed as a result of longwall mining is not known at this stage, in Simulation No. 5, the ratio of the post- to pre-mining hydraulic conductivity is taken as 50. Since in the collapsed zone vertical fractures are formed, the original anisotropy in the system is not preserved. Hence, the post-mining hydraulic conductivity of the goaf and the collapsed zone are assigned as  $7 \times 10^{-5}$  m/s and  $1 \times 10^{-6}$  m/s, respectively for  $K_x$ ,  $K_y$  and  $K_z$ . The change of the hydraulic conductivity with respect to time and mine progress is applied similar to Simulation No. 4, where the conductivity values are increased gradually (Figure 8.23). The groundwater inflow rate to the panel is simulated by the hydraulic head boundary condition with maximum flow rate constraint, whereas modulations functions are also used to activate the boundary conditions.

The simulated groundwater inflow rate to the panel is given in Figure 8.24. Although the model has no convergence problems, the calculated rates show abnormal fluctuations. The maximum inflow rates observed at days 3720 and 3780 reach 1200 L/s. and 1300 L/s, respectively. The average inflow rate is calculated as 444 L/s. The decreasing pattern in the inflow rates that are observed at the simulation of each region in all previous simulations cannot be maintained in this simulation.

#### **8.2.2.6. Simulation No. 6**

The increase in the post-mining hydraulic conductivity values 50 times compared to pre-mining case and also simulation of the isotropic system at the goaf and collapsed zone results in extremely high groundwater inflow rates. In order to eliminate the impacts of the dramatic changes into the system, the conductivity values at the layers corresponding to the collapse zone is modified gradually in Simulation No. 6. Due to its closeness to the goaf, the maximum increase in the conductivity values is expected to occur at Layer 10. Hence the post- to pre-mining hydraulic conductivity ratio is assigned as 50 for Layer 10. This ratio is gradually decreased to 25, 12.5, 6.25 and 3 for Layers 9, 8, 7 and 6, respectively. Unlike Simulation No.5, in this simulation the

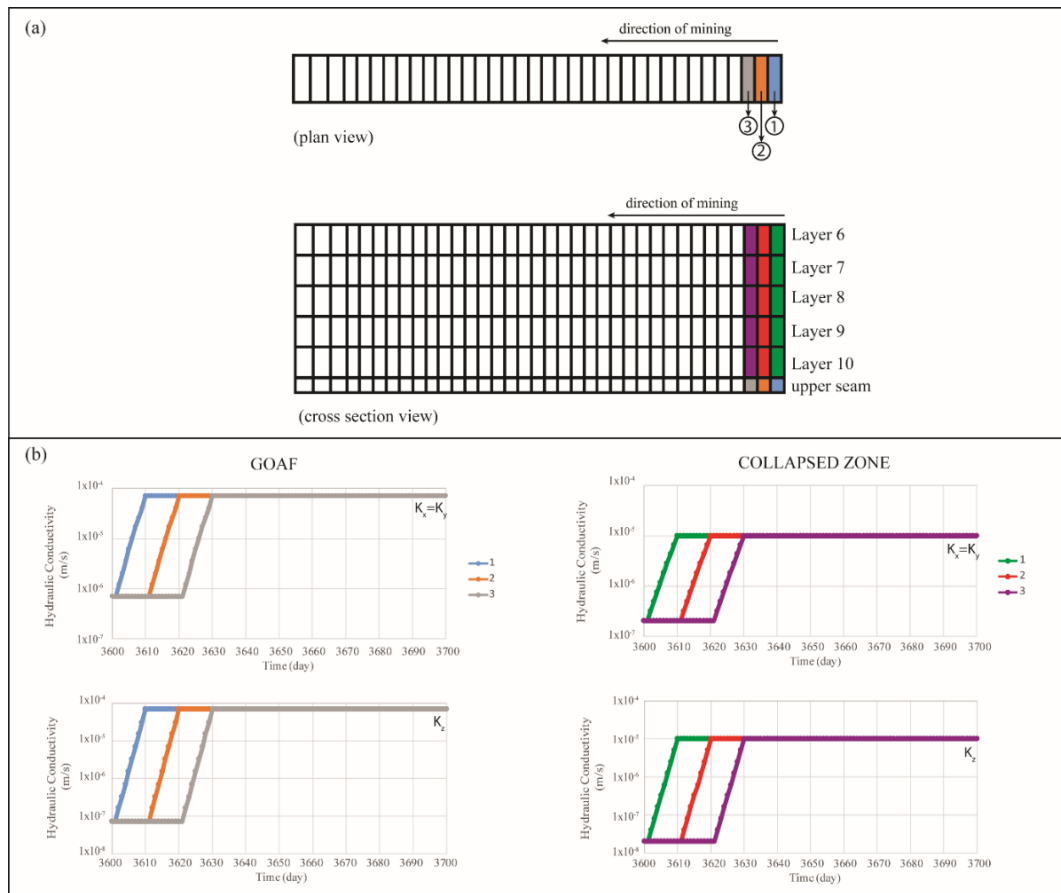


Figure 8.23. (a) Schematic representation of the assigned hydraulic conductivity field in the goaf and collapsed zone, and (b) Hydraulic conductivity change of the goaf and collapsed zone with respect to time and mine progress in Simulation No. 5

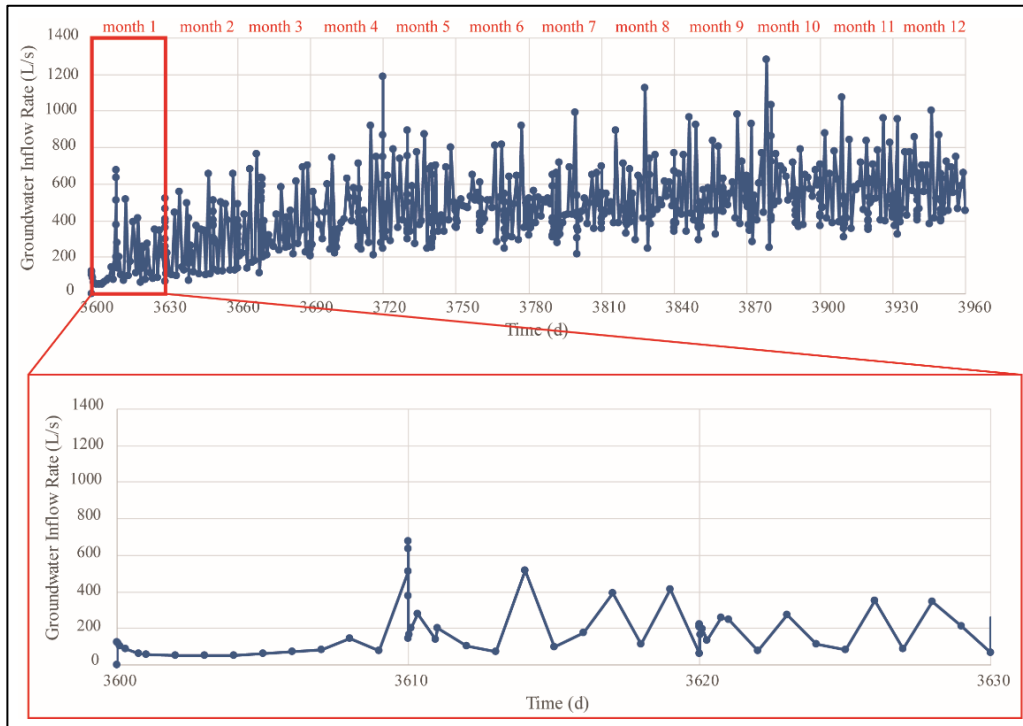


Figure 8.24. Simulated groundwater inflow rate into the panel with respect to time for Simulation No. 5

ratio of horizontal to vertical conductivity in the calibrated model is maintained in the collapsed zone. The assigned hydraulic conductivity values to the goaf and collapsed zone are shown in Table 8.1. For each layer, pre-mining hydraulic conductivity values are increased gradually, where at the end of simulation of each region, the post-mining conductivity values are obtained (Figure 8.25). The groundwater inflow rate to the panel is simulated by the hydraulic head boundary condition with maximum flow rate constraint, whereas modulations functions are also used to activate the boundary conditions.

Table 8.1. Assigned hydraulic conductivity values at the goaf and collapsed zone for Simulation No. 6

Longwall Mining Zone	Corresponding Layer in the Numerical Model	Pre-mining Hydraulic Conductivity (m/s)		Post-mining Hydraulic Conductivity (m/s)		Post-mining to Pre-mining Ratio (R)
		$K_x=K_y$	$K_z$	$K_x=K_y$	$K_z$	
Collapsed Zone	Layer 6	$2 \times 10^{-7}$	$2 \times 10^{-8}$	$6 \times 10^{-7}$	$6 \times 10^{-8}$	3
	Layer 7	$2 \times 10^{-7}$	$2 \times 10^{-8}$	$1.25 \times 10^{-6}$	$1.25 \times 10^{-7}$	6.25
	Layer 8	$2 \times 10^{-7}$	$2 \times 10^{-8}$	$2.5 \times 10^{-6}$	$2.5 \times 10^{-7}$	12.5
	Layer 9	$2 \times 10^{-7}$	$2 \times 10^{-8}$	$5 \times 10^{-6}$	$5 \times 10^{-7}$	25
	Layer 10	$2 \times 10^{-7}$	$2 \times 10^{-8}$	$1 \times 10^{-5}$	$1 \times 10^{-6}$	50
Goaf	Layer 11	$7 \times 10^{-7}$	$7 \times 10^{-8}$	$7 \times 10^{-5}$	$7 \times 10^{-5}$	100 to 1000

Figure 8.26 shows the simulated groundwater inflow rate to the panel with respect to time. As can be seen from the figure, rapid increase in the inflow rate is observed at day 3720, which corresponds to the change in the slope of the upper seam. The maximum groundwater inflow rate is calculated as 650 L/s, whereas the average rate is determined as 363 L/s. After day 3750 (i.e. month 6) the inflow rates shows extraordinary oscillations, which can reach about 300 L/s. When compared to Simulation No. 5, in Simulation No. 6, dramatic decrease in the inflow rates can be clearly seen, where the maximum groundwater inflow rate is lowered by about 50 % in Simulation No. 6 (Figure 8.27). Although the calculated inflow rates show sharp oscillations, assignment of the gradually changing hydraulic conductivity values results in a more stable solution.

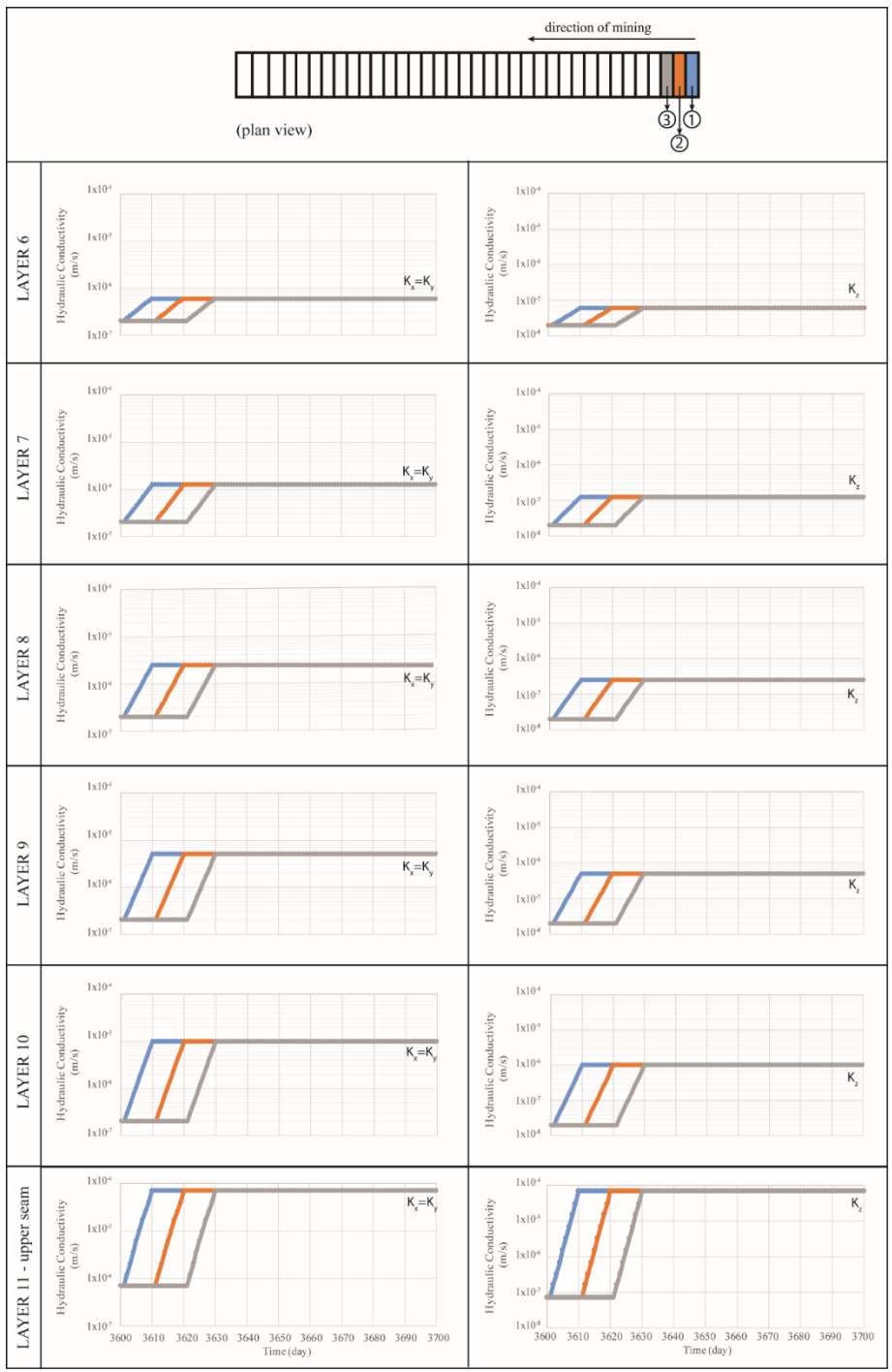


Figure 8.25. Hydraulic conductivity change of the goaf and collapsed zone with respect to time and mine progress in Simulation No. 6

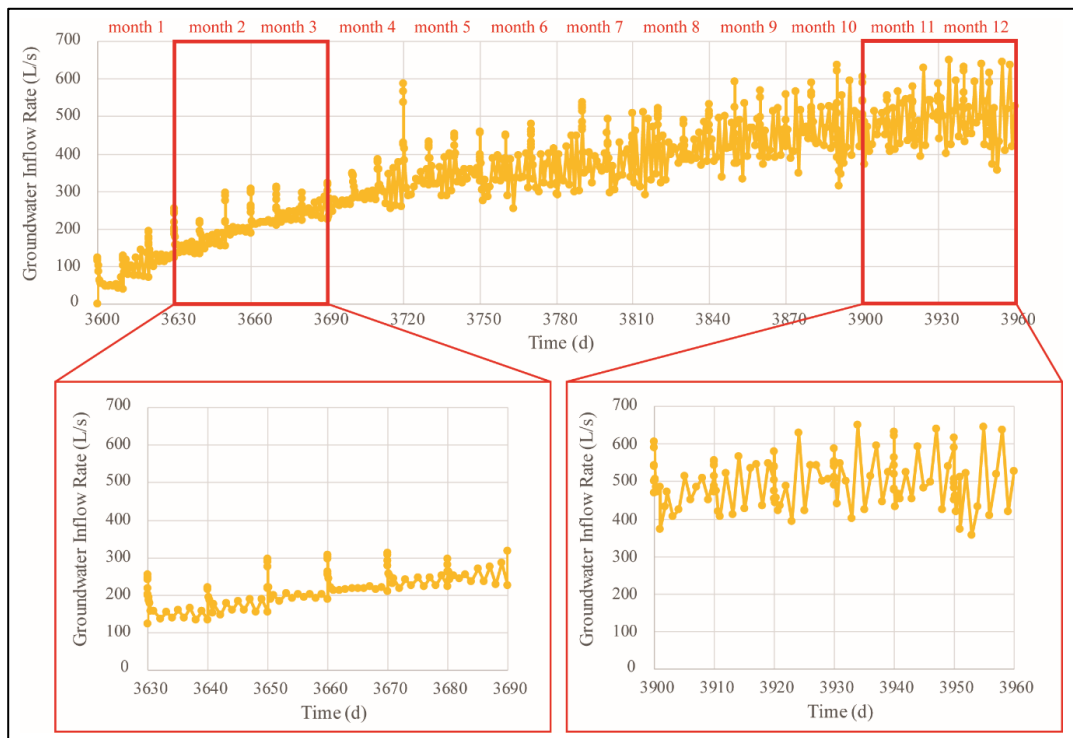


Figure 8.26. Simulated groundwater inflow rate into the panel with respect to time for Simulation No. 6

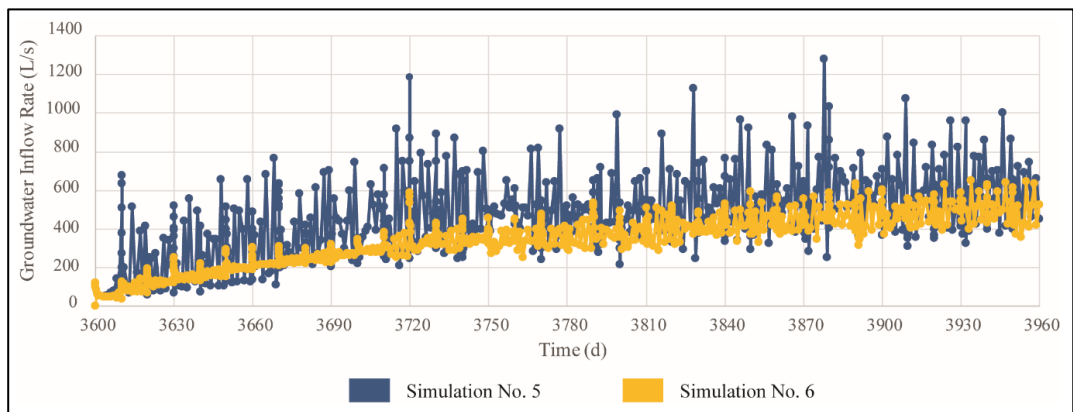


Figure 8.27. Comparison of the calculated groundwater inflow rates of Simulation No. 5 and Simulation No. 6

### **8.3. Impacts of Longwall Panel Dewatering on Groundwater Resources**

The impacts of longwall mining as a result of dewatering activities are evaluated in terms of (i) simulated water table profile at the end of mining, (ii) the areal distribution of the cone of depression and also (iii) the timewise change of simulated hydraulic head values at the monitoring wells in the vicinity of the panel.

Around the selected panel, at a distance of 1 km, seven monitoring wells are selected to control timewise change of the simulated hydraulic head values, namely, CEL-18, CEL-24, CEL-27, CEL-57, CEL-85, CEL-93A and CEL-102. Among these wells, three wells were screened at the volcanics (CEL-18, CEL-27, and CEL-57), one well is screened in the coal and Lower Çavuşlar member (CEL-85), whereas one was screened in the Lower Çavuşlar member (CEL-24). Remaining two wells, namely CEL-93A and CEL-102 were screened in the upper aquifer and selected to observe the impact of the longwall mining to the overlying aquifer. The detailed information about the wells can be found in Table 4.5, whereas the location of them with respect to the selected panel is shown in Figure 8.28.

The impacts of longwall dewatering as a result of transient simulations were assessed for Simulation No. 2, No. 4 and No.6, where three different changes in the system are simulated. In Simulation No. 2, dewatering is simulated by assigning hydraulic head boundary conditions where mine progress is simulated with the help of modulation functions. The change in the hydraulic properties as a result of dewatering is not considered. In Simulation No. 4, the dramatic increase in the hydraulic conductivity of the goaf is simulated. Finally, in Simulation No. 6, the change in hydraulic conductivity of both the goaf and the layers comprising the collapsed zone is evaluated. The impacts of dewatering on groundwater resources associated with these simulations are explained below.

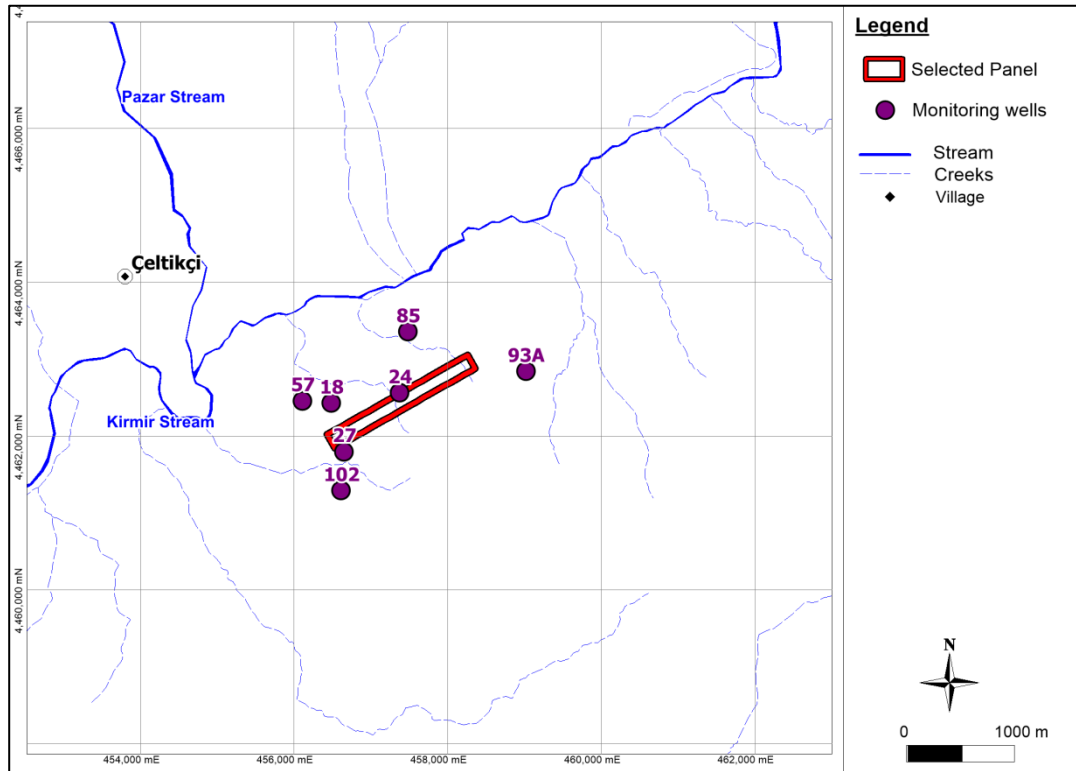


Figure 8.28. Location of the monitoring wells used in the impact assessment of longwall mining

### 8.3.1. Simulation No. 2

The simulated water table profile along the cross-section passing through the center of the long axis of the panel is given in Figure 8.29. As can be seen from the figure, at the top, the saturated zone corresponding to the Upper Aquifer is conserved. Due to the dewatering activities, at the bottom of the upper seam, a very tiny unsaturated zone is formed.

The cone of depression resulted from the dewatering of the selected panel without any changes in the hydraulic properties of the system is given in Figure 8.30 for the Layers 6 to 11. The maximum drawdown is calculated at Layer 11 as 420 m at the region where sudden increase in the groundwater inflow rate is also observed. The drawdown values declines to 5 m at a distance of 1-1.5 km. The faults located within the study

area limit the areal distribution of the cone of depression. From Layer 11 to Layer 6, it can be seen that the impact of longwall mine dewatering decreases.

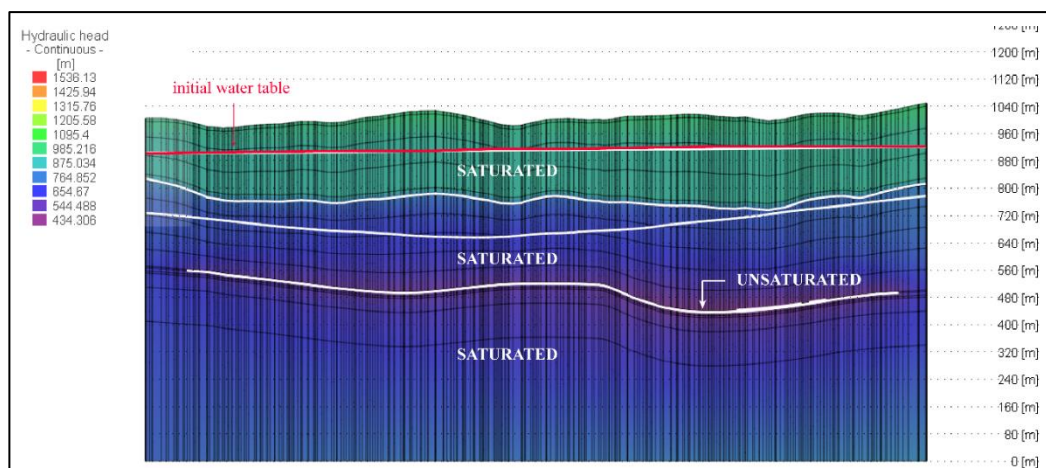


Figure 8.29. Water table profile as a result of Simulation No. 2

The impact of dewatering is also investigated at the groundwater levels measured at the monitoring wells (Figure 8.31). The significant decline of groundwater level is seen at wells CEL-24 and CEL-27, which are closest wells to the panel. The groundwater levels decrease 234 m and 112 m at CEL-24 and CEL-27, respectively. At CEL-18 and CEL-85, due to longwall mining, groundwater levels decrease about 50 m, whereas at CEL-57, 13 m decline in the hydraulic head values is simulated. At CEL-93 and CEL-102, 6 m and 3 m decline in the simulated hydraulic head values is observed respectively. The areal distribution of the cone of depression for the upper aquifer reveals that springs that supply water to Bezcikuzören and Gümele villages are expected to dry out (Figure 8.32).

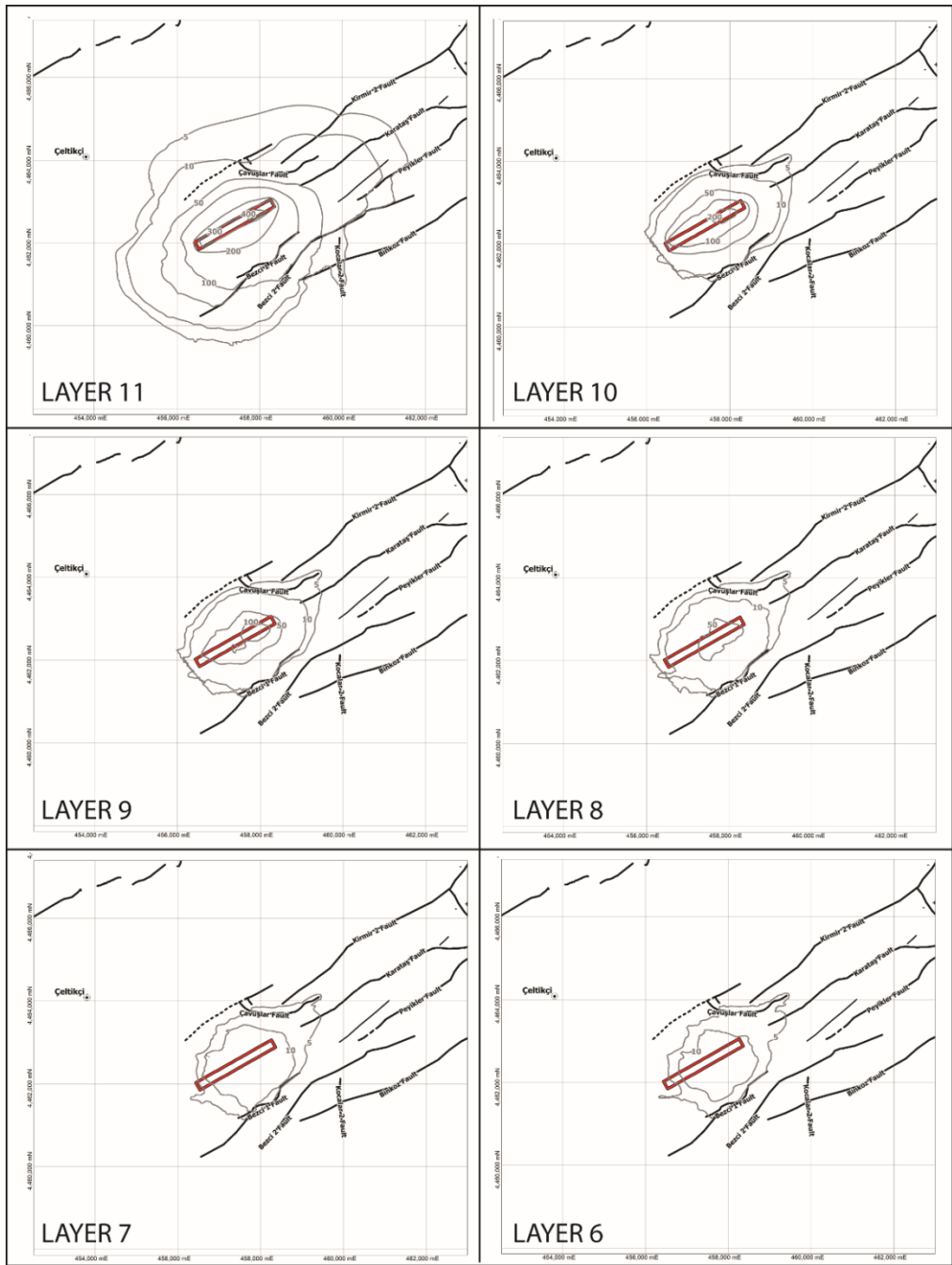


Figure 8.30. Simulated drawdown contours at day 3960 for Simulation No. 2

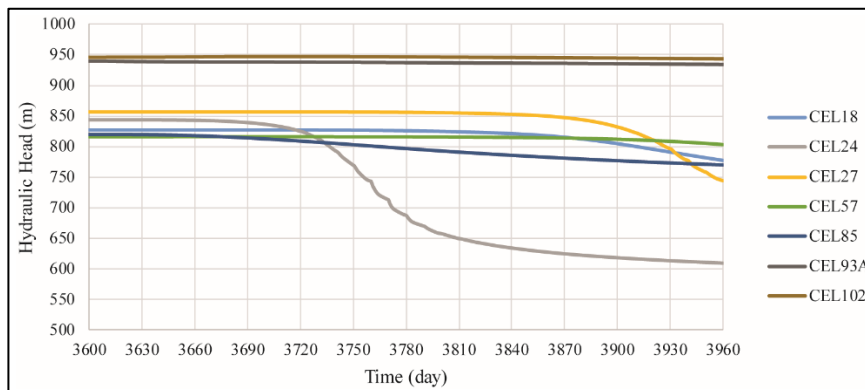


Figure 8.31. Simulated time vs hydraulic head change at the monitoring points as a result of Simulation No. 2

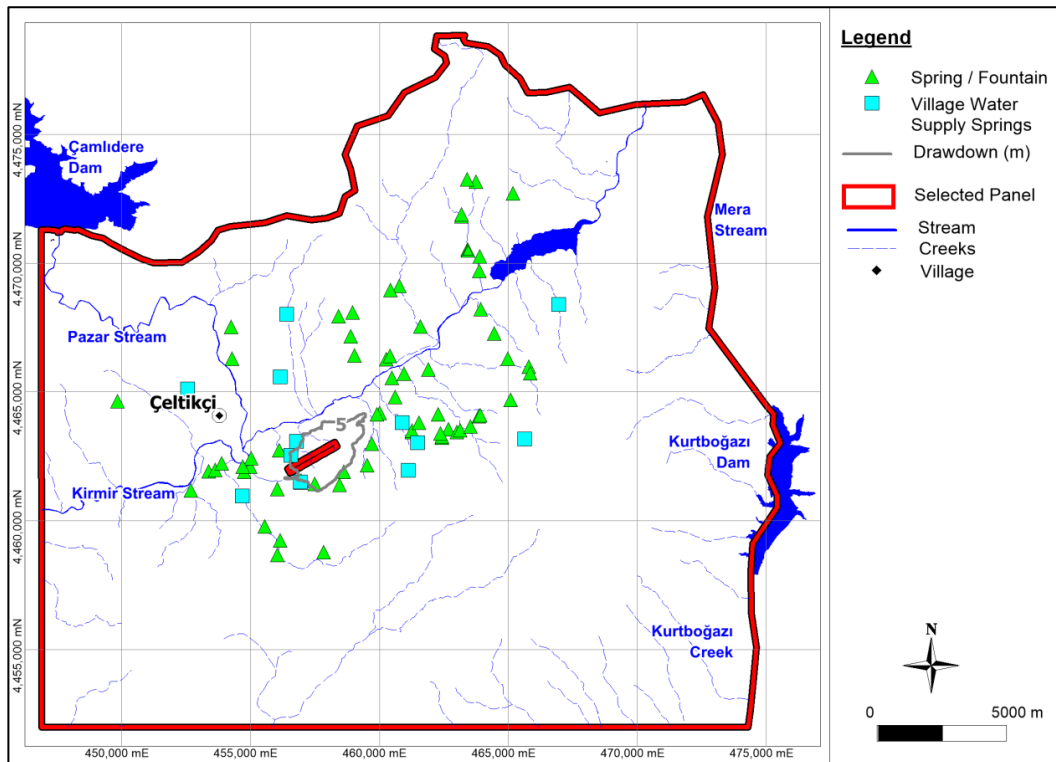


Figure 8.32. Simulated cone of depression of Simulation No. 2 at the upper aquifer

### 8.3.2. Simulation No. 4

The impact of the dramatic increase in the hydraulic conductivity of the goaf due to longwall mining (i.e. 100 times higher than the pre-mining horizontal conductivity and 1000 times higher than the vertical pre-mining conductivity values) is determined in terms of water table profile (Figure 8.33). The profile indicates that the saturated zone of the Upper Aquifer is preserved, whereas the height of the unsaturated zone formed as a result of the dewatering increased when compared to Simulation No. 2.

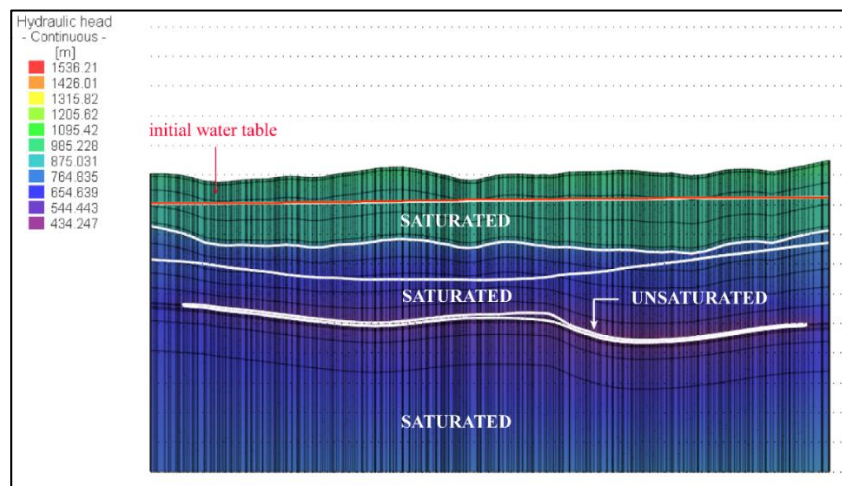


Figure 8.33. Water table profile as a result of Simulation No. 4

The areal distribution of the cone of depression at the end of mining at Layers 11 to 6 is provided in Figure 8.34. As can be seen from the figure, the maximum drawdown value is observed as 420 m at Layer 11, where the minimum elevation at the bottom of upper seam is achieved. The drawdown values then decreased to 50 m at a distance of 1 km. The faults located within the study area limits the areal extent of the cone of depression. The main impact of dewatering is observed mainly at Layers 11, 10, 9 and 8, where from bottom to top, the simulated drawdown values decrease. The simulated maximum drawdown values reduce from 400 m in the Layer 11 to 200 m in Layer 10, 100 m in Layer 9 and 50 m in Layer 8.

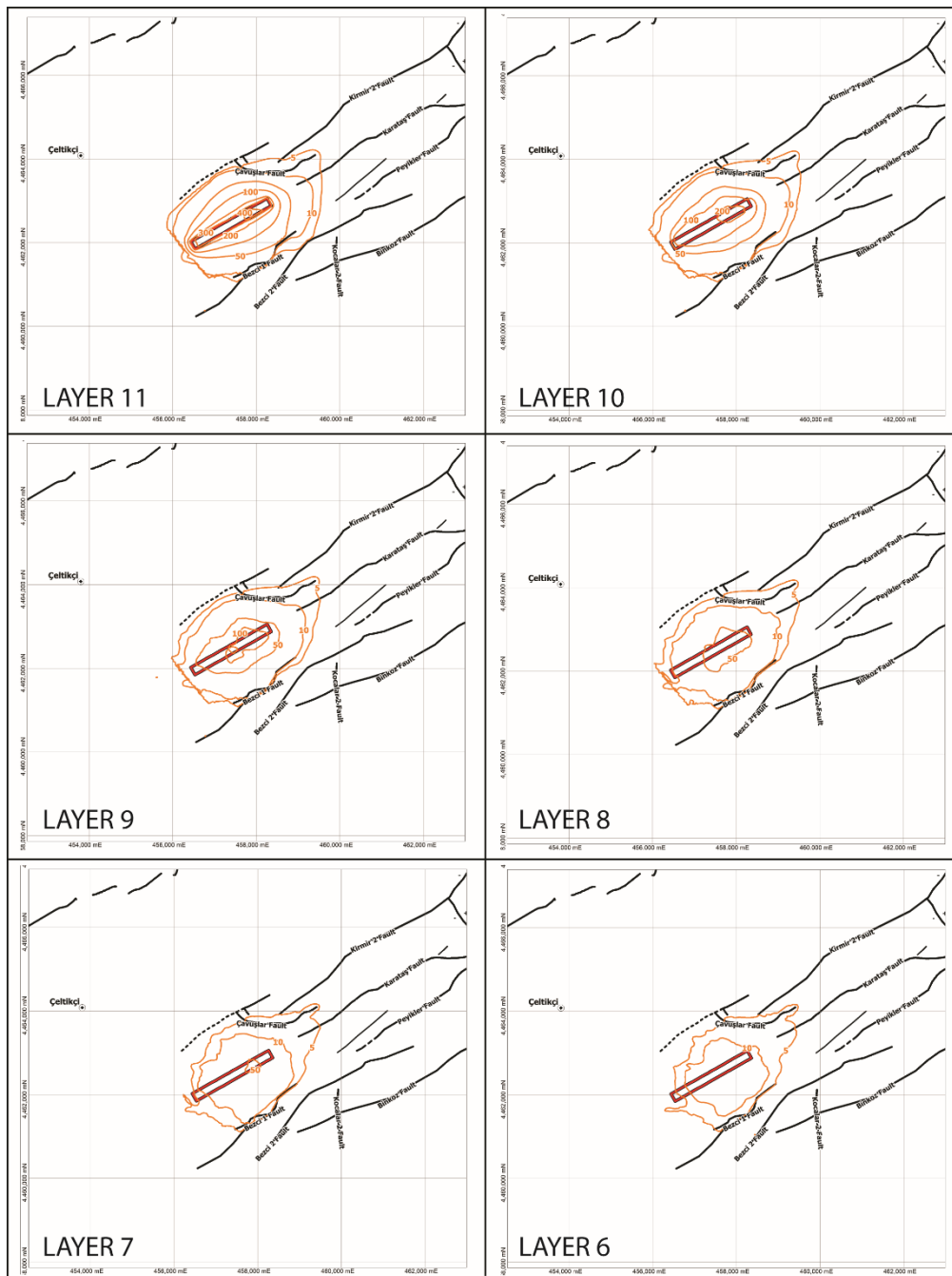


Figure 8.34. Simulated drawdown contours at day 3960 for Simulation No. 4

The impact of dewatering is also investigated at the groundwater levels measured at the monitoring wells (Figure 8.35). A major change in the groundwater levels is seen at wells CEL-24 and CEL-27, which are closest wells to the panel. The groundwater levels decrease 245 m and 120 m at CEL-24 and CEL-27, respectively. At CEL-18 and CEL-85, due to longwall mining, groundwater levels decrease about 50 m, whereas at CEL-57, 14 m decline in the hydraulic head values is simulated. At the wells screened within the Upper Aquifer, 7 m and 3 m decline in the hydraulic head values is simulated at CEL-93 and CEL-102, respectively. Due to the model errors, it is estimated that the springs and fountains located within 5 m drawdown contour will fade. In that context, as a result of Simulation No. 4, in addition to three monitored springs, springs that supply water to Bezcikuzören and Gümele villages are expected dry out (Figure 8.36).

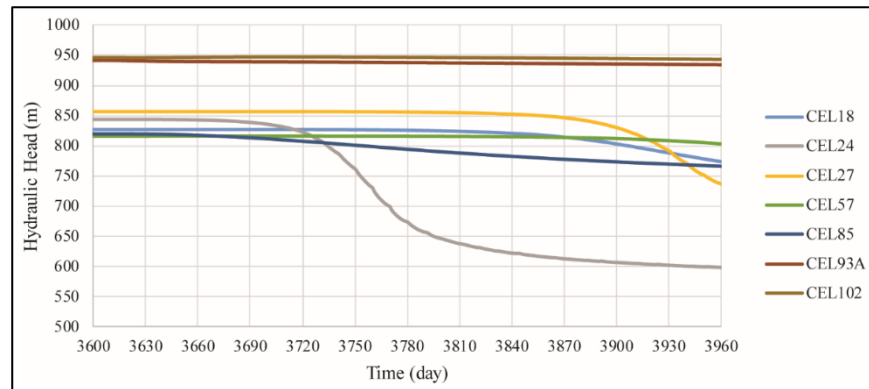


Figure 8.35. Simulated time vs hydraulic head change at the monitoring points as a result of Simulation No. 4

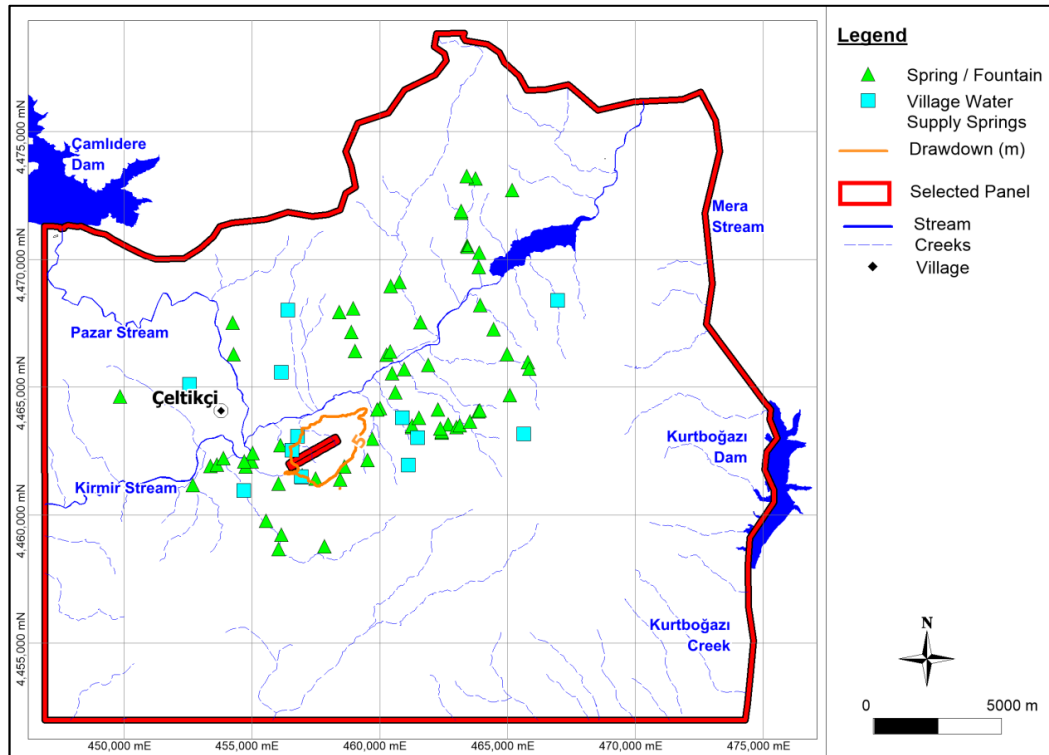


Figure 8.36. Simulated cone of depression of Simulation No. 4 at the upper aquifer

### 8.3.3. Simulation No. 6

The impact of the increase in the post-mining hydraulic conductivity values both at the goaf and the layers comprising the collapsed zone is investigated in Simulation No. 6. Based on the literature, due to longwall mining, presence of an unsaturated zone in the collapsed zone is expected. In the model, the collapsed zone composed of Layer 10 to 6. The water table profile at the end of simulation reveals that, the unsaturated zone is significantly enlarged when compared to Simulation No. 2 and 4 (Figure 8.37).

The impacts of longwall mining are further evaluated in terms of areal distribution of the cone of depression as a result of Simulation No. 6 (Figure 8.38). The maximum drawdown value occurs in Layer 11, with a value of 420 m. This value reduces to 100 m and 50 m at a distance of 500 m and 1 km, respectively. The faults located around the panel limits the areal extent of the cone of depression. The simulated maximum

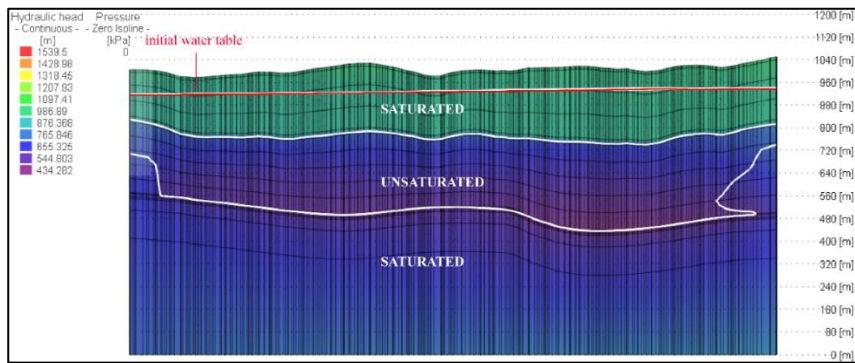


Figure 8.37. Water table profile as a result of Simulation No. 6

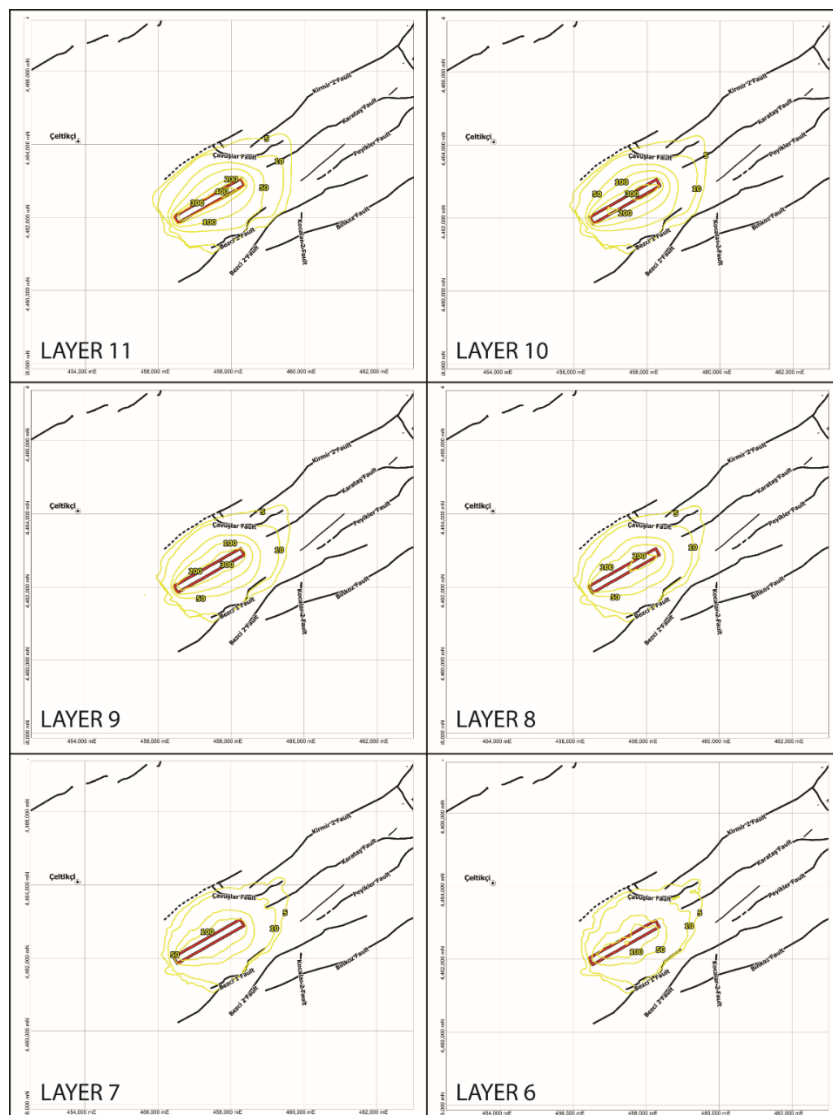


Figure 8.38. Simulated drawdown contours at day 3960 for Simulation No. 6

drawdowns within the panel margins in the collapsed zone range from 300 m to 100 m from Layer 10 to 6. When compared to Simulation No. 4, the drawdown values simulated in the collapsed zone (i.e. at Layers 6 and 10) are significantly increased in Simulation No. 6.

The hydraulic head values at the selected monitoring wells are also investigated to assess the longwall dewatering impacts (Figure 8.39). As expected, a major decline in the hydraulic head values is simulated at CEL-24 and CEL-27 as 253 and 127 m, respectively. The decline of the groundwater levels at wells CEL-18 and CEL-85 elevated to 60 m as a result of Simulation No. 6. At CEL-57, hydraulic head values are lowered 16 m. Similar to Simulation No. 4, at the wells CEL-93A and CEL-102, groundwater levels are decreased 7 m and 3 m, respectively. The 5 m drawdown contour obtained as a result of the simulation at the Upper Aquifer indicates that the water supply springs of Bezcikuzören and Gümele villages and 4 other monitored springs are expected to dry up (Figure 8.40).

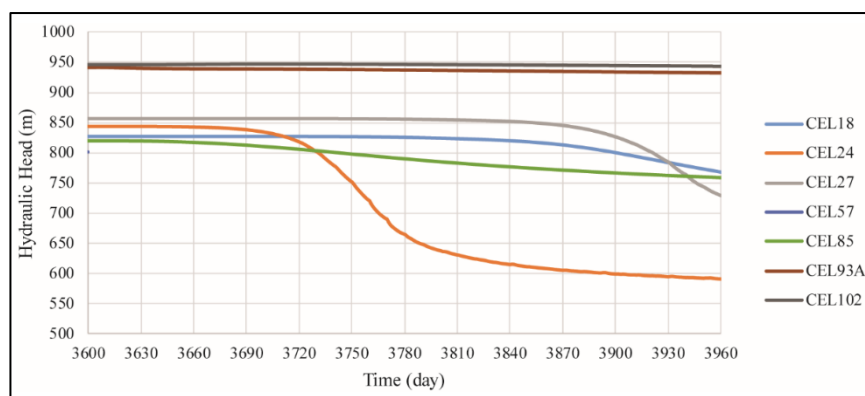


Figure 8.39. Simulated time vs hydraulic head change at the monitoring points as a result of Simulation No. 6

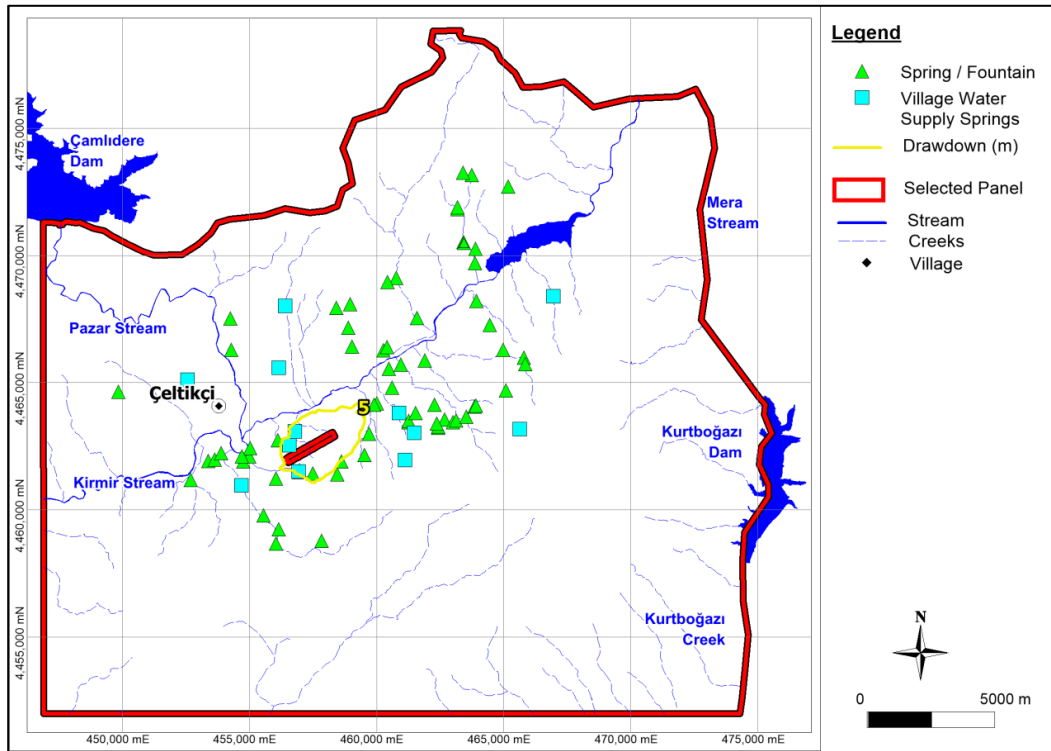


Figure 8.40. Simulated cone of depression of Simulation No. 6 at the upper aquifer



## CHAPTER 9

### DISCUSSION

#### 9.1. Open Pit Simulations

The open pit is located at the southern part of the Kirmir stream, where the distance between the pit and stream approaches to 35 m. In the open pit, 11 years of mining is envisaged based on the prefeasibility studies. The yearly mine plans indicate that the surface area of the excavation ranges from 0.5 km<sup>2</sup> to 1.20 km<sup>2</sup>, whereas the excavated depth changes between 70 m and 104 m. Since the mine advance is provided on a yearly basis, in the simulations, the hydraulic head boundary condition assigned at the bottom of the excavated area is activated for the corresponding year. When mining in a particular year is simulated, the boundary conditions become active for the excavation area of the consecutive year. The flow of any water into the groundwater system is prevented by constraining the boundary condition. Since the system is forced to lower the groundwater levels below the excavation depth, the yearly simulation of the mine progress results in the simulation of the sharp and elevated groundwater inflow rates at the start of mining. The groundwater inflow rates, then show a decreasing trend. Based on the simulated maximum inflow rates, the groundwater inflow to the pit ranges between 25 L/s to 285 L/s, whereas these values reduce to 11 L/s to 154 L/s when the inflow rates simulated at the end of each year (i.e. minimum groundwater inflow rates) is considered. The more refined mine progress will result in a more smooth change in the simulated groundwater inflow rates.

The groundwater inflow rate into the open pit is also influenced by the Kirmir 2 and Karataş faults, which bound the pit from north and south, respectively. Since their hydraulic conductivities are not tested, the groundwater inflow rates are recalculated by 10 times higher and lower conductivity values in order to eliminate the uncertainty

a little. Based on the results, the average groundwater inflow rate of 79 L/s is changed to 69 L/s and 114 L/s, whereas the maximum groundwater inflow rate of 285 L/s is modified to 185 L/s and 690 L/s.

It should be noted that the calculated rates are only the groundwater component of the inflow coming to the pit. The direct precipitation and surface runoff from pit walls are not included. While designing dewatering system, 24-hour 100-year rainfall events and surface runoff components should be taken into consideration. Besides, since the aquifer to be dewatered has low hydraulic conductivity, it drains slowly. Hence, the dewatering time may take longer than expected.

Based on the mine plans, the pit is backfilled starting from the southeast boundary, except for the area excavated lastly. When the mining activities cease, the groundwater levels will start to rise, and can create a pit lake if the area is not backfilled. The formation of pit lake is not within the scope of this study, hence no evaluations will be made here.

## **9.2. Longwall Simulations**

The longwall mining method is selected to extract the upper seam in the study area. Based on the prefeasibility studies, the upper seam only mine plans involve 19 longwalls, which are oriented in northeast-southwest direction. The longwalls are generally 200 m wide, whereas their lengths range between 1 and 3.6 km. Although one of the scopes of the thesis is to determine groundwater inflow rates to the panels, the simulations can be done on one selected panel. The one-year simulation of longwall panel lasts at least 72 hours for a laptop computer having Intel® Core™ i7-6700HQ CPU @2.60GHz with 16 GB RAM. Hence, between the simulations, there is a wide gap to control the impact of any change to the system and also to design the next move. In addition to the hardware constraints, the nature of the longwall mine impact on groundwater system still remains uncertain. There are a few studies describing the change of the hydraulic properties as a result of longwall mining, but either all evaluates the system conceptually or documents the results of observations before and after longwall mining. Hence, the changes in the system are known in

theory but to what extent these changes impact the system is not very clear. For instance, it is known that from the observations worldwide, the post to pre-mining hydraulic conductivity of the collapsed zone is more than 40 as a result of longwall mining. Some of the unknowns on the other hand are (i) the timing of the changes (i.e. when the shearer move forward and let the overlying strata collapse, do the change in the system start immediately or the hydraulic conductivity change starts sometime after?), (ii) the change in the conductivity values (i.e. do the conductivity values immediately increase 40 times as the strata collapsed or a gradual change in the system is expected? If the gradual change occurs, how does the conductivity values change?), (iii) the vertical propagation of the fractures due to longwall mining (i.e. should the vertical resolution of the system be in orders of meters or tens of meters, etc.?), etc. With all these and many more questions in mind, this study shows a preliminary approach to simulate the impacts of longwall mining on the groundwater system. In that sense, this is a novel study.

In the simulations, the longwall mining at the selected panel starts at day 3600. The duration before activation of the panel is required to let the system stabilize under transient conditions. When the longwall simulations start at day 1, the calculated groundwater inflow rates reach astronomically high values (more than 40000 L/s). Hence, before applying any change to the system, the model is run under transient conditions for about 10 years. The selection of 10 year period is chosen arbitrarily.

In the finite element method, the selection of element size also plays a significant role in model results. The finer the mesh, the more realistic results one will get. However, the mesh refinement will also increase the simulation time. The impact of element size on the simulation results are also evaluated. When the element sizes reduce from 30-50 m to 10 m in the area covering the pit and underground panels, the simulated inflow rates are reduced about 10000 L/s, which is very dramatic. Hence, throughout the simulations, finer mesh design is used. The more refinement of the mesh results in enormous number of nodes and elements, which can not be handled with the specified computer.

The mine progress at the selected panel is simulated by dividing the panel into 12 regions, each representing the monthly mined area. Indeed, the actual mine advance in the longwall method occurs when the hydraulic roof supports move forward, which may be about 1 – 2 m. However, due to the mesh design, the actual mine progress cannot be simulated. In order to approach the actual conditions, the panel is divided into 36 regions, where the monthly mined area is simulated by 3 regions. The results of panel refinement are given in Simulation No. 1 and Simulation No. 2, whereas the comparison of the simulated groundwater inflow rates is provided in Figure 8.16. Although the maximum inflow rates decreased significantly, the rates obtained at the end of simulation of each month remained the same. The finer progress of the panel results in more smooth changes in the inflow rates.

The studies indicate that post-mining hydraulic conductivity of the goaf is increased tremendously, which is described by infinity. The infinitely high post-mining hydraulic conductivity is quantified in this study by 100 times higher horizontal and 1000 times higher vertical conductivity values. The transition from pre-mining to post-mining conditions is evaluated in two different approaches, explained in Simulation No. 3 (sudden change in the conductivity values) and Simulation No. 4 (gradually increased conductivity values). The calculated average inflow rates are close to each other, around 300 L/s, whereas the maximum inflow rates decreased about 60 % when gradual change is applied. The comparison of simulated inflow rates (Figure 8.22) reveals that although peak rates show dramatic decrease, at the end of simulation of each region, the obtained rates are similar.

Due to the longwall mining, the conductivity field not only changed in the goaf but also modified in the goaf and collapsed zones. The height of the collapsed zone is calculated as 280 m from the empirical equation developed by Tammeta, which corresponds to Layers 10 – 6 in the model. The studies indicate that post to pre-mining hydraulic conductivity ratio in the collapsed zone is more than 40. With the light of this information, the hydraulic conductivity of the layers increased 50 times in the simulations. The 50 times increase is applied gradually for all layers in Simulation No.

5, which results in abnormal oscillations at the calculated inflow rates, indicating that the model results are not stable, and hence are not reliable. Therefore, due to the collapse of the strata, the change in the hydraulic conductivity is simulated in such a way that, maximum change (i.e. 50 times) is applied to Layer 10, and increase in hydraulic conductivity is assigned in a decreasing manner till Layer 6. With this smoothing in the assigned parameters, the simulated inflow rates show more reliable results. The fluctuations in the groundwater inflow rates are minimum at the beginning of the simulation, whereas they increased significantly as the area of increased conductivity is spreading. The maximum inflow rate is increased to 650 L/s whereas the average value is determined as 363 L/s.

When the simulation results are evaluated together, it is seen that the change in the applied parameters results in a change in the maximum inflow rates, whereas the average rates are close to each other. Since the sudden increase in groundwater inflow rates occurs in a short span of time, the average rates are not influenced much. On the other hand, the impacts of longwall mining on water table profiles and also calculated drawdown values show great differences when the complexity of the system is increased. The simulation of increase in hydraulic conductivity in the goaf and collapsed zone creates a huge unsaturated zone above the mined seam, whereas simulation of the hydraulic conductivity in the goaf results in formation of a small unsaturated zone, limited to Layer 11. The drawdown values show similar trends at Layer 11 (i.e. goaf) with expansion of the areas as the complexity increases. As moving upward from goaf to the top of the collapsed zone, a significant change in the calculated drawdown contours observed at Simulation No. 6, where the maximum drawdown value is still about 100 m at Layer 6. The simulations show that the upper aquifer is not much influenced by longwall mining due to the presence of a thick collapsed zone. It should be noted that the simulations conducted here are results of a single panel mining. When the whole panels are mined via longwall mining, the impacts and groundwater inflow rates may be far different. Hence, the results

presented in this study aim to give a perspective about longwall mine simulations and their impact on groundwater resources.

## CHAPTER 10

### CONCLUSIONS AND RECOMMENDATIONS

This study aims to determine the dewatering/depressurization requirements by predicting the groundwater inflow rates of the open pit and longwall panels based on the mine advance and also to assess the anticipated impacts of dewatering/depressurization on the groundwater resources. In order to achieve these purposes, the meteorological, geological, hydrological and hydrogeological data were compiled and analyzed. Following the data collection, the conceptual model of the area was developed. In order to simulate the dewatering requirements and assess corresponding impacts, a 3D numerical groundwater flow model was set up by using the FEFLOW software. The model is calibrated with an RMSE of 16.09 m and NRMSE of 4.56 %, indicating that the model was capable of simulating actual field conditions. The calibrated model, then, was used as a base model for simulations of open pit and longwall panel dewatering.

The following conclusions are made from this study:

- Based on the yearly mine progress the average groundwater inflow rate to the open pit is calculated as 79 L/s. The maximum inflow value is determined as 285 L/s, which is observed at the lastly excavated area, where the deepest pit bottom is achieved. In the simulations the effects of direct rainfall and surface water flow from the benches are not considered.
- The open pit is bounded by the Kirmir 2 and Karataş faults at the north and south, respectively. The uncertainty at the hydraulic conductivity of these faults also affects the groundwater inflow rates. In order to evaluate their impacts on the groundwater inflow rates, simulations are repeated when the hydraulic conductivity of the faults are increased and decreased 10 times. The

simulation results indicate that the amount of groundwater that should be pumped out from the system ranges between 69 L/s and 114 L/s based on the assigned conductivity value of the fault zones.

- The impacts of 11 years of mining at the open pit are evaluated according to the timewise change of the baseflow component of the Kirmir stream and areal distribution of cone of depression. The results indicate that the baseflow rate of the Kirmir stream is decreased by 10 % as a result of open pit mining. On the other hand, due to the mining, the maximum drawdown is calculated as 161 m at the northwestern corner of the pit, which reduces to 50 m at a distance of 1 km. The areal extent of the cone of depression is mainly influenced by the fault zones. The simulation results reveal that the springs that supply water to the Değirmenönü, Çavuşlar and Peyikler villages as well as 29 monitored springs and fountains will dry up due to open pit mining. The total average groundwater discharge rate from these springs is determined as 7 L/s, excluding discharge rates of village water supply springs.
- The dewatering requirements and impact assessment of the longwall panel are simulated along a representative panel which is located in the middle part of the longwall mining area, where one year of mining is planned. The panel is 2 km in length and 200 m in width, where the thickness of upper seam is 4 m. Above the panel, the average overburden thickness is calculated as 504 m.
- The dewatering requirements at the selected panel is first determined under steady state conditions, where the groundwater inflow rate is calculated as 230 L/s. As a result of steady state dewatering, an unsaturated zone is formed around the coal seam, whereas the water table profile of the upper aquifer is conserved.
- The transient simulations of longwall mining are handled in 6 different simulations, where the complexity of the system is increased progressively. The impact of longwall mining on groundwater resources is evaluated under

three main phases. In phase 1, the mine progress is evaluated, where the selected panel is divided into 12 and 36 regions, in simulations No. 1 and No. 2, respectively. In the second phase the impact of the hydraulic conductivity change in the goaf area is investigated in detail in Simulations No. 3 and No. 4. In the final phase, the change in the hydraulic conductivity of both goaf and the layers comprising the collapsed zone is assessed in simulations No. 5 and 6. The calculated maximum and average groundwater inflow rates are summarized in Table 10.1.

Table 10.1. *Summary of calculated groundwater inflow rates for longwall simulations*

Simulation	Change in the system		Simulated Groundwater Inflow Rate	
			Maximum (L/s)	Average (L/s)
No. 1	Mine Progress	12 regions	755	375
No. 2		36 regions	406	261
No. 3	Hydraulic Conductivity of the Goaf	Sudden increase	819	321
No. 4		Gradual increase	525	266
No. 5	Hydraulic Conductivity of the Goaf & Collapsed Zone	K increased 50 times at Layers 10 - 6	1200	444
No. 6		K increased gradually from Layer 10 - 6	650	363

- The impacts of longwall mine simulations are determined in terms of (i) simulated water table profile at the end of mining, (ii) the areal distribution of the cone of depression and also (iii) the timewise change of simulated hydraulic head values at the monitoring wells in the vicinity of the panel. The results indicate that due to longwall mining, the water table profile of the upper aquifer is maintained, whereas an unsaturated zone is formed around the coal seam. As the complexity in the system increases, the expansion of the unsaturated zone increases. The maximum drawdown as a result of dewatering

is observed at Layer 11, where maximum deformation is expected. The drawdown values then decrease from Layer 10 to Layer 6. The calculated hydraulic head values at the monitoring wells indicate that the maximum decline in the levels is observed at the wells located at the close vicinity of the panel. The change in hydraulic head values at the wells screened in the upper aquifer reveals that longwall mining has no significant influence on the upper aquifer.

- This study intends to show the impact of variations of the hydraulic properties of the overlying strata as a result of longwall mining, and the complexity of modeling such a system, rather than presenting actual longwall mine dewatering results.

The following recommendations are made from this study:

- The layering in the model is based on the lithological units outcropping in the area. The point data corresponding the top and bottom elevations of each unit are interpolated to obtain areal distribution of the units. In order to reflect the pinch out nature of the coal seams, a 3D geological model of the study area can be used.
- The major uncertainty in the study arises from hydraulic conductivity of the faults. The sensitivity analysis and simulation results reveal that the dewatering requirements of the area is closely related to the permeability of these zones. Hence, further studies should be done to obtain hydraulic conductivities of the faults.
- Within the study area, there is a thermal water well drilled by MTA in 2015. Based on the information obtained from MTA, this well is completed at 1500 m depth and the measured temperatures were about 70 °C. However, the existing studies related to the thermal potential of the study area is very limited. Hence, with the light of more information, thermal potential of the area should also be considered in the future studies.

- The pit lake formation and its impacts on groundwater resources should also be investigated at the areas where backfill is not applied.
- The change in the system due to longwall mining is mainly influenced by the fracture system, which is developed as a result of strata collapse. Coupling the groundwater model with the fracture model will result in more comprehensive evaluation of the actual response of the system.



## REFERENCES

- Adams R., and Younger P. L. 2001. A Strategy for Modeling Ground Water Rebound in Abandoned Deep Mine Systems. *Groundwater*, 39:2, 249–261.
- Anderson, M. P., Woessner, W. W., and Hunt, R. J. 2015. *Applied Groundwater Modeling, Simulation of Flow and Advective Transport*, Elsevier Academic Press, UK, 564 p.
- Ardejani F. D., Singh R. N., Baafi E., and Porter I. 2003. A finite Element Model to: 1. Predict Groundwater Inflow to Surface Mining Excavations. *Mine Water and the Environment*, 22:1, 31–38.
- Aryafar A., Ardejani F. D., Singh R. N. 2009. Numerical Modeling of Groundwater Inflow from a Confined Aquifer into Sangan Open Pit Mine, Northeast Iran. *Geomechanics and Geoengineering International Journal*, 4:3, 189–199.
- Asia Minor Mining (AMM), 2015. *Geology of the Çeltikçi Project Area*, 55 p.
- Bell, F. G. and Genske, D. D. 2001. The influence of subsidence attributable to coal mining on the environment, development, and restoration: some examples from western Europe and South Africa. *Environmental and Engineering Geoscience*, 7:1, 81-99.
- Bochenska T., Fiszer J., and Kalisz M. 2000. Prediction of Groundwater Inflow into Copper Mines of Lubin Glogow Copper District. *Environmental Geology* 39:6, 587–594.
- Booth C. J., 1986. Strata-Movement Concepts and the Hydrogeological Impact of Underground Coal Mining. *Groundwater*, 24:4, 507-515.

- Booth, C. J., Spande, E. D., Pattee, C. T., Miller, J. D., and Bertsch, L. P. 1998. Positive and Negative Impacts of Longwall Mine Subsidence on a Sandstone Aquifer. *Environmental Geology*, 34:2/3, 223-233.
- Booth, C. J. and Spande, E. D. 1992. Potentiometric and aquifer property changes above subsiding longwall mine panels, Illinois Basin Coalfield. *Groundwater*, 30:3, 362-368.
- Booth, C. J., 2006. Groundwater as an environmental constraint of longwall coal mining. *Environmental Geology*, 49:6, 796-803.
- Booth, C. J. 2007. Confined-Unconfined Changes above Longwall Coal Mining Due to Increases in Fracture Porosity. *Environmental and Engineering Geosciences*, 13:4, 355-367.
- Brouyere S., Orban P. H., Wildemeersch S., Couturier J., Gardin N., Dassargues A. 2009. The Hybrid Finite Element Mixing Cell Method: a New Flexible Method for Modeling Mine Groundwater Problems. *Mine Water and the Environment*, 28:2, 102–114.
- Brunetti, E., Jones, J. P., Petitta, M., Rudolph, D. L. 2013. Assessing the impact of large scale dewatering on fault controlled aquifer systems: a case study in the Acque Albue basin (Tivoli, central Italy). *Hydrogeology Journal*, 21:2, 40-423.
- Castendyk, D. N., and Eary, T. (eds) 2009. *Mine pit lakes: characteristics, predictive modeling, and sustainability*. Society for Mining, Metallurgy and Exploration (SME), Littleton, CO, USA.
- Connelly R. J., Gibson J. 1985. Dewatering of the Open Pits at Letlhakane and Orapa Diamond Mines, Botswana. *International Journal of Mine Water* 4:3, 25–41.
- DHI-WASY, 2015, FEFLOW (Finite Element subsurface FLOW simulation system) v7.

Dowling, J., Atkin S., Beale G. and Alexander G. (2004), Development of the Sleeper Pit Lake. *Mine Water and the Environment* 23, 2-11.

Ekmekci, M. and Yazicigil, H. 2016. Progressive Sinkhole Occurrence Induced by Dewatering Activities in a Large Lignite Mine (SE Turkey). In *Proceedings IMWA 2016 : Mining Meets Water – Conflicts and Solutions*, 486-493.

Elsworth, D. and Liu, J. 1995. Topographic influence of longwall mining on groundwater supplies. *Groundwater*, 33:5, 786-793.

Esterhuize, G. S., and Karacan, C. O. 2005. Development of Numerical Models to Investigate Permeability Changes and Gas Emission Around Longwall Panel Mining. In *Proceedings of the 40<sup>th</sup> US Symposium on Rock Mechanics*, Anchorage, AK, June 25-29, Alexandria, VA, 1-13.

Fan, G. and Zhang, D. 2015. Mechanisms of aquifer protection in underground coal mining. *Mine water and the environment*, 34, 95-104.

Fernandez-Rubio R., Lorca D. F. 1993. Mine Water Drainage. *Mine Water and the Environment*, 12:1, 107–130.

Fontaine R. C., Davis A., Fennemore G. G. 2003. The Comprehensive Realistic Yearly Pit Transient Infilling Code (CRYPTIC): a Novel Pit Lake Analytical Solution. *Mine Water and the Environment*, 22:4, 87–193.

Garritty, P. 1983. Water Flow Into Undersea Mine Workings. *International Journal of Mining Engineering*, 1:3, 237-251.

Gammons, C. H., Harris, L.N., Castro J.M., Cott, P.A., and Hanna, B.W. (2009), Creating lakes from open pit mines: processes and considerations - with emphasis on northern environments. *Can. Tech. Rep. Fish. Aquat. Sci.* 2826: 106 p.

- Guo, H., Adhikary, D. P., and Craig, M. S. 2009. Simulation of mine water inflow and gas emission during longwall mining. *Rock Mechanics and Rock Engineering*, 42, 25-51.
- Hawkins, J. W., and Dunn, M. 2007. Hydrologic Characteristics of a 35-Year-Old Underground Mine Pool. *Mine Water and the Environment*, 26, 150-159.
- Huber, A.; Ivey, G. N.; Wake, G., Oldham, C. E. (2008), Near-surface wind induced mixing in mine lake. *Journal of Hydraulic Engineering* 134(1): 464-1,472.
- Hutcheson, S.M., Kipp, J. A., Dinger, J. S., Carey, D. I., Sendlein, L. V. A., and Secrist, G. A. 2000. Effects of Longwall Mining on Hydrogeology, Leslie County, Kentucky; part 2: During-mining conditions. Report of Investigations 6, Series XII. Lexington, Kentucky: Kentucky Geological Survey.
- Jankowski, J. and Spies, B. 2007. Impact of longwall mining on surface water – groundwater interaction and changes in chemical composition of creek water. Proceedings of the 35<sup>th</sup> IAH Congress: Groundwater and Ecosystems, Lisbon, Portugal, 17-21 September.
- Jankowski, J. and Madden, A. 2009. The design of hydrological and hydrogeological monitoring programs to assess the impact of longwall mining on water resources. IAH NSW, Groundwater in the Sydney Basin Symposium, Sydney, NSW, Australia, 4-5 August, 118-125.
- Jiang, S., Kong, X., Ye, H., Zhou, N. 2013. Groundwater dewatering optimization in the Shengli no. 1 open pit coal mine, Inner Mongolia, China. *Environmental Earth Sciences*, 69:1, 187-196.
- Jones, P.M. (2002), Characterization of ground-water flow between the Canisteo Mine Pit and surrounding aquifers, Mesabi Iron Range, Minnesota, U.S. Geological Survey Water Resources Investigations Report 02-4198.
- Kadnuck, L. L. M. 1995. Hydrologic Responses to Underground Coal Mining, Wasatch Plateau, Utah. *Environmental and Engineering Geoscience*, 1:1, 101-107.

- Karacan, C. Ö., and Goodman, G. 2009. Hydraulic conductivity changes and influencing factors in longwall overburden determined by slug tests in gob gas ventholes. *International journal of rock mechanics and mining sciences*, 46, 1162-1174.
- Kendorski, F. S. 1993. Effect of Full-Extraction Underground Mining on Ground and Surface Waters. In *Proceedings of 12<sup>th</sup> International Conference on Ground Control and Mining*, West Virginia University, Morgantown, West Virginia, 412-425
- Kendorski, F. S. 2006. Effect of Full-Extraction Underground Mining on Ground and Surface Waters a 25-yr Retrospective. In *25<sup>th</sup> International Conference on Ground Control in Mining*, West Virginia University, Morgantown, West Virginia.
- Kesseru, Z. 1982. Water barrier pillars. *Proceedings of the 1<sup>st</sup> International Mine Water Congress, IMWA, Budapest, Hungary*, vol. B, 91-117.
- Kibria, MD. G., Quamruzzaman, C., Ullah, A. S. M. W. and Kabir, A. K. M. F. 2012. Effect of longwall mining on groundwater for underground coal extraction in Barapukuria, Bangladesh. *Journal of Mines, Metals and Fuels*, 60-66.
- Marinelli F., Niccoli W. L. 2000. Simple Analytical Equations for Estimating Ground Water Inflow to a Mine. *Groundwater*, 38:2, 311–314.
- Matetic, R. J., Liu, J., and Elsworth, D. 1995. Modeling the effects of longwall mining on ground water system. US Department of the Interior, Report of Investigation 9561, 14 p.
- Meng, L., Feng, Q., and Li, Q. 2018. Coupled simulation – optimization model for draining confined aquifer via underground boreholes
- Miller, G. E., Lyons, W. B., Davis, A. (1996), Understanding the water quality of pit lakes. *Environmental Science and Technology* 30: 118A-123A.

- Morton K. L., Mekerck F. A. 1993. A Phased Approach to Mine Dewatering. *Mine Water and the Environment*, 12:1, 27–34.
- Müller, M., Eulitz, K. (2010), Characterizing Water Quality of Pit Lake through Modeling. – In: Wolkersdorfer, Ch. & Freund, A.: *Mine Water & Innovative Thinking*, 375 – 379; Sydney, Nova Scotia (CBU Press).
- Öngür, T., 1977, Kızılcahamam GB'sının volkanolojisi ve petroloji incelemesi, TJK Bülteni, 20, 1-12.
- Palaris 2015. Pre-feasibility Studies (PFS) of Çeltikçi Coal Basin, Asia Minor Mining Inc., Chapters 6 and 7, 102 p.
- Peksezer-Sayit, A., Cankara-Kadioglu, C., and Yazicigil, H. 2015. Assessment of Dewatering Requirements and their Anticipated Effects on Groundwater Resources: A Case Study from the Caldag Nickel Mine, Western Turkey. *Mine Water and the Environment*, 34:122-135.
- Pongpanya, P., Sasaoka, T., Shimada, H., Hamanaka, A., and Wahyudi, S. 2017. Numerical study on effect of longwall mining on stability of main roadway under weak ground conditions in Indonesia. *Journal of Geological Resource and Engineering*, 3, 93-104.
- Rapantova N., Grmela A., Vojtek D., Halir J., and Michalek B. 2007. Ground Water Flow Modeling Applications in Mining Hydrogeology. *Mine Water and the Environment*, 26:4, 264–270.
- Rojay, F. B. 2013. Structural evolution of Çeltikçi – Gümele Area during Post Miocene, METU Report, 38 p.
- Singh, R. N. 1986. Mine Inundations. *International Journal of Mine Water*, 5:2, 1-10.
- Singh R. N. and Atkins A. S. 1985. Analytical Techniques for the Estimation of Mine Water Inflow. *International Journal of Mining Engineering*, 3, 65–77.

Sing, M. M. and Kendorski, F. S. 1981. Strata disturbance predictions for mining beneath surface water and waste impoundments. In Proceedings of the 1<sup>st</sup> Annual Conference on Ground Control in Mining, West Virginia University, Morgantown, West Virginia, 76-89.

Soil Conservation Service (SCS), 1964. SCS National Engineering Handbook, Section 4: Hydrology, Updated 1972, U.S. Department of Agriculture, Washington D.C.

Tammeta, P. 2013. Estimation of Height of Complete Groundwater Drainage Above Mined Longwall Panels. *Groundwater*, 51:5, 723-734.

Tammeta, P. 2015. Estimation of the Change in Hydraulic Conductivity Above Mined Longwall Panels. *Groundwater*, 53:1, 122-129.

Tammeta, P. 2016. Estimation of the Change in Storage Capacity Above Mined Longwall Panels. *Groundwater*, 54:5, 646-655.

Thornthwaite CW (1968) An approach towards a rational classification of climate. *Geographical Review*, 38:1, 55-94.

Tokgoz, M., Yilmaz, K. K., Yazicigil, H. 2002. Optimal aquifer dewatering schemes for excavation of collector line. *Journal of Water Resources Planning and Management*, 128:4, 248-261.

Unsal, B. and Yazicigil, H. 2016. Assessment of Open Pit Dewatering Requirements and Pit Lake Formation for the Kışladağ Gold Mine, Uşak, Turkey. *Mine Water and the Environment*, 35, 180-198.

Vakili, A., Albrecht, J. and Gibson, W. 2010. Mine scale numerical modelling of longwall operations. 2010 Underground Coal Operators' Conference, 11-12 February, Australia, 115-124.

- Varli, D. and Yilmaz K. K. 2018. A Multi-Scale Approach for Improved Characterization of Surface Water – Groundwater Interactions: Integrating Thermal Remote Sensing and in-Stream Measurements, *Water*, 10, 853-854.
- Wang, J. A. and Park, H. D. 2003. Coal mining above a confined aquifer. *International Journal of Rock Mechanics and Mining Sciences*, 40, 537-551.
- Whittles, D. N., Lowndes, I. S., Kingman, S. W., Yates, C., and Jobling, S. 2006. Influence of Geotechnical Factors on Gas Flow Experienced in UK Longwall Coal Mine. *International Journal of Rock Mechanics and Mining Sciences*, 43, 369-387.
- Williamson S., Vogwill R. I. J. 2001. Dewatering in the Hot Groundwater Conditions at Lihir Gold. In *Proceedings IMWA Symposium, Belo Horizonte*, 1–15.
- Wu, Q., Liu, Y., Zhou, W., Li, B., Zhao, B., Liu, S., Sun, W. and Zeng, Y. 2015. Evaluation of Water Inrush Vulnerability from Aquifers Overlying Coal Seams in the Menkeqing Coal Mine, China. *Mine Water and the Environment*, 34:3, 258-269.
- Yazıcıgil, H., Çamur, M. Z., Süzen, M. L., Yılmaz, K. K., Kahraman, C., Peksezer Sayıt, A., 2014, Hydrogeological Characterization and Investigation of the Çeltikçi Coal Basin, Project No: 11-03-09-02-00-36, Middle East Technical University, Ankara, Unpublished Report (in Turkish).
- Yazıcıgil, H., Çamur, M. Z., Yılmaz, K. K., Peksezer Sayıt, A., Kahraman, C., 2015a, Development of Groundwater Flow Model, Design of Dewatering System and Assessment of Impacts on Groundwater Resources for Çeltikçi Coal Basin, Project No: 14-03-09-02-00-03, Middle East Technical University, Ankara, Unpublished Report (in Turkish).
- Yazıcıgil, H., Yılmaz, K. K., Peksezer Sayıt, A., Kahraman, C., 2015b, Water Supply Evaluation of Çeltikçi Coal Mine and Thermal Power Plant, Project No: 14-03-09-02-00-21, Middle East Technical University, Ankara, Unpublished Report (in Turkish).

Younger, P. L., and Adams, R. 1999. Predicting Mine Water Rebound. R&D Technical Report W179, Environmental Agency, Bristol, 109 p.

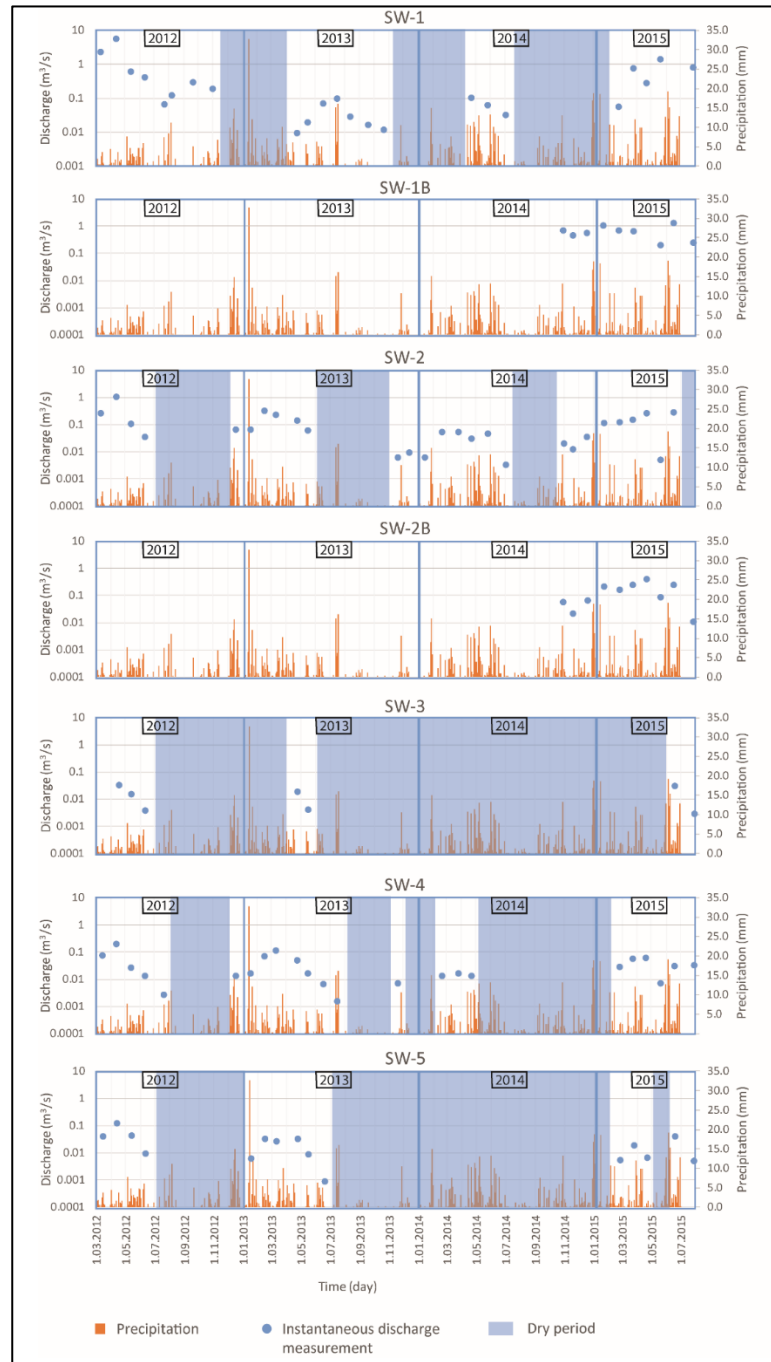
Younger, P. L., Banwart, S. A., and Hedin, R. S. 2002. Mine Water: Hydrology, Pollution, Remediation. Springer-Science+Business Media, B. V., 442 p.

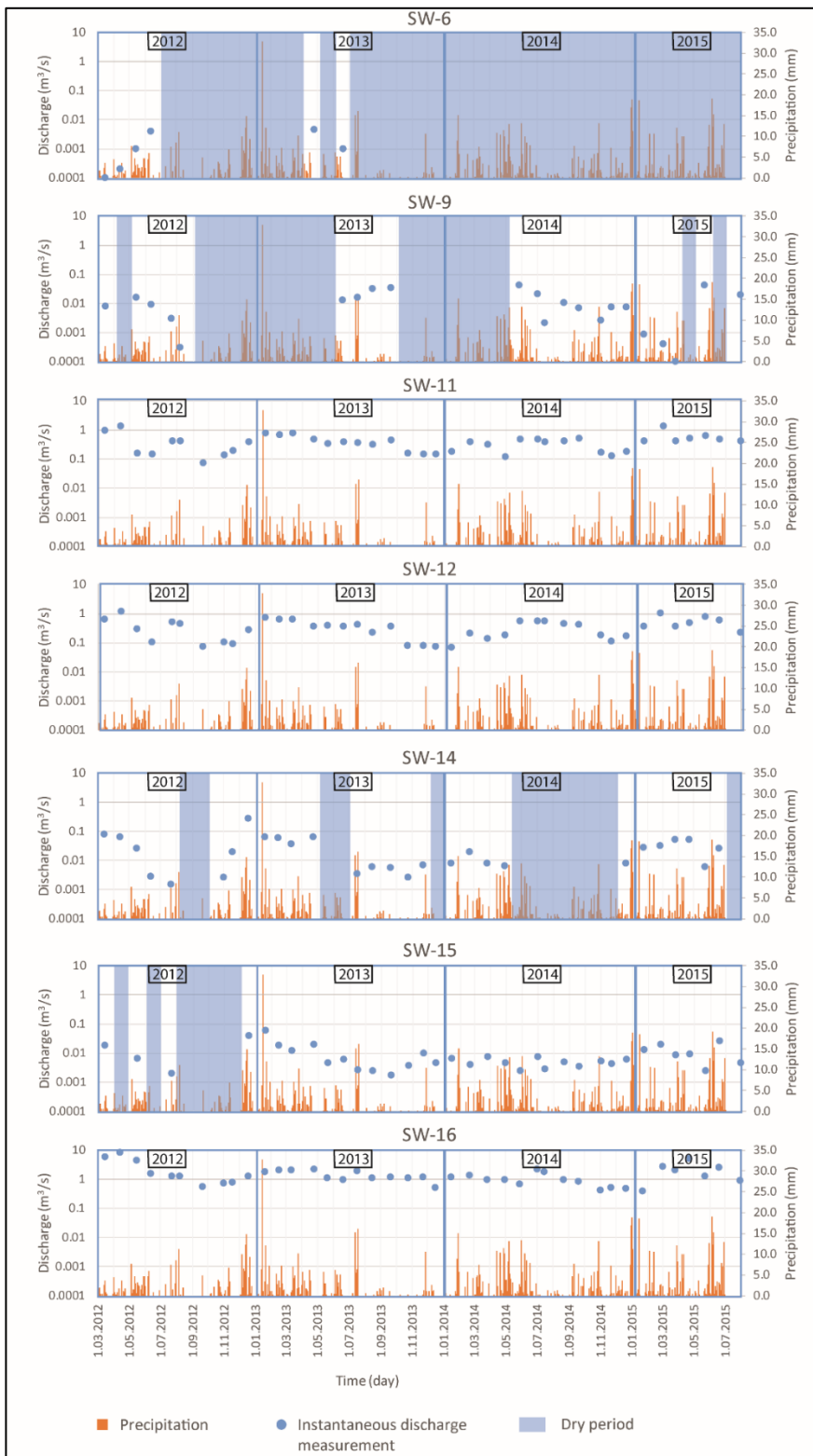
Zaidel J., Markham B., and Bleiker D. 2010. Simulating Seepage into Mine Shafts and Tunnels with MODFLOW. Groundwater, 48:3, 390–400.

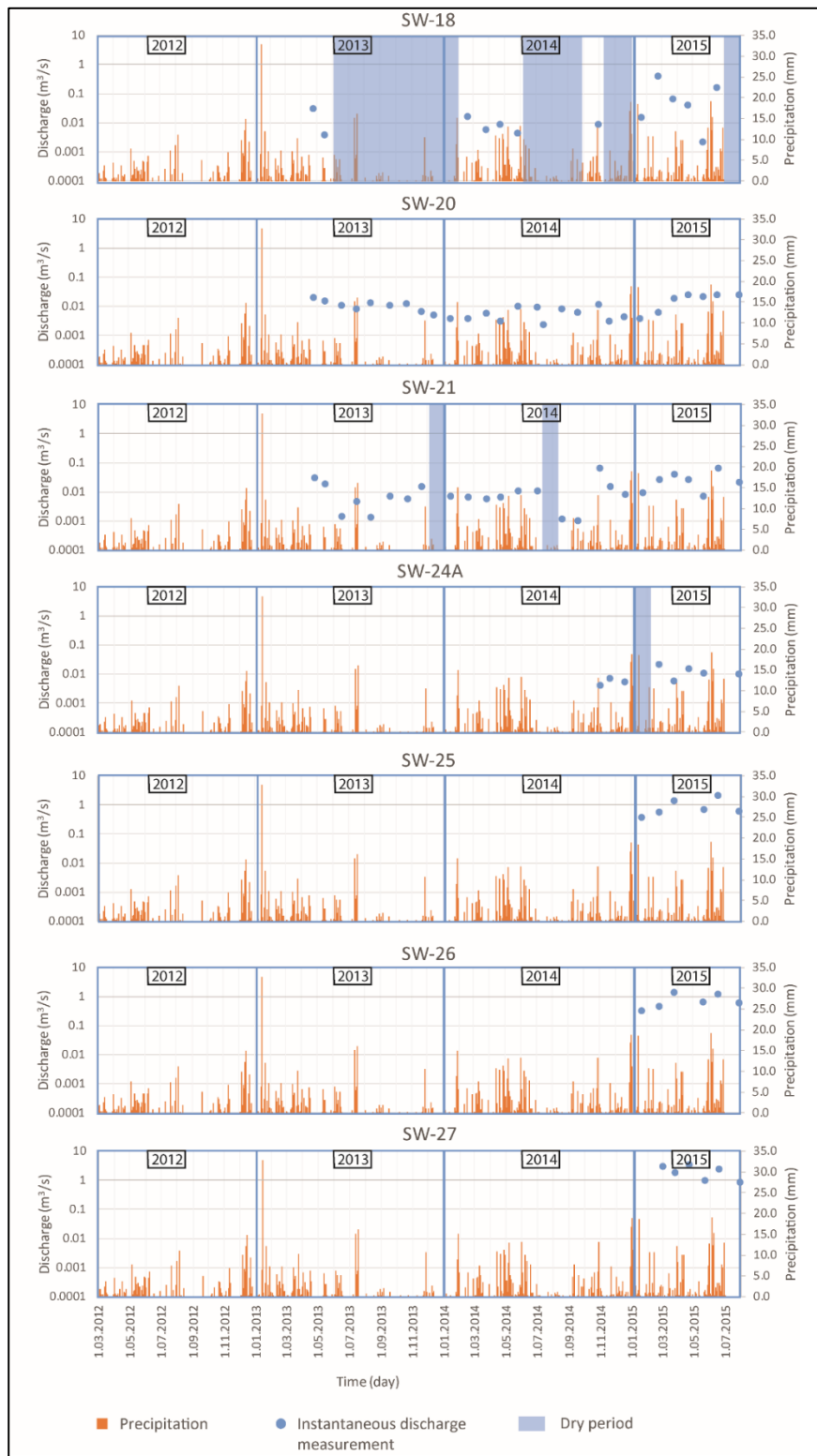


# APPENDICES

## A. Surface Water Flow Rates

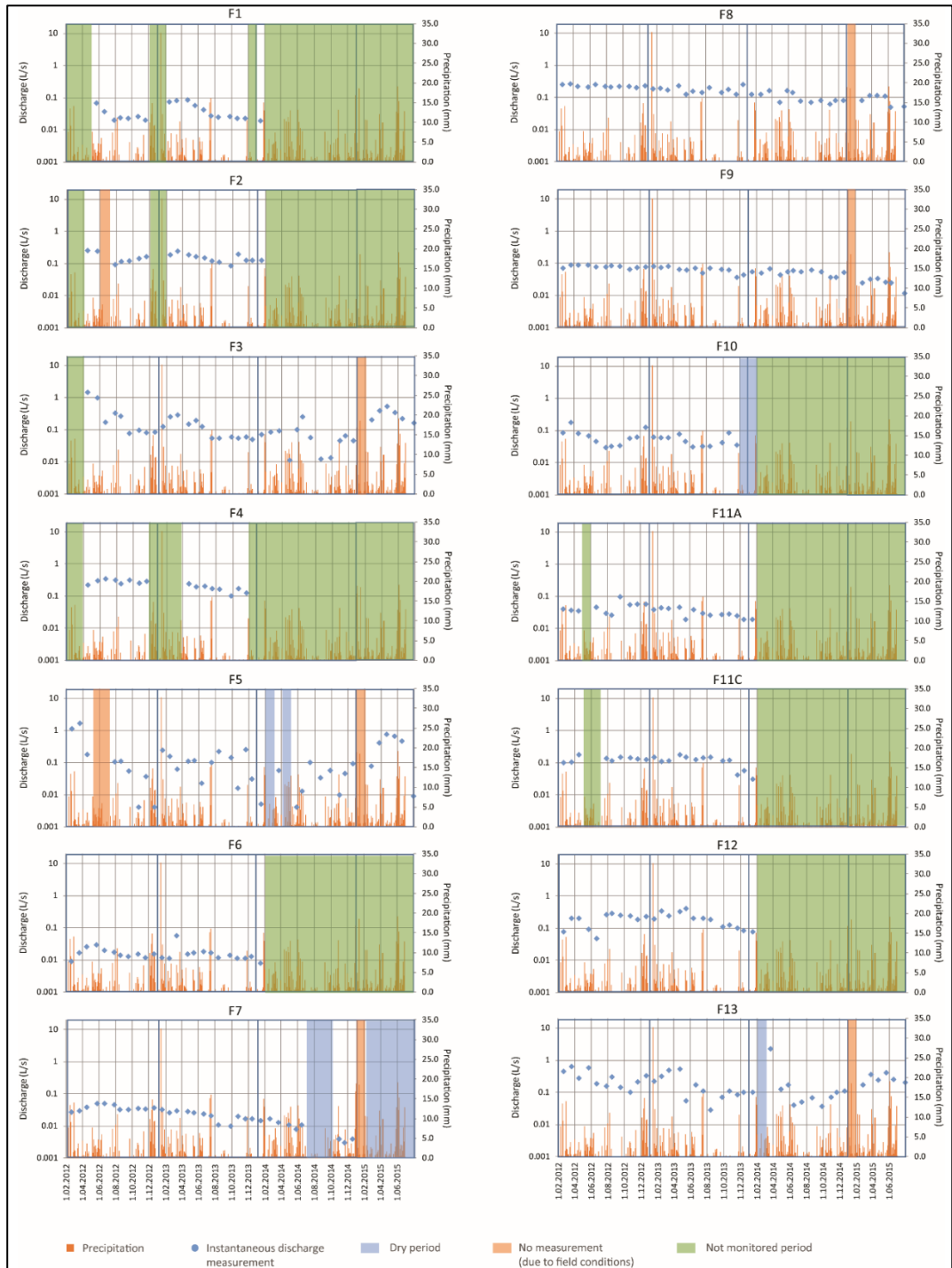


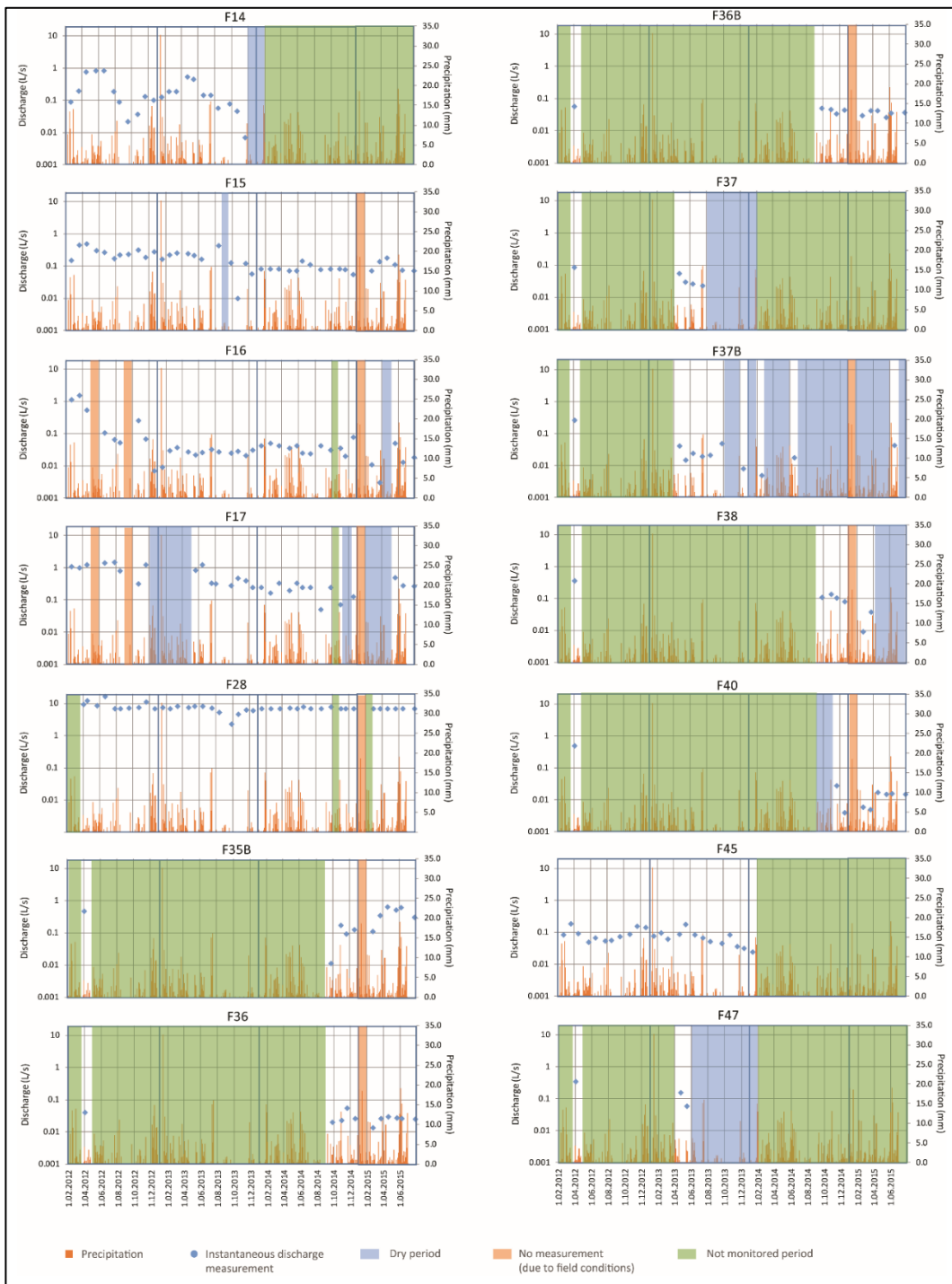


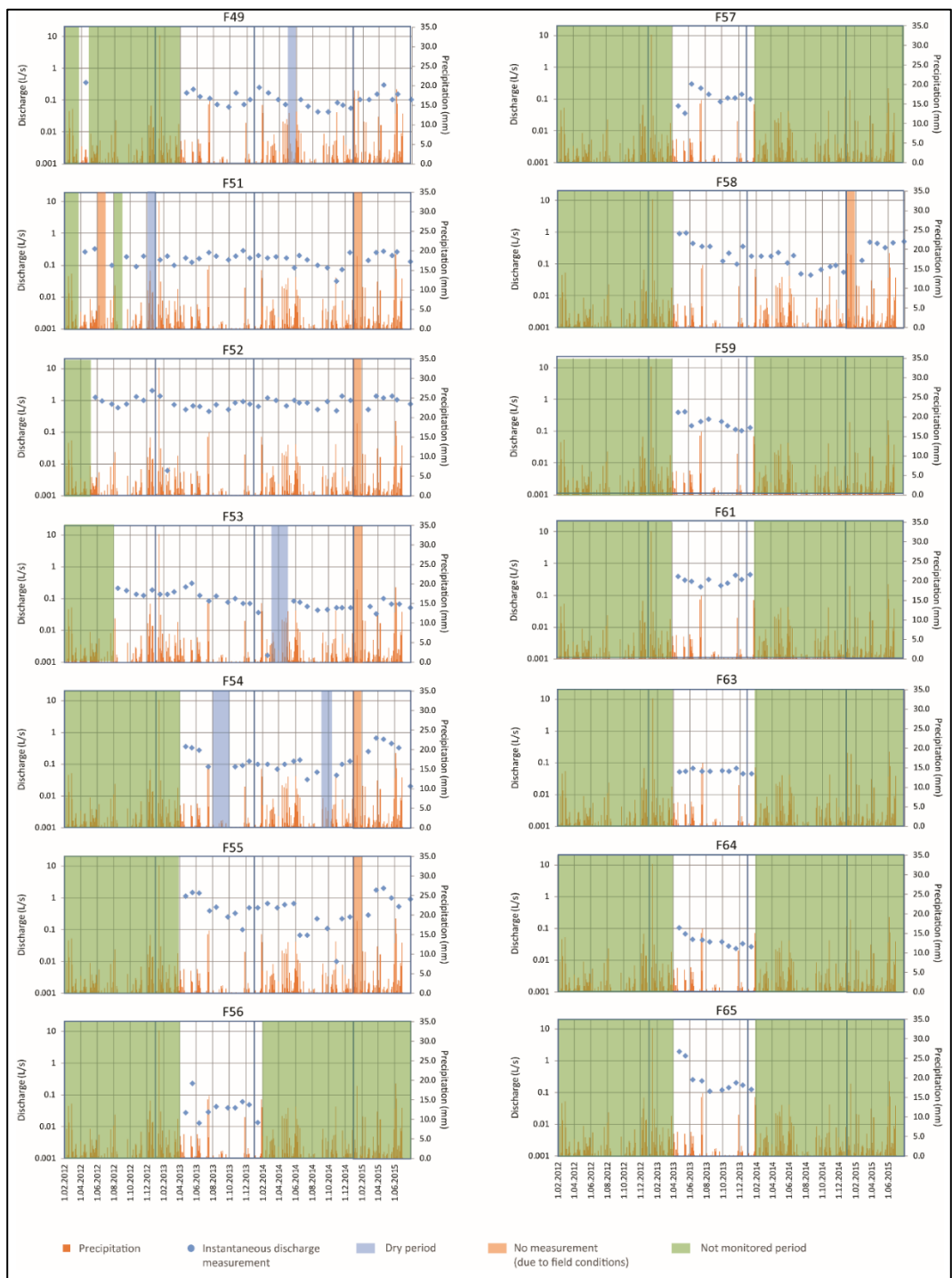


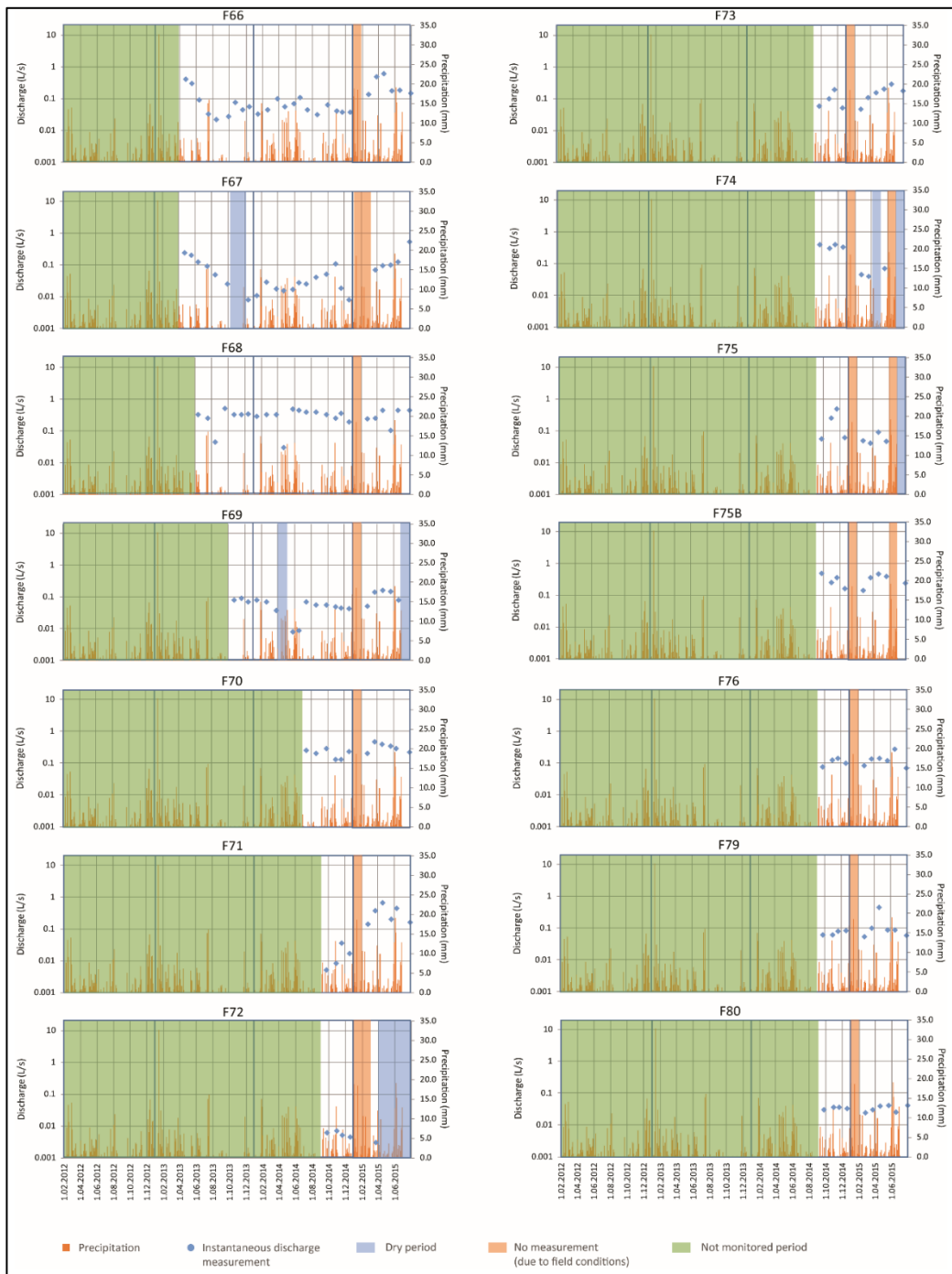


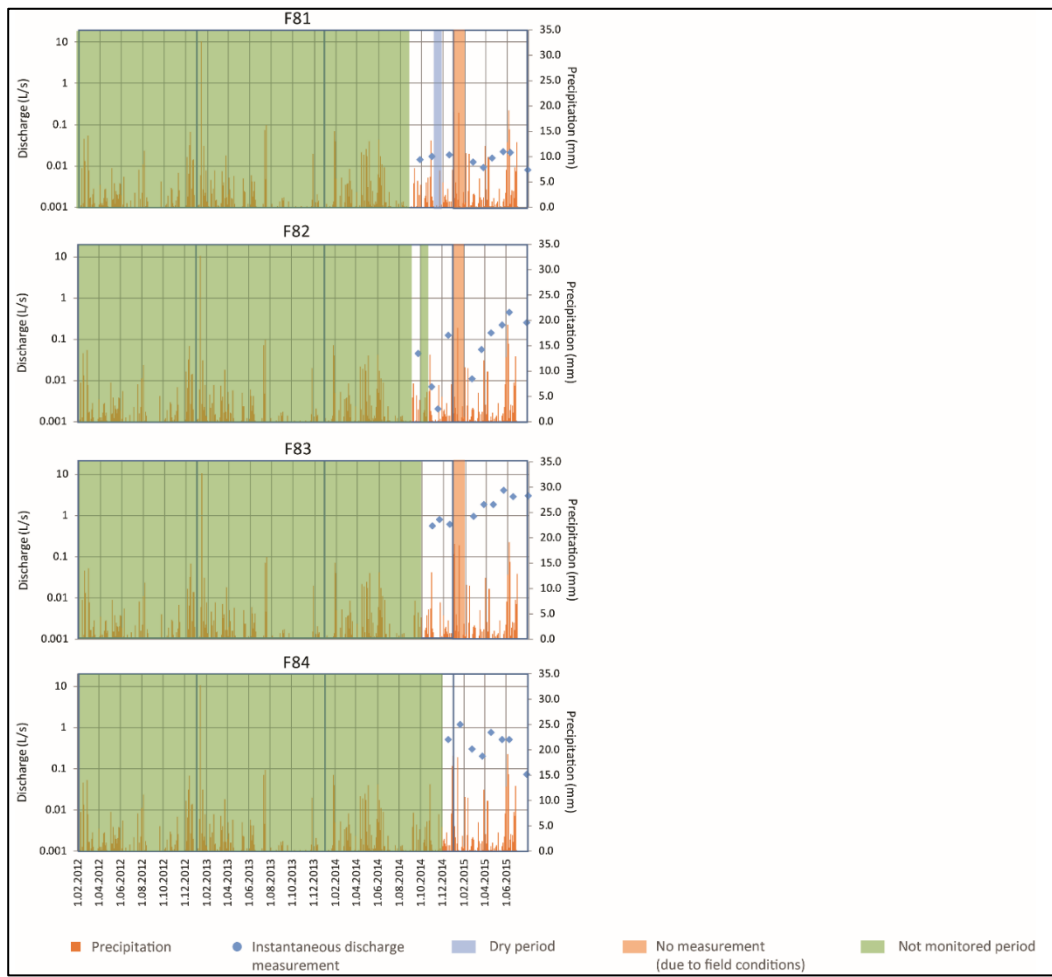
## B. Spring / Fountain Discharge Measurements





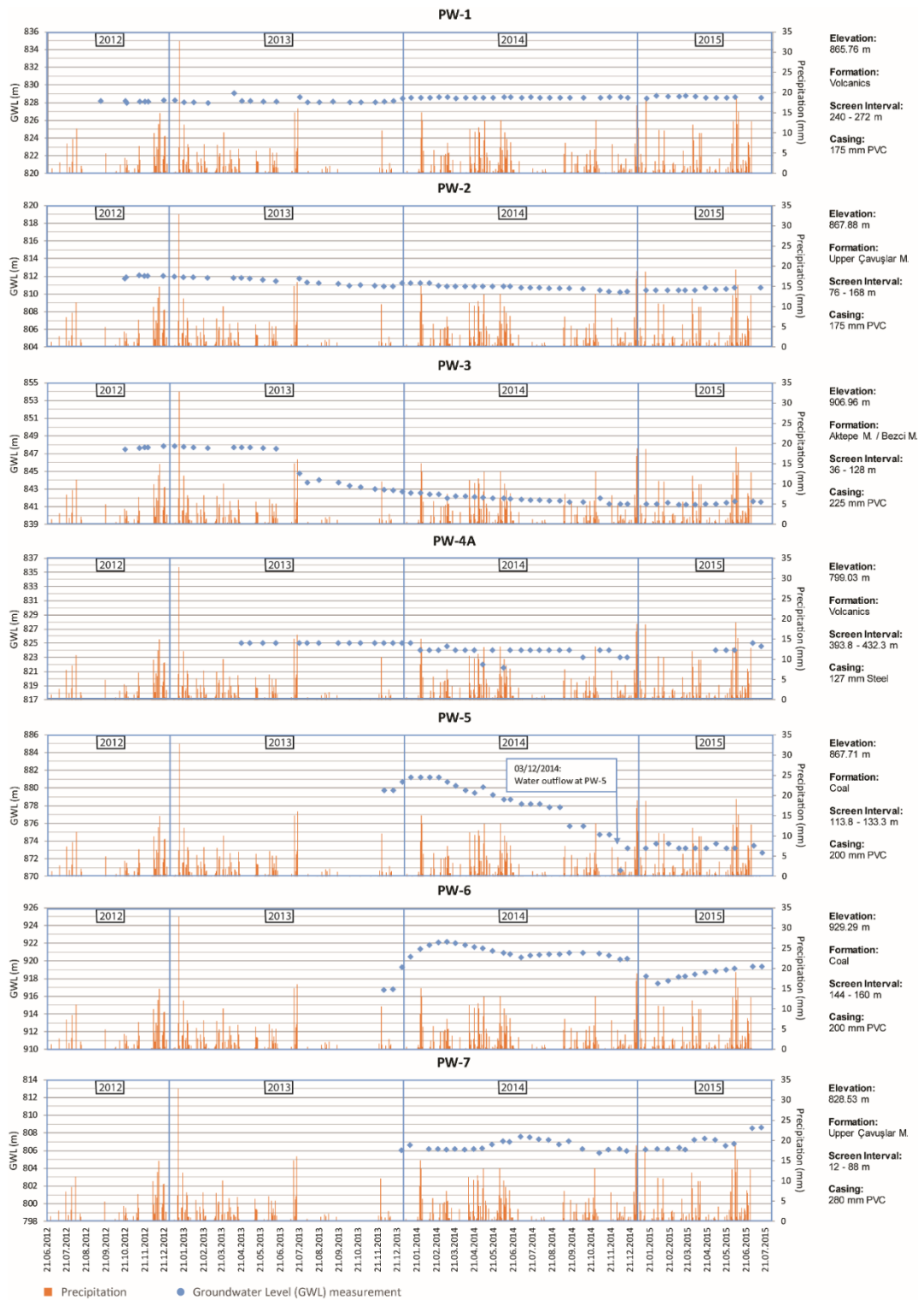


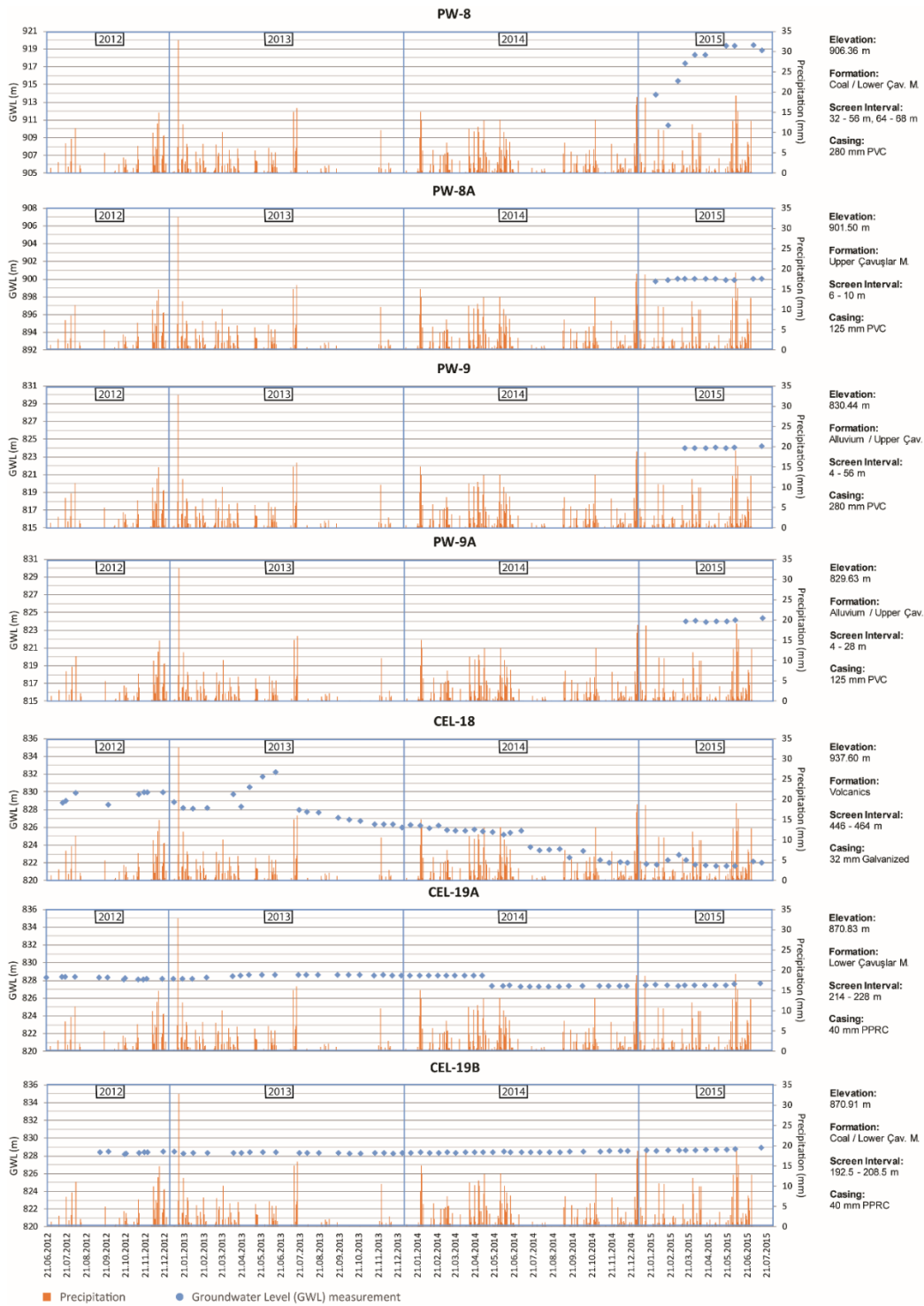


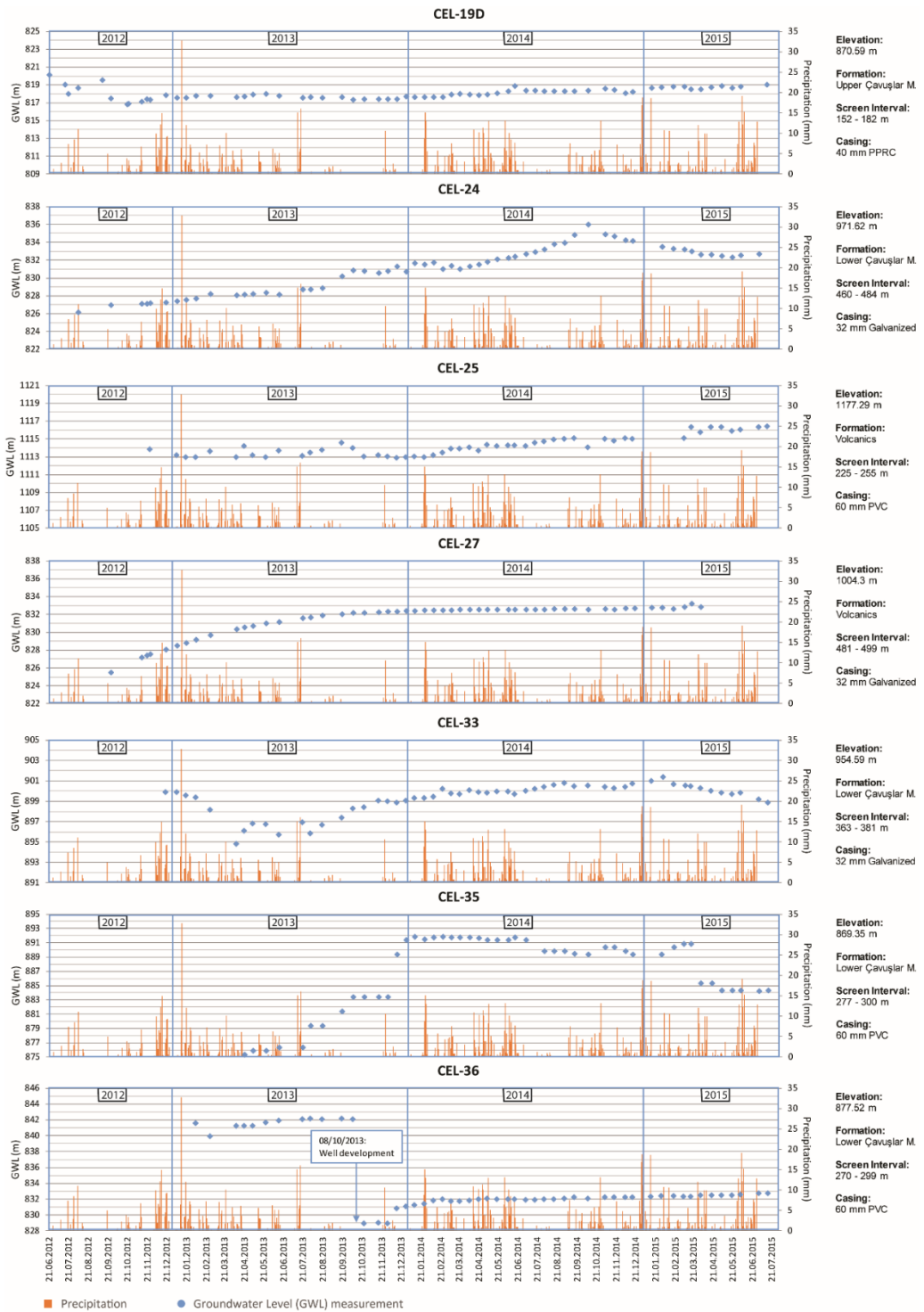


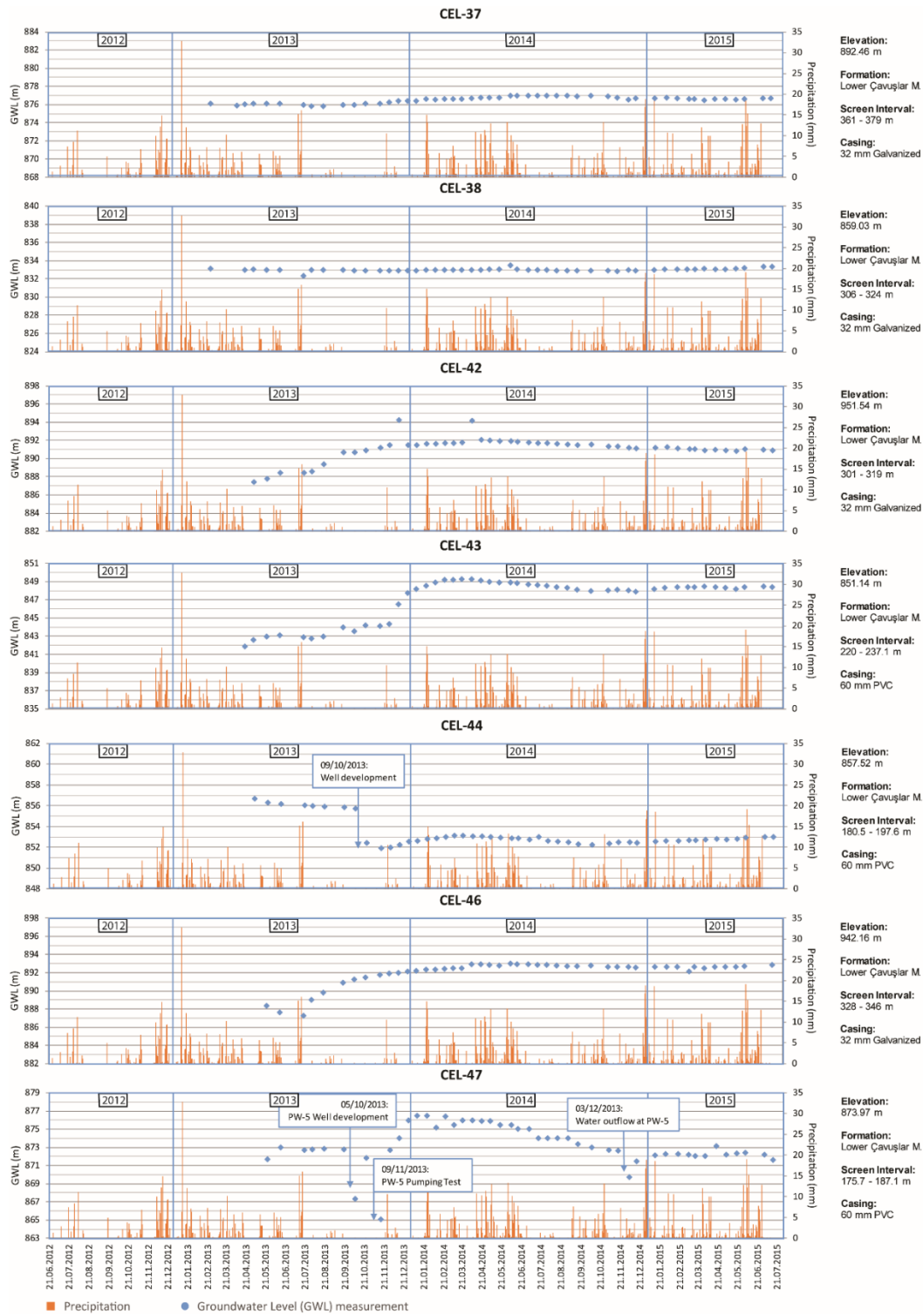


## C. Groundwater Level Measurements

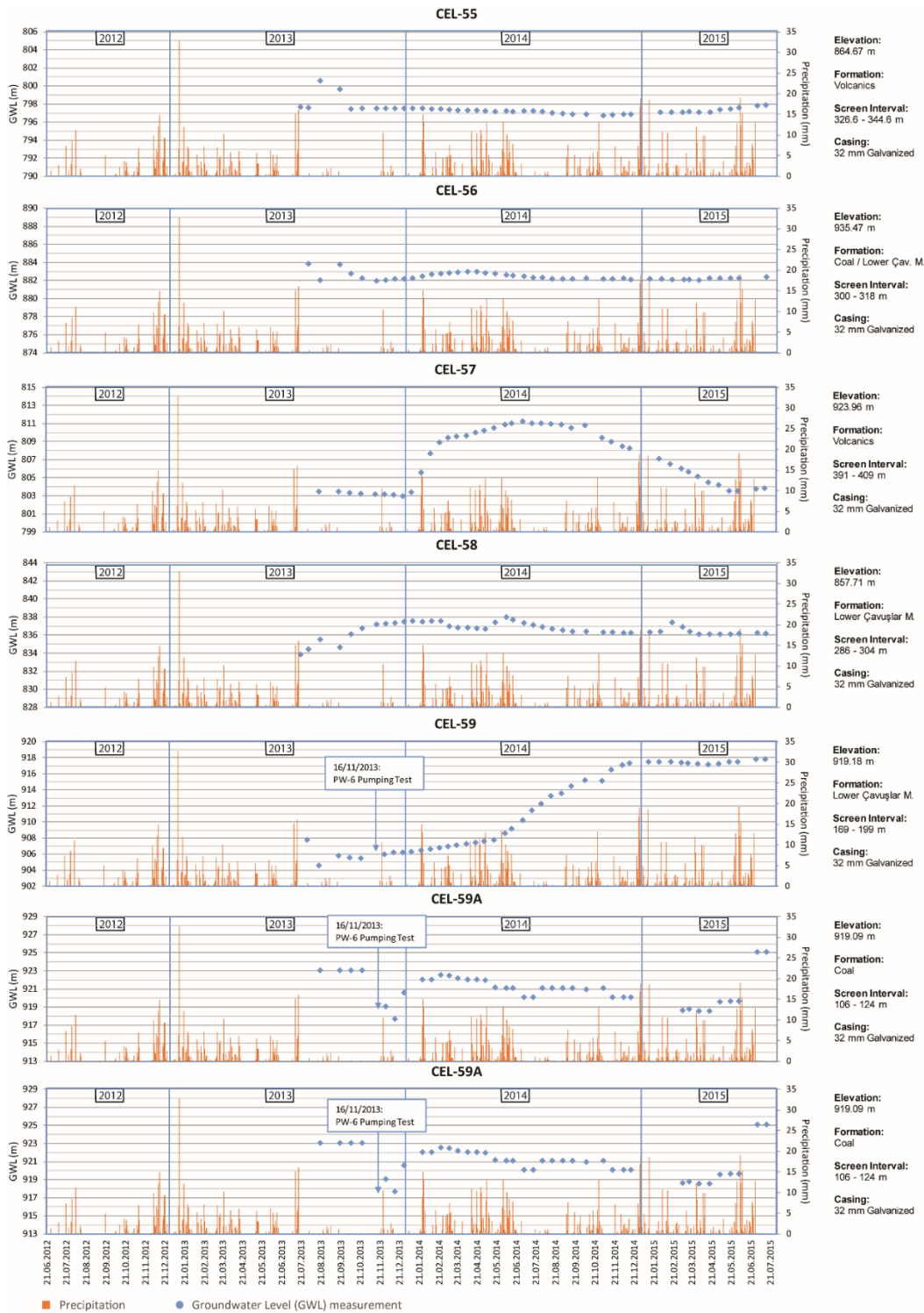


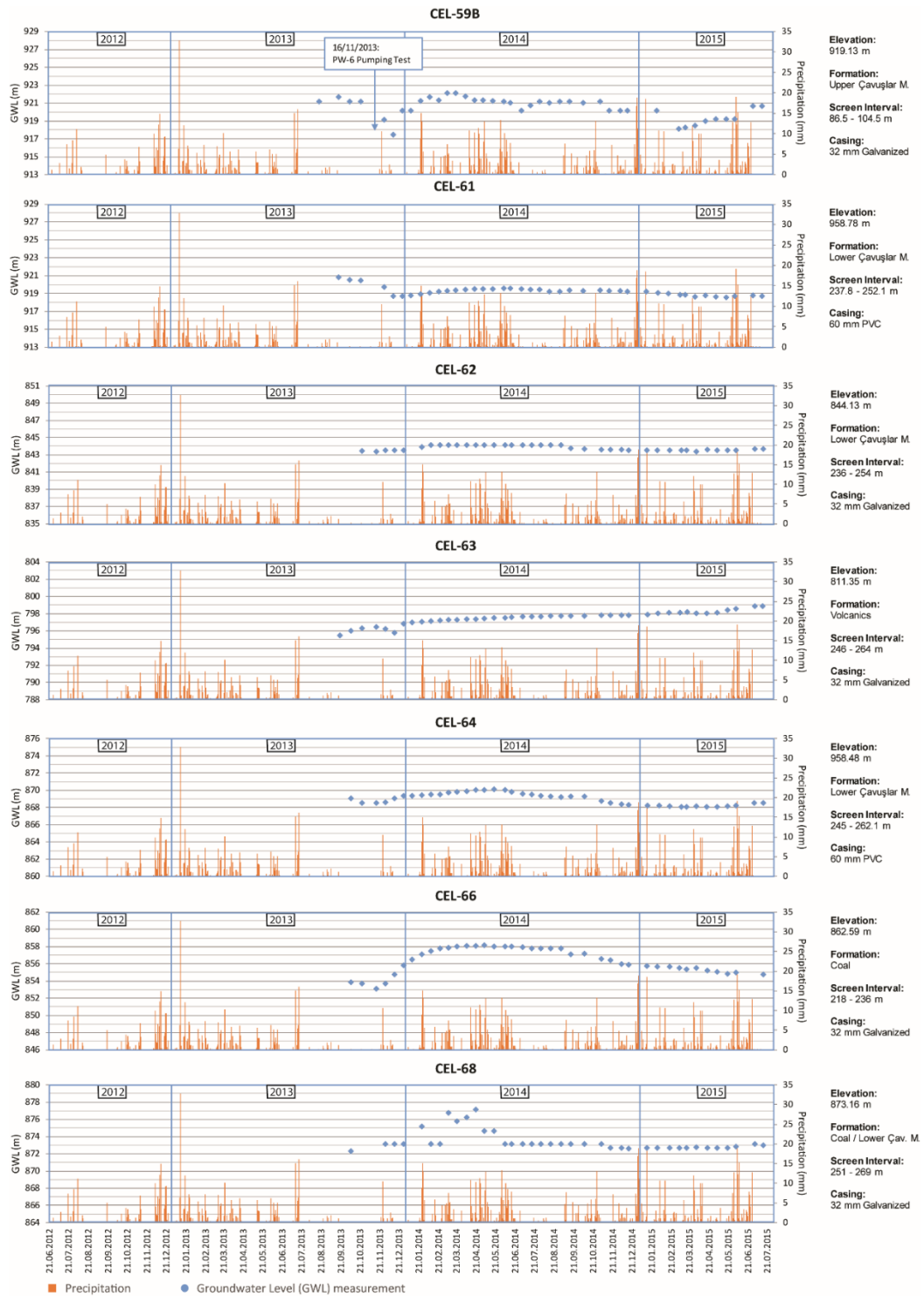


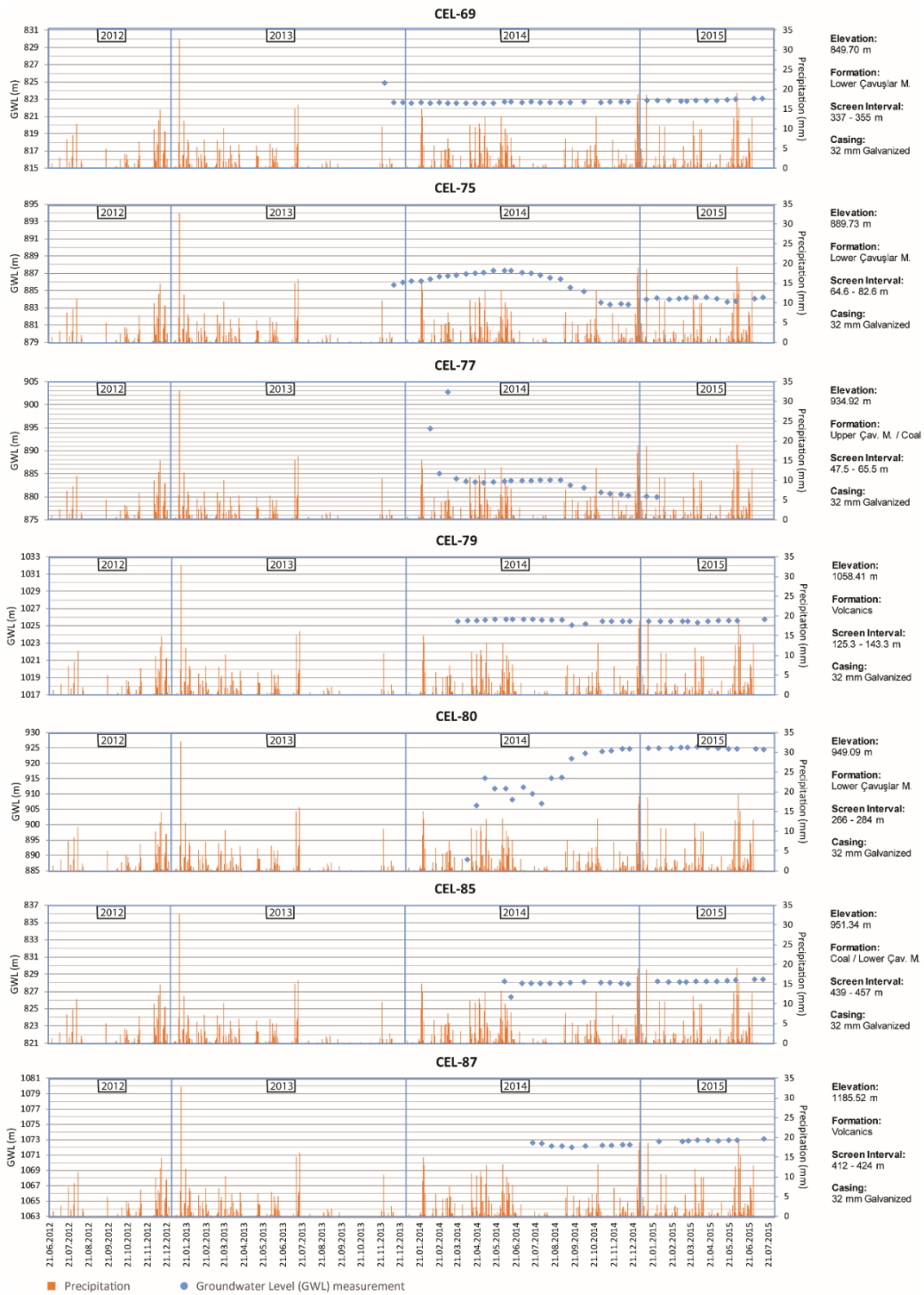


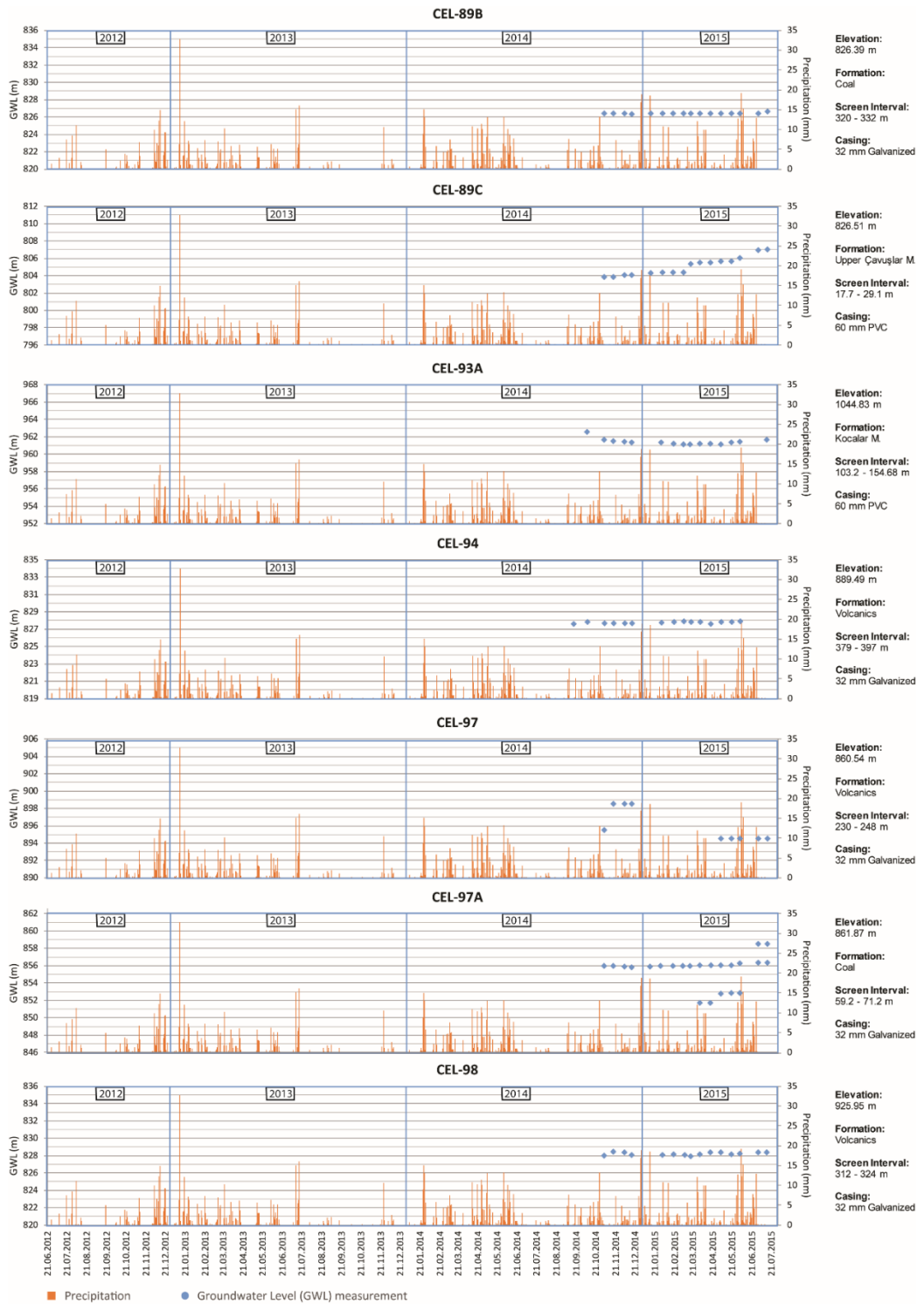


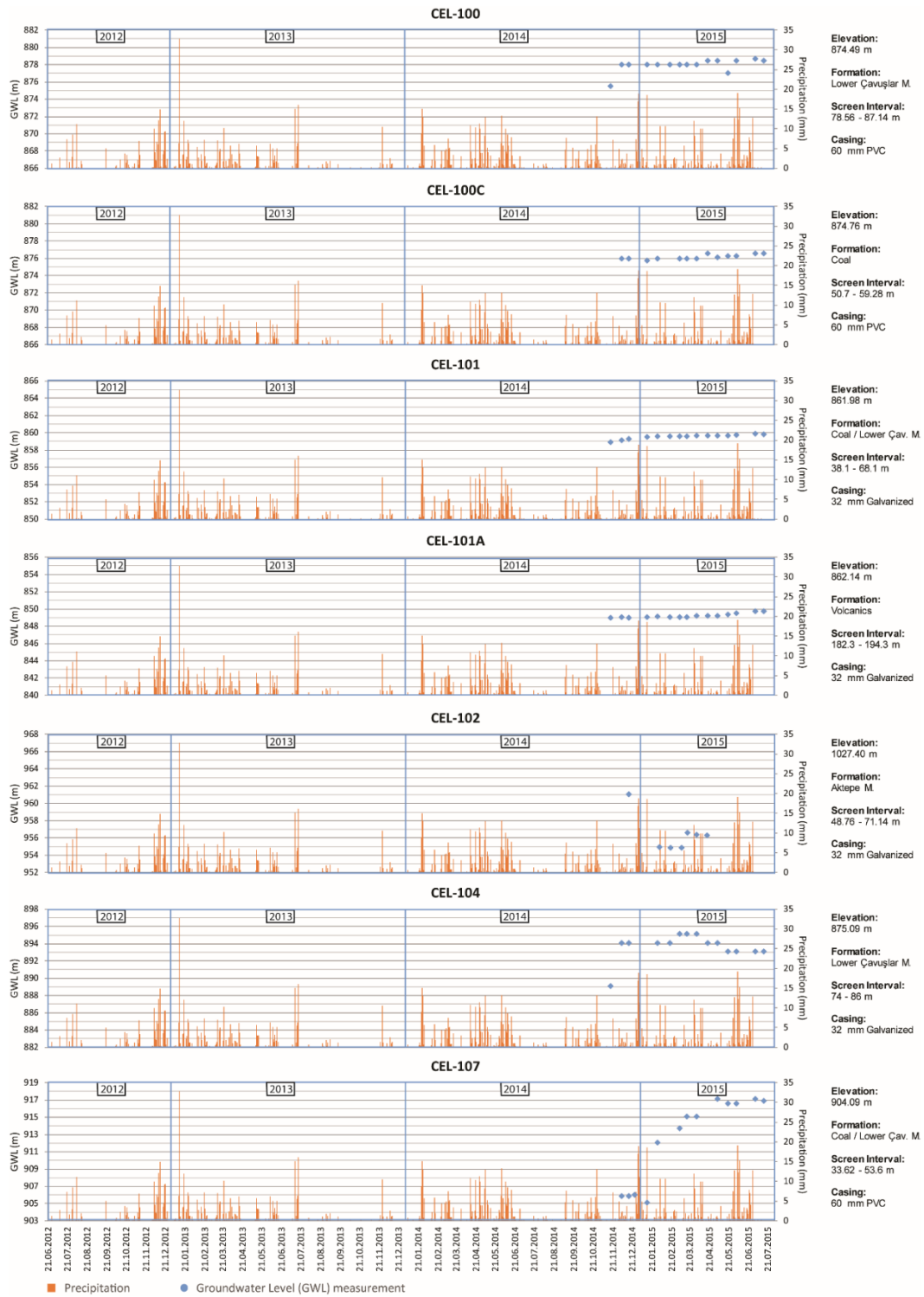


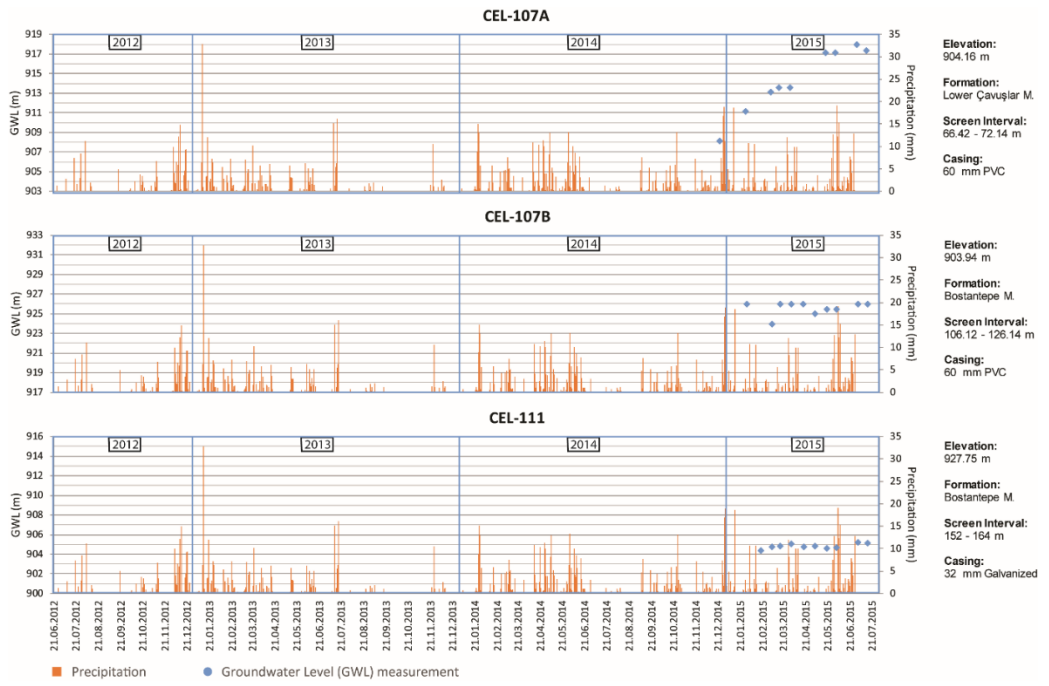














## CURRICULUM VITAE

### PERSONAL INFORMATION

Surname, Name : Peksezer Sayıt, Ayşe  
Nationality : Turkish (TC)  
Date and Place of Birth : 16 September 1984, Ankara  
Phone : +90 312 210 57 41  
E-mail : aysepeksezer@gmail.com

### EDUCATION

<b>Degree</b>	<b>Institution</b>	<b>Year of Graduation</b>
MS	METU Geological Engineering	2010
BS	METU Geological Engineering	2007
High School	Çağrıbey Anadolu High School, Ankara	2002

### WORK EXPERIENCE

<b>Year</b>	<b>Place</b>	<b>Enrollment</b>
2014-2019	METU Geological Engineering	Research Assistant
2012-2013	METU Geological Engineering	Project Engineer
2010-2011	Golder Associates, Turkey	Hydrogeologist

### FOREIGN LANGUAGES

Advanced English, Basic Japanese

### PUBLICATIONS

#### JOURNAL PAPER

1. Peksezer-Sayıt A., Cankara Kadiođlu Ç. and Yazıcıgil H. "Assessment of Dewatering Requirements and Their Anticipated Effects on Groundwater Resources: A Case Study from the Caldag Nickel Mine, Western Turkey", Mine, Water and the Environment, 34, 122-135 (2015)

2. Peksezer-Sayit A. and Yazıcıgil H. “Assessment of Artificial Aquifer Recharges Potential in the Kucuk Menderes River Basin, Turkey”, Hydrogeology Journal, 20, 755-766 (2012)

#### ABSTRACTS / CONFERENCE PROCEEDINGS

1. Yazıcıgil H., Peksezer Sayit A., Yağbasan Ö., Argunhan Atalay Ç. and Kılıç H. “Madencilikte Hidrojeolojinin Önemi ve Problemleri”, Hidro’2018 Hidrojeoloji ve Su Kaynakları Sempozyumu, Ankara – Turkey, September 27-29, 2018 (oral presentation).

2. Peksezer-Sayit A. and Yazıcıgil H. “Uzun Ayak Kömür Madenciliğinin Yeraltısuyu Sistemine Etkileri”, 71.Türkiye Jeoloji Kurultayı, Ankara, Turkey, April, 23-27, 2018 (oral presentation).

3. Yazıcıgil H. and Peksezer-Sayit A. “Dewatering Design for an Open Pit Coal Mine and Assessment of Anticipated Impacts on the Groundwater Resources”, 44th IAH Congress, Dubrovnik, Croatia, Sept 25-29, 2017 (oral presentation).

4. Yazıcıgil H. and Peksezer-Sayit A. “Dewatering Impact Assessment of Longwall Coal Mining on Groundwater Resources in Central Turkey”, 43rd IAH Congress, Montpellier, France, Sept 25-29, 2016 (oral presentation).

5. Peksezer-Sayit A. and Yazıcıgil H. “Groundwater Impact Assessment of Tailings Storage Facility, Western Turkey”, Fall Meeting of the American Geophysical Union, San Francisco, CA, USA, December 14-18, 2015 (poster presentation).

6. Peksezer A. and Yazıcıgil H. “Yapay Yeraltısuyu Beslenimi: Küçük Menderes Havzası’ndan Bir Örnek”, 64. Jeoloji Kurultayı, Ankara, Turkey, April, 25-29, 2011 (oral presentation).

7. Toklu M.M., Peksezer A. and Yazıcıgil H. “Assessment of Potential Seepage beneath the Planned Embankments of the Filyos Stream in Zonguldak”, IAHR Groundwater Symposium, Valencia, Spain, Sep 22-24, 2010 (poster presentation).

8. Peksezer A. and Yazıcıgil H. “Yapay Yeraltısuyu Beslenimi: Küçük Menderes Havzası’ndan Bir Örnek”, 35. Yıl Jeoloji Sempozyumu, Konya, Turkey, Oct 4-7, 2010 (oral presentation).

9. Peksezer A. and Yazıcıgil H. “Artificial Recharge of Groundwater in K. Menderes River Basin”, Fall Meeting of the American Geophysical Union, San Francisco, CA, USA, December 14-19, 2009 (poster presentation).

#### HOBBIES

Reading, Movies, Origami, Swimming